M2NU-16-NE-UNL-030207-021 Deliverable

NEUP Project 16-10214: Final Report

Online Monitoring System for Concrete Structures Affected by Alkali-Silica Reaction

Jinying Zhu [1], Hongbin Sun [1], Clayton Malone [1],
Li Ai,[2],Mahmoud Bayat[2], Paul Ziehl[2],
Taeyong Shin[3], Ying Zhang[3], Eric Giannini [4]

December 2021

[1]The University of Nebraska-Lincoln
[2]The University of South Carolina
[3]Georgia Institute of Technology
[4]RJ Lee Group, Inc

Prepared for the
U.S. Department of Energy
Office of Nuclear Energy
Under Contract DE-NE0008544

DISCLAIMER

Abstract

This report presents a comprehensive study of developing ultrasonic wave and acoustic emission (AE) techniques for long-term monitoring of alkali-silica reaction (ASR) development in concrete. Small, medium, and full-scale concrete specimens were cast, conditioned, and monitored for various periods, from at least one year to 2.4 years. The reactive concrete specimens contain coarse or fine reactive aggregates to study the effects of different types of reactive aggregates. Confinements were also designed to simulate the 2-dimensional confinement effects of reinforcement in the shield building of nuclear power plants. The concrete specimens were stored in a environmental chamber with high humidity and high temperature to accelerate the ASR development.

The ultrasonic monitoring data shows high sensitivity to ASR development and could detect cracking initiation well before visible surface cracks occurred. However, the linear ultrasonic analysis based on wave velocity is strongly affected by temperature variation. Therefore, a nonlinear ultrasonic method was proposed to measure thermally induced nonlinear acoustic responses of concrete (thermal modulation of ultrasonic wave). The measured nonlinear acoustic parameter shows a high correlation with ASR expansion across specimens with different reactive aggregates and confinement conditions. The same conclusion was obtained from nonlinear resonance tests on small concrete prisms. Compared to the linear acoustic methods, the nonlinear tests show high sensitivities to ASR damage from internal microcracking initiation at the early stage to visible cracks at the late stage of ASR. The attributes of the thermal modulation of nonlinear ultrasonic method include high sensitivity, immunity to temperature effects, and strong correlation with ASR expansion, which demonstrate great potentials of the nonlinear ultrasonic method for diagnosis of ASR damage and prediction of concrete deterioration process.

Acoustic emission is a passive sensing technique for damage assessment, and access to only one surface is needed even for thick and heavily reinforced elements such as the walls utilized for nuclear shield building. Additionally, relatively few sensors are required to monitor the progression of the damage process. Results indicate that the AE data can be related to the damage rating index, which is a petrography-based means of assessing damage due to ASR in reinforced concrete. Furthermore, AE is capable of detecting ASR damage long before surface cracking is visually noticeable. Boundary conditions play in important role in the progression of ASR damage and differences in boundary conditions are reflected in the AE data. Entropy based data assessment methods provide a means to assess the damage state, and convolutional neural network based data assessment provided a means to assess the damage state in real-time. Results indicate that artificial neural network models may be used as a means to predict volumetric expansion based on AE data.

Contents

Executive Summary

This report presents a comprehensive study of developing a structural health monitoring (SHM) system for long-term monitoring of alkali-silica reaction (ASR) development in concrete structures. The proposed SHM approaches include the ultrasonic wave and acoustic emission techniques. Both sensing methods have shown high sensitivity to microcrack initiation and development in concrete, and they complement each other in spatial and temporal coverage. The two SHM systems may be integrated into a single acoustic sensing system by using the same sensors for both active and passive acoustic sensing.

Specimens

Small, medium, and full-scale concrete specimens were cast, conditioned, and monitored for various periods, from at least one year to 2.4 years. Each set of concrete specimens include control and reactive specimens, where the reactive specimens contained either coarse (RCA) or fine reactive aggregates (RFA). Confinements were also designed to simulate the 2-dimensional confinement effect of reinforcements in the shield building of nuclear power plants. The concrete specimens were stored in an environmental chamber with high humidity and high temperature to accelerate the ASR development. Through collaboration with University of Tennessee-Knoxville (UTK), the ultrasonic and acoustic emission monitoring systems were installed on the full-scale specimens cast and conditioned at the UTK laboratory. At the end of monitoring periods, the maximum volumetric expansion reached 0.9% on the medium-scale specimens, and 0.46% on the full-scale specimens.

Resonance tests on small specimens

Small concrete prism specimens were cast using the same mix design as for the medium-scale specimens. These prisms were conditioned in an environmental chamber at 38°C and 95% relative humidity, and monitored with linear resonance test and nonlinear impact resonance acoustic spectroscopy (NIRAS) test for over 400 days. The linear resonance test could detect ASR damage in the specimens with coarse reactive aggregate, where the interconnected microcracks reduced the elastic modulus of concrete. In the specimens with fine reactive aggregate, where the microcracks were isolated, the linear resonance method could not detect ASR damage although the specimens showed measurable expansions. The NIRAS results showed high sensitivity to microcracking damage and a strong correlation with ASR expansion. This correlation may be used for quantitative evaluation of ASR damage in small concrete specimens.

Ultrasonic monitoring on medium-scale specimens

On medium-scale specimens, the continuous ultrasonic monitoring data showed high sensitivity to ASR development and could detect cracking initiation well before visible surface cracks occurred. The wave velocity dropped nearly 20% during the monitoring period (more than 400 days) and then became saturated at the late stage. However, the velocity change did not show strong correlation with the ASR expansions, and the linear ultrasonic analysis based on wave velocity is also strongly affected by temperature variation.

Therefore, a nonlinear ultrasonic method was proposed to measure thermally induced nonlinear acoustic response of concrete (thermal modulation of ultrasonic wave). The measured nonlinear acoustic parameter shows a high correlation with ASR expansions in all specimens with different reactive aggregates and confinement conditions. The conclusion is consistent with the nonlinear resonance test results obtained on the small concrete prisms. Compared to the linear acoustic methods, the nonlinear tests show high sensitivities to ASR damage from internal microcracking initiation at the early stage to visible cracks at the late stage of ASR development. The thermal modulation of nonlinear ultrasonic method has the following advantages: high sensitivity, no need of baseline measurement, immunity to temperature effects, and strong correlation with ASR expansion. These attributes demonstrate great potentials of the nonlinear ultrasonic method for diagnosis of ASR damage and prediction of concrete deterioration process.

Acoustic emission monitoring

Acoustic emission (AE) monitoring was pursued for fifteen small-scale concrete specimens in addition to six medium-scale specimens as well as three full-scale specimens. AE is by definition a passive means of structural assessment, and therefore data is produced as damage progresses. AE sensors are very sensitive to damage initiation and growth, and damage progression may be assessed long before surface cracking is noticeable through visual assessment. AE monitoring only needs access to one surface and requires relatively few sensors for the assessment of damage progression. To minimize spurious, or non-genuine AE events in the data set, appropriate means of filtering are required.

The AE analysis methods pursued included intensity analysis, frequency component analysis, and entropy analysis in combination with petrography. In addition, an ASR damage diagnosis method was developed utilizing convolutional neural networks, and a means of prediction for volumetric expansion based on AE data was developed. Results indicate that ASR damage can be detected via AE regardless of the scales investigated. An AE based intensity analysis chart for the classification of ASR damage agreed with the damage rating index achieved through petrographic analysis.

Boundary conditions cause a considerable difference in alkali-silica reaction related damage modes and the effect of boundary conditions was reflected in the AE data. AE was used to calculate signal entropies and to thereby assess the temporal trend of data due to damage progression. Average entropy values generally showed similar patterns to global voltage entropy and counts-entropy.

Monitoring full-scale specimens

Through collaboration with UTK, the ultrasonic and acoustic emission monitoring systems were installed on the full-scale specimens at the UTK laboratory. The AE system focused on the early stage of ASR development (200 days since casting), while the ultrasonic monitoring focused on the late stage of ASR expansion (278 days to 866 days). For both monitoring systems, similar conclusions were obtained from the full-scale and medium-scale specimens. These results validated the developed passive and active health monitoring systems and their applicability to in-situ monitoring of large-scale concrete structures.

Part I

Introduction, Materials, and Tests on Small Specimens

1 Introduction

1.1 Introduction

Alkali-silica reaction (ASR) has been recognized as a degradation mechanism affecting many concrete structures, including bridges, pavements, and dams. ASR is a chemical reaction between the alkali hydroxides in the pore solution of concrete and reactive silica minerals in some aggregates. The reaction product, when absorbing water, will expand and cause cracking and degradation of concrete. Since ASR expansion is a a very slow process, cracks may occur many years or decades after construction. However, once initiated, ASR may be coupled with other damage mechanisms, such as freezing and thawing, corrosion etc., which further accelerate the deterioration of concrete and reduce the durability and capacity of concrete structures.

ASR was recently discovered as a challenge for management of aging concrete structures in nuclear power plant (NPP). In 2010, the shielding wall of Seabrook nuclear power plant in New Hampshire was confirmed to be affected by ASR, which is the first documented case of ASR at nuclear power plants in United States. To ensure safe functions of NPP concrete structures during extended period of operation, research is needed to understand the long term effects of ASR on durability, serviceability, and safety of NPP concrete structures, which will then provide needed technical supports for evaluation of licence renewals of NPPs.

Currently there is no effective way to identify and evaluate ASR damages in the early stage, or predict the expansion rate in future. In current practice, the ASR assessment programs mostly rely on visual inspection for qualitative assessment of surface cracks. However, visual inspection cannot provide reliable information for the internal damage in concrete. Expansion measurement is a common technique for ASR damage assessment, which requires a reference measurement before initiation of ASR expansion. Concrete coring with subsequent petrographic examination [1] may provide more detailed information about the ASR damage in the microscale, but petrographic examination is time consuming and destructive, not suitable for critical and sensitive NPP structures.

Nondestructive testing and evaluation (NDT/NDE) methods, such as vibration-based method, acoustic emission (AE), ultrasonic method, have been studied to assess ASR damage development in concrete. The ultrasonic test method measures stress wave propagating in concrete and evaluates ASR damage by measuring wave velocity or signal amplitude. Because an ultrasonic source is needed to transmit the ultrasonic energy into concrete, it is an active sensing method. AE is a passive sensing method, which detects the energy released from the cracking events in concrete. Both the ultrasonic and the AE methods are suitable for continuous and long-term monitoring.

This NEUP project aims to developing an online health monitoring system to evaluate ASR damage in concrete structure using the active ultrasonic and passive AE sensing methods. This report presents research efforts and findings on using the developed sensing technologies to monitor ASR development in concrete specimens. Specific research objectives and tasks are summarized in the next section.

1.2 Research Objectives and Scope

The objective of this research project is to develop an online structural health monitoring (SHM) system that integrates active and passive sensor networks and advanced signal processing algorithms to monitor ASR induced degradation in concrete structures. Six research tasks were proposed to achieve this research objective. The University of Nebraska-Lincoln (UNL) team was responsible for ASR concrete specimen fabrication (Task 1) and ultrasonic monitoring research (Task 2); the University of South Carolina (SC) team led the AE monitoring research (Task 3); and Georgia Institute of Technology (GT) contributed to diagnosis and prediction models based on the monitoring data (Task 5). The UNL and SC teams collaborated with the University of Tennessee-Knoxville (UTK) team to test on full-scale concrete specimens with ASR damage (Task 6). Detailed efforts and findings are presented in this final report.

This final report includes three Parts and 9 Chapters.

- **Part I: Introduction, Specimens, and Tests on Small Specimens**

    1. Chapter 1 is the introduction and research objective.

2. Chapter 2 presents concrete specimen design and fabrication (Task 1). Two sets of medium-size concrete specimens (six specimens) were cast for long-term monitoring at UNL and SC laboratories.
3. Chapter 3 presents nonlinear resonance tests on small-scale concrete prisms for over one year. A strong correlation is found between the nonlinear resonance parameter and ASR expansion, which provides a quantitative NDE method for evaluation of ASR damage at the early stage for small concrete specimens (Task 4).

- **Part II: Monitoring Medium-Scale Concrete Specimens** Part II presents ultrasonic and AE monitoring results on medium-scale concrete specimens.

4. Chapter 4 describes development of the ultrasonic monitoring system and wave velocity monitoring results. The specimens were monitored for more than 500 days. It was found the wave velocity dropped nearly 20% and then saturated after 400 days of conditioning. Limitations are discussed regarding the linear ultrasonic wave method (Task 2).
5. In Chapter 5, a new nonlinear ultrasonic wave technique was proposed. The proposed thermal modulation method uses temperature variation as a driving force for nonlinear response of materials. Wave velocities on the specimens with ASR damage demonstrated higher sensitivity to temperature change than on the control specimens. The nonlinear ultrasonic technique does not need baseline measurements and shows great potential for ASR damage assessment and prediction of ASR expansion.
6. Chapter 6 presents AE monitoring results on medium-scale specimens. An ASR damage diagnosis method was developed through utilizing a convolutional neural network approach. (Task 3)
7. In Chapter 7, machine learning techniques were developed to analyze ultrasonic and AE data and detect ASR initiation. (Task 5)

- **Part III: Monitoring Full-Scale Concrete Specimens.** Part III presents ultrasonic and AE monitoring results on full-scale concrete specimens at UTK. (Task 6)

8. Chapter 8 first describes the design of full-scale concrete specimens at UTK, then presents the development of a long-term ultrasonic monitoring system and the monitoring results. The ultrasonic monitoring started after visible cracking on the ASR specimens (275 days) and ended at 866 days. It was found the linear

analysis of wave velocity could not differentiate the ASR specimens from the control specimen. Then the thermal modulation of nonlinear ultrasonic wave analysis method was proposed.

9. Chapter 9 presents acoustic emission monitoring on full-scale specimens.

1.3 Conclusions and Recommendations

This report presents a comprehensive study of developing ultrasonic and acoustic emission techniques for long-term monitoring of ASR development in concrete structures. Both the ultrasonic and acoustic emission systems were used to monitor medium-scale and full-scale concrete specimens with different expansion rates and confinement conditions. Resonance tests and acoustic emission were also used to monitor ASR development in small concrete prism specimens.

The ultrasonic monitoring data shows high sensitivity to ASR development and could detect cracking initiation well before visible surface cracks occurred. However, the linear ultrasonic analysis based on wave velocity is strongly affected by temperature variation. Therefore, a nonlinear ultrasonic method was proposed to use measure thermally induced nonlinear acoustic response of concrete (thermal modulation of ultrasonic wave). The measured nonlinear acoustic parameter shows a high correlation with ASR expansion across specimens with different reactive aggregates and confinement conditions. The same conclusion was obtained from nonlinear resonance tests on small concrete prisms. Compared to the linear acoustic methods, the nonlinear acoustic test methods show high sensitivities to ASR damage from internal microcracking initiation at the early stage of ASR to visible cracks at the late stage. Research findings show that thermally induced nonlinear ultrasonic wave is a promising nondestructive evaluation (NDE) method for in-situ evaluation of large concrete structures with microcracking damage.

Acoustic emission is a highly sensitive means of detecting damage progression in reinforced concrete, and only needs access to one side of relatively thick concrete structural elements. Due to the high sensitivity of the acoustic emission method damage progression can be detected and assessed long before surface cracking becomes noticeable. Findings indicate that acoustic emission data can be utilized to assess the damage state of thick, reinforced concrete structures using relatively few sensors. The intensity analysis chart provides one means of assessment that can be correlated to the petrographic-based damage rating index. Entropy based methods showed promise for assessing damage progression, and boundary conditions were reflected in the acoustic emission data as is expected due to the differing modes of damage progression caused by differing boundary conditions. Classification of different damage phases was achieved through entropy based methods and damage classification in real time was demonstrated using convolutional neural networks. Prediction of volumetric expansion based on acoustic emission data was also demonstrated.

Recommendations The developed thermal modulation of nonlinear ultrasonic method has the following advantages: high sensitivity, immunity to temperature effects, no need of baseline measurement, and strong correlation with ASR expansion. These attributes show great potentials of using the nonlinear ultrasonic method for diagnosis of ASR damage and prediction of concrete deterioration process.

Entropy based acoustic emission methods show great promise for classification of ASR damage phases even in very thick reinforced concrete elements using relatively few sensors. Convolutional neural networks showed substantial promise for achieving similar damage classification in real time. The use of the intensity analysis chart was likewise promising for damage classification and was correlated to a petrography-based damage rating index. It is recommended that these means of damage classification be further explored and validated in field settings.

2 ASR Specimen Design and Fabrication

This chapter presents the concrete mixture designs and proportions, specimen designs and fabrication details, specimen conditioning, and the fresh and hardened concrete properties. ASR expansion data are also presented.

2.1 Materials Selection and Specimen Design Philosophy

ASR damage development and cracking patterns can be influenced by a number of variables, including, but not limited to: the type, particle size, and distribution of reactive aggregates, the presence of reinforcement and degree of confinement provided, the dimensions of the concrete element, external boundary conditions, and the environmental exposure conditions.

In the context of this project, it was desirable to determine if SHM data could be generally correlated to the total amount of ASR distress, or if the data are influenced in part by these variables. For example, the presence of reactive coarse aggregates will cause ASR damage to be initiated in and propagate from fewer, more widely-distributed points in the concrete matrix than if a reactive fine aggregate is present. Cracking patterns, particularly at the concrete surface, are influenced by confining stresses provided by reinforcement, and align with the direction of principle reinforcement. In the case of certain NPP structures, there is heavy reinforcement in two planar directions (x and y), but no transverse reinforcement in the third (z) direction (thickness). This has the effect of forcing the bulk of the volumetric expansion to occur in the third, z-direction, but does not significantly reduce the total volumetric expansion compared to a completely unconfined structure. By forcing the damage to occur in the z-direction, much of the distress is not observable from the x-y plane, thus heightening the need for advanced sensing systems that can detect this distress. This project permits investigation of the effects of confinement (2-D reinforcement or unreinforced) and reactive aggregate particle size (coarse or fine) on the acquired SHM data.

Although it was important to simulate a high degree of ASR damage within the time constraints of the project, it was deemed critical that the concrete mixture not have such a high degree of reactivity that ASR may initiate long before SHM activities could begin; this was particularly important given that the specimens were not cast independently at UNL and SC. This influenced the selection of highly-reactive aggregates that had been proven through prior laboratory testing to have an initial dormant period of one to two months to permit time for proper curing, transport, and instrumentation of the specimens prior to the initiation of ASR.

Specimen size was influenced by the logistics of fitting sufficient specimens into environmental chambers at USC and UNL capable of conditioning the specimens at 38°C and >95% relative humidity, and the desire that the specimens be as large as practically feasible. Small specimens in such a conditioning environment are known to suffer from alkali leaching, which limits the ultimate progress of ASR [2, 3]. Larger specimens are also easier to reinforce, permit more extensive instrumentation networks, and allow for the extraction of many core samples for forensic and SHM validation purposes at the conclusion of testing. Thus, a specimen dimension of 12 × 12 × 44 inches was chosen.

The materials selection and specimen design was also influenced by the mockup specimens cast at the University of Tennessee-Knoxville (UTK) in 2016 [4], which were used for validation of the SHM methods on full-scale concrete containment wall specimens in this project. The same reactive coarse aggregate from North Carolina that was used for the UTK specimens was also selected for this project, and the reinforcement layout was as similar as a possible given the size constraints for specimens cast for this project. No. 7 headed reinforcing bars were used to provide 2-D confinement with fully-developed reinforcement. For the second reactive aggregate, a highly-reactive fine aggregate from Robstown, Texas was selected. This aggregate is somewhat less-reactive than the more widely-known Jobe aggregate from Texas, but exhibits a critical dormant period necessary to support the SHM activities of this project.

2.2 List of Specimens and Nomenclature

This section introduces specimen nomenclature and test matrix information. For clarity, the nomenclature discussed here will not be mentioned throughout most of this report. Six beam specimens (12x12x44 inches) were cast for the UNL and the SC teams. These specimens are called “medium size” or ”large” specimens in this report to be differentiated from “small” prism specimens (3x3x11.25 inches) and "full-scale" specimens at UTK.

Depending on the reactive aggregates used in mix designs, the specimens are named as Control or "CTRL" (no reactive aggregate), RCA (reactive coarse aggregate), and RFA (reactive fine aggregate). The prefix "UNL-" or "SC-" indicates the conditioning and monitoring locations. The suffix "-2D" is added to specimens with 2D reinforcement confinement. For example, "UNL-RCA-2D" refers to the specimen conditioned at UNL, containing reactive coarse aggregate and reinforced with 2D headed rebars. The prefix "UNL" or "SC" is only used in this chapter. Becasue the UNL team only used the "UNL-" specimens for ultrasonic monitoring, and the SC team only did acoustic emission (AE) monitoring on the "SC-" specimens, the prefix is omitted in the following chapters for clarity. All ultrasonic results were obtained from the "UNL-" specimens and all AE results were obtained from the "SC-" specimens unless specified otherwise.

At UNL site, in addition to the six medium-scale specimens, two smaller beams (12"x12"x24") were cast in August 2019 using the RCA aggregates. These two beams were also conditioned in the same chamber and monitored using the ultrasonic system.

Table 2.1 shows all medium-scale specimens cast for long-term health monitoring. The "SC-" specimens with casting date of April 2017 were cast at University of Alabama (UA) and then shipped to SC. All other specimens were cast at UNL.

Table 2.1: List of specimens and casting dates

Specimen ID	Cast date	Monitoring technique
UNL-CTRL, UNL-RCA, UNL-RCA-2D	10/2018	Ultrasonic
UNL-CTRL-2D, UNL-RFA, UNL-RFA-2D	01/2019	Ultrasonic
UNL-sRCA, UNL-sRCA-2D (12"x12"x24")	08/2019	Ultrasonic
SC-CTRL, SC-RCA, SC-RCA2D	04/2017	AE
SC-CTRL-2D, SC-RFA, SC-RFA-2D	01/2019	AE

In addition to these medium-scale beam specimens, prisms with dimensions of 3x3x11.25 inches were also cast using the Control, RCA, and RFA mix designs. The small-scale prisms were also conditioned in the same condition as the medium-scale specimens, and experimental results on these prisms are presented in Chapter 3.

2.3 Material Properties and Mix Design

2.3.1 Material Properties

Aggregate Properties

Four different aggregates were used for this project: a reactive coarse aggregate from Gold Hill, North Carolina and a reactive fine aggregate from Robstown, Texas, and a non-reactive coarse and non-reactive fine aggregate from Omaha, Nebraska, with similar gradation as the two reactive aggregates. Pictures of the four aggregates are shown in Figure 2.1. Specific gravity (SG), absorption, dry rod unit weight (DRUW), and gradation of the four aggregates were determined based on ASTM C127 (2015), ASTM C128 (2015), ASTM C29 (2017), and ASTM C136 (2014) respectively. The aggregate properties determined by the mentioned tests are listed in Table 2.2 and the gradation are shown in Figure 2.2.

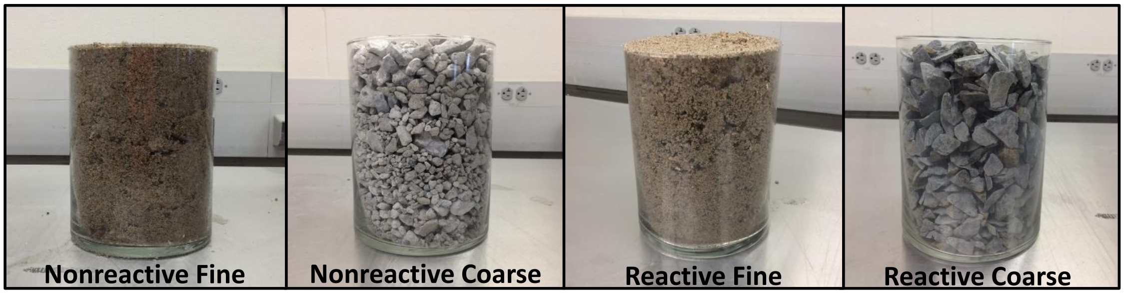

Figure 2.1: Aggregates used in study

Table 2.2: Aggregate properties

Label	Location	SG (SSD)	Absorption	DRUW (lb/ft^3)
A	Nebraska	2.617	2.57%	103.97
B	Nebraska	2.651	0.42%	-
C	North Carolina	2.722	0.39%	92.42
D	Texas	2.658	0.70%	-

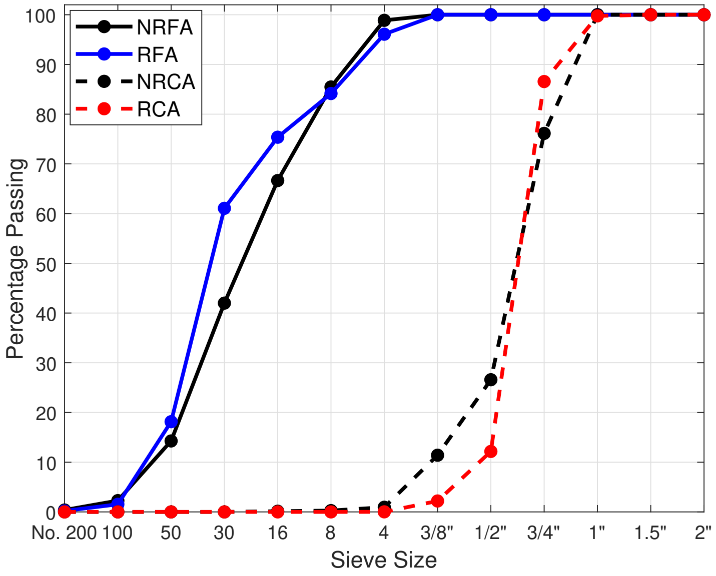

Figure 2.2: Sieve plot (aggregate gradation)

Cement

ASTM C150 (2018) Type I/II Portland cement was used as cementitious material in the concrete. The chemical compositions and physical properties of cement used in the study are reported in 2.3.

Table 2.3: Cement properties

Chemical Properties	Oxide (%)	SiO_2	20.4
		Al_2O_3	4.1
		$Fe_2O_3$3	3.1
		CaO	63.8
		MgO	2.3
		SO_3	2.7
	Na_2O_{eq}		0.47
	Loss on Ignition		2.5
Physical Properties	Blaine Fineness, m^2/kg		443
	Specific Gravity		3.15

Chemical admixtures

A polycarboxylate-based HRWR was used to enhance the flowability of the concrete. The recommended dosage of the HRWR is 3-12 fl oz/cwt.

2.3.2 Formwork and Rebar Design

Formwork Design

Wooden formwork was prepared for the casting of the specimens (12”×12”×44”), as shown in Figure 2.3. The inner material of the formwork used is a 3/4 in. white medium-density fiberboard. The fiberboard was used to ensure a smooth concrete surface. Additional plywood was installed along the perimeter of the form to add strength and stability. High strength wood screws were used. A thin plastic sheet was placed on the bottom of the form to allow for easy specimen movement once it was demolded. To prevent concrete leakage hot glue was used to seal the edges of the form.

Figure 2.3: Formwork Design

Rebar Design

Reinforced specimens were cast to simulate field performance of concrete, as shown in Figure 2.4. The specimens cast were either unconfined or 2-D reinforced. The reinforcement pattern consisted of four 40 in. #7 bars (Grade 60) in the longitudinal direction and twelve 9 in. #6 bars (Grade 60) in the vertical direction. All rebar used was headed rebar. The rebar was fastened together using cable ties.

The rebar was placed into position and supported in the form by four small metal rods,as shown in Figure 2.5. Small holes were drilled into the form to allow the rods to pass through. After casting, the metal rods were cut to a short length for safety. To connect the rebar to the rods, cable ties were placed around the rebar and pulled until fastened tightly.

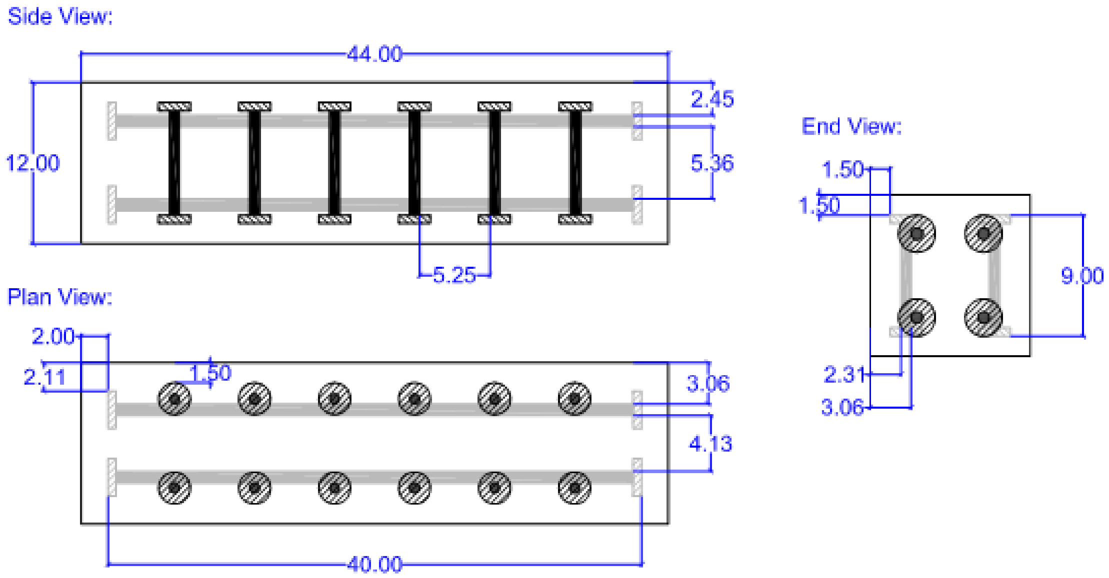

Notes:
2.45" and 3.06" cover to #7 bars.
Least cover= 1.5" (to #6 T-head)
Darker shade indicates that component is in front/top.

Figure 2.4: Specimen 2-D Reinforcement Plan

2.3.3 Mix Design

All specimens involved three different concrete mix designs: (1) a Control mix using innocuous coarse (aggregate A) and fine aggregates (aggregate B), (2) a RCA reactive mix using a reactive coarse aggregate (aggregate C) and an innocuous local fine aggregate (aggregate B) with added NaOH to boost the alkali content to 1.50% Na_2Oeq by mass of cement, and (3) a RFA reactive mix using a reactive fine aggregate (aggregate D) and an innocuous local coarse aggregate (aggregate A) with added NaOH to boost the alkali content to 1.50% Na_2Oeq by mass of cement. The admixture was added into the mixing water prior to mixing. Detailed mix designs are shown in Table 2.4.

To allow for a highly reactive mix design, a sodium hydroxide solution was added to the mixing water of the reactive specimens. The 50/50 NaOH solution was added in a quantity to bring the total alkali loading of the concrete to 1.50% Na_2Oeq by mass of cement. While handling the chemical directly, proper personal protective equipment (PPE), including a rubber apron, goggles, and gloves was always utilized.

Figure 2.5: Rebar Placed in Formwork Prior to Casting

Table 2.4: Theoretical Mix Design (SSD)

Component	Control	RCA	RFA
Cement (lb/yard^3)	590	590	590
Water (lb/yard^3)	295	295	295
Coarse aggregate (SSD) (lb/yard^3)	1900	1751	1846
Fine aggregate (SSD) (lb/yard^3)	1195	1415	1252
HRWR (oz./cwt.)	4	4	4
50/50 NaOH, lb	0	15.69	15.69
w/c	0.50	0.50	0.50

For each reactive mix, prior to mixing, the 50/50 NaOH solution was diluted into the one half of the mixing water (approximately 25 lbs.). The NaOH solution was added to the mixer with the first half of the mixing water with the coarse aggregate. The diluted NaOH solution was handled with care and proper PPE including long sleeves, safety glasses and long rubber gloves was always utilized to protect against coming into contact with the chemical.

2.3.4 Concrete Mixing and Casting

Mixing Procedure

Prior to mixing, all materials were gathered and prepared approximately 24 hours in advance. Moisture contents of aggregates used in each batch were measured with a representative sample prior to batching and the amount of water in each batch were adjusted accordingly. To ensure no changes in moisture content, all mixing materials were kept inside and covered prior to mixing.

A drum mixer with a capacity of 9 cubic feet was used in all medium-scale specimen preparation. The mixing power is 8 horse power. At the beginning of each mix, water was poured into the mixer and the mixer was turned on for approximately one minute to moist the inside of mixer. To help to ensure the consistency of material collected from the mixer, the mixer was "buttered" in accordance with ASTM C192 (2007). "Buttering" the mixer involves mixing a small batch of 1 ft3 using the same mixture proportions to simulate the test batch. The mortar left on the inside of the mixer will help compensate for the loss of mortar during batching.

Concrete was mixed in accordance with ASTM C192 (2007). For the reactive mixes, slight variances from the standard mixing procedure were made. Once the mixer has been moist and "buttered", the coarse aggregate and half of the mixing water were added. For non-reactive batches the high-range water-reducer was included in the initial water added. For reactive batches the 50/50 NaOH solution was added with the initial water and the HRWR was added with the remaining water.

Casting and Curing

After mixing, the concrete was then transported to the location of forms for the medium-scale specimens, cylinders and prisms using a wheel barrow and deposited using a scoop or a shovel. The 4"x8" cylinders were cast in accordance with ASTM C192 (2007). The 3"x3"x11.25" prisms were filled in one layer and a vibration table was used to consolidate the concrete. The 12"x12"x44" medium-scale specimens were filled in two layers each being vibrated with an internal vibrator. The second layer was vibrated approximately 1 inch deep into the first layer. The four corners of each specimen were vibrated, along with vibration in the middle of the specimen spaced at approximately 10 inches apart.

After both layers of the specimens were consolidated, the surface was carefully finished with a 14-inch trowel. The specimens were then covered with moist towels and then plastic sheet to ensure the moisture was retained. After 24 hours, the specimens were demolded. The cylinders were moved to the curing room until testing was performed. The medium-scale specimens and prisms were kept in the lab, under the same curing conditions, covered with wet towels and plastic sheet for 28-days.

2.4 Concrete Testing and Properties

2.4.1 Fresh Concrete

Fresh concrete testing was done prior to casting to ensure the required fresh concrete properties were met. Slump, unit weight, air content, and temperature of each cast batch were measured per ASTM C143 (2015), C138 (2017) and C231 (2017) respectively and the results are summarized in Table 2.5.

Table 2.5: Fresh Concrete Property Summary

Specimen	Cast Date	Air Content (%)	Unit Weight (lb/ft^3)	Slump (in.)
UNL-CTRL	09/14/2018	1.5	150.7	5.00
UNL-RCA	10/09/2018	1.4	153.9	5.00
UNL-RCA-2D	10/16/2018	1.4	155.5	4.00
UNL-CTRL-2D	01/17/2019	1.5	142.1	7.50
UNL-RFA	01/21/2019	3.0	152.8	2.75
UNL-RFA-2D	01/22/2019	3.0	151.2	6.50
SC-CTRL	12/19/2018	1.5	151.2	4.50
SC-RFA	12/26/2018	3.0	148.6	5.25
SC-RFA-2D	12/26/2018	3.0	146.8	4.75

2.4.2 Hardened Concrete Testing

After curing of the specimens hardened concrete property tests were performed to verify the quality of the specimens. The hardened properties tested included the compressive strength at 7 and 28 days were measured per ASTM C39 (2010) and results are shown in Table 2.6.

Table 2.6: Hardened Concrete Property Summary

Specimen	f_c' (7-day) (ksi)	f_c' (28-day) (ksi)
UNL-CTRL	3.95	5.39
UNL-RCA	3.09	4.66
UNL-RCA-2D	3.32	-
UNL-CTRL-2D	3.86	5.42
UNL-RFA	4.22	4.9
UNL-RFA-2D	4.00	4.6
SC-CTRL	4.59	6.30
SC-RFA	4.40	5.95
SC-RFA-2D	4.27	5.39

2.5 Conditioning plan

2.5.1 Specimens Storage Before Conditioning

To minimize the impact of the age of specimens to ASR expansion, all medium-scale specimens were cured in a moist condition (covered with moist towels and plastic sheets) in room temperature for a minimum of 28 days before being moved into the environmental chamber for conditioning . As shown in Figure 2.6, the specimens were moved from the curing area to the area outside of the chamber using a overhead crane in the laboratory. To move the specimens into the chamber, high-strength carts were used to push the specimens up a small ramp. The specimens remain on these carts for convenient movement.

Figure 2.6: Moving specimens in the laboratory using crane and supporting carts.

2.5.2 Environmental Chamber and Layout

A walk-in environmental chamber with footage of 90” by 136” (total floor area 85 square feet) was used for all medium-scale specimens conditioning. A photo of the layout of the environmental chamber is shown in Figure 2.7. All medium-scale (12” × 12” × 44”) specimens were stored inside along with select prisms and cylinders which are stored on a large heavy-duty rack. Cables for data acquisition from sensors were run through a small hole in the back of the chamber to an external data logger.

Figure 2.7: Environmental chamber and specimen storage layout.

2.5.3 Conditioning and Measurement

The environmental chamber was set to a temperature of 38°C and a humidity of 95% to accelerate ASR activity. Measurement was taken every two weeks. Prior to each measurement of specimen expansions, the chamber temperature is set to 23°C overnight. When the internal temperature of the specimens reach a stable 23°C, expansions are measured on the medium-scale specimens, and other NDT tests are performed on small scale prisms. The entire shut off period typically lasts for less than 24 hours.

2.6 Sensors and Monitoring

2.6.1 Sensors for Ultrasonic Monitoring

For ultrasonic monitoring at UNL, acoustic emission (AE) sensors R15I-AST and R6I-AST by Mistras were used as ultrasonic receivers (see Figure 2.8). Piezoceramic (PZT) disks were used as the ultrasonic transmitter (Figure 2.8(b). Each specimen has one PZT transmitter and multiple receivers, and the receiver layout had changed during monitoring. Details can be found in Chapter 4.

Figure 2.8: ASR sample: (a) top and left surfaces, (b) top and right surfaces, with the PZT transmitter highlighted.

2.6.2 Temperature Sensors

Thermocouples were used for monitoring the surface and internal temperature of the concrete samples.One thermocouple was glued on the surface of the control sample measuring the surface temperature, as shown in Figure 2.9(a). Another thermocouple was embedded in the ASR unconfined sample to measure the internal temperature, as shown in Figure 2.9(b). Since all the samples were conditioned in the same chamber environment, the measured surface and internal temperature data can represent the temperatures for the three samples. A TC-08 thermocouple data logger (PICO Technology, UK) was used for the temperature recording, as shown in Figure 2.9(c).

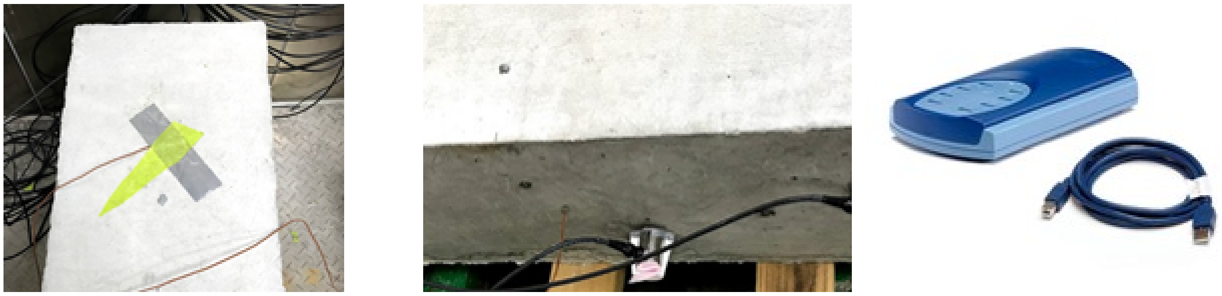

(a) (b) (c)

Figure 2.9: (a)Thermocouple on surface, (b) Embedded thermocouple, (c) Temperature data logger.

The chamber temperature and humidity were monitored using a DH22 sensor. The temperature and humidity data were acquired by a Python program on a Raspberry Pi 3, as shown in Figure 2.10. All the data were immediately uploaded to Google drive for instant monitoring.

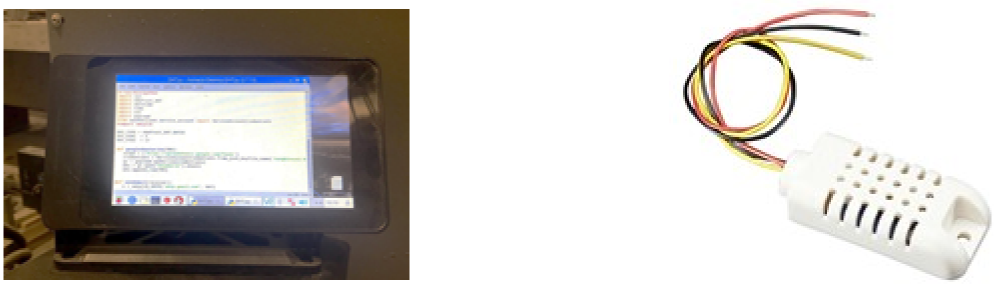

(a)

(b)

Figure 2.10: (a) Raspberry Pi 3, (b)Temperature and humidity sensor for chamber environment monitoring.

2.6.3 DEMEC Target Installation and Monitoring

The demountable mechanical strain gauge (DEMEC) were used to monitor the expansion of specimens. The gauge length 150 mm was used along the transverse and vertical directions, and the 500 mm gauge length was along the longitudinal direction. Stainless steel DEMEC targets were installed on five sides of every specimen. Fast-setting, high-strength epoxy (Double/Bubble®) was used to glue the DEMEC targets to concrete surface. Targets were covered with tape until the epoxy hardens. Once the targets were installed, the distance between the two target locations were measured using the DEMEC mechanical strain gauge. The targets and the mechanical strain gauge are shown in Figure 2.11. The DEMEC target design layout is illustrated in Figure 2.12 .

(a) (b)

Figure 2.11: (a)DEMEC targets on specimen, (b) DEMEC mechanical strain gauge (150 mm).

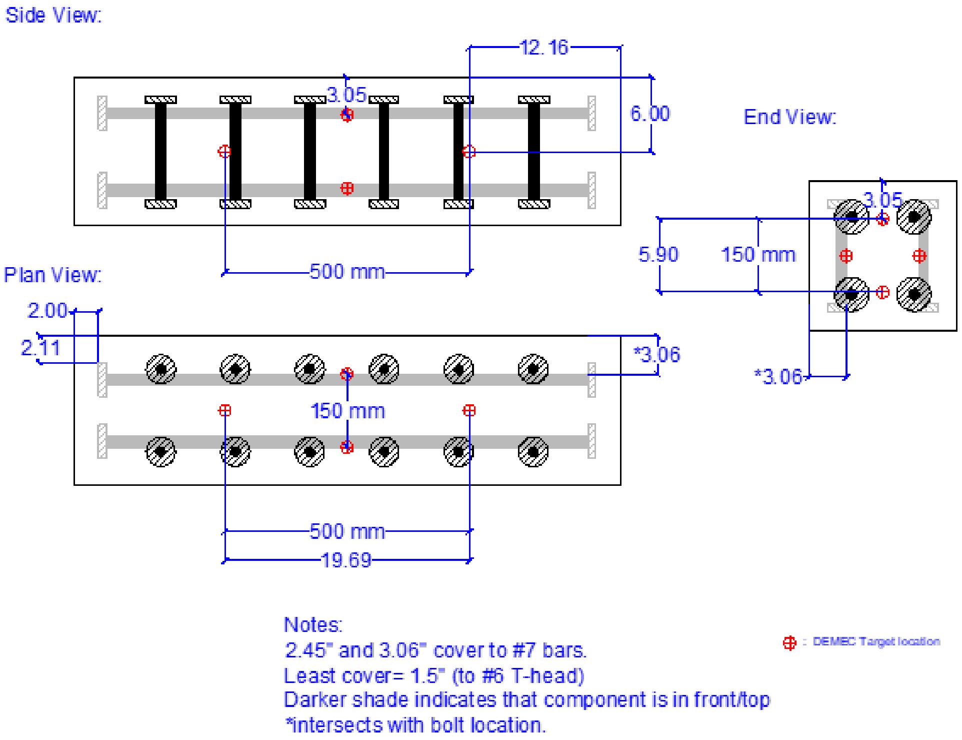

Notes:
2.45" and 3.06" cover to #7 bars.
Least cover= 1.5" (to #6 T-head)
Darker shade indicates that component is in front/top
*intersects with bolt location.

Figure 2.12: DEMEC target design layout.

2.7 Expansion Measurements

Expansion measurement results from all medium-scale specimens are presented in this section. Expansions were measured in three directions (longitudinal, transverse and vertical directions). The longitudinal measurements include two side surfaces and the top surface, and an average of the three surface measurements was taken. The transverse expansion was based on three surface measurements (two ends and the top) and vertical expansion was based on four surface measurements (two sides and two ends). The volumetric expansion was the summation of the average expansions in longitudinal, transverse, and vertical directions. For concrete structures affected by ASR, the volumetric expansion is usually used to represent the global ASR damage.

For “UNL-” specimens, expansions were measured every two weeks; for “SC-” specimens, the expansions were measured every month.

2.7.1 Expansion results on ”UNL-” specimens

Volumetric expansion

Figure 2.13 plots the volumetric expansion histories for all “UNL-” specimens. In both the medium-scale RCA and RFA specimens (see Figure 2.13(a)(b)), the unconfined ASR (RCA and RFA) and reinforced ASR (RCA-2D, RFA-2D) specimens show different expansions, although the ASR specimens cast from the same group were supposed to have similar volumetric expansions. The difference in the volumetric expansions could be caused by variations in casting. Due to capacity limit of the concrete mixer, only one medium-scale specimen could be cast from each batch of concrete mix. Therefore, RCA and RCA-2D were cast from two mixes. Although they had the same mix design, small variations in water content and consolidation could affect their properties. The sudden increase of expansion rate may indicate crack initiation due to ASR development. Although RCA and RCA-2D specimens have different volumetric expansions, cracks initiated around 69 days in both specimens. The chamber was malfunctioning from 302 to 343 days (Figure 2.13(a)). No expansion was measured during this time. The control specimen had no expansion during the entire monitoring period.

As designed, the volumetric expansions in RFA specimens developed at slower rates than

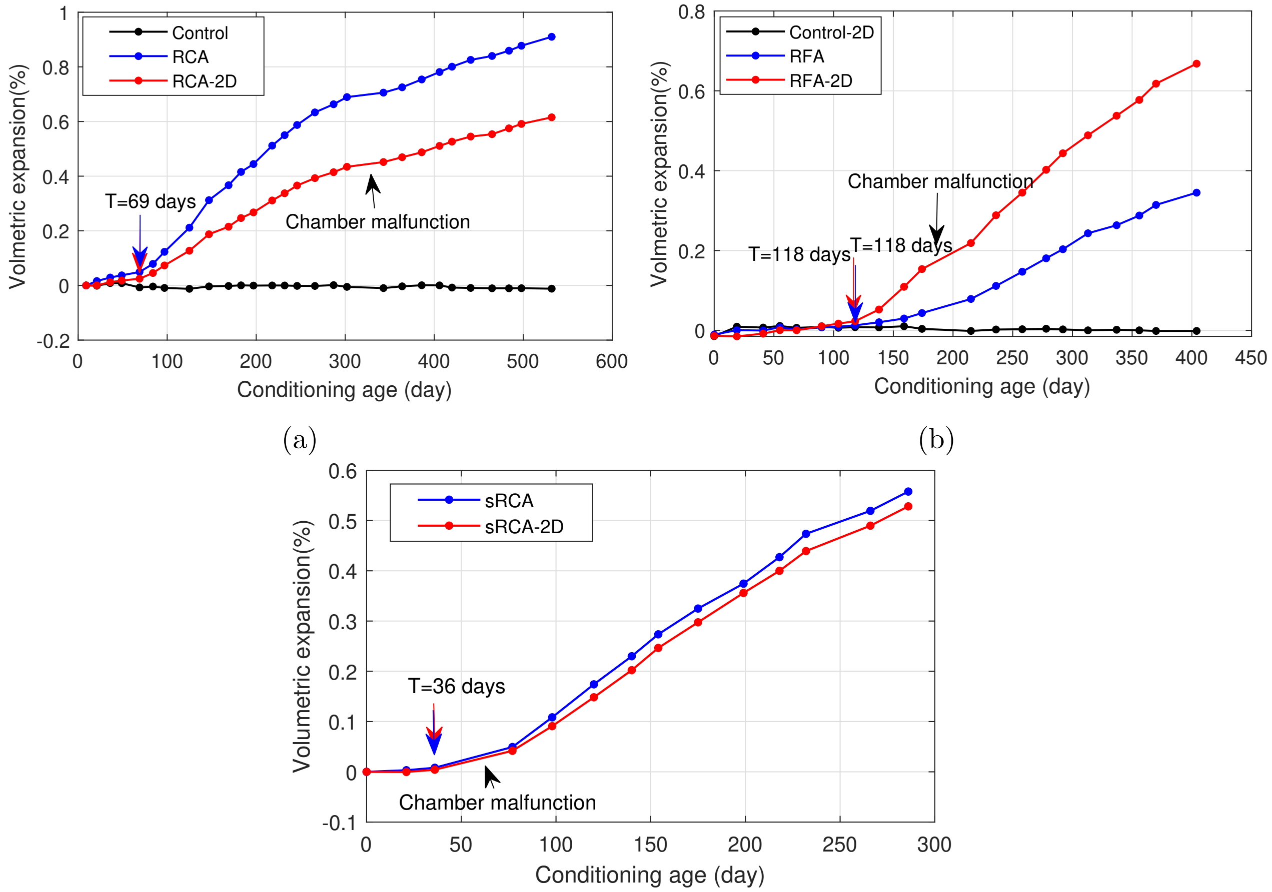

(a) (b)

(c)

Figure 2.13: Volumetric expansion histories of ”UNL-” specimens. : (a) Control, RCA, RCA-2D specimens, (b) Control-2D, RFA, and RFA-2D specimens, (c) Small RCA (sRCA) and Small RCA-2D (sRCA-2D) specimens

in the RCA specimens. Crack initiated in both RFA specimens around 118 days. Similar to the RCA case, the two RFA specimens showed different expansion rates because they were cast from different mixes.

The two small RCA specimens (sRCA and sRCA-2D) were cast from the same batch of concrete mix. Their expansion curves showed very similar volumetric expansion histories (Figure 2.13(c)). It demonstrates that the casting process will affect the ASR development process even with the same mix design. Since crack initiation occurred during the chamber malfunctioning period, the initiation dates should be between 36 days and 84 days. The actual initiate dates were around to 60 days and close to the initiation date of the medium-scale RCA specimens. Detailed results of ASR damage in UNL specimens are presented in Chapter 4.

2.7.2 Expansion results on ”USC-” specimens

Specimens RCA, RCA-2D, and control were conditioned for 300 days. The ”confined” specimen in this section refers to RCA-2D, whereas the ”unconfined” specimen with reactive coarse specimen is referred to as RCA. The volumetric strains of the three specimens are illustrated in Figure 2.14(a). Based on the measured volumetric expansion, the crack initiation date was around 80 days. Specimens RFA, RFA-2D, and Control-2D were conditioned for 250 days.

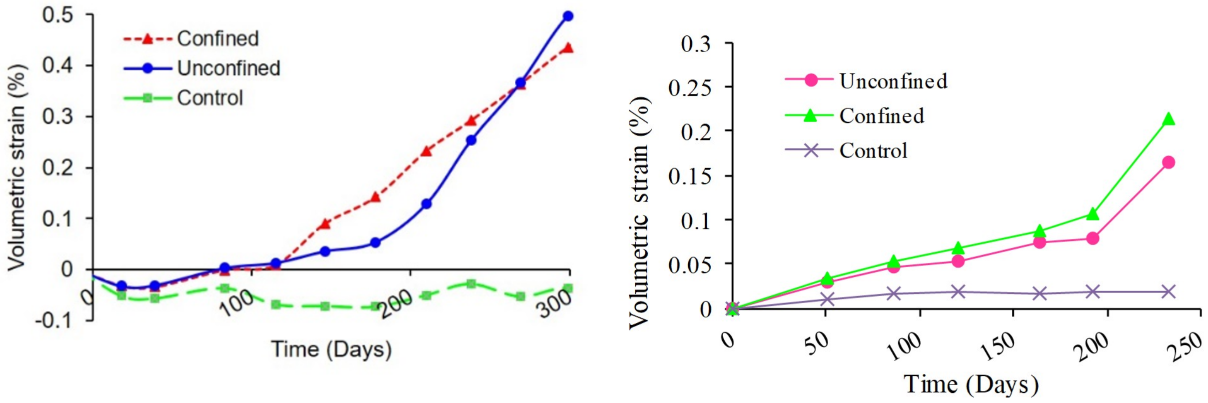

(a) (b)

Figure 2.14: Volumetric expansion histories of ”SC-” specimens: (a) Control, RCA, RCA-2D specimens, (b) Control-2D, RFA, and RFA-2D specimens

3 Nonlinear Resonance Tests of Small Concrete Prisms

This chapter presents continuous expansion and NDT monitoring results on small-scale concrete prisms. Two mix designs were used to cast the prism specimens. Group 1 prisms used the same mix designs as for the medium-size specimens (Control, RCA, RFA), and group 2 prisms followed the specifications of ASTM 1293 [5]. Both linear and nonlinear resonance methods were used to measure the damage progression and the results were correlated to the expansions.

3.1 Background of Nonlinear Acoustic Tests

ASR damage in concrete may be monitored by measuring wave velocities and dynamic stiffness, because cracks will cause stress wave scattering and attenuation of and decrease of Young's modulus. Several NDT techniques have been used to evaluate ASR damage development by relating linear parameters to the Young's modulus of elasticity of concrete specimens. Commonly used linear acoustic techniques include monitoring the resonance frequency (ASTM C215 [6]), and ultrasonic pulse velocity (UPV) in concrete [7]. Rivard and Saint-Pierre [8] found the ultrasonic velocities only dropped about 4%, and the resonance frequency decreased by 12% when the ASR expansion reached 0.18% during a 48-week monitoring period. Giannini et al. [9] also investigated UPV, impact-echo, surface wave velocity and transmission, and the resonance frequency method for much larger expansion ranges (0.3% $\sim$ 1.6%). They found that the UPV results decreased 20% at higher expansions, but it was difficult to obtain consistent UPV measurements. Linear resonance frequency tests showed high sensitivity at low ASR expansion levels, but the frequency drop became insensitive at high expansion levels. These measurements require a baseline measurement, which limit the applicability of linear acoustic analysis to concrete damage characterization for in-service structures.

Concrete is an inherent nonlinear material due to its complex microstructure. Microcracking will further increase the material's nonlinearity. Nonlinear acoustic responses include resonance frequency shift, wave velocity decrease, and generation of higher harmonics [10]. Several nonlinear acoustic techniques based on these nonlinear responses have been used to evaluate micro-damage in concrete. The nonlinear resonance acoustic/ultrasound spectroscopy (NRAS/NRUS) test [11, 12] measures the resonance frequency shift Δf under excitation by frequency sweeps at increasing strain levels. The nonlinear impact resonance acoustic spectroscopy (NIRAS) technique is a variation of the NRAS method and has been applied to mortar bars [13] and concrete specimens [14] with ASR damage. NIRAS uses an impact hammer to induce the flexural mode resonance of a sample under increasing impact amplitudes, and the resonance frequency shift is measured. Lesnicki et al. showed that NIRAS is able to detect ASR damage in concrete prisms at early stages of damage development [14, 15].

Although these studies indicate that the acoustic nonlinearity generally increases with ASR damage and microcrack density in early damage, quantitative characterization of damage was not available because there is no clear correlation between material nonlinearity and ASR damage. This study focuses on ASR damage characterization at early stages. Linear resonance and the NIRAS techniques were used to monitor the the concrete specimens for more than one year, and the expansion reached 0.085% at the end of the monitoring program. Petrographic analysis results were used to build an understanding of the underlying damage mechanisms.

3.2 Materials and Experiments

3.2.1 Concrete specimens

The aggregates used in this study have been described in Chapter 2: a reactive coarse aggregate (RCA), a reactive fine aggregate (RFA), and a non-reactive coarse aggregate (NRCA) and non-reactive fine aggregate (NRFA) with similar gradation as the two reactive aggregates as shown in Figure 2.2. The properties of the aggregates can be found in Table 2.1.

Six different concrete mix designs were used in this study (Table 3.1). The first set of three mix designs match the mix designs for the medium-scale specimens in Chapter 2, including Control, RCA, and RFA, which are designated as #1 in this chapter. The second set (#2) of mix designs follows ASTM C1293 [5], where the reactive coarse aggregate in the RCA (#2) design was crushed to meet the ASTM C1293 gradation requirement for the smallest aggregate category. For the reactive mix designs, NaOH was added to boost the alkali content of the mix to promote accelerated ASR damage. Six concrete prisms (3 x 3 x 11.25 in^3) were cast for each mix designs.

Table 3.1: Mix designs for small prism specimens.

Component (kg/m^3)	Ctrl 1	RFA 1	RCA 1	Ctrl 2	RFA 2	RCA 2
Cement	350	350	350	420	420	420
Water	175	175	175	189	189	189
Coarse aggregate	1127	1095	1039	1196	1038	1196
Fine aggregate	709	743	839	544	744	545
Water reducer (mL/kg)	2.3	2.3	2.3	2.3	2.3	2.3
50/50 NaOH	0	9.31	9.31	0	8.46	8.46
w/c	0.5	0.5	0.5	0.45	0.45	0.45

3.2.2 Curing, conditioning, and expansion measurements

The specimens were stored in the same environmental chamber as described in Chapter 2. Expansion, linear resonance, and nonlinear resonance measurements were taken every two weeks. Prior to each measurement, the chamber temperature was set to 23°C. A separate concrete prism with an embedded thermocouple sensor was used for continuous monitoring of the internal temperature. When the internal temperature of the specimens reached a stable 23°C, expansions and resonance frequency tests were performed on the prisms. Prism length change measurements were made using a Humboldt H-3250D length comparator. The entire shut down period typically lasted for less than 24 hours.

3.2.3 Linear and nonlinear resonance acoustic techniques

Resonance frequency tests used a test setup as described in ASTM C215 [6] (Figure 3.1). Each specimen was impacted at multiple times with increasing force for nonlinear analyses. An accelerometer (PCB Piezotronics 352C65, sensitivity 10.2 mV/(m/s^2) was used to measure the vibration response. Signals were digitized by a 16-bit oscilloscope (PicoScope 4262) at a 100 kHz sampling rate.

The NRAS method measures the relative resonance frequency shift with the strain change

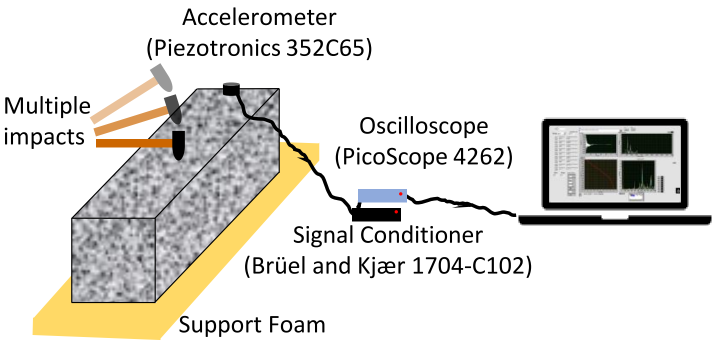

Figure 3.1: Resonance test setup [16]

as [11]:

$$\frac{f_0 - f}{f_0} = \alpha_f(\varepsilon - \varepsilon_0) \tag{3.1}$$

where α_f is defined as the nonlinear parameter, f_0 is the linear frequency measured at a low strain level ε_0, and f is the frequency at a high strain level ε. In experimental studies, a relative nonlinear parameter α is commonly used by replacing the strains in Eq. (3.1) with accelerations. The parameter α referred in this study is the relative nonlinear parameter.

The NIRAS technique uses a hammer impact to excite the fundamental vibration mode and measures the resonance frequency shift under increasing impact forces. Figure 3.2(a) shows the signal processing procedures. It can be seen that for the RCA specimen, a larger decrease in resonance frequency is observed with increasing amplitude. The nonlinear parameter (α) is then determined from the slope of the resonance frequency shift $(f_0 - f)/f_0$ vs. the acceleration amplitude plot, as shown in Figure 3.2(b).

3.2.4 Petrographic analysis

Petrographic examination was performed on two prisms: one RFA#1 specimen and one RCA#1 specimen, at the conclusion of the monitoring period. Each prsim was prepared and analyzed following ASTM C856 [17] and ASTM C1723 [18]. Each prism was cross sectioned longitudinally and a 45 x 45 x 5 mm section was taken from an area of interest at approximately mid-length of each prism. Optical examination of each polished section was conducted in reflected light at low magnification. SEM examination included collecting both backscattered electron (BSE) micrographs and chemical composition from locations of interest using electron dispersive spectroscopy (EDS).

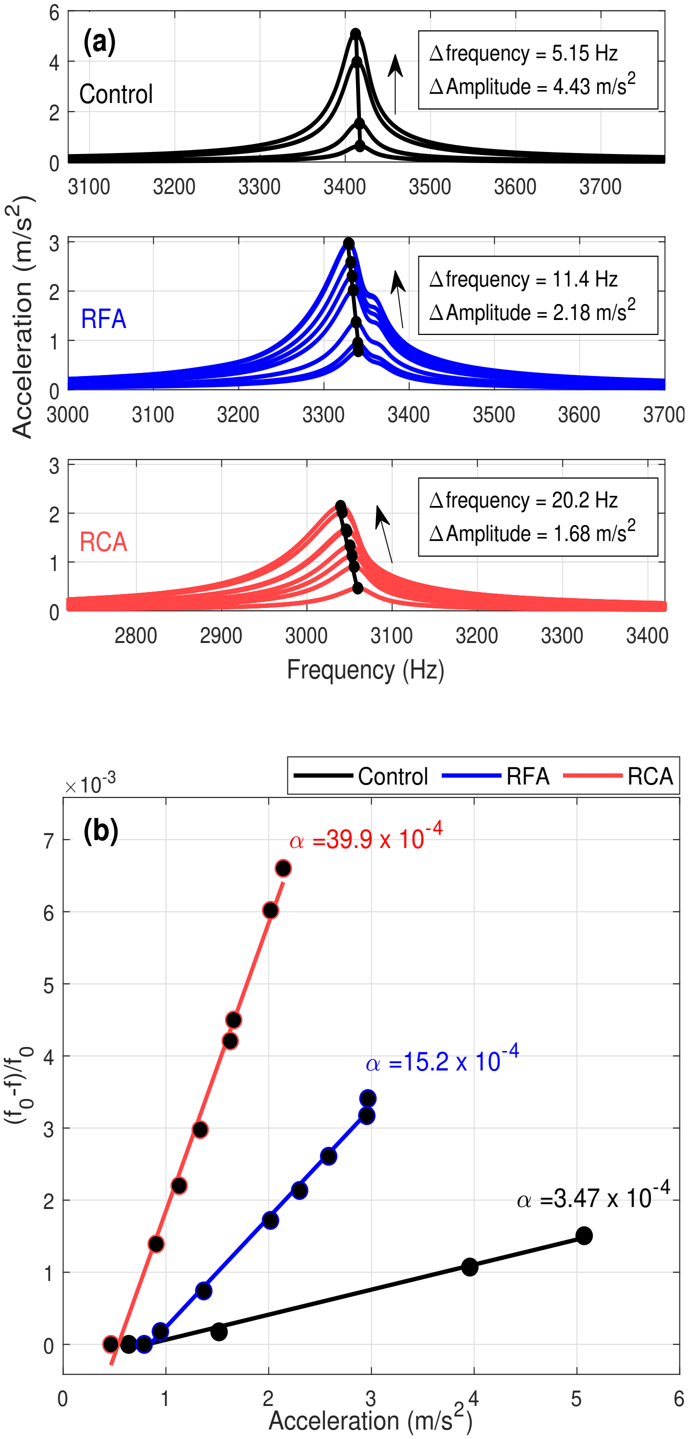

Figure 3.2: NIRAS signals and analysis including (a) frequency spectra, (b) multi-impact nonlinear analysis. [16]

3.3 Results and Discussions

3.3.1 Expansion results

Figure 3.3 shows the expansion history of specimens from all six mix designs. During the first 50 days of monitoring, all specimens showed minor shrinkage due to hydration. The Control specimens then kept relatively stable expansion levels thereafter. For both sets of specimens (#1 and #2), the RCA specimens showed consistently larger expansions earlier crack initiation time than the RFA specimens, which indicates that the RCA aggregate is more reactive than the RFA aggregate.

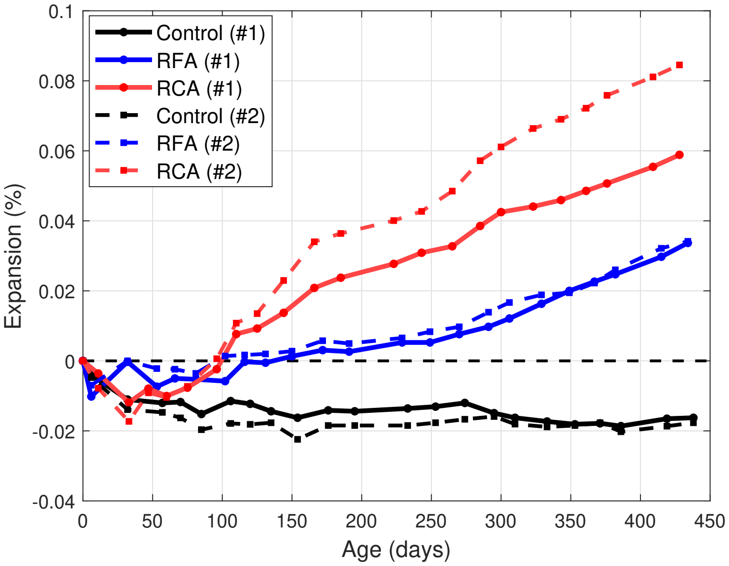

Figure 3.3: Expansion measurement results during testing period (Solid lines for mix design #1, dashed lines for design #2, black, blue and red colors represent control, RCA, and RFA specimens respectively). [16]

3.3.2 Linear resonance frequency results

In the NIRAS test, the signals from the lowest impacts were used for the linear resonance frequency analysis. Because resonance frequency of a specimen is related to the specimen's Young's modulus as $f \propto \sqrt{E}$, the measured resonance frequency will increase as concrete strengthens, and decrease with development of ASR damage. Figure 3.4 presents the progression of the linear resonance frequency of the specimens for more than 400 days. Both sets of control specimens experienced a small increase in resonance frequency due to continued strength increase.

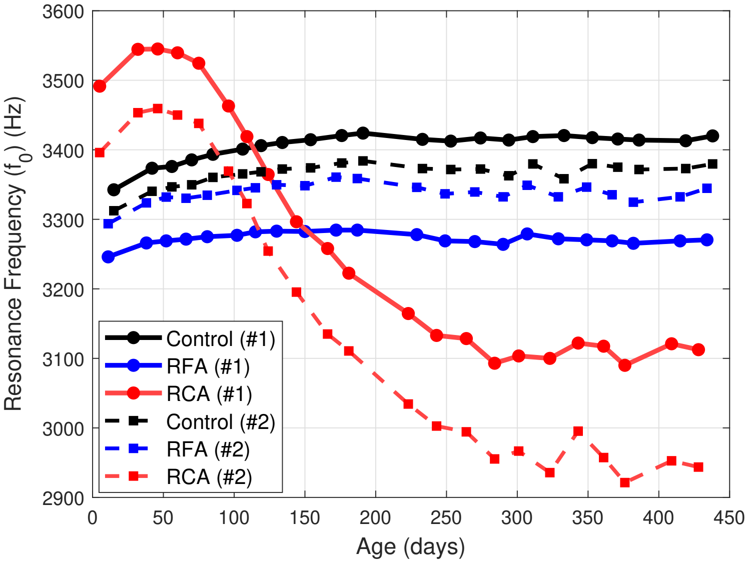

Figure 3.4: Linear resonance frequency results during testing period. [16]

The RCA specimens first showed an increase in linear resonance frequency before 50 days, followed by a large drop during the testing period. The initial large drop for both sets of specimens occurred around 75 days after specimen casting, which are consistent with the expansion results. The resonance frequencies dropped more than 10% for both sets of RCA specimens around 300 days, and then stopped decreasing although the expansion was still progressing. This result is consistent with previous findings by Rivard and Saint-Pierre [8] and Giannini et al. [9], where they noticed the resonance frequency became saturated at late stage of ASR damage.

The RFA specimens did not show clear frequency drop during the entire monitoring period, although they had clear expansions of 0.033%.

These results present several limitations of the linear acoustic method. First, the linear resonance frequency depends on the dimensions of the specimens. Figure 3.4 shows that specimens had different starting frequencies due to slight difference in dimensions. In order to use the linear resonance frequency for ASR evaluation, a baseline measurement for each specimen is needed. Second, at the late stage of RCA specimens, although the expansions continued to increase, the linear resonance frequency was no longer sensitive to further damage development. Third, the linear resonance test could not detect ASR damage in the RFA specimens, even though clear expansion was measured. In the RFA specimens, reactive fine aggregates might cause localized micro-damage that has minimum impact on the modulus. More detailed discussions on specimen microstructures are presented in the petrographic analysis section.

3.3.3 Nonlinear resonance test results

Figure 3.5 presents the nonlinear parameter (α) change during the testing period for all specimens. This plot is similar to the expansion result in Figure 3.3. The control (undamaged) specimens have a nearly constant low value of nonlinearity, with α remaining around 3×10^{-4} during the entire test period.

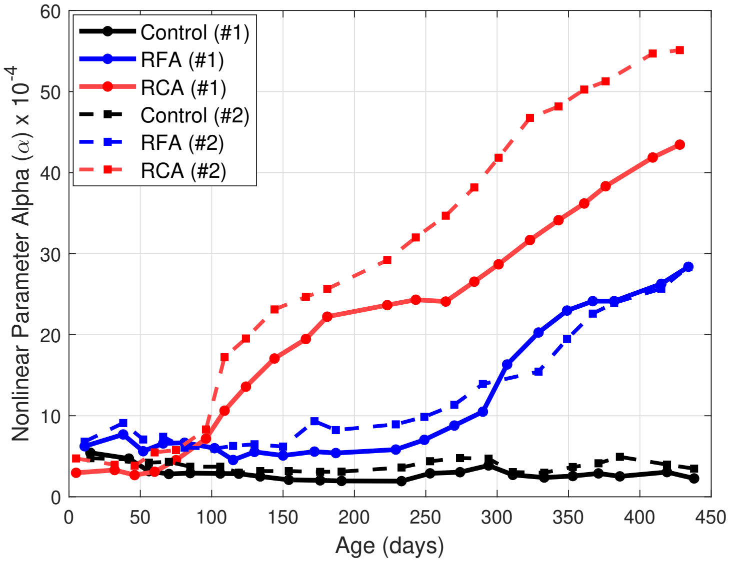

Figure 3.5: Nonlinear parameter α measured from NIRAS method during testing period [16]

The RFA specimens showed a significant increase in nonlinearity beginning around 187-229 days, consistent with the time when a large increase in expansion was observed. For the RFA specimens, the measured nonlinear parameter (α) is more than 7 times larger than the average α value of the Control specimens, validating that the nonlinear testing is highly sensitive to microcracking damage. The RCA specimens showed an earlier increase in nonlinearity, with a noticeable change after 75 days had passed in the testing period, the same time when the expansions started to increase. The final values of nonlinear parameter (α) for the RCA specimens were more than 10 times larger than for the Control specimens.

3.3.4 Correlation of nonlinear results and ASR expansion

The similarity between the nonlinear results (Figure 3.5) and expansions (Figure 3.3) indicates a strong correlation between these two measurements. Figure 3.6 shows the correlation between the nonlinear parameter and the expansion for all specimens. A nearly linear relationship is obtained for all ASR specimens, regardless of their mix design and type of reactive aggregate. This result means that the ASR expansion and nonlinear acoustic response are related to a same parameter due to ASR damage. Attar et al. [19] found the ASR induced crack density initially increases with time at the early stage of ASR damage. Therefore, ASR expansions in the early stage can be attributed to initiation of new cracks and extension of existing cracks, and both increase the crack density. The nonlinear resonance response is governed by clapping and slipping interactions between crack interfaces, which are also directly related to the crack density. Therefore, the increase of crack density at early stage of ASR damage contributes to the increase of ASR expansion and acoustic nonlinearity.

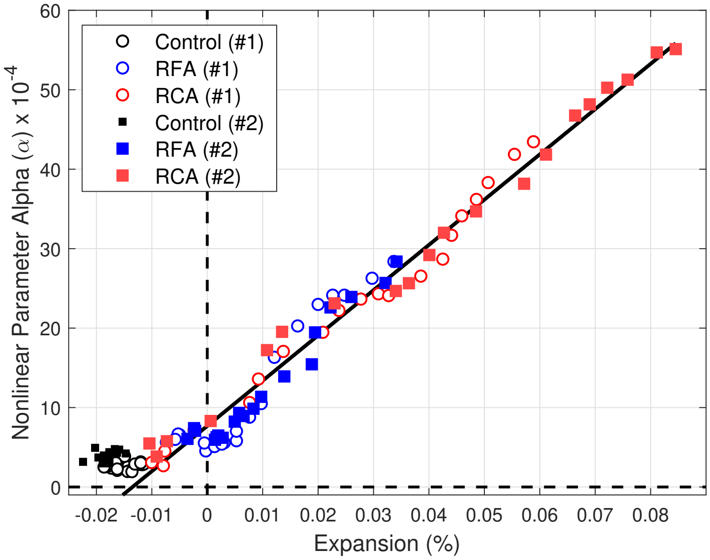

Figure 3.6: Relationship between nonlinear parameter (α) and specimen expansion.

Unlike the expansion measurement which needs a baseline value, the nonlinear parameter can be measured at any time without a reference measurement. The results validate that the nonlinear parameter α has high sensitivity to microcracks but is not affected by other factors such as aggregate type or gradation, and therefore can be used for quantitative evaluation of ASR damage.

3.3.5 Petrographic results

Petrographic analysis can be used to help us understand the difference between the RCA and RFA specimens in the resonance frequency test and analyze the damage mechanism in both reactive specimen types.

In the RFA specimen, microcracking could not be detected using optical microscopy, but limited microcracking was observed in the SEM at higher magnifications. Figure 3.7(a) shows microcracking within the aggregate particles. A smaller number of sand grains showed cracking within the aggregate particles with some cracks extending into the paste. Most cracks were empty, and gel was observed in the cracks only near the paste-aggregate interface; an example is shown in Figure 3.7(b).

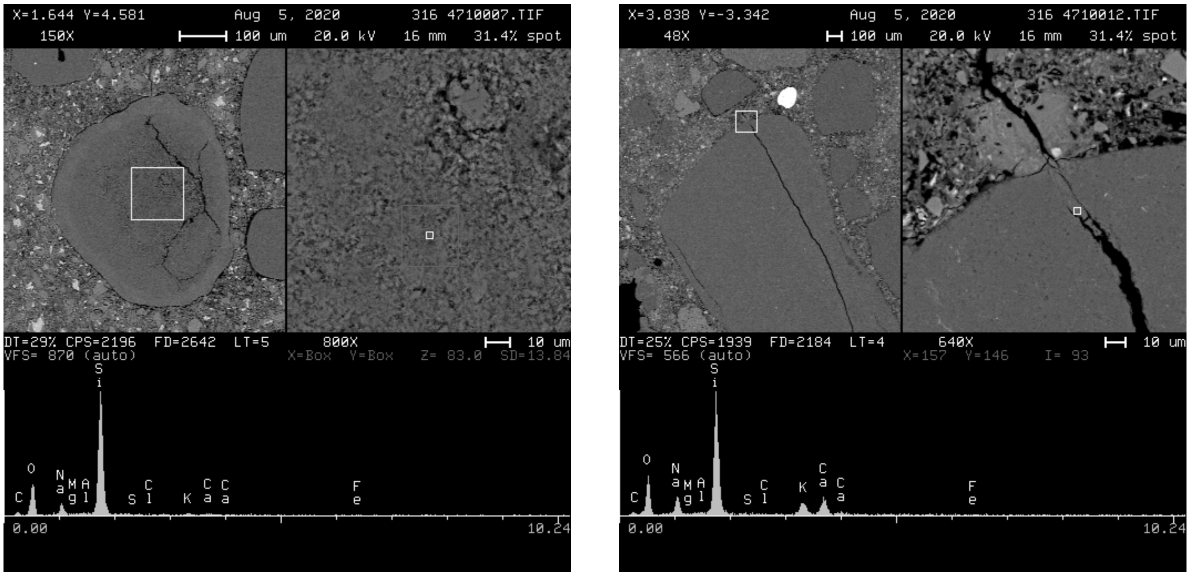

(a) (b)

Figure 3.7: RFA specimen: BSE image and EDS point spectrum of (a) chert sand particle with ASR gel formation and microcracking confined within the particle (b) cracked siliceous fine aggregate particle with microcracking extending into paste and ASR gel within the mouth of the crack [20]

In the RCA specimen, microcracking was observed in coarse aggregate particles and extending into the paste and bridging other reacted aggregate particles (see Figure 3.8). ASR gel was found within microcracks both in the aggregate and in the paste, as well as lining adjacent air voids (see Figure 3.9).

Both the RFA and RCA specimens exhibited very low degrees of ASR-induced damage under petrographic examination, but the damage patterns in the RFA and RCA specimens

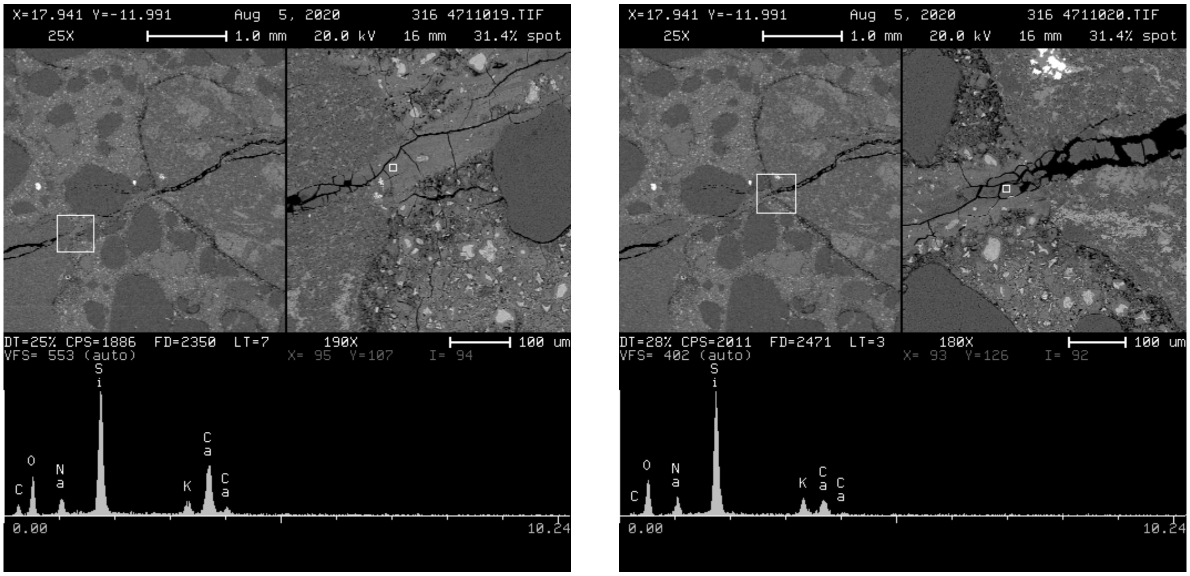

(a) (b)

Figure 3.8: RCA specimen: BSE images and EDS point spectra showing (a) ASR gel in a crack in the paste, and (b) cracks bridging between two coarse aggregate particles.[20]

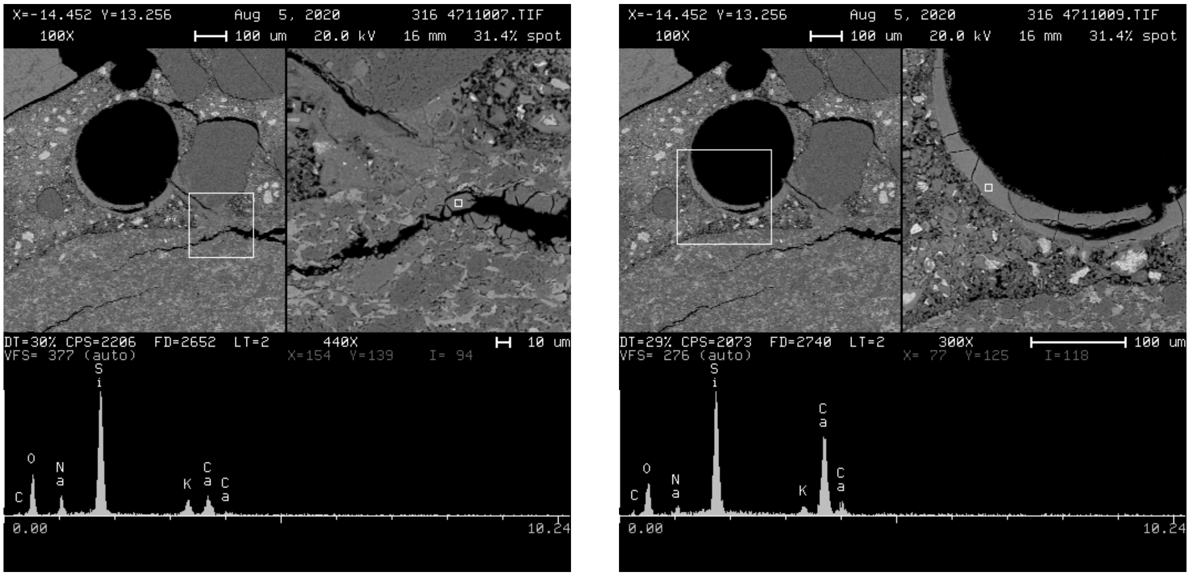

(a) (b)

Figure 3.9: RCA specimen: BSE images and EDS point spectra showing (a) ASR gel lining a crack that begins in a coarse aggregate particle and extends into the paste; (b) gel is also seen partially lining an air void.[20]

are different. In the RCA specimen, microcracking extended into the paste and had begun to bridge between aggregate particles. In the RFA specimen, microcracks jsut began to exit the reactive aggregate particles into the paste but not yet forming an interconnected network.

The petrographic analysis helps explain the difference between the RFA and RCA specimens in the resonance frequency test. Although the isolated microcracks in the RFA specimens did not lead to significant decrease of resonance frequency, they still contribute to increase of nonlinearity. These results confirm the high degree of sensitivity of the NIRAS technique to early-stage initiation of ASR damage.

3.4 Summary of Nonlinear Resonance Tests on Small Concrete Prisms

Linear and nonlinear resonance tests were used to evaluate ASR damage in small concrete prism specimens. The concrete specimens included six mix designs. Different types of reactive aggregates (coarse or fine) were used to cast the reactive specimens, which resulted in different levels of ASR damage and cracking patterns. The specimens were conditioned in an environmental chamber for 400 days.

The linear resonance test could detect crack initiation and ASR development in the RCA specimens, but it became insensitive at the later stage. Because the resonance frequency depends on dimensions of specimens, baseline measurements are needed for each specimen. Isolated microcracks in the RFA specimens could not be detected by the linear resonance test, although the RFA specimens had shown clear expansion. The difference between RCA and RFA specimens in the linear resonance test is attributed to different microcracking patterns, where interconnected microcracks were found in the RCA specimen, while isolated microracks in the RFA specimen. This explanation was confirmed by petrographic analysis.

The nonlinear resonance test showed high sensitivity to microcracking damage in concrete, in both the RCA and RFA specimens. At the early stage of ASR damage, the nonlinear parameter and ASR expansion showed a strong correlation with each other. It is believed that both the nonlinear parameter and ASR expansion are related to the crack density in material. The test results demonstrate the feasibility of using nonlinear acoustic resonance methods for quantitative NDT evaluation of ASR damage.

Part II

Monitoring Medium-Scale Concrete Specimens

4 Ultrasonic Monitoring – Linear Analysis

This chapter describes the experimental setup and linear ultrasonic analysis results on the medium-size concrete beams. All specimens studied in this chapter refer to the "UNL" specimens that were cast and conditioned at UNL. These specimens were continuously monitored for more than 400 days using ultrasonic waves. The linear ultrasonic analysis focuses on wave velocity change with conditioning ages and ASR expansion levels.

4.1 Experimental Setup for Ultrasonic Monitoring

A hybrid monitoring system was developed to continuously monitor ASR damage in the concrete specimens. The system can be used for active ultrasonic monitoring and passive acoustic emission (AE) monitoring. The system diagram is shown in Figure 4.1(a). Fifteen AE sensors (R6I-AST and R15I-AST, Mistras, NJ, USA) were installed on the concrete specimens, and used as AE sensors and ultrasonic receivers. These sensors were connected to the AE system for most of the time. At specific times (01:05 am and 13:05 pm) every day, the switch (Agilent 34970, CA, USA) disconnected all sensors from the AE system and connected them to the ultrasonic system as the receivers. When the system switched to ultrasonic test, the switch board controlled data acquisition from each sensor one by one. An AE amplifier system (AE-2A) was used to power the AE sensors and connect to the ultrasonic system. An ultrasonic pulser/receiver (Olympus 5077PR) emitted square wave pulses to drive the transmitters (PZT disks) at the frequency of 100 kHz. A second switch board was used to switch among the transmitters and specimens (one transmitter on each specimen). The received signals were digitized by a digital oscilloscope (PICO4262) with a sampling rate of 10 MHz. Only the ultrasonic results are presented in this report.

Sensor arrangements and sensor positions for group 1 specimens (Control and RCA) are shown in Figure 4.2. The number of sensors on each specimen was changed several times during the monitoring. Based on the sensor arrangement, the entire monitoring process can

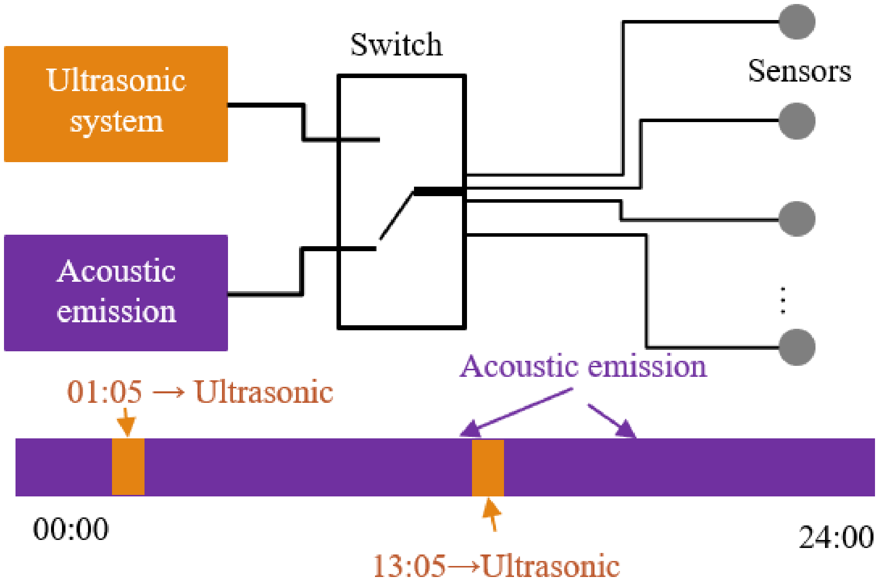

Figure 4.1: Ultrasonic-acoustic emission hybrid monitoring system

be divided into four periods. During the first period (12/09/2018-01/14/2019), three sensors were installed on the control, the RCA and the RCA-2D specimens with S1 for the high-frequency sensor (R15I-AST, 150kHz) and S2, S3 for the low-frequency sensors (R6I-AST, 60kHz). During period 2 (01/20/2019-03/31/2019), six sensors were installed on the RCA and the RCA-2D specimens and three on the control sample. During period 3 (04/06/2019-08/08/2019), only one high-frequency sensor (R15I-AST) was installed on the control sample and four sensors on the ASR and ASR-2D specimens. After that, S1 sensor was replaced with a R6I-AST sensor and S4 sensor was removed from the ASR sample and the ASR 2D sample in period 4. A PZT disk (T) was used as the ultrasonic transmitter and installed on the opposite surface of sensor S1. The sensor arrangement is summarized in Table 4.1.

Table 4.1: Sensor arrangement on group 1 specimens

Period	Control	RCA	RCA-2D
12/09/2018-01/14/2019	S1(150 k),S2,S3	S1(150k),S2,S3	S1(150k),S2,S3
01/20/2019-03/31/2019	S1(150 k),S2,S3	S1(150k),S2,S3, S4,S5,S6	S1(150k),S2,S3, S4,S5,S6
04/06/2019-08/08/2019	S1(150 k)	S1(150 k),S3,S4,S5	S1(150k),S3,S4,S5
08/10/2019-end	S1	S1(150 k),S3,S5	S1(150 k),S3,S5

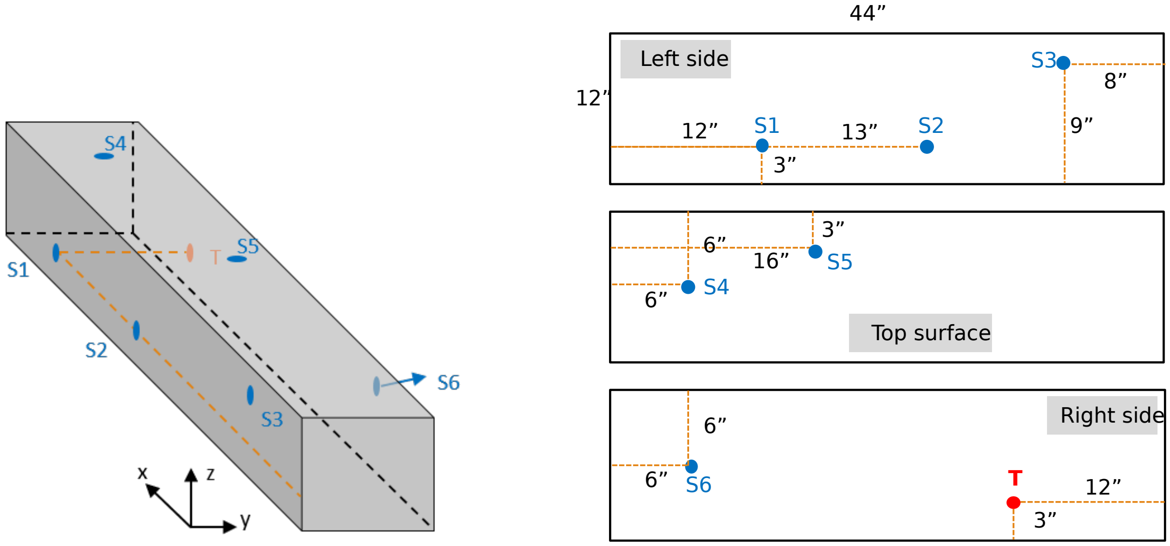

(a) Sensors arrangement on RCA specimens (b) Sensor positions

Figure 4.2: Sensor arrangement on the RCA specimens

Table 4.2: Sensor arrangement on RFA and sRCA specimens (groups 2 and 3)

Group	Monitoring period	Control-2D	ASR	ASR-2D
2	04/06/2019- end	S1	S1,S2	S1,S2
3	08/09/2019- end	N/A	S1 (150 kHz)	S1 (150 kHz)

On the RFA specimens, two sensors (R6I-AST) were used as the ultrasonic receivers and one PZT disk was used as the transmitter. The sensor positions are shown in Figure 4.3. On the Control-2D sample, one R6I-AST sensor was used (S1). The sensor arrangement is summarized in Table 4.2.

On the two small RCA concrete specimens (sRCA), one AE sensor (R15I-AST, 150kHz) was used as the ultrasonic receiver, and one PZT sensor was installed as the transmitter. The sensor positions are shown in Figure 4.4, and sensor arrangement is in Table 4.2.

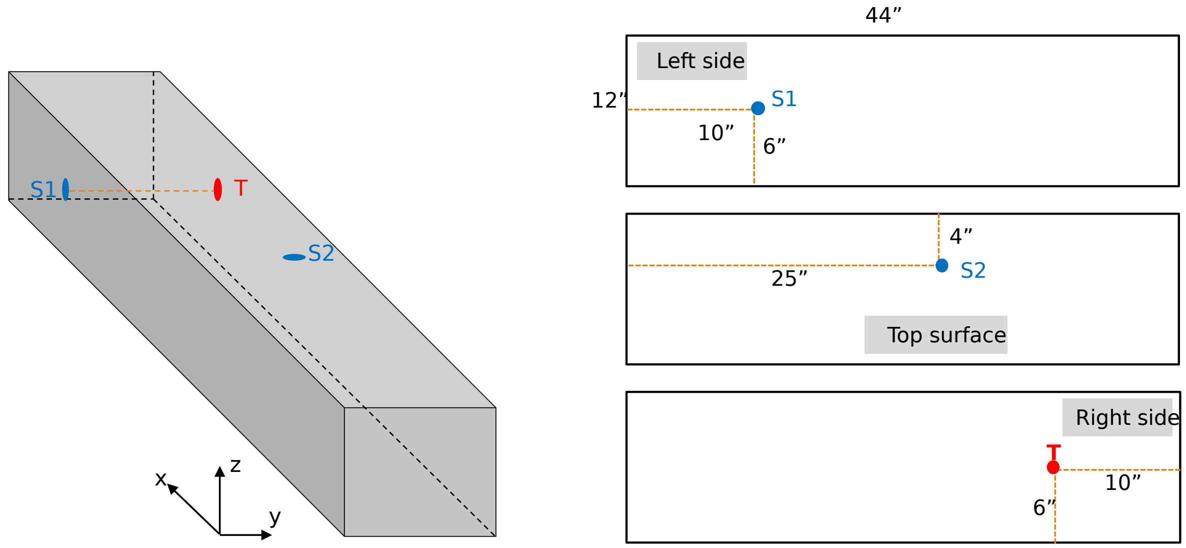

(a) Sensors arrangement on RFA specimens (b) Sensor positions

Figure 4.3: Sensor arrangement on the RFA specimens

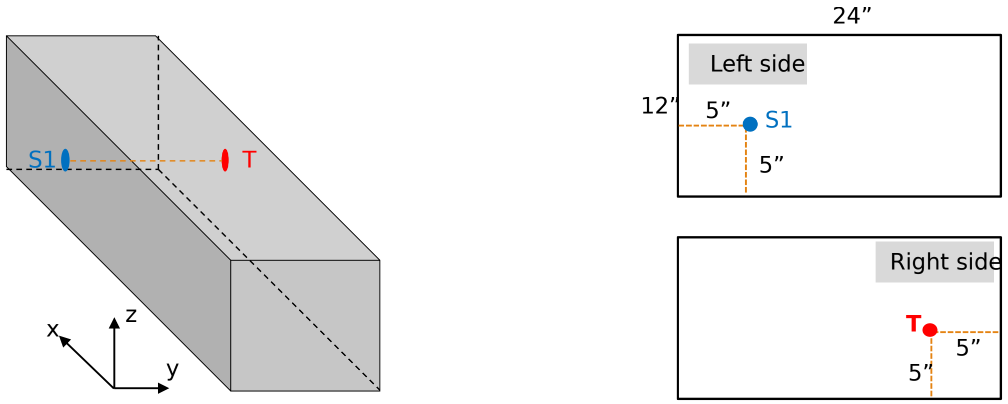

(a) Sensors arrangement on sRCA specimens (b) Sensor positions

Figure 4.4: Sensor arrangement on the sRCA specimens

4.2 Signal Processing Algorithms

At the early stage of ASR, the relative velocity change is very small so that it cannot be reliably measured by the time-of-flight (TOF) method. Coda wave analysis technique is commonly used to track small ultrasonic velocity change due to minor changes in materials. There are two commonly used methods for coda wave interferometry analysis: the doublet method and the stretching technique. The doublet method was first proposed by Poupinet et al.[21] and Roberts et al.[22] and later developed by Snieder et al.[23]. The time delay of a small window T at time t is calculated using cross-correlation between the original signal φ and the perturbed signal φ' as:

$$CC(t, \delta t) = \frac{\int_{t-T/2}^{t+T/2} \varphi(t)\varphi'(t + \delta t)dt}{\sqrt{\int_{t-T/2}^{t+T/2} \varphi^2(t)dt \int_{t-T/2}^{t+T/2} \varphi'^2(t)dt}} \tag{4.1}$$

The time delay δt that maximizes the cross-correlation coefficients represents the time lag between the two signals and the relative velocity change is expressed as: $dv/v = -\delta t/t$. Figure 4.5(a) shows the time domain signals on an aluminum block with blue curve for the original signal (at 23°C) and red for the perturbed signal (at 40°C). In the zoomed inset, the perturbed signal has a clear time delay to the original signal. Figure 4.5(b) shows the time delay at different signal travel time and the slope $\delta t/t$ is 0.254%, which indicates the relative velocity change is -0.254%.

The stretching technique was first proposed by Lobkis and Weaver [24] and this method allows processing the full waveform by applying a stretching factor ε to the perturbed signal φ'. Using the stretching technique, the cross-correlation coefficient is evaluated as:

$$CC(\varepsilon) = \frac{\int_{t_1}^{t_2} \varphi'[t(1-\varepsilon)]\varphi(t)dt}{\sqrt{\int_{t_1}^{t_2} \varphi'^2[t(1-\varepsilon)]dt \int_{t_1}^{t_2} \varphi^2(t)dt}} \tag{4.2}$$

The stretching factor ε_{max} which maximizes the cross-correlation coefficient represents the relative velocity change dv/v. Figure 4.6 shows the cross-correlation coefficient CC at different stretching factors for the two signals in Figure 4.5(a). A window from 0.15 ms to 0.65 ms is used for the analysis.

The stretching factor at the maximum cross-correlation coefficient ε=-0.231% represents the relative velocity change. The stretching and doublet techniques give very close results,

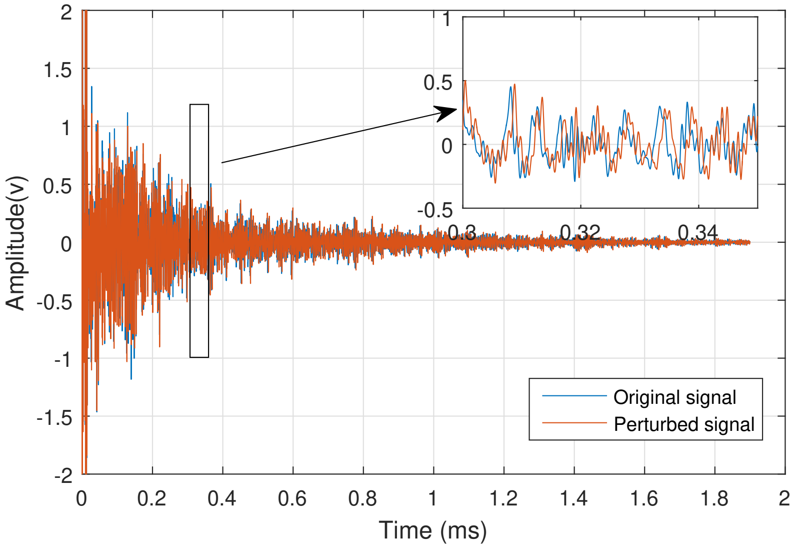

(a) Time domain signals on an aluminum block

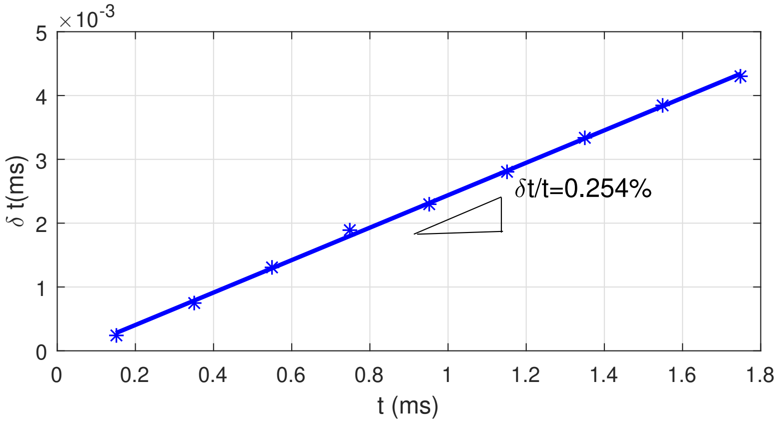

(b) Time delay at different time

Figure 4.5: Doublet results on an aluminum sample for temperature of 23°C (original) and 40°C (perturbed)

but the stretching technique is more stable and precise than the doublet method according to Hadziioannou et al. [25]. Therefore, the stretching technique is used for coda wave analysis in the following works.

The stretching method uses a fixed reference signal (e.g., the first signal of starting monitoring), and all other signals are compared to this reference signal. However, when the test specimen experiences large changes in stress, temperature, or internal structure change (cracks), the disturbed signals will be very different from the reference signal and the CWI analysis has a very low cross-correlation coefficient. Therefore a moving reference algorithm based on the cross-correlation coefficient is proposed in this study. Let dv/v^i represent the

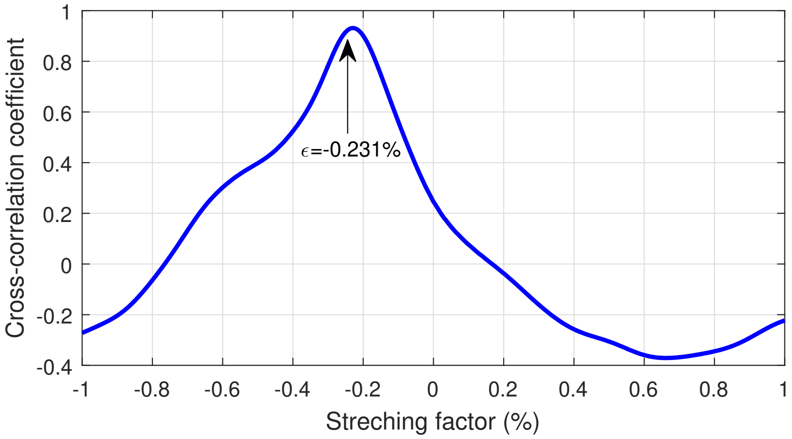

Figure 4.6: Cross-correlation coefficient at different stretching factors

relative velocity change of the i^{th} signal to the reference signal S_0, which is recorded at the beginning of the monitoring. The relative velocity changes dv/v^i, and the correlation coefficients CC_i are calculated using the stretching technique. If the correlation coefficient CC_k of the k^{th} signal is lower than a threshold value (e.g., 0.95), the k^{th} signal is used as the new reference for the signals after it. For example, the relative velocity change dv/v^{k+1} of the $(k+1)^{th}$ signal is calculated as below:

$$dv/v^{k+1} = dv/v^k + \Delta dv/v^{(k+1,k)} \tag{4.3}$$

where the $\Delta dv/v^{(k+1,k)}$ is the relative velocity change between the $(k+1)^{th}$ signal and k^{th} signals calculated by the stretching method. The reference signal may change several times for the signals experiencing large changes. If the total velocity change is very large, we may also need to consider the compound effect, as shown in the following equation

$$dv/v^{k+1} = dv/v^k + \Delta dv/v^{(k+1,k)} \times (1 + dv/v^k) \tag{4.4}$$

In the CWI analysis, the relative velocity change dv/v approximately equals to the relative time delay $\delta t/t$. When there is a temperature change, two effects contribute to the relative time delay $\delta t/t$: thermal expansion of the sample, and temperature dependence of the wave velocity [24, 26]. The relative velocity change is calculated as $dv/v = -(\delta t/t - \alpha_T \Delta T)$. If the thermal strain is negligible ($\epsilon = \alpha_T \Delta T \ll dv/v$), the relative velocity change can be calculated as $dv/v = -\delta t/t$.

4.3 Expansion Measurements

Detailed expansion measurement results from the eight "UNL-" specimens are presented in this chapter. Expansion was measured every two weeks in three directions (longitudinal, transverse and vertical directions). The longitudinal measurements include two side surfaces and the top surface, and an average of the three surface measurements was taken. The transverse expansion was based on three surface measurements (two ends and the top) and vertical expansion was based on four surface measurements (two sides and two ends). The volumetric expansion was the summation of the average expansions in longitudinal, transverse, and vertical directions.

4.3.1 Volumetric expansion

Table 4.3: Dates for ASR initiation.

specimen	Determined by expansion	Date of first surface crack
RCA	69 days	144 days
RCA-2D	69 days	160 days
RFA	118 days	173 days
RFA-2D	118 days	158 days
sRCA	36 days	144 days
sRCA-2D	36 days	160 days

Volumetric expansions have been presented in Chapter 2. The expansion curves are shown in this chapter again for convenience (Figure 4.7). The specimen surfaces were inspected when the chamber was shut down. The date was recorded when the first surface crack was observed and this information is summarized in Table 4.3. Comparing to the ASR initiation dates determined by the volumetric expansions, the dates of surface cracking are about 70-100 days later than For the RCA specimens. Because internal ASR cracks could occur much earlier than the surface cracks, it is not accurate to determine ASR initiation using surface crack. For the RFA and RFA-2D specimens, the first surface cracking dates were about 40 days later than the crack initiation dates determined by the expansions. The ASR initiation dates determined by expansion in RFA specimens were much later than in the RCA and RCA-2D specimens, which indicates that the RFA specimens had a slower ASR development rate. For all four ASR specimens, the dates of first surface cracking were later than the internal ASR initiation, which indicates that the surface cracks are late alarms

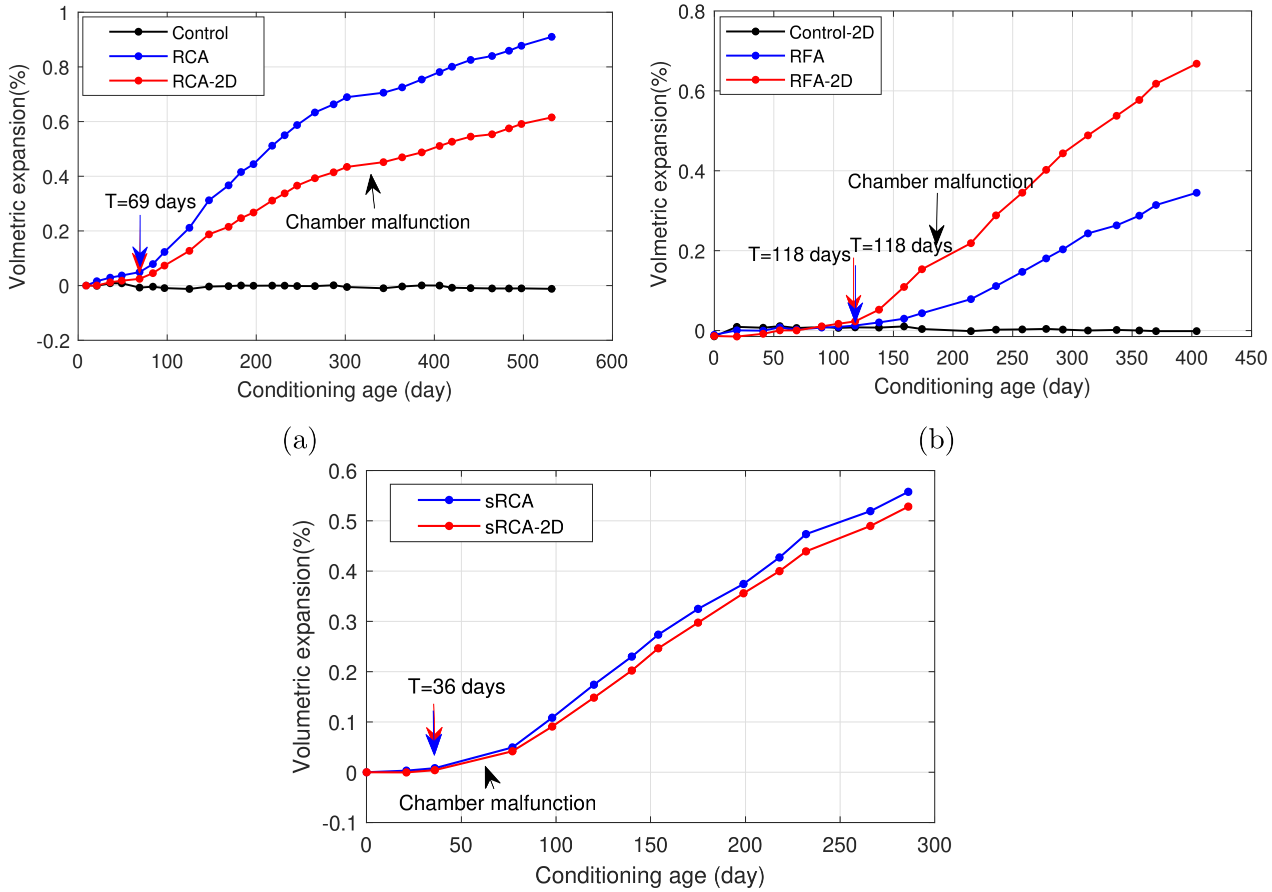

(a)

(b)

(c)

Figure 4.7: Volumetric expansion histories of: (a) Control, RCA, RCA-2D specimens, (b) Control-2D, RFA, and RFA-2D specimens, (c) Small RCA (sRCA) and Small RCA-2D (sRCA-2D) specimens

to the ASR damage initiation. Both the unconfined and confined specimens had the same ASR initiation time, which indicates that the rebar confinement had little effect on the ASR initiation dates of these specimens.

4.3.2 Expansions in three directions

The expansions in longitudinal (L), transverse (T), and vertical (V) directions are plotted in Figure 4.8 for the reactive specimens: RCA, RCA-2D, RFA, RFA-2D, sRCA, and sRCA-2D. In Figure 4.8(a), the vertical expansions (two red curves) for the RCA and RCA-2D specimens are larger than others due to the effect of the horizontal casting plane which was reported by Smaoui et al. [27]. Horizontal cracks occurred near the half-height on the side surfaces where the casting planes were located (see Figure 4.9(a) and (b)). The RCA specimen had similar expansions in the longitudinal and transverse directions (solid black and solid blue), which is consistent with expectation for unconfined ASR specimens.

The RCA-2D specimen had much smaller expansion in the longitudinal direction due to confinement by the headed rebars. The vertical expansion was affected by both casting effect and vertical confinement effect, so the vertical expansion was still the largest for RCA-2D specimen, but smaller than the vertical expansion in the RCA specimen. The transverse expansion (dashed blue) in RCA-2D is smaller than that of the RCA specimen (solid blue), which is unexpected, because the confined direction in the RCA-2D specimen was expected to have large expansion. But it showed a higher expansion rate after 300 days and eventually exceeded the vertical expansion of RCA curve. The comparison between RCA and RCA-2D expansions indicates that the headed rebar confinement was effective in the RCA-2D specimen.

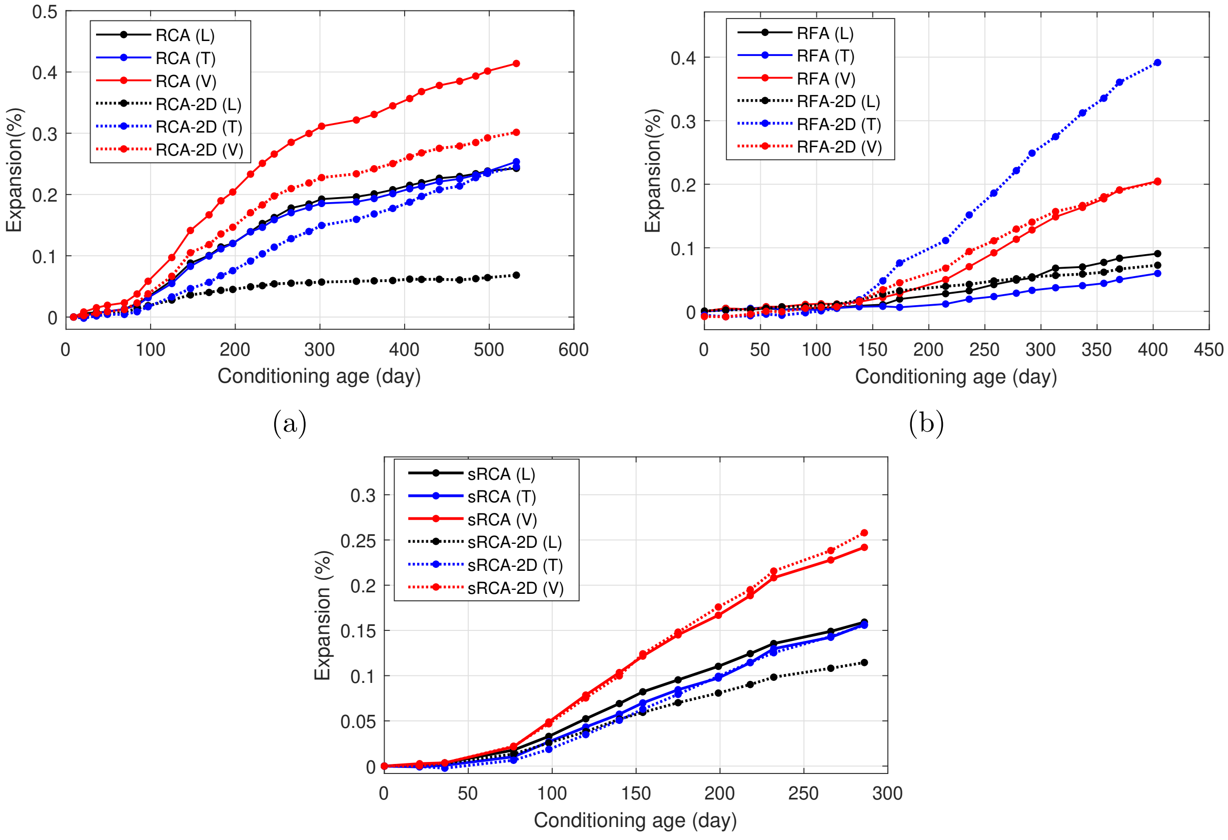

(a) (b)

(c)

Figure 4.8: Expansion in three directions: (a) RCA and RCA-2D specimens, (b) RFA and RFA-2D specimens, (c) sRCA and sRCA-2D specimens.

In Figure 4.8(b), the vertical expansions of RFA and RFA-2D (solid red and dashed red)

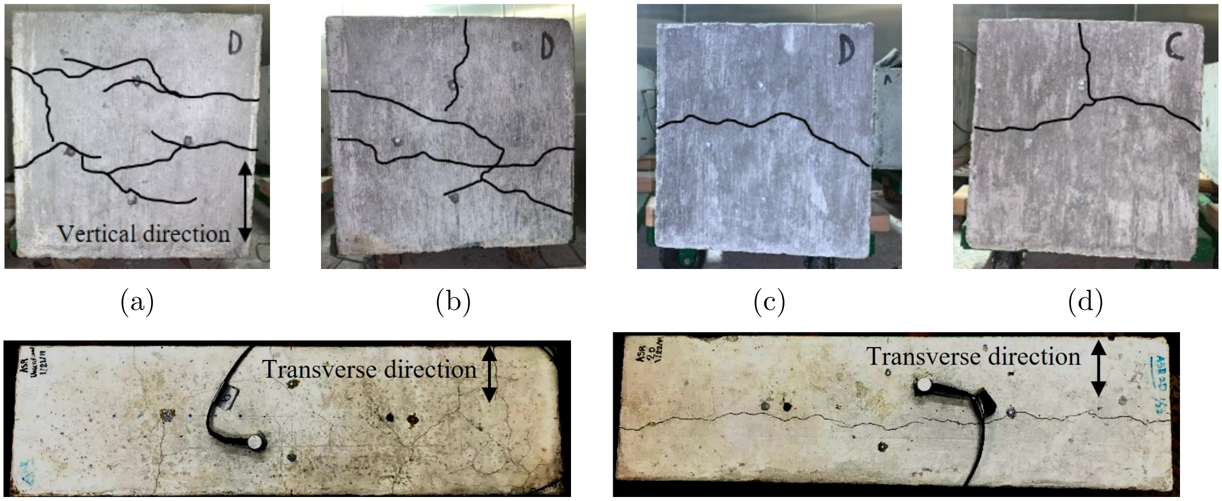

(a) (b) (c) (d)

(e) (f)

Figure 4.9: Surface cracks of: (a) RCA (side), (b) RCA-2D (side), (c) RFA (side), (d) RFA-2D (side), (e) RFA (top surface), (f) RFA-2D (top surface). Cracks are highlighted in black lines for clarity.

were also larger than other expansions due to the casting plane effect that cracks existed at the half-height positions on the side surface (see Figure 4.9 (c) and (d)). The RFA longitudinal (solid black) and RFA-2D longitudinal (dashed black) showed similar trends over the whole period. The RFA specimen only showed some random cracks on its top surface (see Figure 4.9 (e)). The RFA-2D transverse expansion (dashed blue) was the largest among all expansions. A single longitudinal crack was observed on the top surface of the RCA-2D specimen leading to the large transverse expansion (see Figure 4.9 (f)). In Figure 4.9 (b) and (d), both RCA-2D and RFA-2D specimens showed a vertical crack on the side surfaces, which contributed to the large transverse expansions. Both vertical cracks on the two specimens only penetrate the one-third of the depth.

In Figure 4.8(c), the sRCA and sRCA-2D had very similar vertical expansions (solid and dashed red) since the two specimens were cast from the same batch. They were also larger than expansions in other direction due to the casting plane effect. The sRCA longitudinal, sRCA transverse, and sRCA-2D transverse directions showed very similar expansions while the sRCA-2D longitudinal expansion was smaller than all the other expansions since this direction was confined using headed rebar.

4.4 Relative Velocity Change History

4.4.1 Temperature history

The internal and surface temperature histories of the specimens are plotted in Figure 4.10. Since all the specimens were conditioned in the same chamber, we use the same internal and surface temperatures for all specimens. Each temperature data point corresponds to a daily ultrasonic test. Because the ultrasonic data was collected when the chamber status was stable, the internal temperature and surface temperature have good agreement in the figure. Most temperature points are around 38°C, which is the designed conditioning temperature. The RCA specimens were conditioned from 11/27/2018, while the RFA specimens were conditioned from 131 days later (04/04/2019) and sRCA specimen from 255 days later (08/09/2019). Temperature was not recorded from 301 days to 327 days during chamber malfunctioning period.

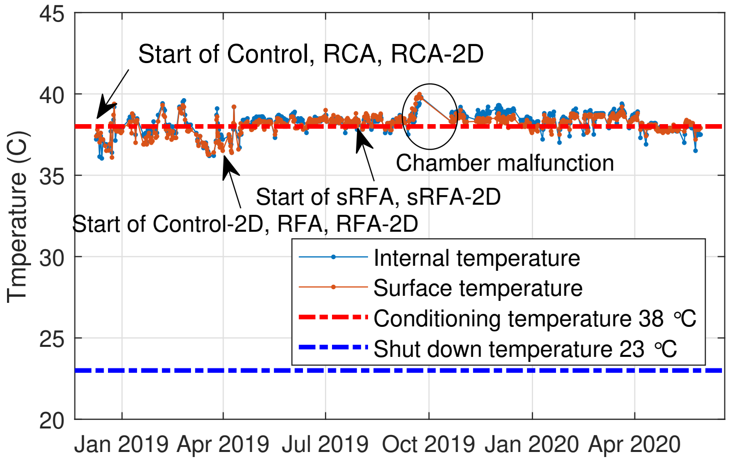

Figure 4.10: Internal and surface temperatures of the concrete specimens

4.4.2 Velocity change for group 1 specimens: Control, RCA, RCA-2D

The ultrasonic relative velocity change for each specimen was analyzed using the stretching technique. The results for the Control, RCA, and RCA-2D specimens were plotted in Figure 4.11(b). The transverse expansions of the three specimens was also plotted in Figure 4.11(a) for comparison since the ultrasonic wave propagated in the transverse direction.

The relative velocity change of the control specimen (black) increased to about 3.6% at 265 days due to the cement hydration and decreased after that, which was caused by temperature increase due to chamber malfunction. Then the chamber was shut down at 301 days and the temperature dropped to 23°C and the humidity to 50% RH. After the chamber resumed normal conditioning at 327 days, the velocity had a large drop and was never recovered to the previous velocity. This might be caused by the moisture evaporation and the shrinkage of the control specimen, as shown in the expansion curve. After that, the velocity stayed constant. During the entire monitoring period, the transverse expansion of the Control specimen stayed nearly constant (black curve in Figure 4.11(a)).

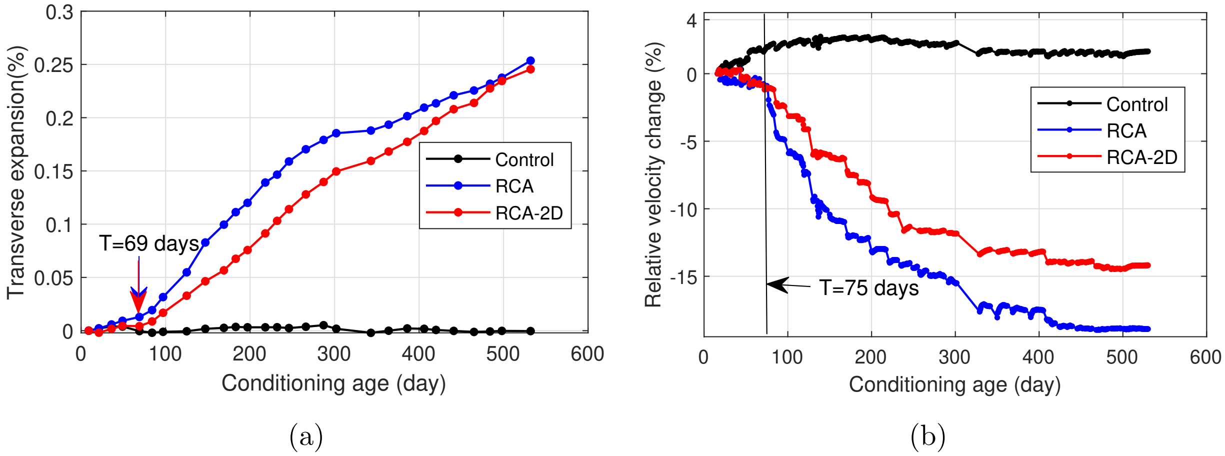

Figure 4.11: RCA specimens: (a) Transverse expansion history, (b) Relative velocity change histories.

Both RCA and RCA-2D specimens began to show a fast velocity drop at 75 days. This time was close to the date of transverse expansion initiation (69 days) shown in Figure 4.11(a). Both relative velocity change histories of the RCA and RCA-2D first had a fast decreasing rate till 250 days for RCA-2D, and 295 days for RCA, and then the velocity drop rate started to slow down. The two expansion curves in Figure 4.11(a) also show similar trends of fast-increasing before 300 days and the RCA expansion slowed down after that. However, the expansion histories of the two reactive specimens were still increasing after 420 days while the two velocity curves became saturated after 400 days. This result indicates that the ultrasonic velocity became insensitive to the ASR expansion after 400 days. A possible explanation is that, at a late stage of ASR damage, the expansion is mainly attributed to widening of existing cracks rather than generation of new cracks; while the wave velocity is mainly affected by crack density instead of crack width. From 301 days to 327 days, no ultrasonic signal was recorded due to the chamber malfunction. At the end of the monitoring period (530 days), the relative velocity changes of the RCA and RCA-2D were 18.9% and

14.2% respectively. However, the transverse expansions for the two specimens were very close (0.254% and 0.246%) at 530 days. The volumetric expansions for the two specimens were 0.910% and 0.615% and the ratio of the two volumetric expansions is close to the ratio of the two relative velocity changes at 530 days.

4.4.3 Velocity change for group 2 specimens: Control-2D, RFA, RFA-2D

The relative velocity histories for the Control-2D, RFA, and RFA-2D specimens were plotted in Figure 4.12. For the Control-2D specimen (black curve), the relative velocity change increased until the chamber malfunction period. The velocity has a large drop and then stayed constant after chamber resumed conditioning.

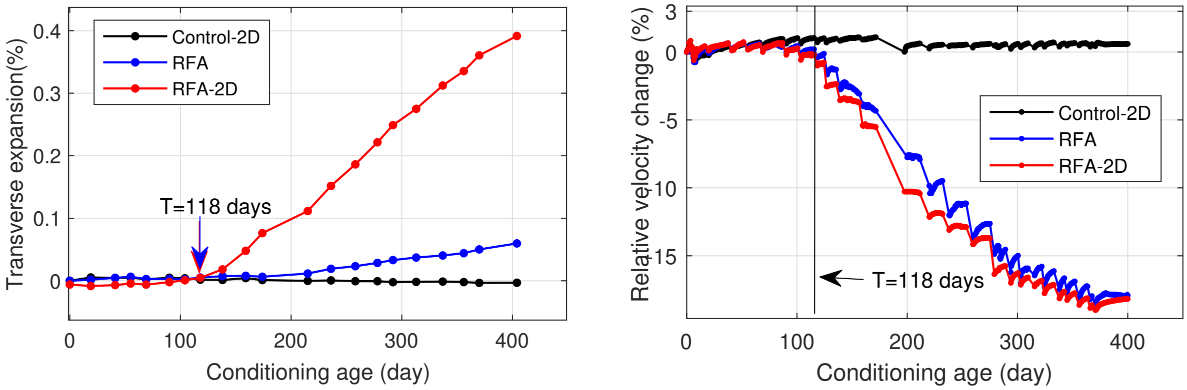

(a)

(b)

Figure 4.12: RFA specimens: (a) Transverse expansion history, (b) Relative velocity change histories.

For the RFA and RFA-2D specimens, the relative velocity change started to drop at 118 days, which was same to the transverse expansion initiation time 118 days for the RFA and RFA-2D specimens. Actually, the relative velocity change histories had small drop before 118 days, which indicates that the ultrasonic velocity monitoring may be able to detect the ASR development earlier than the expansion measurement.

The relative velocity change histories of the RFA and RFA-2D specimens had similar trend for the whole period, although RFA-2D had a much larger transverse expansion than the RFA specimen after crack initiation at 118 days, as shown in Figure 4.12(a). On the top surface of the RFA specimen, surface cracks with random orientations were observed (see Figure 4.9(e)), while the RFA-2D specimen only had a single large longitudinal crack which caused the large transverse expansion (see Figure 4.9(f)). The longitudinal crack on the RFA-2D specimen only penetrated 1/3 depth of the specimen which did not block the wave propagation path. Further widening of the large crack only increased the transverse expansion but did not affect the velocity change, which explained why these two specimens had similar velocity change curves.

4.4.4 Velocity change for group 3 specimens: sRCA, sRCA-2D

The relative velocity histories for the two sRCA specimens are plotted in Figure 4.13. The velocities of both ASR specimens starts to drop at 35 days, which matches the expansion initiation time of 36 days for the two ASR specimens. Both the expansions and velocities of the two ASR specimens indicates they have similar ASR damage development over time. This result indicates that the two-way confinement has little effect on volumetric expansion and velocity change in ASR specimens.

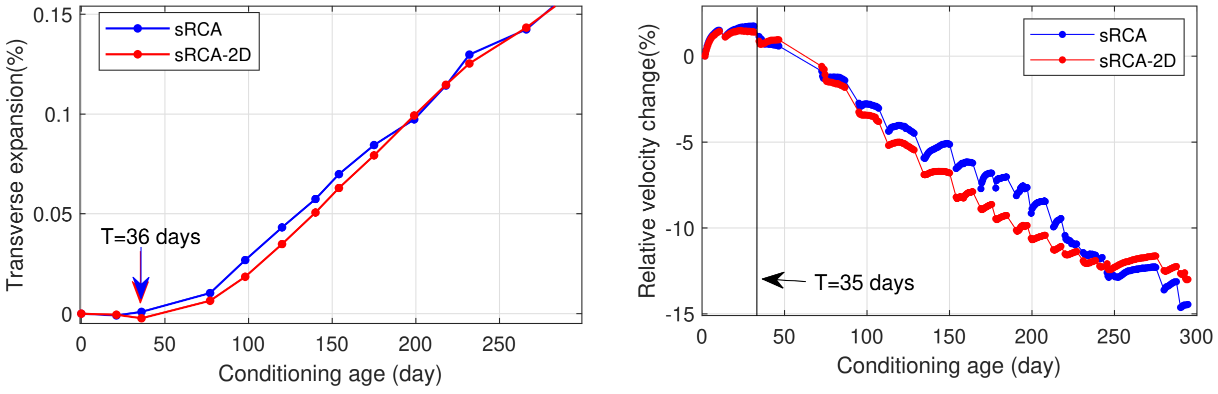

(a) (b)

Figure 4.13: sRCA and sRCA-2D specimens: (a) Transverse expansion history, (b) Relative velocity change histories.

4.4.5 Temperature cycle effect on wave velocity

An interesting phenomenon was observed in the relative velocity histories for all specimens. Figure 4.14 shows the relative velocity histories of the Control-2D, RFA, and RFA-2D specimens from 340 days to 400 days. There are many sudden relative velocity drops in the figure, caused by temperature drop during the chamber shutdown, such as the drop between time T1 and time T2. At time T1, the chamber was shut down, and the temperature of the specimens began to drop from 38°C to 23°C, and the chamber humidity from 90% RH to 50% RH. At the time T2, the chamber was restarted, and the specimen temperature was resumed and maintained at 38°C with the chamber humidity of 90% RH. After the specimen experienced a complete cycle of cooling and heating and a cycle of dehumidification and humidification, the velocity at T2 was lower than the velocity at T1, although the specimen temperature and chamber humidity returned to the pre-shutdown condition. Both reactive specimens had large velocity drops with 1.34% for the RFA and 0.88% for the RFA-2D, while the Control-2D specimen had a much smaller velocity drop (0.18%). Although there was a cycle of dehumidification and humidification in the chamber, the specimens were assumed to be moisture saturated in such a short time. We attribute this velocity drop to the cooling/heating temperature cycle. We denote this phenomenon as the irreversible temperature effect. The velocity can not recover to its original value after the specimen experiences a close temperature cycle when the specimen temperature returns to its original temperature. This effect could be related to the material damage level and material hysteresis and deserves further study.

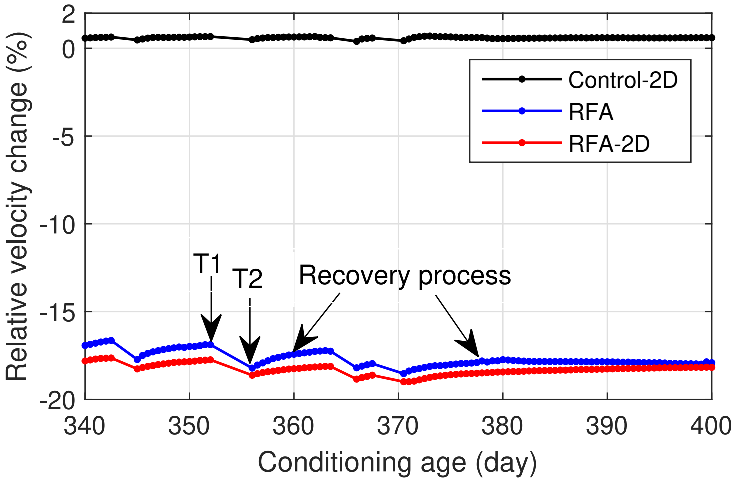

Figure 4.14: Relative velocity change histories of the Control-2D, RFA, RFA-2D specimens from 340 days to 400 days.

After the specimen temperature returned to stable 38°C and the humidity to 95% RH, the velocity gradually increased with time. This slow recovery phenomenon existed after every chamber shutdown. When the chamber maintained a constant temperature and humidity for 30 days after 370 days, the relative velocity history demonstrated a long and slow recovery process. When we review the entire velocity change curves for all ASR specimens, we may notice that velocity drop mainly occured during the chamber shutdown period, or caused by thermal cycles. In control specimens, the slow velocity recovery during the stable temperature and humidity condition could cancel the small velocity drop during the shutdown period, which give an overall increase trend of velocity curve. In ASR specimens, the velocity recovery was always smaller than the drop during each chamber on/off cycles. This phenomenon indicates strong nonlinear behavior in the ASR damaged concrete specimen, and it will be described in next chapter.

4.5 Correlation Between Relative Velocity Change and Expansion

The relative velocity changes at the expansion measurement dates were extracted and correlated with the transverse expansions and volumetric expansions for all ASR specimens. The correlations for the Control and the Control-2D specimens are not presented here since the expansions for these specimens can be neglected comparing to that of the reactive specimens. Figure 4.15(a) shows the correlation curves between the relative velocity change and the transverse expansion for the six reactive specimens while Figure 4.15(b) presents the correlation curves between the relative velocity change and the volumetric expansion. In Figure 4.15(a), all the curves show similar correlation relationships, except for the RFA specimen. The RFA specimen has similar level of velocity change but very small transverse expansion.

In Figure 4.15(b), the correlation curves for the RCA, RCA-2D, sRCA, and sRCA-2D specimens still demonstrated similar trends, which may be explained by the same mix design used in these RCA specimens. It indicates that the ultrasonic velocity could be a useful indicator for the ASR damage evaluation at least for the RCA, RCA-2D, sRCA, and sRCA-2D specimens regardless the confinement condition. However, the correlation curves for the RFA and RFA-2D specimens showed different trends with the other four curves and these two curves also showed different correlations. The RFA and RFA-2D specimens had similar relative velocity change (Figure 4.12(b)) while the RFA-2D specimen showed higher transverse expansion and volumetric expansion than those of the RFA specimen due to the longitudinal crack on the top surface (see Figure 4.9(f)). It indicates that the wave velocity may not be used for ASR damage evaluation for concrete with different mix designs. Ever for the same mix designs, the specimens may demonstrate different crack patterns due to the confinement conditions which will affect the correlation between wave velocity and expansion.

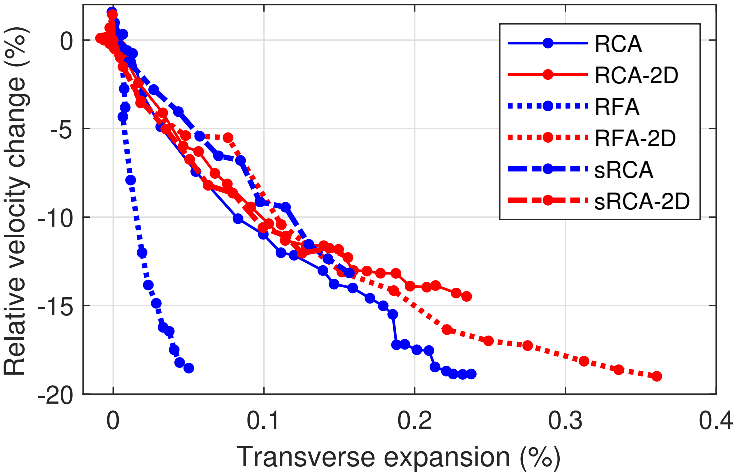

(a)

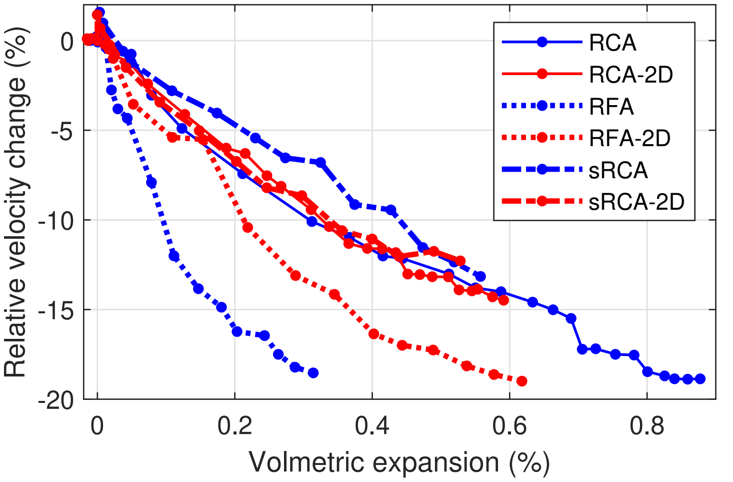

(b)

Figure 4.15: Correlation between the relative velocity change and expansion: (a) Correlation with transverse expansion, (b) Correlation with volumetric expansion.

4.6 Diagnosis Model Using Ultrasonic Signals

Anomaly detection is a potential approach for detecting the occurrence of damage in various applications. Anomaly detection refers to the problem of finding patterns in data that do not conform to the expected behavior [28]. Correctly identifying areas which deviate from the norm is an important problem in many applications. For example, Jiang and co-authors suggested using reconstruction-error based anomaly detection for defect detection of wind turbines [29]. Alex et. al. proposed an anomaly detection method to detect brain lesions using magnetic resonance images [30]. In the structural health monitoring field, Chow et. al. proposed using a convolutional autoencoder to detect cracks in concrete structures using image data [31].

The studies mentioned above use a reconstruction-error-based anomaly detection. The advantages of such a method is that a model can be trained without the need for labeled data and that it has been shown to generalize across different specimens. For many applications, normal data is abundant and can be readily collected. However, anomalous data can be scarce, hard to collect, and hard to identify. A reconstruction-error-based anomaly detection method is not hindered by this issue as it only requires normal data for training of the model. Furthermore, because the anomaly detection model is used to detect deviations from the normal data, it is able to generalize across specimens it has not seen during training. Any sufficient deviation from the normal training data is considered to be an anomaly, suggesting a change in the material. The disadvantages of reconstruction-error-based anomaly detection methods that a large number of training samples are required, should not be an issue as data should be readily collectable from undamaged concrete structures, and the high latency time associated with such models will not pose a problem as the volume of data streamed is very small, in the case of our experiment there are two samples collected per day.

Inspired by previous work, a reconstruction-error-based anomaly detection method is proposed for detecting ASR damage initiation in concrete. The method is based on an autoencoder that utilizes convolutional and recurrent layers, hereon referred to as the Long Short-Term Memory Convolutional neural network (LSTM-CNN) autoencoder. The LSTM-CNN autoencoder attempts to extract the representational and local features of relative velocity variation and decorrelation of coda waves. Then, by using a reconstruction-error based anomaly detection method, a model is developed to identify crack initiation in concrete. Experimental studies are conducted for model development and validation of the model's effectiveness.

4.6.1 Methodology

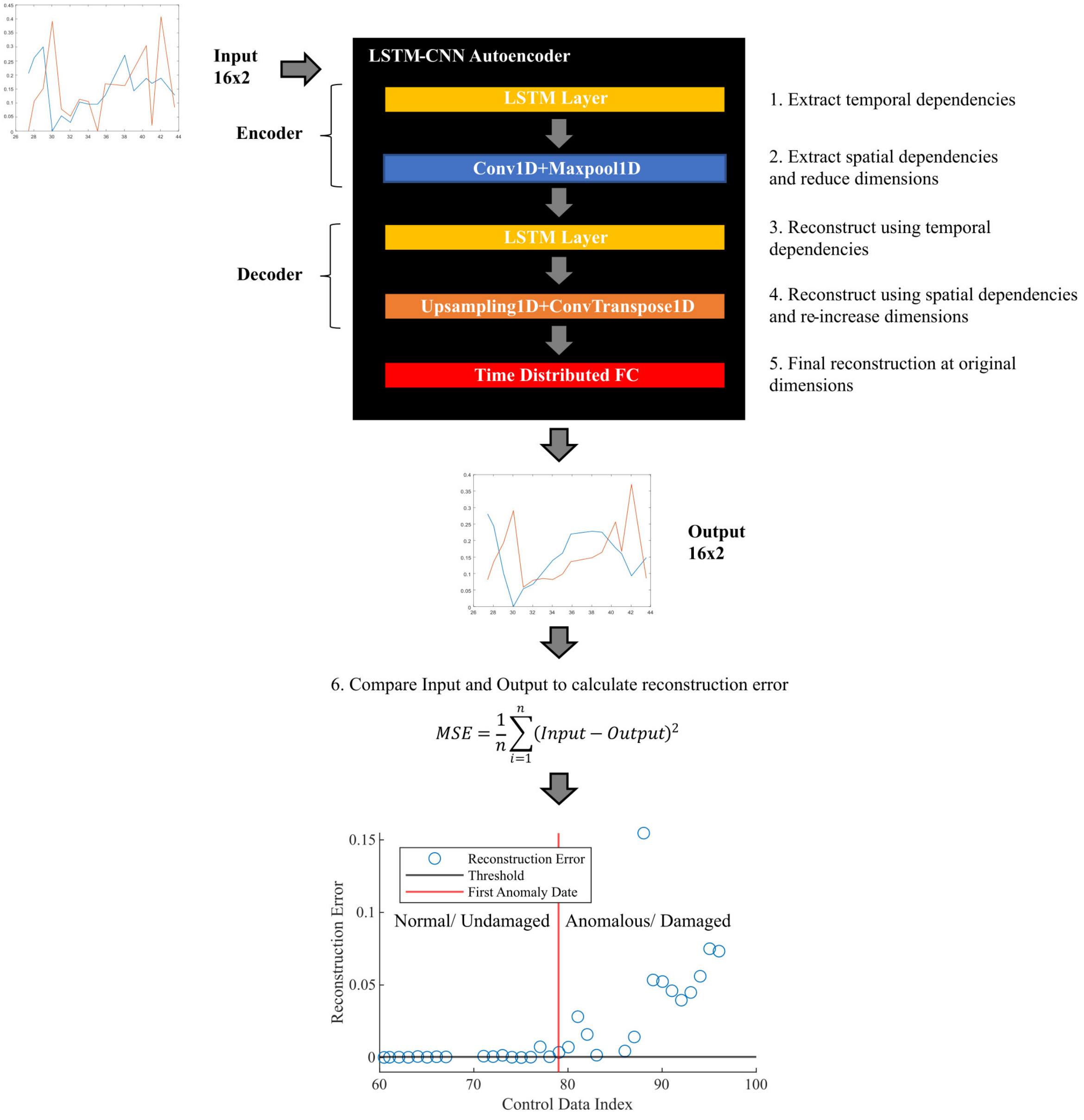

Figure 4.16: Flowchart of steps using the LSTM-CNN Autoencoder for anomaly detection

A reconstruction-error based anomaly detection method is proposed to detect the initiation of ASR damages in concrete using coda waves. Instead of using the raw coda waves as inputs for the anomaly detection model, small input sequences are created using the damage indicative traits, velocity variation, and decorrelation, since certain behaviors of the velocity variation and decorrelation have been shown to be representative of changes in complex material. An autoencoder is used to extract the features of the velocity variation and decorrelation sequences. Then, using these extracted features, the autoencoder is trained to reconstruct the input sequence. The reconstructed sequences are compared to the original input sequences using mean-squared error to obtain a measure of reconstruction error. The reconstruction error is then used to determine whether or not an input sequence is anomalous. Fig. 4.16 illustrates the main steps of the reconstruction-error-based anomaly detection method.

4.6.2 Damage Indicative Features

Coda Wave Velocity Change through CWI

Coda wave shows high sensitivity to minor changes in materials caused by microcracks, temperature variation, or stresses. The relative velocity change dv/v can be obtained by the CWI analysis. In this study, dv/v is used as a damage indicative feature.

Coda Wave Decorrelation

Changes in solid materials, such as concrete, have been found to not only cause amplitude differences and phase shifts, but also cause distortion of signals. Velocity variation best captures the phase changes between the reference signal and perturbed signal, while decorrelation has been found to be a better representation of distortions induced by cracks. Coda wave decorrelation (CWD) calculates the residual distortion of the signal after phase changes have been accounted for as shown in Eq. (4.5) [32].

$$Kd = 1 - CC_k(\epsilon_0) \tag{4.5}$$

Because the decorrelation is calculated after accounting for velocity variation, it is a measure of changes in the coda wave caused by factors other than temporal stretching, such as distortion by localized defects.

Reference Updating Algorithm for Coda Wave Feature Extraction

If too much distortion is present, CWI fails as the velocity variation calculations are no longer meaningful. To combat this issue, researchers have proposed a variety of methods to update the reference signal when necessary. In [33], Zotz-Wilson et. al proposed using a rolling reference, in which a new reference is chosen after a predetermined number of measurements. Niederleithinger et al. proposed two methods of updating the reference. First, they proposed a stepwise method, in which the reference signal is updated after each measurement. Second, they proposed an automated, data-driven procedure for selecting a new reference signal for coda wave interferometry [34]. The authors propose that when the correlation coefficient found using CWI exceeds a predetermined threshold, the reference should be switched to the current signal. The proposed automated method has been shown to decrease the number of reference changes compared to the rolling reference method or the stepwise method, and have shown to reduce rounding errors associated with frequent reference changes. In this report, that threshold is chosen as 0.9, similar to the value used in [35], and the reference is updated when correlation coefficients fall below this value.

4.6.3 Reconstruction-Error Based Anomaly Detection

For early damage detection in concrete, an autoencoder was trained to reconstruct short sequences of velocity variation and decorrelation collected on undamaged control specimens (UNL-Control specimen). More information about the control specimen is provided in Chapter 2. The autoencoder consists of an encoder-decoder network. The encoder portion of an autoencoder extracts features from the input by reducing the input data to a lower dimensional representation. The decoder portion then uses this lower dimensional representation to reconstruct the original input. This encoder-decoder network is trained to minimize the error of this reconstruction. The reconstruction error of each feature is found using the mean squared error (MSE) equation given by Eq. (4.6), where y_i is the input data point and $\tilde{y}_i$ is the reconstructed data point.

$$MSE = \frac{1}{n}\sum_{i=1}^{n}(y_i - \tilde{y}_i)^2 \tag{4.6}$$

The reconstruction errors of the two features are then averaged to gain an overall reconstruction error of the data.

If such a network is trained only on normal data, or in our study data collected from undamaged concrete structures, the model will be able to reconstruct data from undamaged concrete structures with very small reconstruction error. However, if the model is used to reconstruct input data representative of a damaged structure, the model will return a high reconstruction error [28]. Therefore, the reconstruction error of the model can be used as a damage indicator.

To utilize the time-dependent patterns of the coda wave features, the coda wave features were organized into sequences. The sequences were created using a fixed-width sliding window of length sixteen and a sliding step size of one. To further preprocess our data, each feature was normalized using a Min-Max scaling method to normalize the features of the training data from zero to one. The preprocessed sequences were then used as inputs for our LSTM-CNN autoencoder.

Furthermore, to determine if an input sequence is an anomaly, or damaged, a reconstruction error threshold must be chosen to make a binary classification. If the reconstruction error falls below the threshold, it is classified as normal, or undamaged, and if the reconstruction error falls above the threshold it is classified as anomalous, or damaged. This threshold is chosen during the training. During training, the reconstruction error of every sequence in the training set is collected. The threshold was then chosen using the interquartile range (IQR). IQR is often used to measure the statistical dispersion and data variability of data by dividing the data into quartiles based on their magnitude. Q1 is defined as the median of the bottom half of the data set based on magnitudes, Q2 is defined as the median of the entire data set, Q3 is defined as the median of the top half of the data set, and Q4 is defined as the maximum value of the entire data set. The interquartile range is defined as the difference between the Q3 and Q1, or IQR=Q3-Q1. A standard method of identifying anomalies in data uses (Q3+1.5×IQR) to determine the threshold [36].

Lastly, for our implementation, a specific date was considered anomalous only if every sequence including data from that date returned a reconstruction error greater than the threshold. Because the length of an input sequence of our model is sixteen, a date is considered an anomalous date only if sixteen consecutive sequences including the corresponding data return reconstruction errors exceeding the threshold. This criterion was enforced for the anomaly detection method because we are not worried about point outliers, but are more concerned with collective outliers. A point outlier is a single point which extremely deviates from well defined norms. A collective outlier, on the other hand, group of data points that fall extremely far from well defined norms of a data set [37]. Point outliers can occur due to reasons that do not necessarily indicate damage in concrete. Sensor malfunctions and environmental changes, for example, can cause point outliers in the measured data when there is no damage to the concrete specimen, but data measured from a damaged concrete specimen will exhibit a shift in the data through consecutive measurements. Using this criterion, the training data returns no anomalous dates and there are more than sixteen consecutive samples exhibiting reconstruction errors above the chosen threshold.

4.6.4 Autoencoder Architecture

For the proposed autoencoder, a recurrent layer and a 1-d convolutional layer are used due to the nature of our data. The two main advantages of using a convolutional layer are their computational efficiency as well as their ability to extract features from raw data, while recurrent layers have the advantage of being able to capture changes over time. To determine the number of hidden layers, the number of nodes, and the number of epochs that the model is trained, 3-fold cross validation was used. Only the control data was used for training and validation. After determining the aforementioned hyperparameters, the model was retrained on the entire control data set for optimal model performance [38].

Convolutional Layers

Convolutional layers perform a convolution operation using kernels, or a small matrix of weights, of a predefined size. The kernel slides over the input data computing the dot product, or convolving, with the part of the input it is currently on. For example, given a kernel, w, of length p and an input matrix, x, the resulting matrix, h, of the convolution operation for a 1-dimensional matrix is given by Eq. (4.7).

$$h[i] = \sum_{k=0}^{p-1} x[i+k]w[k] \tag{4.7}$$

This operation produces an activation map of that kernel. The activation maps act as filters which activate when a specific feature is detected at some spatial position in the input. The filters are therefore able to detect patterns occurring in groups equal to the size of the kernel. By using a different kernel size for each convolutional layer, both general features, learned by using a larger kernel size, and more local features, learned by using a smaller kernel size, can be extracted from the raw data [39]. Because our data is sequential, a 1-dimensional convolutional layer was used, and zero-padding was used to maintain the shape of the input data.

Recurrent Layers

Recurrent layers make use of information from the input x_t at time t as well as information from the previous hidden state h_{t-1}, allowing the network to hold information about previous inputs in the sequence. This makes recurrent layers ideal for sequential data. The hidden state, h_t, of the recurrent neural network is found using Eq. (4.8) where W_x and W_h are matrices learned during the training process and f is the activation function.

$$h_t = f(W_x x_t + W_h h_{t-1}) \tag{4.8}$$

However, the vanilla RNN has been found to face the vanishing gradient problem when dealing with long-term dependencies. Therefore, for this model long-term short-memory (LSTM) layers were used as the recurrent layers. The LSTM layer makes use of gates, the forget gate, the input gate, and the output gate, to regulate the cell state to allow learning of long-term dependencies. The forward pass of the LSTM layer is given by:

$$f_t = \sigma(W_x^{(f)} x_t + W_h^{(f)} h_{t-1} + b^{(f)}) \tag{4.9}$$

$$i_t = \sigma(W_x^{(i)} x_t + W_h^{(i)} h_{t-1} + b^{(i)}) \tag{4.10}$$

$$o_t = \sigma(W_x^{(o)} x_t + W_h^{(o)} h_{t-1} + b^{(o)}) \tag{4.11}$$

$$c_t = f_t \odot c_{t-1} + i_t \odot tanh(W_x^{(c)} x_t + W_h^{(c)} h_{t-1} + b^{(c)}) \tag{4.12}$$

$$h_t = o_t \odot tanh(c_t) \tag{4.13}$$

Here, b refers to the bias value, W, refers to the weights, and the superscripts f, i, and o describe which gate the bias and weights refer to, the forget gate, input gate, and output gate respectively. Furthermore f_t, i_t, and o_t are the activation vectors of the forget gate, input gate, and output gate respectively, and c_t is the cell state.

Model Implementation

For the proposed model, a time-step of sixteen was used to create short sequences of velocity variation and decorrelation which represent the current status of a concrete specimen, as described in section 4.6.3. Then, these short sequences were used as inputs for the autoencoder anomaly detection model. After experimenting with different architectures, a LSTM-CNN

Table 4.4: LSTM-CNN Autoencoder Hyperparameters

Layer #	Layer Type	# of Units	Output Shape
1	Input	N/A	16 × 2
2	LSTM	32	16 × 32
3	Conv1D & Maxpool1D	32	8 × 32
4	LSTM	16	8 × 16
5	Conv1D & Maxpool1D	32	4 × 16
6	LSTM	4	4 × 4
7	Conv1D	4	4 × 4
8	LSTM	4	4 × 4
9	Upsampling1D & Conv1DTranspose	16	8 × 16
10	LSTM	16	8 × 16
11	Upsampling1D & Conv1DTranspose	32	16 × 32
12	LSTM	32	16 × 32
13	Time Distributed Fully Connected	2	16 × 2

model has been found to perform better than a CNN-LSTM model. Zhang et al. have also found this to be true in their model for text classification. They have found that a LSTM-CNN model causes lower feature loss than CNN-LSTM models [40].

For the encoder part of the encoder-decoder architecture, LSTM layers were first used to generate a new encoded sequence containing temporal features of the original input sequence. Next, convolutional layers were used to extract time-invariant, spatial features from the output of the LSTM layer before it. Then, a maxpooling layer was used to reduce redundant features found by the preceding layers and to reduce the dimensionality. The process was then repeated on the features extracted by the convolutional layer and maxpooling layer. A LSTM layer was used to generate an encoded sequence containing temporal features from the features extracted by its preceding layers and a convolutional and maxpooling layer followed that LSTM layer. The decoder part of the encoder-decoder architecture was the inverse of the encoder structure, where a transpose convolutional layer was used as the inverse of the convolutional layer and an upsampling layer was used as an inverse of the maxpooling layer. The model architecture is shown in Fig. 4.17. The hyperparameters of the autoencoder model is shown in Table 8.2.

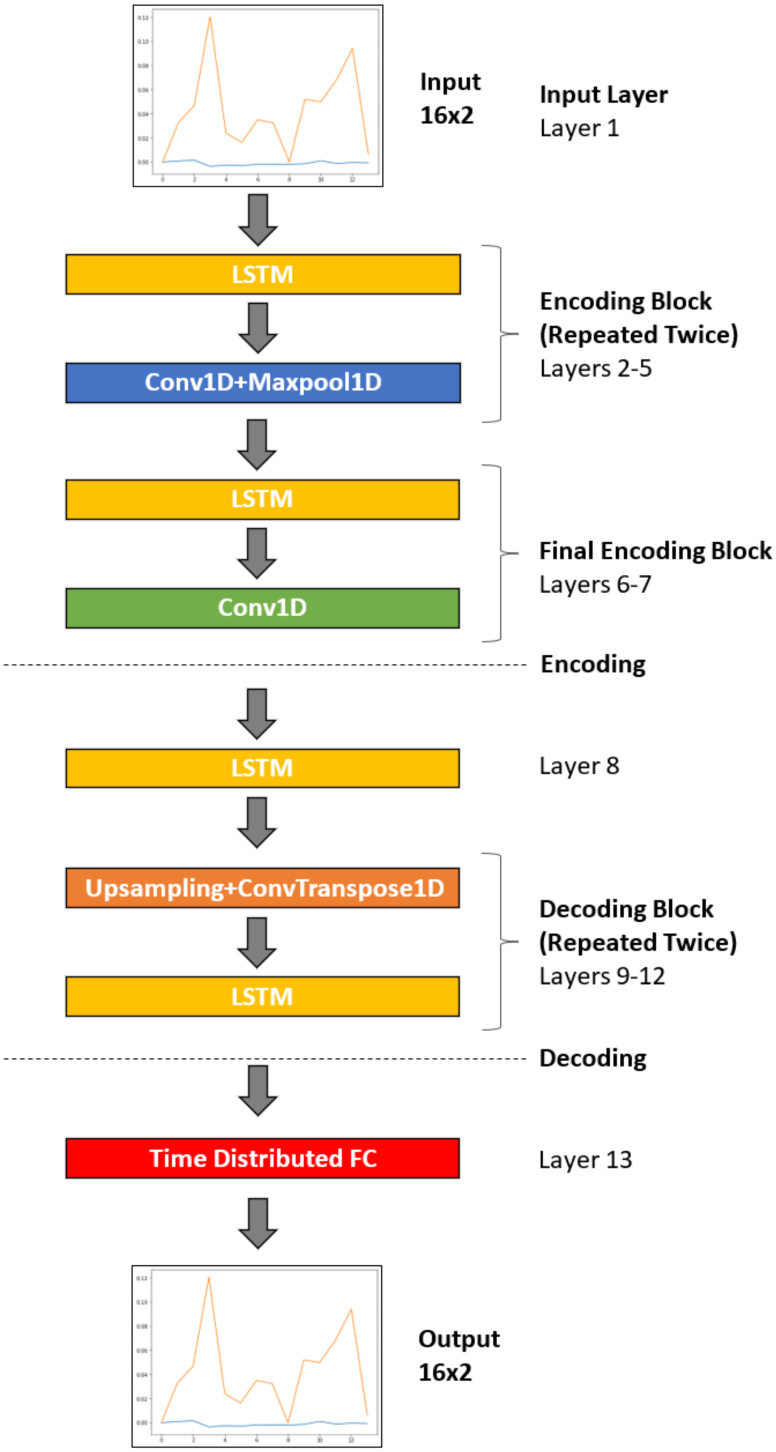

Figure 4.17: Anomaly detection model architecture where FC is a fully connected layer.

4.6.5 Experimental Setup and Data Collection

Concrete Specimens and sensor setup

Experimental data collected on the medium-scale control and ASR concrete specimens were used to develop and test the performance of the autoencoder anomaly detection model. The data include expansion measurements and ultrasonic signals. The measured expansions were used to indicate damage initiation in each reactive specimen. Ultrasonic signals were used to calculate velocity variation and decorrelation using CWI and CWD respectively before being restructured as inputs for the anomaly detection model.

Data presented in this section was collected on the following specimens: Control, Control-2D, RCA, RCA-2D. The sensor positions are shown in Figure 4.18. The S1 sensor is directly opposite to the ultrasonic transmitter on all specimens.

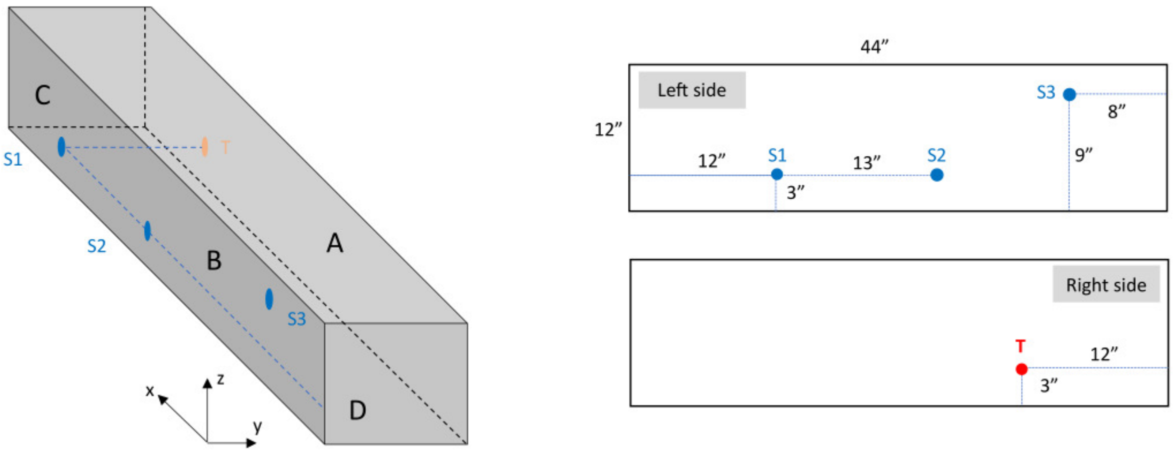

Figure 4.18: Sensor positions on concrete specimens [35].

Concrete Expansion

Fig. 4.19 shows the expansion of each specimen that were taken every two weeks. Both control specimens showed very little expansion throughout the duration of the experiment. The reactive specimens showed very little expansions before day 69, but exhibited a sudden increase in expansion after day 69, as shown by the change in slope. The day at which the slope of the expansion began to increase significantly, between days 69 and 84, was used to represent the estimated date of damage initiation [35]. For both reactive specimens (RCA and RCA-2D), the expansion measurements show a significant increase between days 69 and

84. The trend is most noticeable in the vertical expansion measurements, which had the largest increase during the experiment.

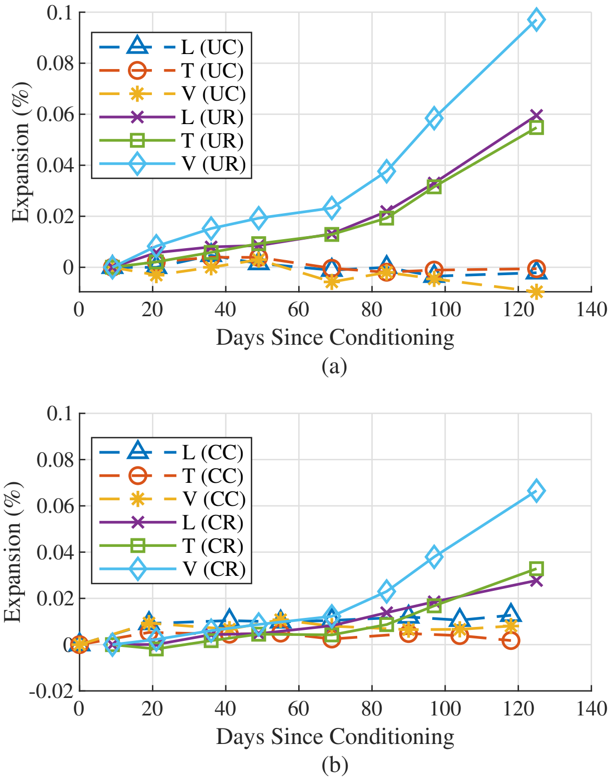

Figure 4.19: Expansion of (a) Control and RCA specimens (b) Control-2D and RCA-2D specimens (L: longitudinal; T: transverse; v: vertical; UC: Control; UR: RCA; CC: Control-2D; and CR: RCA-2D).

4.6.6 Data Set Composition

The experiment for this report was conducted using seven different data sets, one training data set and six testing data sets. The training data consists of all of the data collected for the two control specimens, the unconfined control specimen and the confined control specimen. For the unconfined control specimen, S1 collected 709 samples, while S2 and S3 only collected 116 samples as they were removed during the experiment. For the confined control specimen, which only had one sensor S1, 593 samples were collected. After rearranging the data from each of the sensors into sequences of length sixteen and then combining them, the total number of sequences used for training was 1474.

For the testing data sets, data from each sensor of each reactive specimen comprised its own testing data set, resulting in a total of six testing data sets. Furthermore, because we are focused on when the initial damage occurs in concrete specimens undergoing ASR damage, only the data from the first four months of the experiment was used. Each sensor of the reactive specimens collected 116 samples, resulting in 101 sequences used for each testing data set.

4.6.7 Results and Discussion

As described in section 4.6.3, the reconstruction-error based anomaly detection model is developed using the data from the two control specimens. Using the model described in section 4.6.4 the model was able to achieve a low training loss of 0.000198. To visualize how well the model reconstructs the velocity variation and decorrelation values of the training data, the reconstructed values are compared with the calculated values from the measurements in Fig. 4.20 using sensor S1 from the unconfined control specimen as an example.

The reconstruction error of the model using the training data, shown in Fig. 4.21, is used to choose the reconstruction error threshold for the model. Using the IQR, as described in section 4.6.3, the threshold is chosen to be 0.000470. The reconstruction error threshold will be then used to determine which input data sequence is anomalous. Sequences which returned a reconstruction error greater than the threshold will be classified as anomalous while sequences which returned reconstruction errors less than the threshold will be classified as normal.

The trained anomaly detection model is then applied to data collected from different sensors on the reactive specimens to test the model's ability to detect early damage in concrete structures undergoing ASR. The reconstruction errors of the model for each sensor from each reactive specimen and its corresponding first anomaly detection date are shown in Fig. 4.22. As demonstrated in Figure 4.22, for each sensor, the reconstruction errors of most data points are below the threshold before the first anomaly detection date, which can be more clearly observed in Fig. 4.23, a zoomed-in plot before the first anomaly date of S2 from the unconfined reactive specimen.

On average, only twenty-one sequences had reconstruction errors above the threshold before the first anomaly detection date, and the average reconstruction error before the first anomaly detection date was 0.0043. The average reconstruction error before the first anomaly detection date is boosted by a few points which had large reconstruction errors. These

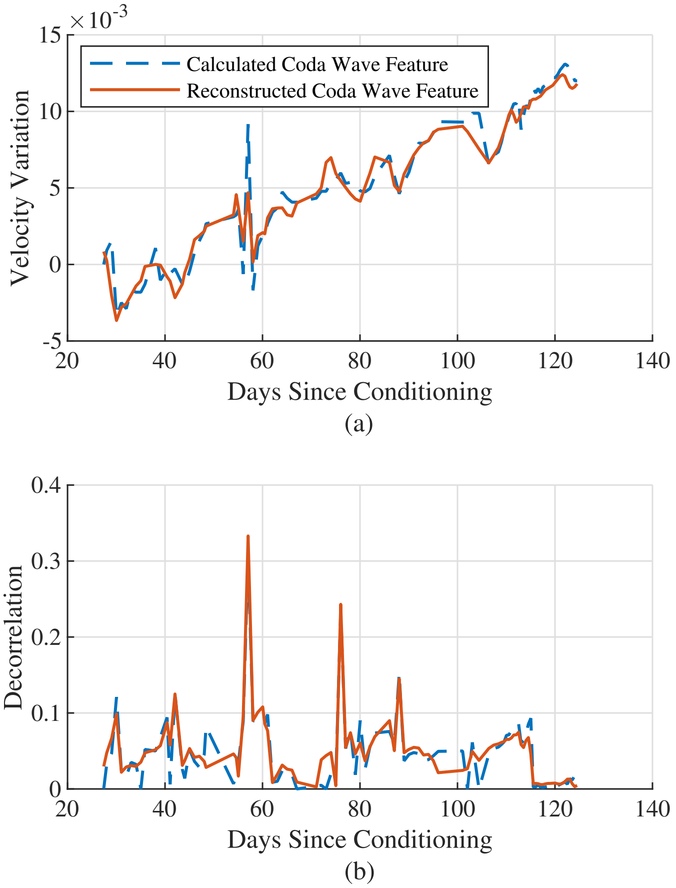

Figure 4.20: Comparison of (a) velocity variation and (b) decorrelation between reconstructed values and calculated values using S1 data collected from unconfined ”Control” specimen using proposed method.

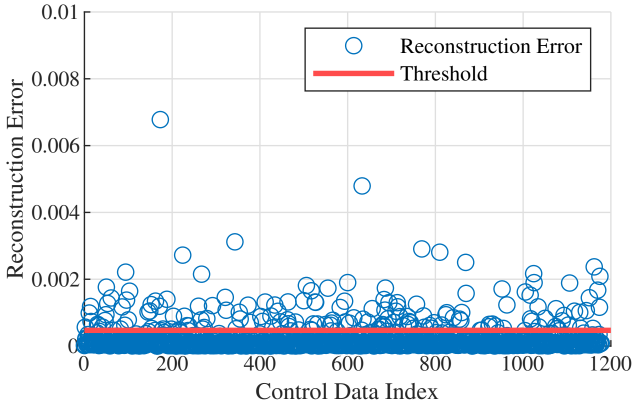

Figure 4.21: Reconstruction error of training data

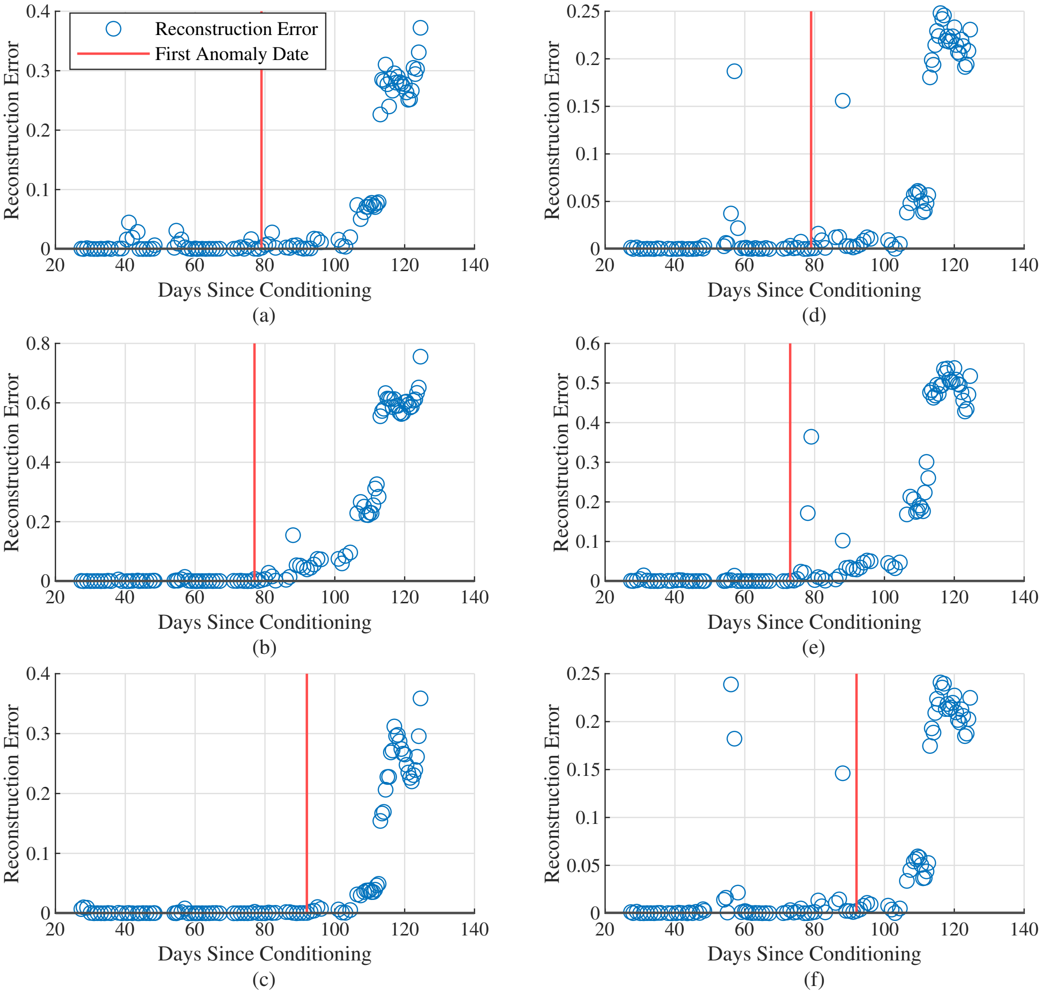

(a) (d)
(b) (e)
(c) (f)

Figure 4.22: Reconstruction errors of (a-c) unconfined reactive specimen (RCA) and (d-f) of the confined reactive specimen (Top: S1, Middle: S2, Bottom: S3 respectively).

samples with unusually large errors occurred right after chamber shutdowns, which were necessary for expansion measurements and sensor reinstallations. The effect of the chamber shutdown may have contributed to these large errors before the first anomaly detection date. Furthermore, although the reconstruction errors of some data points before the first anomaly date are above the threshold, they are not, however, classified as anomaly dates because they do not satisfy the criterion of having sixteen or more consecutive data points over the threshold, as stated in Section 4.6.3. After the first anomaly detection date, in general, the reconstruction error of each sensor does not fall below the threshold, and tends to increase with time. The average reconstruction error after the first anomaly detection date is 0.1791, which is significantly larger than the average reconstruction error before the first anomaly

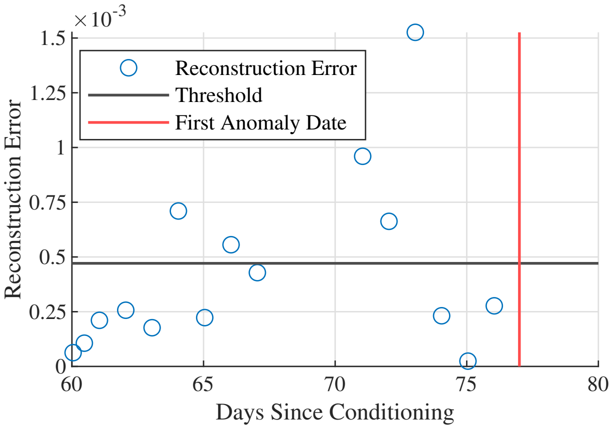

Figure 4.23: Reconstruction errors of S2 of the unconfined reactive specimen (RCA) before the first anomaly date.

detection. The first date that anomalies were detected by all sensors are also summarized in Table 4.5. From Table 4.5 we can see that the first anomaly detection dates of all sensors except S3 from the unconfined specimen are within the date range (between days 69 and 84) during which the average expansion begins to increase significantly as demonstrated in Fig. 4.19. These results demonstrate the feasibility of using the developed LSTM-CNN autoencoder model and the coda wave signals to detect early damage in concrete structures.

Table 4.5: First anomaly detection dates from all sensors on ASR specimens using LSTM-CNN autoencoder

Reactive Specimen Type	Sensor Location	Anomaly Detection Date (days)
Unconfined	S1	79
	S2	77
	S3	92
Confined	S1	79
	S2	73
	S3	79

In addition, Table 4.5 shows that the date at which each sensor detects the first anomaly may vary. The variation of anomaly dates detected by different sensors may be explained by the sensitivity kernels of coda-wave interferometry that show high sensitivity around the direct path between source and receiver [41]. Use S1 and S3 as examples. Since the transmitter was placed opposite to S1 and S1 is closer to side C of each specimen, the anomaly date detected by S1 might be more correlated to the transverse expansion measured on side C, compared with that detected by S3. Similarly, the anomaly date detected by S3, which is closer to side D of each specimen, might be more correlated to the transverse expansion measured on side D. This phenomenon is observed in both unconfined and confined reactive specimens.

Figure 4.24(a) shows the transverse expansion measured on side C for the unconfined specimen. It shows a significant increase between measurements taken on day 69 and day 84, while that on side D does not start to increase significantly until between days 84 and 97. Accordingly, S1 detects anomaly on day 79, earlier than S3 that detects anomaly on day 92. For the confined specimen, as shown in Fig. 4.24(b), the transverse expansion measurements on both sides C and D start to increase significantly between days 69 and 84. As a result, both S1 and S3 detect anomaly on the same day.

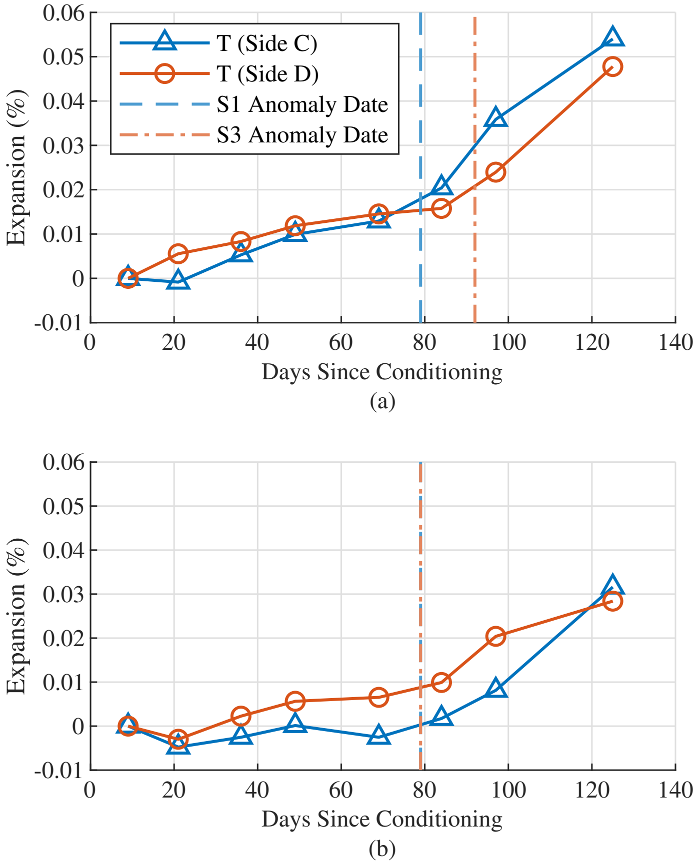

(a)

(b)

Figure 4.24: Axial expansion measurements of (a) transverse axis of sides C and D of the unconfined reactive specimen (RCA) (b) transverse axis of sides C and D of the confined reactive specimen (T: Transverse Axis).

As a baseline comparison anomaly detection using the same coda-wave features was conducted using an one-class support vector machine (SVM). For the one-class SVM a radial basis function (RBF) kernel was used for non-linear mapping and the parameter ν, which determines the upper bound on the fraction of outliers and the lower bound on the number of support vectors [42], and the parameter γ of the RBF kernel which determines how far the influence of a single training example reaches, were tuned so that the radius of the decision boundary containing most of the data was minimized [43]. A ν value of 0.05 and a γ value of 10 best minimized the radius of the decision boundary while containing most of the data as shown in Fig. 4.25.

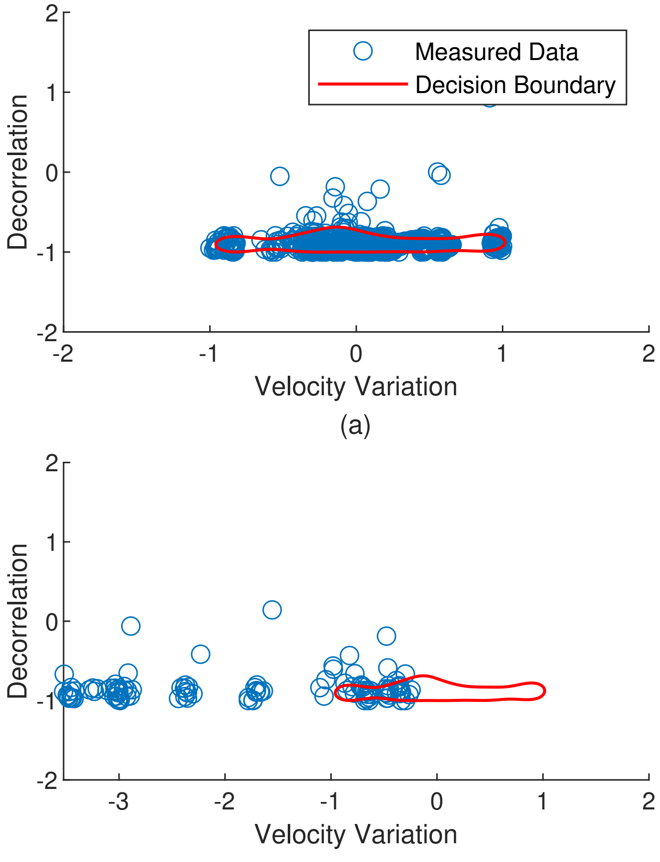

(a)

(b)

Figure 4.25: Decision boundary of one-class SVM for (a) training data (b) testing data of S2 data from the unconfined reactive specimen (RCA)

The distribution of the control data, as well as the decision boundary determined by the one-class SVM can be seen in Fig. 4.25(a). From the figure it can be seen that there are three main clusters of data for the training data set. The boundary decision encompasses most of the middle cluster and extends towards the cluster to the right which has a higher density than the cluster to the left.

The distribution of the testing data for S2 of the unconfined reactive specimen and the decision boundary can be seen in Fig. 4.25(b). A few of the points lie within the decision boundary, but majority of the data exists outside of the decision boundary as the velocity variation decreases far more for the unconfined reactive specimen. Fig. 4.25(b) showed the results obtained using the testing data for S2 of the unconfined reactive specimen, because it deviated most significantly from our expectations, but the results using all of the sensors are summarized in Table 4.6.

Table 4.6: First anomaly detection dates using One-Class SVM

Specimen	Sensor Location	Anomaly Detection Date (days)
Unconfined (RCA)	S1	76
	S2	62
	S3	75
Confined (RCA-2D)	S1	71
	S2	60
	S3	71

The one-class SVM detected anomaly dates that were generally earlier than that of the proposed method. In particular, S2 of both the unconfined and confined reactive specimens detected an anomaly much earlier than the expected damage date, day 62 and 60 respectively. Based on the expansion of the reactive specimens in Fig. 4.19, there is little evidence to suggest damage is occurring before day 69, suggesting that the one-class SVM is detecting anomalies before damage occurs.

Another method used as comparison to the proposed method was a reconstruction-error-based anomaly detection method using an autoencoder with no recurrent or convolutional layers. The same training and testing steps were taken for this method, and the anomaly detection dates using this method but a training loss of only 0.000713 was achieved, more than three times greater than the training loss achieved by the proposed method. First anomaly detection dates have been summarized in Table 4.7. To visualize how well this model reconstructs the velocity variation and decorrelation values of the training data, the reconstructed values are compared with the calculated values from the measurements in Fig. 4.26 using sensor S1 from the unconfined control specimen as an example. As seen in Fig. 4.26, the standard autoencoder which does not include recurrent or convolutional layers was unable to reconstruct the input sequences as accurately as the proposed method, as seen in Fig. 4.20. The first anomaly detection dates for the standard autoencoder method as shown in Table 4.7 is very similar to that of the one-class SVM method. As stated before, it is unlikely that a change occurred in the material before day 69, suggesting that the two comparison methods are detecting anomalies before damage has occurred.

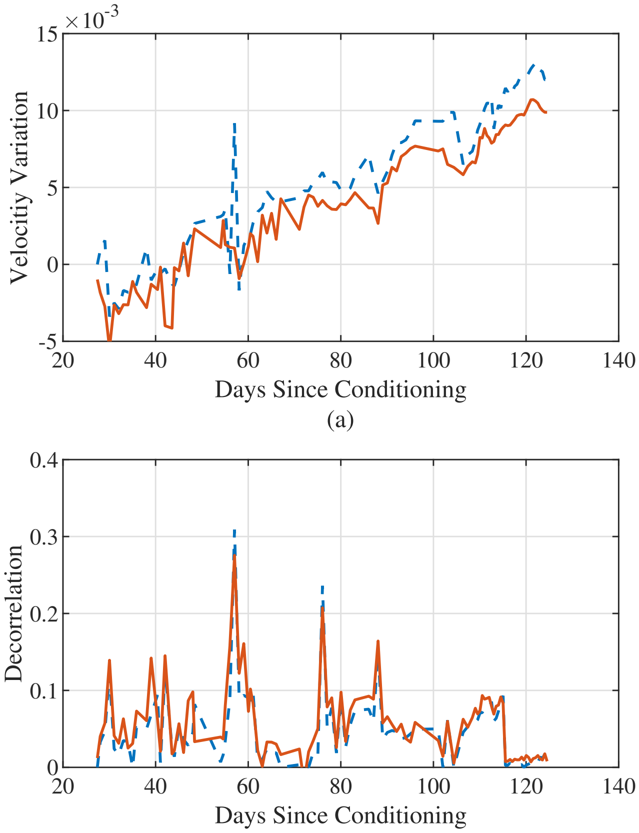

(a)

(b)

Figure 4.26: Comparison of (a) velocity variation and (b) decorrelation between reconstructed values and calculated values using S1 data collected from unconfined control specimen using a standard autoencoder.

Table 4.7: First anomaly detection dates using standard autoencoder

Specimen	Sensor Location	Anomaly Detection Date (days)
Unconfined (RCA)	S1	77
	S2	62
	S3	75
Confined (RCA-2D)	S1	71
	S2	63
	S3	71

4.6.8 Summary

An anomaly detection model based on coda waves is investigated for early damage detection of concrete structures undergoing ASR, and its feasibility is demonstrated. The model trained on data from multiple undamaged concrete structures is used to detect early damage in two different ASR specimens. By making use of the advantages of convolutional and recurrent layers, an autoencoder was trained to achieve a very low training loss of 0.000198. A reconstruction error threshold was chosen using interquartile ranges of the reconstruction errors of the training data. When the reconstruction error of the ASR specimens exceeds the threshold, the input sequence is marked as an anomaly. An anomaly date for each specimen is detected when all sequences containing data from that date is marked as anomalous. The experimental validation results show that the anomaly dates detected by the developed model are consistent with that derived from the expansion measurements, which demonstrates that the model developed from control specimens can be used for detecting initiation of damages in different specimens. Previous works have used damage detection and damage prediction methods which were dependent on specimen specific metrics. However, the proposed method has been shown to be able to detect damage in concrete undergoing ASR for two different specimens. The proposed method is trained on data from completely different specimens and has shown to be able to make predictions for two different test specimens, suggesting that it can be generalized across specimens. With more undamaged concrete specimens, the proposed method will likely be able to better reconstruct data of normal data, improving the performance and robustness of the proposed method. In addition, the anomaly dates detected by sensors at different locations seem to be highly correlated to the expansion measurements at locations and directions close to the direct path between source and receiver, consistent with the conclusions derived by other researchers based on the sensitivity kernels of coda-wave interferometry.

5 Ultrasonic Monitoring – Thermal Modulation of Nonlinear Ultrasonic Wave

5.1 Nonlinear Ultrasonic Method

Nonlinear ultrasonic techniques have attracted considerable attention due to their high sensitivity to microcracking damage in concrete. Concrete is a kind of nonlinear mesoscopic material and its nonlinearity comes from the mesoscopic linkages (order 10^{-6} to 10^{-9} m) among cement, aggregates and cracks. Cracks and microcracks in concrete will dramatically increase the concrete material nonlinearity. Its nonlinearity manifests as the hysteretic stress-strain relation and discrete memory. Following the phenomenological description of stress-strain hysteresis of rock by McCall and Guyer [44–46], a nonlinear hysteresis model is used to describe the modulus of nonlinear mesoscopic materials such as concrete and rock. The strain and strain rate related modulus is expressed as:

$$E(\varepsilon, \dot{\varepsilon}) = E_0 \left\{1 - \beta\varepsilon - \delta\varepsilon^2 - \alpha\left[\Delta\varepsilon + \varepsilon \text{sign}(\dot{\varepsilon})\right]\right\} \tag{5.1}$$

where E_0 is the linear modulus. ε and $\dot{\varepsilon}$ are the strain and strain rate, β and δ are the quadratic and cubic nonlinear parameter, and α is the hysteresis parameter. When concrete experiences dynamic excitation, even at the strain level as lows as 10^{-8}, the concrete modulus shows a softening behavior resulting in frequency/velocity shift [11]. When ultrasonic waves propagate in a nonlinear material, the ultrasonic waveform is distorted by the nonlinear response of the material, and higher harmonic waves are generated. These phenomena are very weak for undamaged samples and become remarkably large when microcracking and cracking develop in concrete. Most existing nonlinear ultrasonic methods are based on the behaviors of modulus softening or higher harmonics. Several nonlinear ultrasonic methods have been widely studied in the last few decades, such as Second Harmonic Generation (SHG) [47–50], Nonlinear Resonance Acoustic Spectroscopy (NRAS) [11–13, 45, 51, 52], Nonlinear Wave Modulation Spectroscopy (NWMS) [51, 53, 54], Dynamic Acousto-elastic

Testing (DAET) [55–58] and etc.

Although these existing nonlinear ultrasonic methods show different degrees of success in laboratory tests, there are some limitations of these nonlinear ultrasonic testing methods. The SHG technique needs high precision equipment to detect the high order harmonics. The NRAS method is only applicable to small samples since it needs the free vibration of the test sample. The NWMS method requires either a high amplitude impact source or a low-frequency pumping wave source to modulate the high-frequency wave, which is often challenging for large concrete structures. The DAET method uses a shaker or a large piezoelectric disk to vibrate the sample to generate strain changes inside the sample. Although the strain level needed is low, it is hard to excite large size samples. Additionally, the strain changes generated by impact or pumping only exist in a local area, which indicates only the nonlinear behavior of a small area can be excited. Overall, these nonlinear ultrasonic methods measure the nonlinear responses excited by the stress-induced strain changes. There are two limitations to the stress-induced strain. First, these methods need large energy input to generate strain changes which makes these methods not applicable to large size concrete structures. Secondly, the stress on the sample may only create local strain changes, resulting in that the method may only be sensitive to local damages.

In this work, we proposed a new nonlinear ultrasonic wave method: thermal modulation of nonlinear ultrasonic waves for characterizing the concrete damage level. Instead of using stress-induced strain, thermal strain changes due to temperature change is used as the driving force to excite nonlinear behavior of material and modulate the high-frequency ultrasonic waves in a material. For materials with microcracking damage, the temperature effect is especially effective for generating large thermal strain, which causes closing/opening of microcracks and induce strong hysteretic nonlinearity. Thermal modulation coefficients, which represent the thermal dependence of the relative velocity changes, are used as a nonlinear parameter to evaluate concrete damage levels [59]. Most concrete structures are exposed in ambient environment and experience temperature changes. Temperature changes on concrete can create large enough thermal strains (about 10 $\mu\varepsilon$ per Celsius) which can excite the nonlinear behavior of concrete. Compared to the stress-induced strain, the thermal strain is more uniform in concrete, and the proposed method will be more sensitive to global damage. In this chapter, we use the temperature change during the chamber shutdown to modulate the ultrasonic waves and concrete damage induced by ASR is studied using the thermal modulation method.

5.2 ASR Damage Characterization

When the chamber was shut down, the sample temperature dropped from 38°C to 23°C. Meanwhile, the ultrasonic signals for the sensor pair (T-S1) were recorded every ten minutes. The relative velocity change histories were obtained using the CWI analysis (stretching) for the cooling process. The relative velocity change dv/v and the temperature change ΔT were correlated for the thermal modulation analysis. The slope of the correlation curves k_1^- is defined as the thermal modulation coefficient. Since the whole shutdown process was less than 17 hours, we assume there is not ASR damage development during such short time.

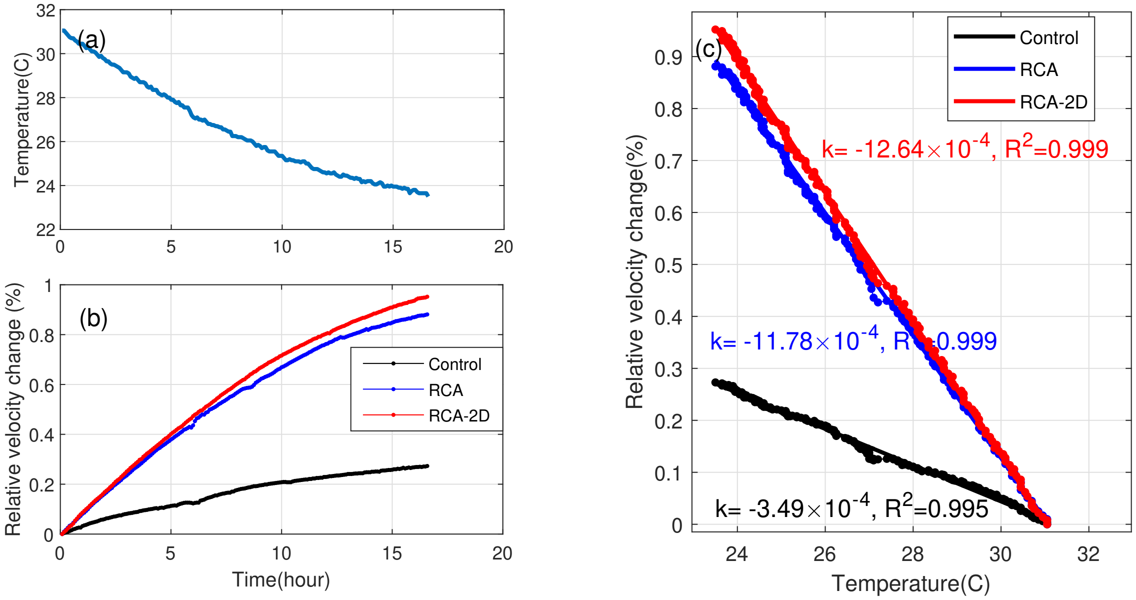

Figure 5.1: Thermal modulation test results for the Control, RCA, and RCA-2D specimens on 01/20/2020: (a) Temperature history, (b) Relative velocity change history, (c) Correlation curves

Figure 5.1(a) and (b) shows the temperature history and the relative velocity change histories for the Control, RCA, and RCA-2D specimens in the temperature range of 31°C to 23°C. The RCA sample had the largest velocity increase, while the control sample had the lowest velocity increase. This test was conducted on 01/20/2020 (age of 420 days) and the transverse expansions of the three specimens were measured as 0.0003%, 0.225%, and 0.232% for the control, RCA, and RCA-2D specimens, respectively. In Figure 5.1(c), the correlation curves for the three specimens all have good linearity and the goodness of fit coefficients R^2 are all very close to 1. The curve for the RCA-2D sample shows highest k_1^-, while the curve of the control sample has the lowest coefficient. The RCA sample has a slightly smaller k_1^-

than that of the RCA-2D sample, which is also consistent with their transverse expansions.

Figure 5.2(a) and (b) shows the temperature history and the relative velocity change histories of the Control-2D, RFA, and RFA-2D specimens in the temperature range of 34°C to 26°C. The test was also conducted on 01/20/2020 (age of 292 days) and the transverse expansions of the three specimens were measured as 0.006%, 0.038%, and 0.156% for the Control 2D, RFA, and RFA-2D specimens, respectively. In Figure 5.2(c), The RFA-2D sample had the highest k_1^- and the trend of the three coefficients matches the damage levels of the three specimens. The correlation curves for the RFA and RFA-2D specimens have some curvatures while the curve of the control sample has good linearity. The curvature of the correlation curves is related to the high order nonlinearity of the material [59].

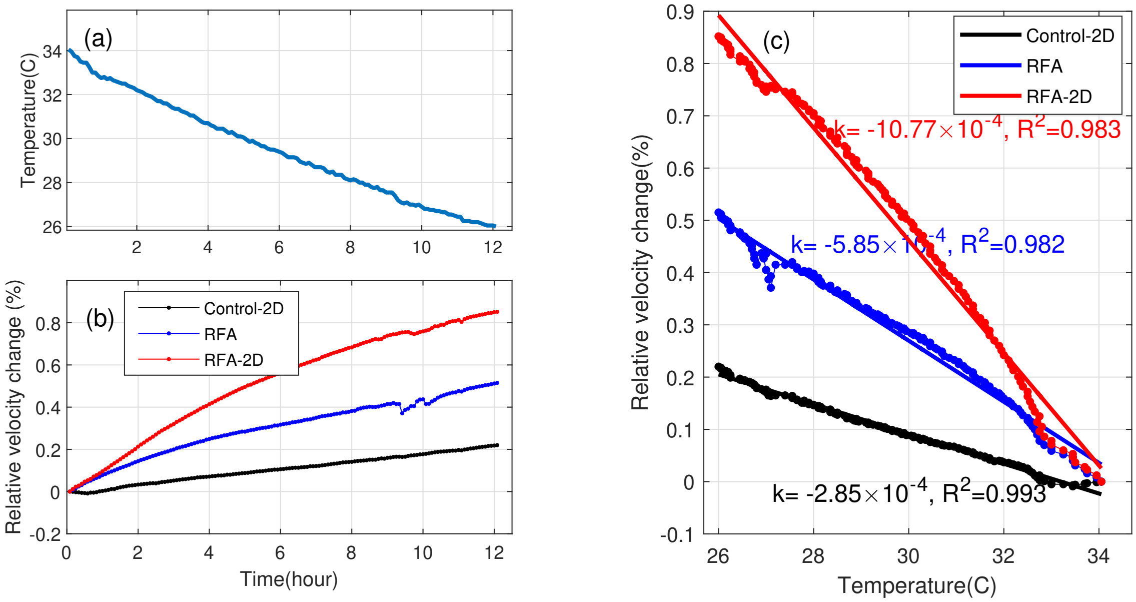

Figure 5.2: Thermal modulation test results for the Control-2D, RFA, and RFA-2D specimens on 01/20/2020: (a) Temperature history, (b) Relative velocity change history, (c) Correlation curves

Figure 5.3(a) and (b) shows the temperature history and relative velocity change histories of the two sRCA specimens in the temperature range of 37°C to 26°C. The test was conducted on 03/23/2020 (age of 216 days) and the transverse expansions of the two specimens were measured as 0.124% and 0.125%. In Figure 5.3(c), both curves have a very close slope and they also had similar transverse expansions. The sRCA sample shows a little bit of curvature while the curve of the sRCA-2D sample shows good linearity, which indicates the sRCA sample has some higher order nonlinearity. At the test time, the volumetric expansion of the sRCA sample was 0.427%, which was slightly larger than the expansion of the sRCA-2D sample 0.400%.

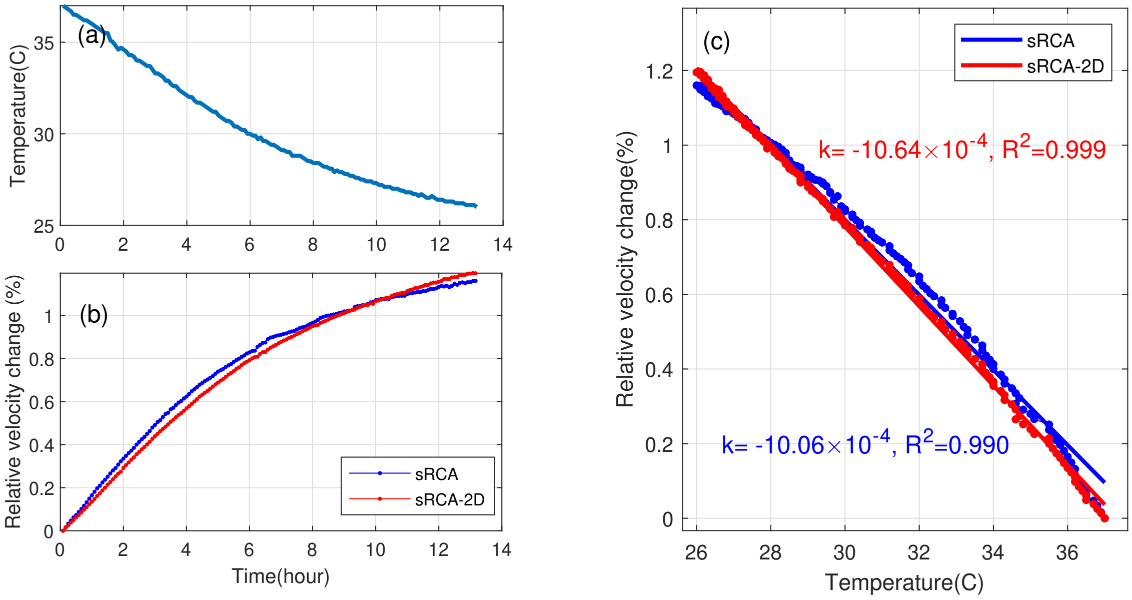

Figure 5.3: Thermal modulation test results for the sRCA and sRCA-2D specimens on 03/23/2020: (a) Temperature history, (b) Relative velocity change history, (c) Correlation curves

The results for all specimens are summarized in Table 5.1. The concrete ages and volumetric expansions are also included in the table. The RCA and RCA-2D specimens had the longest curing age and largest transverse expansions. The two specimens also had the highest thermal modulation coefficients k_1^-. The two specimens in the sRCA batch had the shortest curing age and smallest transverse expansion, which represent lowest damage level. These specimens had smaller coefficient k_1^-. The RFA and RFA-2D specimens had the moderate damage level. Based on these results, the sample with a higher transverse expansion shows higher coefficient k_1^-. The sRCA and sRCA-2D had similar coefficients k_1^- due to similar transverse expansions. However, the higher curvature of the sRCA curve may be related to by its higher volumetric expansion. Therefore we can conclude that the thermal modulation coefficient in this study is dominant by the transverse expansion, but also affected by the volumetric expansion.

Table 5.1: Thermal modulation test results for the concrete specimens

Batch	Sample	Age (day)	Transverse Expansion	Volumetric expansion	k_1^-
RCA	Control	420	0.000%	-0.008%	-3.49$\times 10^{-4}$
	RCA	420	0.225%	0.801%	-11.78 $\times 10^{-4}$
	RCA-2D	420	0.232%	0.526%	-12.64$\times 10^{-4}$
RFA	Control-2D	292	0.006%	0.003%	-2.85$\times 10^{-4}$
	RFA	292	0.038%	0.203%	-5.85$\times 10^{-4}$
	RFA-2D	292	0.156%	0.444%	-10.77$\times 10^{-4}$
sRCA	sRCA	216	0.124%	0.427%	-10.06$\times 10^{-4}$
	sRCA-2D	216	0.125%	0.400%	-10.64$\times 10^{-4}$

5.3 ASR Damage Monitoring

Based on the results in Figure 5.1, Figure 5.2, and Figure 5.3, we can conclude that the thermal modulation coefficient k_1^- can be used to characterize the damage levels of the concrete specimens with ASR damage. The thermal modulation coefficients k_1^- measured from each chamber shutdown period are used to monitor the ASR damage development over time.

RCA specimens Figure 5.4(b) shows the thermal modulation coefficients k_1^- over time for the Control, RCA, and RCA-2D specimens. All the results are extracted from the cooling process of the specimens from 08/19/2019 (265 days) to 5/10/2020 (530 days). The transverse expansions for this period are plotted in Figure 5.4(a). The k_1^- for the Control sample has a range from $3 \times 10^{-4}/°\text{C}$ to $6 \times 10^{-4}/°\text{C}$ during this period. This variation may be caused by the inconsistency of testing conditions for each test, such as the temperature changing rate, humidity condition. The RCA and RCA-2D specimens both showed higher thermal modulation coefficients ($> 8 \times 10^{-4}/°\text{C}$) than of the Control-2D sample. The k_1^- of the RCA-2D sample has a increasing trend as ASR damage developing, while the coefficient of the RCA sample increases first until 420 days and then decreases.

RFA specimens Figure 5.5 shows the thermal modulation coefficients k_1^- during the period pf 08/19/2019 (137 days) to 5/10/2020 (402 days) for the Control-2D, RFA, RFA-2D specimens. The thermal coefficient k_1^- of the Control-2D sample decreases from $5.2\times 10^{-4}/°\text{C}$ to $2 \times 10^{-4}/°\text{C}$ due to cement hydration. The RFA sample had similar k_1^- values with the Control-2D sample until 200 days and then started to increase. The expansion initiation

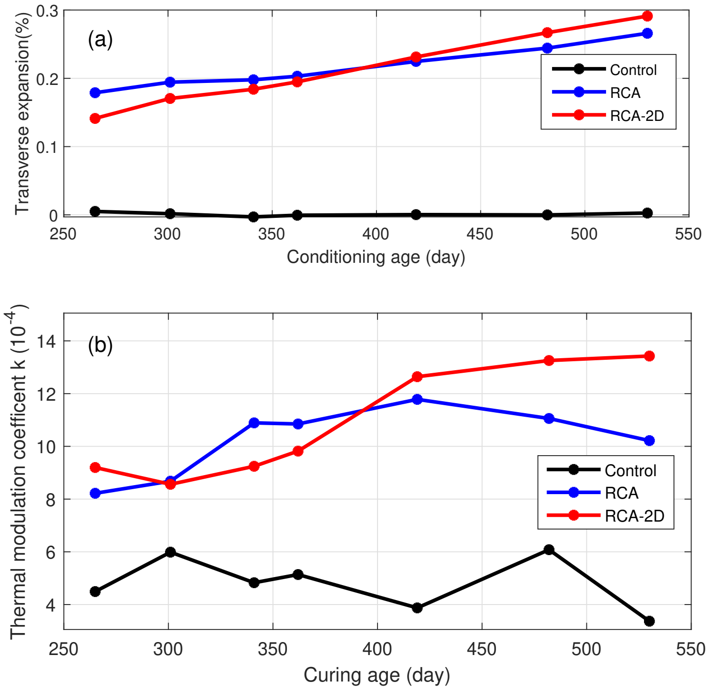

Figure 5.4: Control, RCA, and RCA-2D specimens: (a) Transverse expansion history, (b) Thermal modulation test results

time of RFA sample was around 150 days. The RFA-2D sample had a consistently increasing trend from the beginning (137 days) since the sample began to expand at 118 days and had much higher expansion than the RFA sample. Overall, the trend of the thermal modulation coefficients has a good agreement with the expansion histories of the three specimens.

sRCA specimens Figure 5.6 shows the thermal modulation coefficients k_1^- over time for the sRCA and sRCA-2D specimens. The data points start from 08/19/2019, which is the conditioning start date of the two specimens. The thermal coefficients k_1^- of the two ASR specimens kept increasing from the beginning, while the expansions initiated at 36 days. Before 36 days, the k_1^- values were around $4 \times 10^{-4}/°\mathrm{C}$ or $5 \times 10^{-4}/°\mathrm{C}$, which was similar to the coefficients of the Control and Control-2D specimens. It indicates the two ASR specimens had little ASR damage before the crack initiation date. After 36 days, the thermal modulation coefficients k_1^- of the two specimens kept increasing, which indicates that ASR damage was developing in the two specimens. The increasing trend has a good agreement with the expansion histories of the two specimens. Since the two specimens had similar transverse expansion over time, the thermal modulation coefficients of the two specimens also showed similar values and trends.

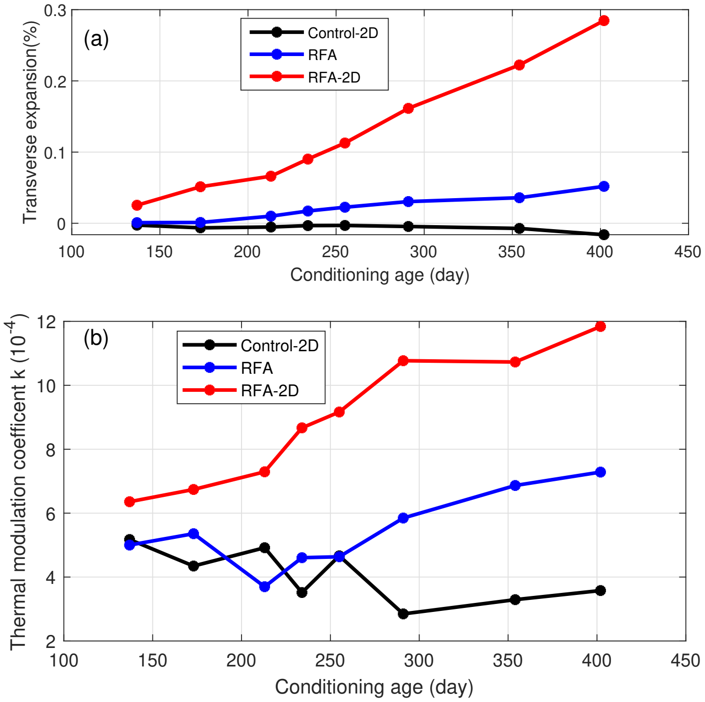

Figure 5.5: Control-2D, RFA, and RFA-2D specimens: (a) Transverse expansion history, (b) Thermal modulation test results

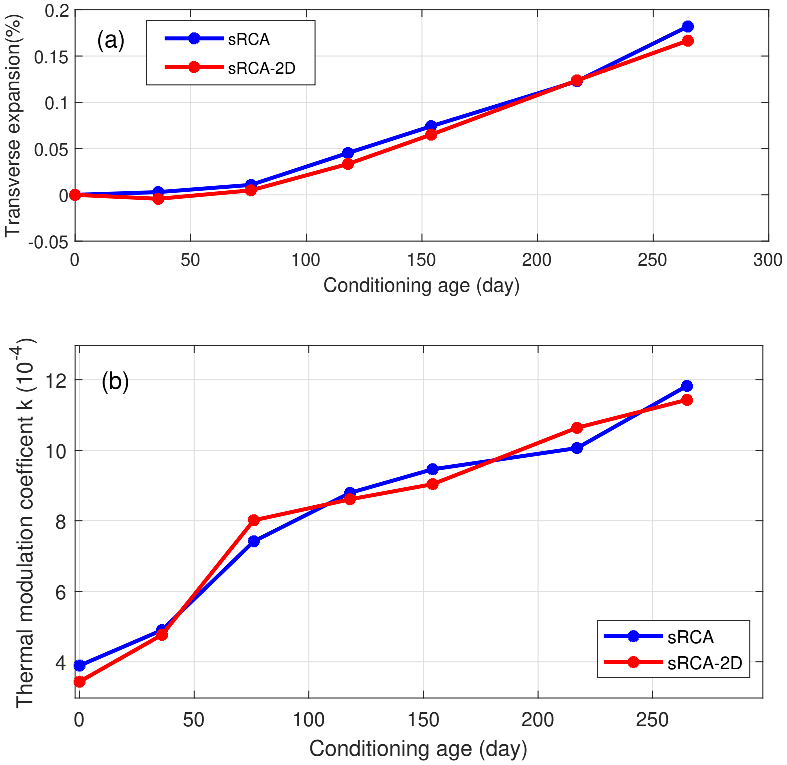

Figure 5.6: sRCA and sRCA-2D specimens: (a) Transverse expansion history, (b) Thermal modulation test results

5.4 Correlation Between Thermal Modulation Coefficient and Expansion

In a separate study on the same concrete specimens, Malone [60] found the relative nonlinear parameter α_{IE} from nonlinear impact-echo had a strong correlation with the expansion. For unconfined specimens, the impact-echo test was only conducted in the vertical direction since the vertical and the transverse have similar damage levels. For concrete specimens with 2D confinement, IE tests were conducted in both transverse and vertical directions. The correlation data points for all tests are plotted in Figure 5.7. The nonlinear parameter α_{IE} has a strong linear relationship with the expansion, which proves the feasibility of using the nonlinear parameter for quantitative evaluation of ASR damage.

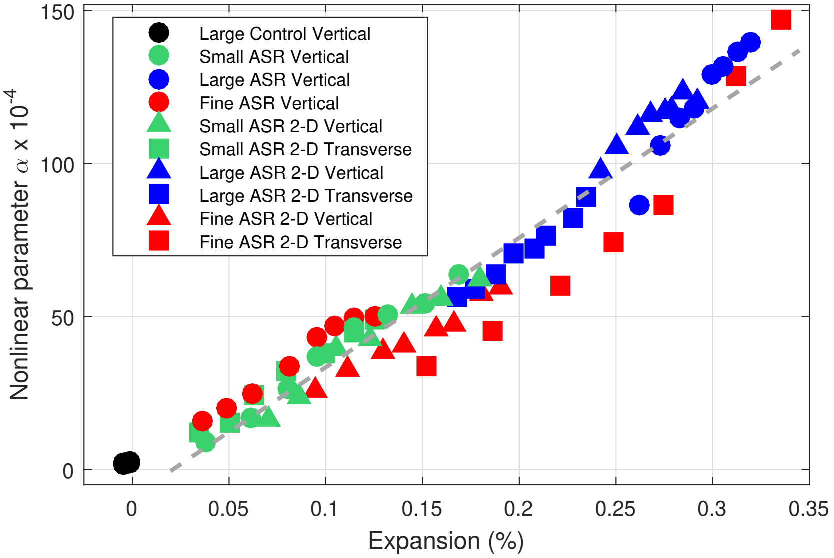

Figure 5.7: Correlation between the nonlinear parameter α_{NLIE} and the expansions in vertical and transverse directions

The results in Figure 5.4, 5.5 and 5.6 demonstrate that the thermal modulation coefficient can be used to monitor the ASR damage development. In this subsection, the thermal modulation coefficient and the transverse expansion were correlated. For each thermal modulation coefficient obtained from the chamber shutdown, expansions were measured at the same time. Figure 5.8 shows the correlation curves between the thermal modulation coefficients and transverse expansions for all eight specimens. In the figure, triangles represent the RCA specimens, while circles for RFA specimens and stars for the sRCA specimens.

For the data points around zero expansion, the thermal modulation coefficient ranges

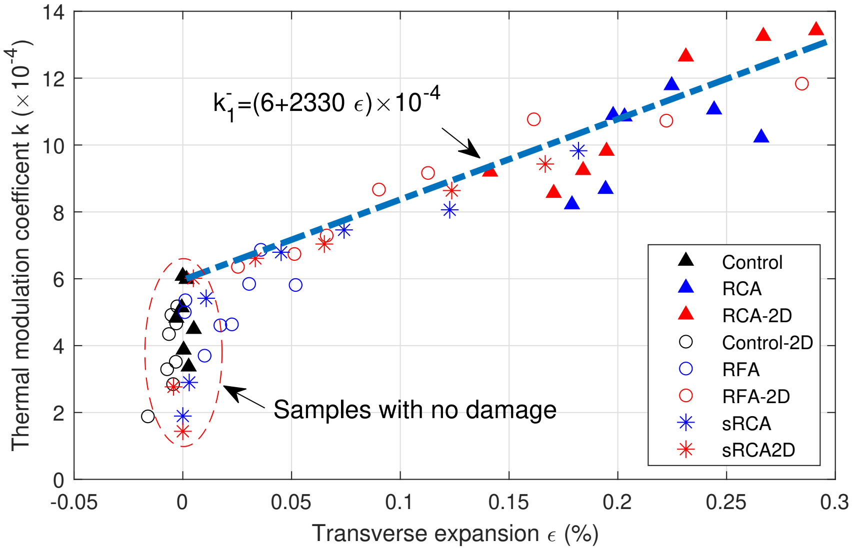

Figure 5.8: Correlation between the thermal modulation coefficient k_1^- and the transverse expansion for all specimens

from $2 \times 10^{-4}/°\mathrm{C}$ to about $6 \times 10^{-4}/°\mathrm{C}$ and these data points represent the results of the control specimens and the ASR specimens before measurable damage. Therefore, the thermal modulation coefficient $k_1^- = 6 \times 10^{-4}/°\mathrm{C}$ can be used as a threshold value to classify ASR damage. Once there is a measurable expansion on the ASR specimens, the thermal modulation coefficient increases almost linearly with the ASR expansion. These data points contain the results from the unconfined specimens and the 2D confined specimens, with reactive coarse aggregate or reactive fine aggregate. Although the ASR specimens had different mixing designs and confinement conditions, these data points show a good linear relationship between thermal modulation coefficient and transverse expansion. We may use a linear relationship to describe the correlation between the two parameters:

$$k_1^- = (6 + 0.23\varepsilon) \times 10^{-4} \tag{5.2}$$

where ε for the transverse expansion. This empirical relationship provides an NDE method to evaluate the damage level of concrete structures affected by ASR without using a baseline measurement and an expansion history. Compared to the linear velocity change parameter presented in 4, the thermal modulation coefficient is a promising parameter for ASR damage evaluation, regardless of mix designs and confinement conditions.

6 Acoustic Emission Monitoring

6.1 Experimental Methodology

6.1.1 Small-scale specimens

The information on small-scale specimens is provided here as background information. This work was completed prior to the current NEUP project and was self-funded. Further information can be found in [61] and portions of this chapter have been adapted from this source.

Fifteen specimens were cast, including twelve conditioned specimens cast with reactive coarse aggregate (RCA) and three control specimens cast with nonreactive coarse aggregate (non-RCA). All specimens have dimensions of 3 x 3 x 11.25 inches (76 x 76 x 286 mm). The w/c ratio, cement content, the volume of coarse aggregate per unit volume of concrete, and alkali content for the conditioned specimens are show in Table 6.1. Table 6.2 shows the concrete mix design. The conditioned specimens were cast using two identical batches (six specimens per batch). The control specimens were cast with ordinary Portland cement and innocuous aggregates.

Table 6.1: Materials ([61], used with permission)

w/c ratio	0.45
Cement content	26.2 lb/ft^3
Volume of coarse aggregate per unit volume of concrete	0.70
Alkali content	5.0% Na2Oeq

To accelerate the ASR test, the concrete specimens were put in a sealed chamber room for one year with a temperature of 100 ± 2°F and a humidity of 100% relative humidity. Three

Table 6.2: Mix design ([61], used with permission)

Constituent	Weight (lbs./cy)
Cement	700
Water	340
Coarse Aggregate	1,830
Fine Aggregate	1100
NaOH Admixture	40
Total	4,010

concrete specimens were placed in one container (Figure 6.1). In total, four containers were used. The petrographic examinations were conducted on three specimens on days 14, 28, and 56. This chapter utilizes 'XY-Z' format to represent the types of all the specimens, where "X" refers to the type of specimen, S means the ASR specimens, and C means the control specimen. 'Y' refers to the specimen number; the specimens in batch one are numbered from 1 to 6, and the specimens in batch two are numbered from 7 to 12. 'Z' denotes the duration of conditioning in days.

Figure 6.1: Test setup. Controlled temperature chamber (left) and specimens placed in 100% relative humidity buckets (right). ([61], used with permission)

The specimens were measured using a length comparator apparatus (Figure 6.2(a)). In the first two months, the measurements of lengths were conducted at 5, 10, 14, 28, and 56 days. Additional measurements were carried out on the three samples that were tested for another year. The measurement readings collected during the year were compared with the measurements conducted on the third day after conditioning. This procedure is designed to minimize the effect of thermal expansion. One R6I-AST resonant sensor with an operating frequency of 40-100 kHz was attached at the mid-length of the specimen as shown in Figure 6.2(b).

(a)

(b)

Figure 6.2: (a) length comparator apparatus, and (b) specimens with AE sensors attached. ([61], used with permission).

6.1.2 Medium-scale specimens

Six medium-scale specimens were cast for ASR experimental program. Three specimens were cast at the University of Alabama, including an RCA specimen, an RCA specimen with two-dimensional confinement (RCA-2D), and a control specimen. Three specimens were cast at the University of Nebraska, including a reactive fine aggregate (RFA), an RFA specimen with two-dimensional confinement (RFA-2D), and a control specimen with two-dimensional confinement (Control-2D). The details of the mix design of all specimens and experimental procedures are described in Chapter 2. Much of the information on medium-scale specimens has been summarized in [62–64], and portions of those sources are adapted for this chapter.

6.2 Reduction of Acoustic Emission Data

Acoustic emission data was recorded over an extended period of time for both small-scale and medium-scale specimens. As acoustic emission is a very sensitive means of detection, it is inevitable that in such long-term programs a significant amount of spurious data was received. Therefore, several filters were developed and utilized to minimize this spurious data.

For the small-scale specimens, the primary reason for the unwanted data is due to the geometry of the specimens, resulting in emission due to reflections. This occurs because the length and width of the specimens is much smaller than the attenuation distance of the AE signal. Different types of parameter-based data filters were utilized. The first filter utilized for small-scale specimens is referred to as a “duration-amplitude filter (D-A)”, also referred to as a Swansong II filter [65]. This filter is based on the observation that a genuine acoustic emission signal with long duration generally has high amplitude and vice versa. The second filter is implemented after the first filter type. This filter is based on the rise time and amplitude (R-A) and reflects the observation that genuine AE signals with long rise time generally have high amplitude and vice versa. The third filter removes AE signals with signal strength larger than 10,000,000 pVs (pico-volt second). Filter four deletes AE signal with small counts (less than 2) and high amplitude (more than 50 dB).

In addition to the feature-based filters two frequency-based filters were utilized to minimize spurious data. The first frequency-based filter removed AE signals whose average frequency is not in the range of 10-200 kHz. The second frequency-based filter removes a signal if its peak frequency is less than 20 kHz. The filters described above were developed with consideration to in-depth inspection of the waveforms, study of the literature, and past experience with similar data.

For the medium-scale specimens, the primary source emission is faulty cable connections and environmental noise. Due to the high humidity environment, water found its way into the cable to sensor connections on some occasions. The data due to these faulty connections was minimized by removing the signal with a low average frequency (less than 60 kHz) and low peak frequency (less than 80 kHz). An additional filter was developed to remove environmental noise, which was based on the AE event definition. Only AE events with at least four hits were considered genuine data and preserved, while the remainder of the data was discarded.

6.3 Results

6.3.1 Small-scale specimens

Results of AE cumulative signal strength (CSS) and the measurement of length for all conditioned specimens are shown in Figure 6.3. The AE activity increases as exposure time increases, demonstrating this method may be well suited for estimating the rate of ASR degradation. Furthermore, the CSS of the specimens exposed over a full year increased, demonstrating that the AE sensors can detect the formation of micro-cracks as ASR deterioration progresses, regardless of the attenuation induced by those cracks. It is observed in Figure 6.3 that length change rises as exposure time increases, which is consistent with the AE data progression. With a value of 0.044 percent, the largest length change was detected in specimen S10-365. ASTM C1293 [5] specifies 0.04 percent expansion after one year of exposure as the cutoff point for determining if an aggregate is prone to harmful ASR expansion, which is consistent with a) the known reactivity of the type of aggregates utilized and b) the petrographic analysis results, which revealed ASR damage as discussed in the following section. The results shown in Figure 6.3, length change measurements and CSS, had a correlation coefficient of 0.81 which indicates a strong correlation between the two variables. This suggests that AE monitoring may be utilized to compute the rate of expansion associated with ASR damage, enabling the detection and quantification of this degradation mechanism.

Using a Damage Rating Index (DRI), a petrographic investigation was conducted on two specimens on day 14, two specimens on day 28, and two specimens at day 56. Figure 6.4 depicts the results of the petrographic research. The specimen with the lowest DRI value had been conditioned for 14 days and the specimen with the highest DRI value had been conditioned for 56 days. It is evident that the average DRI value rises as the duration of exposure time increases. The most common ASR damage features in the investigated specimens were cement paste cracking, cracks with gel in the cement paste, gel formation in air voids, and aggregate cracking.

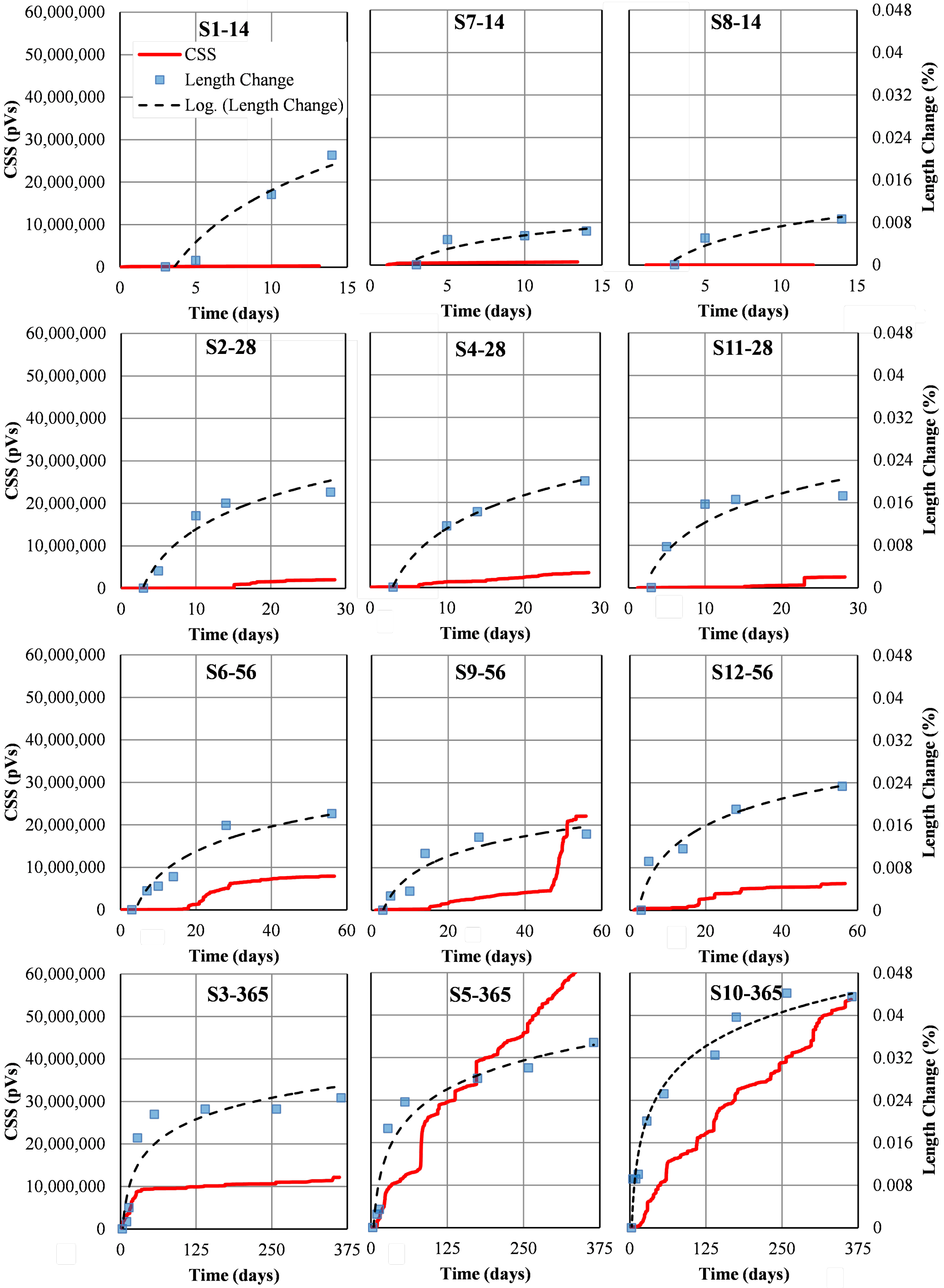

Figure 6.3: CSS and length measurement versus time for all the specimens (S5-365 CSS=6.48e7 pVs). ([61], used with permission)

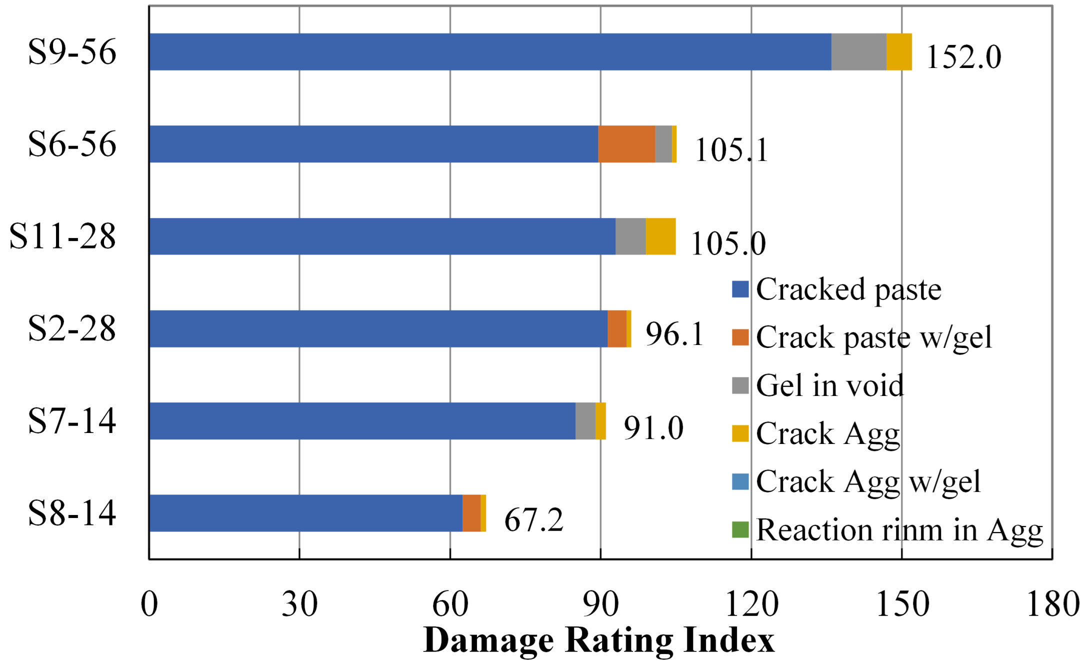

Figure 6.4: DRI measurements for six specimens. ([61], used with permission)

AE Intensity Analysis (IA) [66] is one method to classify ASR damage based on historic index and severity. This method utilizes signal strength to derive historical index H(t) and severity Sr. The historic index H(t) is a trend analysis that calculates the change in the slope of CSS relative to time. The severity Sr is calculated by averaging the signal strength of the largest fifty hits. The historic index and severity can be obtained using Equations 6.1 and 6.2

$$H(t) = \frac{N}{N-K} \frac{\sum_{i=K+1}^{N} S_{oi}}{\sum_{i=1}^{N} S_{oi}} \tag{6.1}$$

$$S_r = \frac{1}{50} \sum_{i=1}^{i=50} S_{oi} \tag{6.2}$$

where N is the number of hits collected up to t, S_{oi} refers to the signal strength of the i-th event, K refers to an empirically determined factor that fluctuates depending on the number of hits. For this work K is described as a) N/A if N≤50, b) K=N-30 if 51≤N≤200, c) K=0.85N if 201≤N≤500, and d) K=N-75 if N≥501.

The greatest $H(t)$ and S_r obtained for each specimen are displayed on an intensity analysis chart. More damage is indicated by points displayed in the top-right quadrant of the chart.

Table 6.3: Length change, DRI and AE results ([61], used with permission)

Specimen	Duration (days)	Length change* (%)	DRI	Historic index	Severity (pVs)
S7-14	14	0.006	91.0	1.514	1.38E+04
S8-14	14	0.009	67.2	1	1.40E+03
S2-28	28	0.018	96.1	1.707	2.68E+04
S11-28	28	0.017	105.0	2.982	4.89E+04
S6-56	56	0.018	105.1	2.167	9.13E+04
S9-56	56	0.014	152.0	3.246	2.15E+05

The IA and DRI values are shown in Figure 6.5. In the lower left corner of the figure, the specimen with minor DRI damage is plotted. IA data points move towards the top-right corner of the figure as DRI readings rise, indicating more damage. The chart can be separated into three parts based on DRI results: A-No damage, B-Minor damage, and C-Moderate damage.

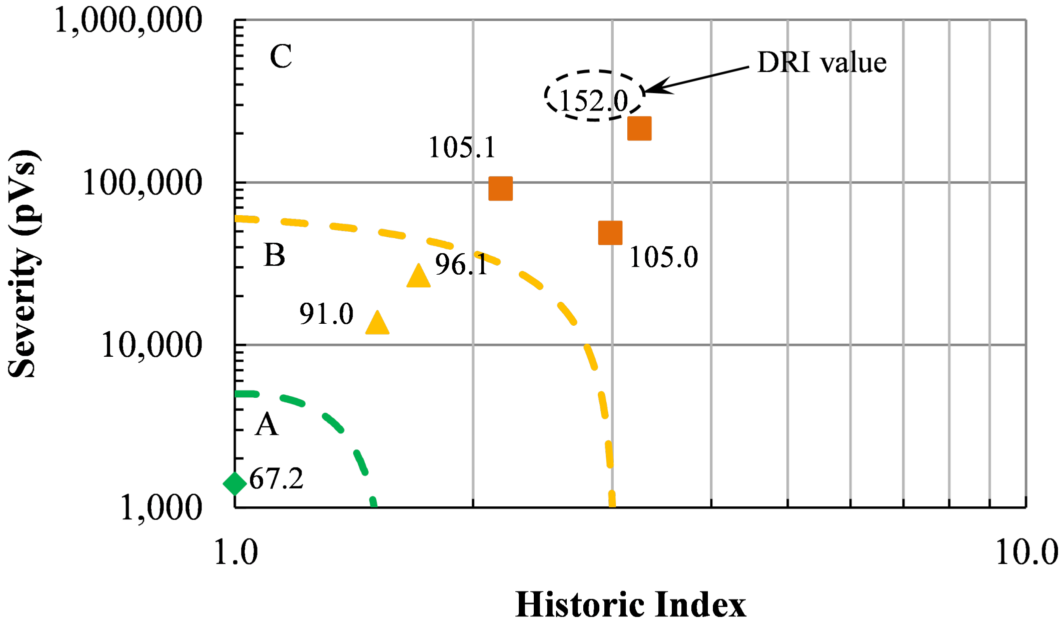

Figure 6.5: Results of intensity analysis (S5-365 CSS=6.48e7 pVs). ([61], used with permission)

The DRI readings and severity have a 0.95 correlation coefficient. The DRI measurements and the historic index have a 0.88 correlation coefficient. According to these findings, DRI levels had a stronger association with AE activity than length change, indicating that AE activity and DRI values are linked.

6.3.2 Medium-scale specimens RCA, RCA-2D, and control

Specimens RCA, RCA-2D, and control were conditioned for 300 days. The ”confined” specimen in this section refers to RCA-2D, whereas the ”unconfined” specimen with reactive coarse specimen is referred to as RCA. The volumetric strains of the three specimens are illustrated in Figure 6.6. The volumetric strain of the confined specimen was higher than the unconfined specimen starting from 115 days, while the unconfined specimen reached the value of volumetric strain of the confined specimen around 269 days. Between 115 and 220 days, the confined specimen is projected to crack more severely than the unconfined specimen, based on the measured volumetric strain.

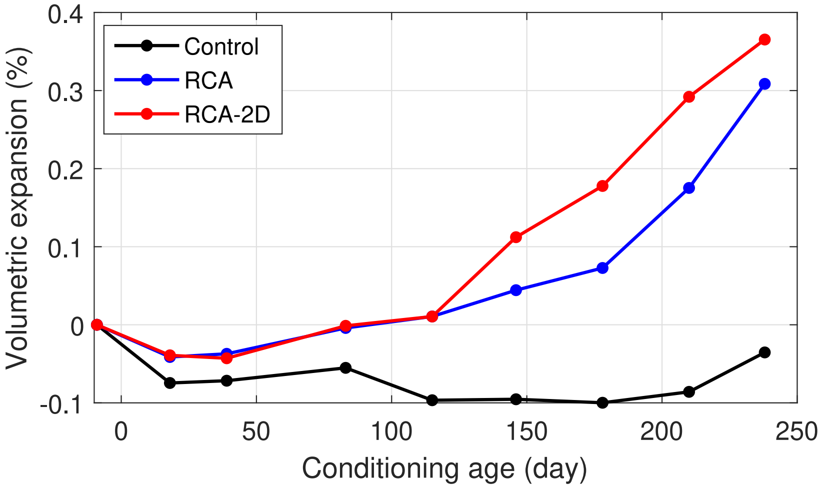

Figure 6.6: Volumetric strains of RCA, RCA-2D, and control specimens. ([62], used with permission)

The control specimen had significantly lower hit rate and cumulative signal strength (CSS) than the reactive specimens. There is greater AE activity in the confined specimen than in the unconfined specimen (Figure 6.7). Furthermore, the rate of AE events in the unconfined specimen is significantly lower than in the confined specimen.

Frequency component analysis was conducted using an unsupervised pattern recognition method. The AE data for the unconfined and confined specimens were clustered into four and three groups, respectively. The fast Fourier transform (FFT) was used to convert the

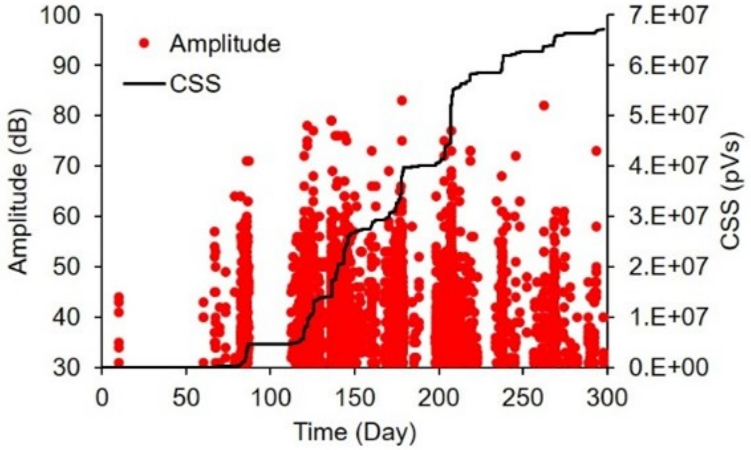

(a) RCA-2D

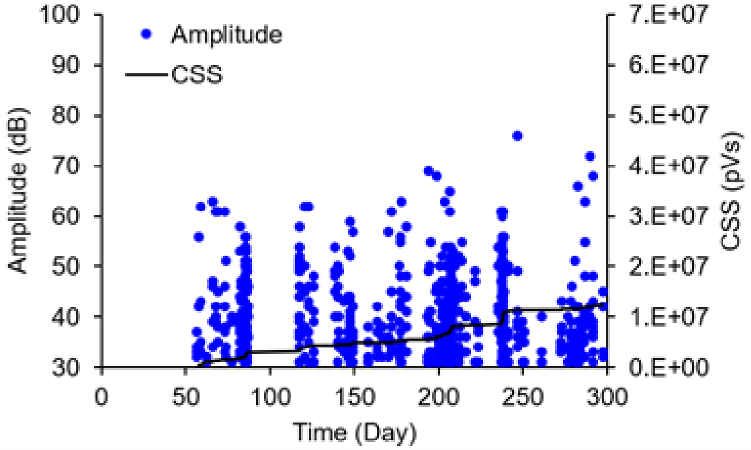

(b) RCA

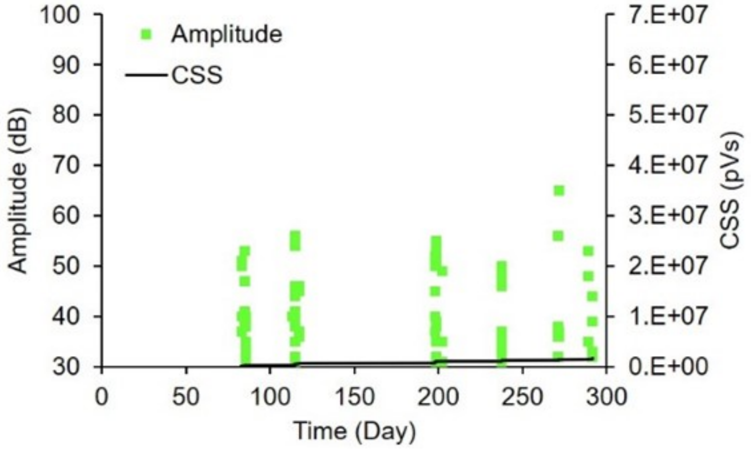

(c) Control

Figure 6.7: Filtered AE hits and CSS versus time. ([62], used with permission).

AE signals to the frequency domain. The frequency-domain of each signal was separated into 10 equal bands, each with a bandwidth of 40 kHz. Calculating the area under the FFT spectrum in each frequency band yielded the energies corresponding to that frequency band. Frequency-energy-based features are normalized energies for distinct frequency bands. The recovered frequency-energy-based features were subjected to principal component analysis (PCA) to minimize the dimension of the features. The dimension-reduced features were utilized as input for the unsupervised pattern recognition algorithm.

Clustering results are presented in Figure 6.8. The results of the confined specimen are C1 through C4, and the results of the unconfined specimens are U1 through U3. The height of linkages in the dendrograms was used to determine the number of clusters, and the red lines in the figure indicate desired levels for clustering. Figure 6.8 shows the resulting dendrograms for confined and unconfined specimens. In the Principal Component (PC) space, Figure 6.9 depicts the first three PCs. Because the clusters share some similar frequency-energy-based properties, some overlaps exist at cluster borders. (Figure 6.9 and Figure 6.10).

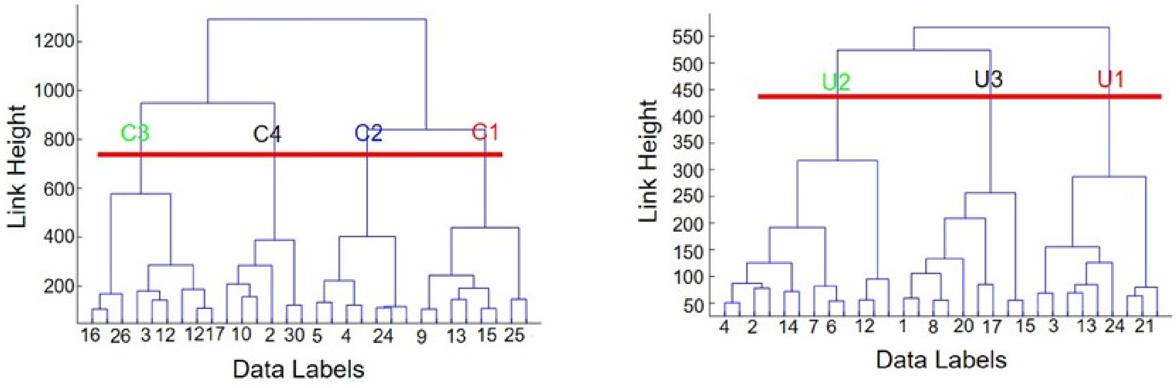

(a) Confined specimen

(b) Unconfined specimen

Figure 6.8: Clustering dendrograms ([62], used with permission).

The average energy distribution in the frequency domain is presented in Figure 6.10. For the confined specimen, C1 and C2 represent ‘low’ frequencies. C3 represents ‘medium’ frequency, and C4 is ‘high’ frequency. For the unconfined specimen, U1 is ‘low’ frequency, U2 is ‘medium’ frequency, and U3 is ‘high’ frequency. Within each time interval, the number of signals in each cluster was determined and normalized to the overall number of AE signals in those intervals (Figure 6.11). According to Figure 6.11, the percentage of low-frequency signals rose in both the unconfined and the confined specimens after 200 days. In contrast, the percentage of high-frequency decreased after 200 days.

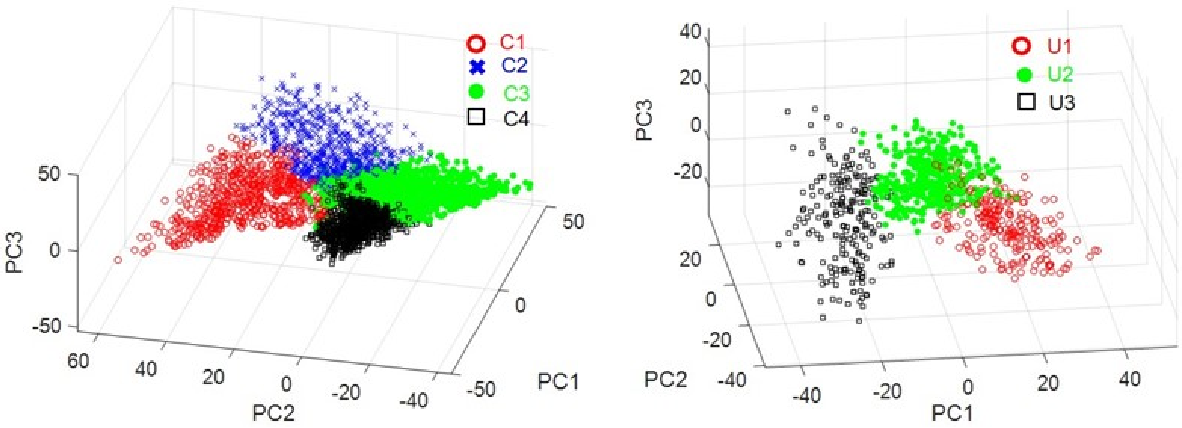

(a) Confined specimen RCA-2D (b) Unconfined specimen RCA

Figure 6.9: Data presentation in principal component space. ([62], used with permission).

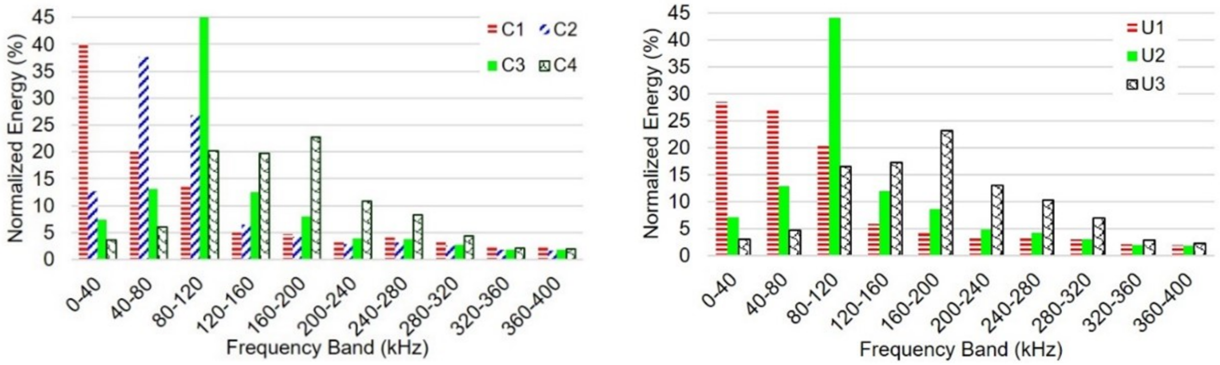

(a) Confined specimen (b) Unconfined specimen

Figure 6.10: Energy-frequency distributions of clusters. ([62], used with permission).

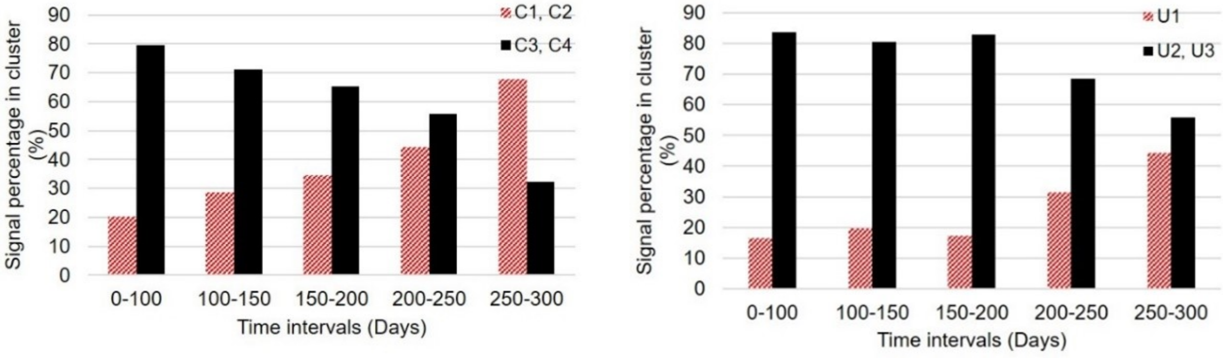

(a) Confined specimen (b) Unconfined specimen

Figure 6.11: Percentage of signals in clusters. ([62], used with permission).

One potential explanation for the trends shown in Figure 6.11 is that in the later stages of the ASR process, the initiation and propagation of macrocracks outnumbered microcrack initiation. Previous literature indicates that low-frequency AE signals can be related to crack extension, while the high-frequency AE signals can be linked to the formation of small-scale cracks[67]. This could explain the decrease of the percentage of high-frequency signals and the increase in the percentage of high-frequency signals after day 200.

Beginning at 146 days after casting crack widths were measured. The visible cracks on the top surfaces of specimens were the focus of this measurement. The maximum crack widths of RCA and RCA-2D are presented in Figure 6.12. The wider crack widths of the confined specimen suggest a higher stress concentration in the mid-width of the specimen, which is to be expected because the reinforcing of the confined specimen generated more anisotropic resistance to the ASR expansion when compared to the unconfined specimen.

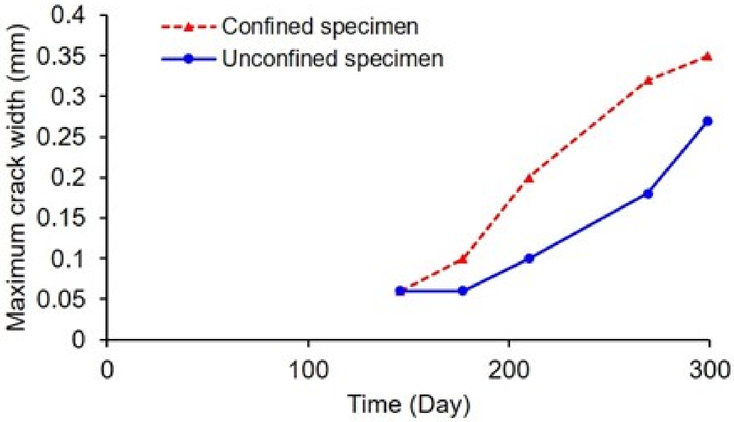

Figure 6.12: Crack quantification time on the top surface of RCA and RCA-2D specimens. ([62], used with permission).

Petrographic analysis was conducted on the reactive specimens at the end of the accelerated aging process. Each specimen was sawn into cross-section slices for about half of its length (core samples were extracted from the opposite half to measure mechanical properties). Each specimen was divided into fourteen 38-mm thick cross-section slices, and each slice was split into quarter sections and polished for stereo-optical microscopy experiments. To give a quantitative assessment of internal damage a manual point count approach (MPCP) was devised. For the confined specimen, the MPCP was performed on thirteen whole slices and one-half slice, and for the unconfined specimen, MPCP was performed on eleven slices. Figure 6.13 shows the weighted normalized cracking score based on the average findings of slices for the confined and unconfined specimens. The cracking score of the confined specimen was generally higher than the unconfined specimen, which is aligned with the surface cracking, expansion stresses, and AE findings. It is worth noting that the slices were oriented perpendicular to the longitudinal reinforcement, which offered significant restriction against X-direction growth while causing anisotropic damage with Y-Z plane expansions. The cracking scores reveal that expansion anisotropy and surface cracking are accompanied by similar variances in interior damage features.

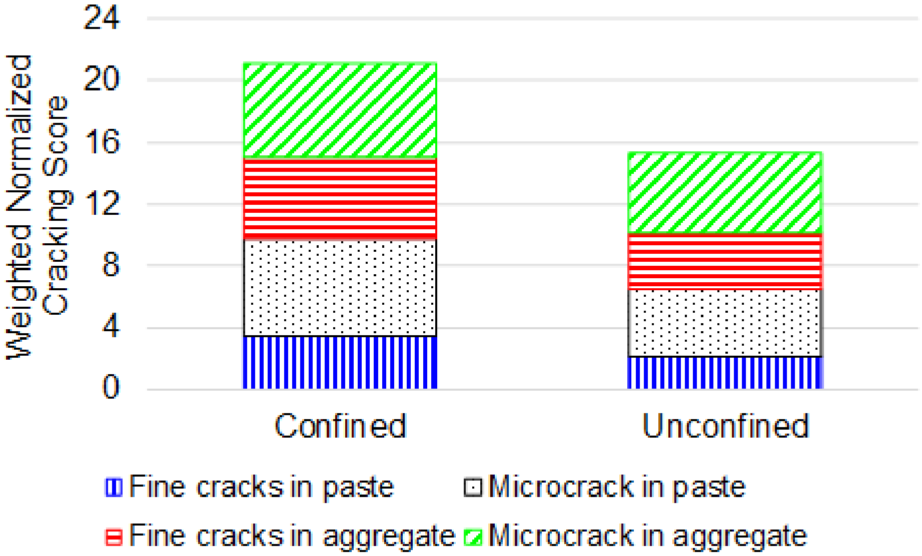

Figure 6.13: Average of the weighted normalized cracking score for reactive specimens. ([62], used with permission).

AE data was also utilized to derive signal entropies and evaluate the temporal trend of data. The discrete voltage entropy (DVE), global voltage entropy (GVE), and counts-entropy were calculated in this chapter. A detailed explanation of these entropies can be found in[63].

The DVE for the confined and unconfined specimen is presented in Figure 6.14. For both specimens the range of entropy values is nearly identical. The average entropy at 50-day intervals is represented by the solid black line. The average entropy in the confined specimen increased for 200 days before declining, but in the unconfined specimen, it increased for 150 days before declining with considerable oscillations.

GVE is shown in Figure 6.15. The GVE increased in the confined specimen until it reached 200 days after which it stayed nearly constant. The GVE grew in the unconfined specimen up to 123 days, then reduced slightly after that, and remained nearly constant after 180 days. The GVE curves in both specimens followed the same patterns as the averaged DVE curves. In addition, the GVE range was similar for the two specimens, although the peak value for the confined specimen was slightly greater than the peak value for the unconfined specimen.

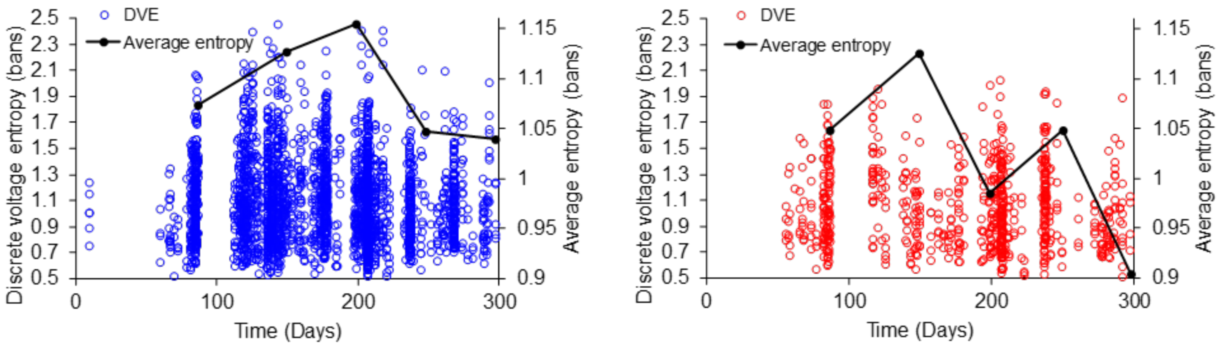

(a) Confined specimen

(b) Unconfined specimen

Figure 6.14: DVE for medium-scale specimens, bin size: 0.0001 volts. ([63], used with permission).

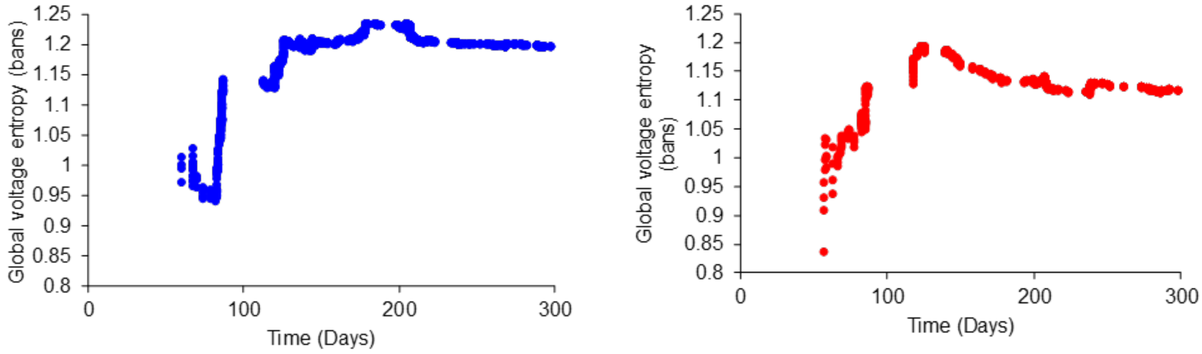

(a) Confined specimen

(b) Unconfined specimen

Figure 6.15: GVE for medium-scale specimens. ([63], used with permission).

Two different approaches were utilized for calculating trends related to counts-entropy. The first method is referred to as count entropy (CE). The results for CE for the confined and unconfined specimens are illustrated in Figure 6.16(a) and Figure 6.16(b). According to the figures, the CE rising rates in the early stage were substantially higher than the later stage. After 200 days, the value of CE in the confined specimen was nearly constant. The confined specimen has higher CE values than the unconfined specimen, as this method is based on the number of signals, which were larger for the confined specimen. The second method is based on cumulative distribution function (CDF), presented in Figure 6.16c and Figure 6.16d. The CDF values of both specimens showed an ascending trend until they reached their greatest value, then a downward trend can be observed.

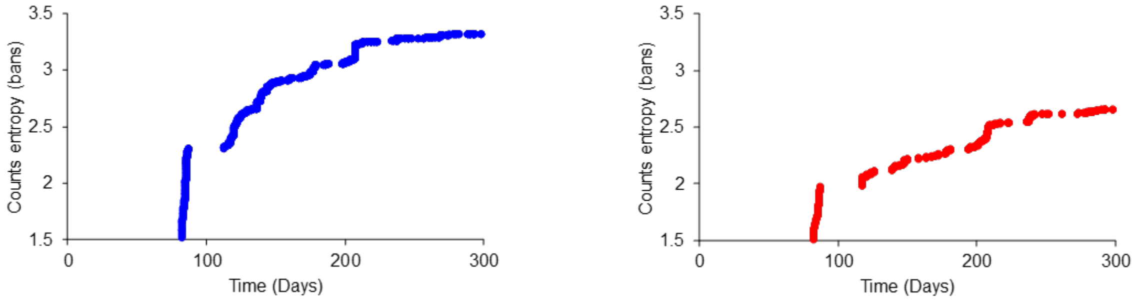

(a) Confined-CE (b) Unconfined-CE

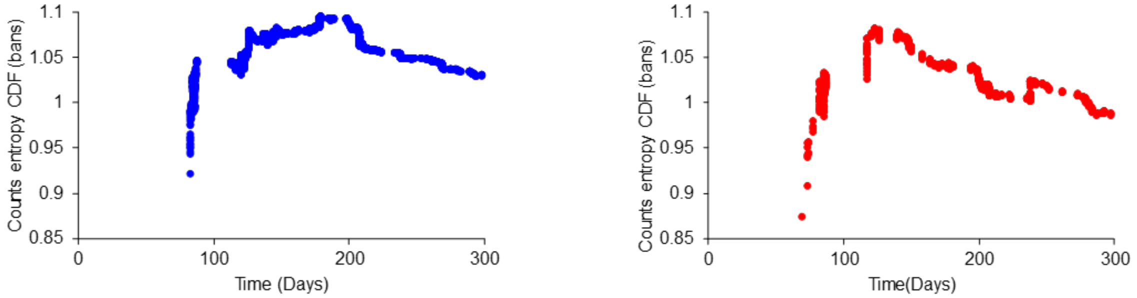

(c) Confined-CDF (d) Unconfined-CDF

Figure 6.16: Counts entropy (CE) for medium-scale specimens. ([63], used with permission).

6.3.3 Medium-scale specimens RFA, RFA-2D, and control-2D

Specimens RFA, RFA-2D, and control-2D were conditioned for 250 days. The RFA-2D specimen represents the "confined" specimen, while the RFA specimen represents the "unconfined" specimen. The volumetric expansion of the reactive fine aggregate specimens (RFA, RFA-2D) and control-2D specimen are plotted in Figure 6.17. The expansion rate of the fine aggregate specimens is generally less than that of the coarse aggregate specimens.

The AE hits and CSS of RFA, and RDA-2D were presented in Figure 6.18. The two reactive fine aggregate specimens (RFA and RFA-2D) have very similar cumulative signal strengths (CSS) in the early phases of ASR growth, but the two reactive coarse aggregate specimens (RCA and RCA-2D) exhibit a rather big variance in CSS. When compared to coarse aggregate concrete, fine aggregate concrete is substantially less impacted by boundary conditions, particularly reinforced steel. Because the ASR gel that surrounds fine aggregates can grow similarly in all directions regardless of the boundary condition, there may be greater AE activity in the unconfined fine specimen. Even if the expansions are comparable, the increase in AE activity could indicate the presence of more microcracks and AE activity inside the unconfined fine specimen than the unconfined coarse specimen.

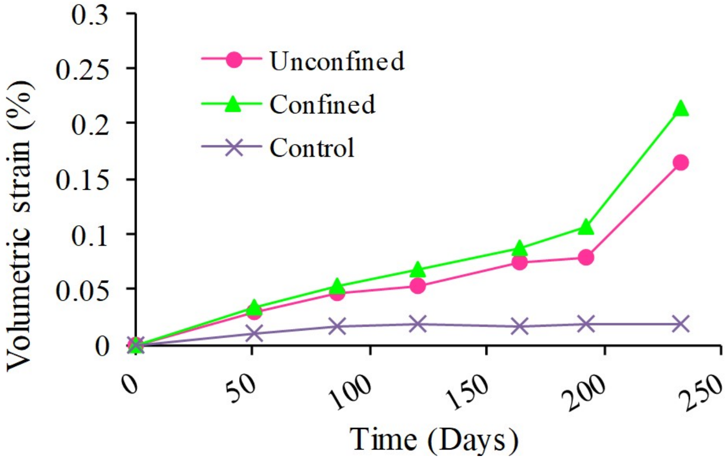

Figure 6.17: Volumetric expansion of reactive fine aggregate (RFA) and Control-2D specimens. ([68], used with permission).

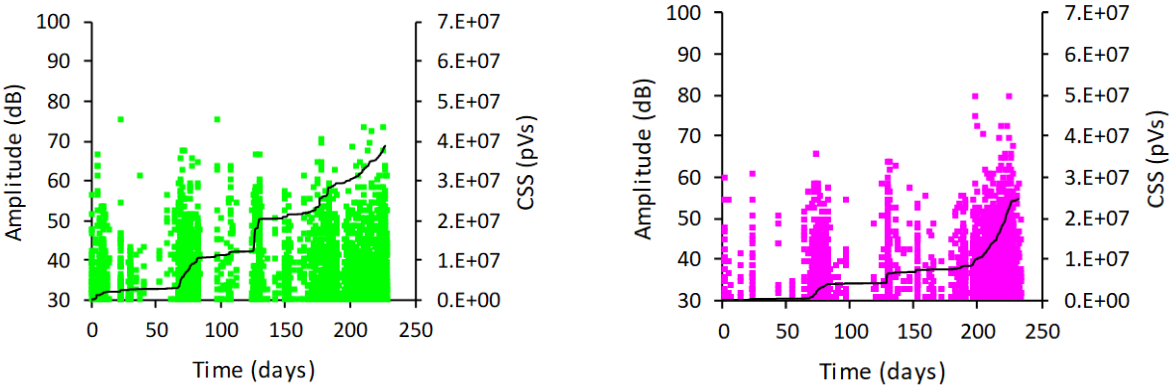

(a) Confined specimen RFA

(b) Confined specimen RFA-2D

Figure 6.18: Filtered AE data in terms of amplitude and CSS. ([68], used with permission).

The maximum crack widths of RCA, RCA-2D, RFA, and RDA-2D are presented in Figure 6.19. Throughout the examination, the fine aggregate specimens show relatively comparable crack widths. This result supports the observation that boundary conditions have a minor impact on reactive fine aggregates.

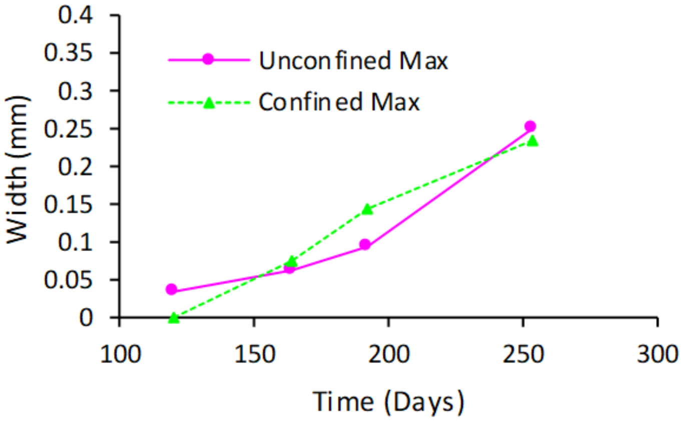

Figure 6.19: Maximum crack width on top surface of RFA specimens. ([68], used with permission).

6.3.4 ASR damage diagnosis based on acoustic emission

An ASR damage diagnosis approach was developed through by leveraging the relationship between AE data collected during the ASR process to the physical damage phases of ASR[64]. The method was developed using 70% of the data collected from the ASR experiment conducted on the medium-scale specimen RCA-2D and was validated through the remaining 30% of the data.

The purpose for utilizing the CNN method was to develop a means for diagnosing the phase of ASR damage for a concrete specimen in real-time as opposed to analyzing the trend of acoustic emission data based on a set of all data from day one onward. This is of interest as in most cases acoustic emission sensors are applied relatively late in the lifespan of a structure and most generally after visible surface cracking becomes readily apparent. The input of the CNN model is acoustic emission signals receive in real-time, and the result is classification of the damage phase (phase 1 or phase 2) also in real-time.

The AE signals were filtered and transferred to the frequency domain to calculate frequency based features. The frequency band features for 0-40 kHz (low frequency) and signal energy for 80-120 kHz are illustrated in Figure 6.20(a) and Figure 6.20(b). Around 190 to 200 days, the trends in these frequency-based features imply a change in the temporal evolution. Figure 6.20(c) shows AE hits for this specimen as well as the cumulative signal strength (CSS). The events of new crack formation and/or crack extension along an existing crack can be reflected in sudden increases in the CSS curve.

Around 200 days a significant increase occurs, approximately corresponding to the time associated with the change in the AE features shown in Figures 6.20a and 20b. The ASR process may be approximately divided into two phases: phase 1 – day 0 to day 190; and phase 2 – day 190 onward. In deep learning models, the phase definition serves as a label for the AE signals.

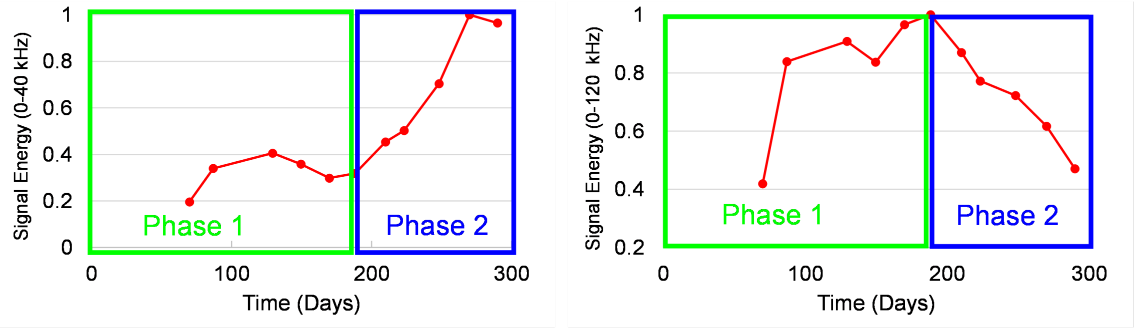

(a) Signal energy (0-40kHz)

(b) Signal energy (80-120kHz)

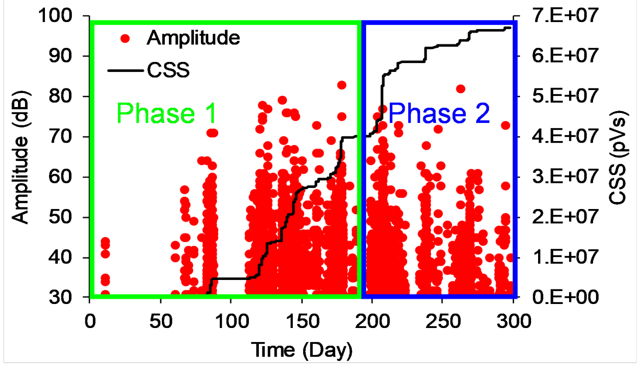

(c) AE hits and CSS

Figure 6.20: Frequency band features and CSS. ([64], used with permission).

An image-based dataset was created by conducting continuous wavelets transform (CWT) on the AE signals. The signals from different phases have different frequency content as seen in Figure 6.21. The CWT coefficients were stored as RGB pictures which were then used as input data for a convolutional neural network (CNN). The CNN model is capable of classify the AE signals into the attributed classes (phase 1 or phase 2).

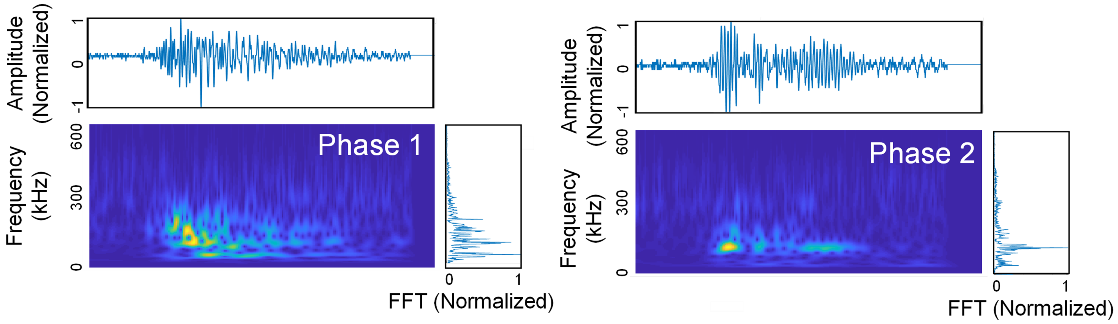

Figure 6.21: CWT images of AE signals in phases 1 and 2.

CNN is a deep neural network with convolutional filters [69]. An input layer, feature extraction layers, and a fully connected layer are the three primary components of a CNN. Convolutional layers and pooling layers make up the majority of the feature extraction layers. Figure 6.22 depicts the structure of a typical CNN with two convolutional layers and two pooling layers.

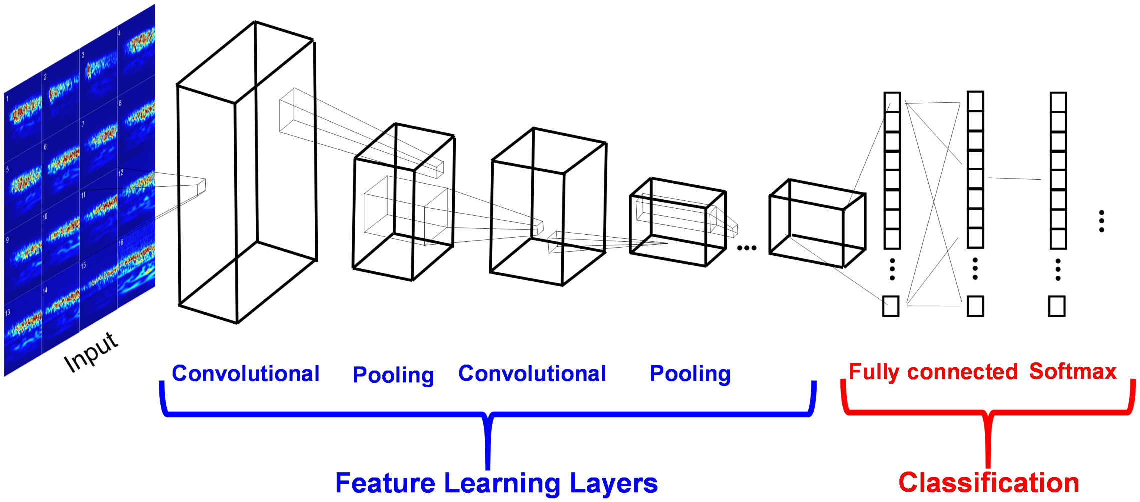

Figure 6.22: Architecture of a typical CNN.

Using the data from all of the sensors, a CNN model was developed. A confusion matrix displays the classification result (Figure 6.23a). In total, 707 images in the validation data set were successfully assigned to the corresponding phases, accounting for 76.7 percent of all images, which means the CNN classifier is 76.7 percent accurate (Figure 6.23a). A new CNN model was then created using the data from a single sensor. The output is shown in Figure fig:stackedcnnb. The overall accuracy is 85.7 percent (Figure 6.23b). Figure fig:stackedcnn also shows the recall rate, precision rate, and F1 scores for phase 1 and phase 2.

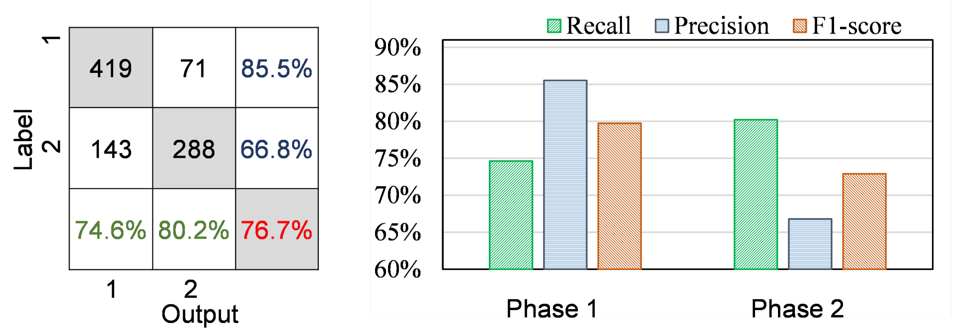

(a) Confusion matrix - all AE signals

(b) Recall, precision, and F1-score - all AE signals

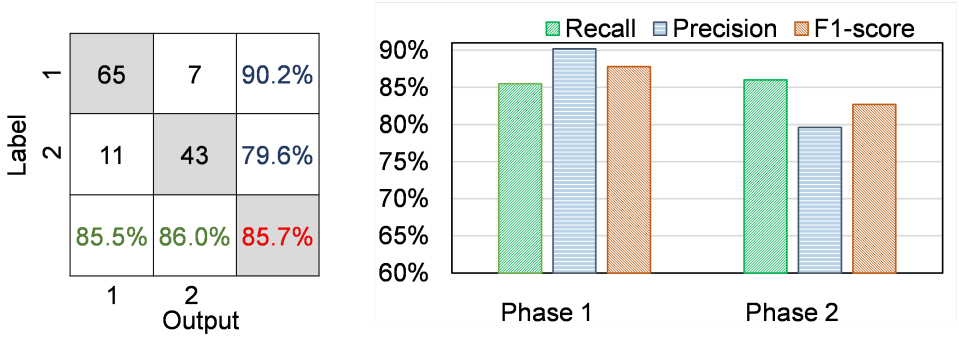

(c) Confusion matrix - signals from sensor a single sensor

(d) Recall, precision, and F1-score - signals from a single sensor

Figure 6.23: Performance of stacked CNN. ([64], used with permission).

6.4 Conclusions

This chapter describes acoustic emission (AE) results gained from the long-term conditioning of fifteen small-scale and six medium-scale concrete specimens to better understand the ASR process itself and to delve into potential capabilities and limitations of acoustic emission to detect and classify the ASR damage progression process. Acoustic emission is by definition a passive means of nondestructive evaluation, meaning that the damage process itself, generally in the form of crack initiation, extension and coalescence, causes the acoustic emission data.

In the absence of damage progression acoustic emission will generally not be recorded. One exception to this is environmental noise in the signals, which can be caused by such items as electric switching, arc welding, and water infiltration into the cables and connectors. In long term experiments involving high humidity, one cause of environmental noise can be condensation forming into water droplets which may impact the specimens. This type of noise was discovered early in the experimental procedure described and was mitigated by shielding of the specimens. When environmental noise does occur, it can generally be filtered from the evaluation data set as was done for the work described. In small scale specimens, a pervasive cause of emission that is not directly related to damage progression is reflections of waveforms from the specimen surfaces. This occurs when the attenuation distance is less than the geometric dimensions of the specimens themselves. This type of spurious emission can be minimized through a number of approaches including the setting of hit definition times, the setting of a certain number of sensors to determine an acoustic emission event, and inspection of waveforms. All of these were employed to varying degrees in the work described.

One advantage of acoustic emission in relation to active methods of evaluation such as ultrasonics or ultrasonic pulse velocity is the fact that the damage itself does produce the acoustic emission signals. Therefore, correlations between damage progression and acoustic emission data are possible. Another advantage of acoustic emission is its extreme sensitivity to damage progression, which allows for detection of damage progression in relatively thick concrete structures such as those used for nuclear containments. It is worth noting that acoustic emission systems can be of the fiber optic type, the piezoelectric type (such as the one used for the work described here) and can also utilized in a non-contact fashion.

One challenge with acoustic emission monitoring is the same as one of its advantages, namely that acoustic emission is extremely sensitive to damage progression. This extreme sensitivity necessarily means that spurious emission is almost always present in the test data and this spurious emission must be dealt with in some fashion, generally through post-processing of the data but also through pre-processing. Another challenge arises from the fact that wave propagation through damaged structures is not a constant and in fact will vary with the degree of damage present due to reflections and other issues associated with cracking and delaminations. For these reasons acoustic emission is often used as a screening method to alert owners or other interested parties to the degree of damage in a degrading structure to then be followed up by an active means of interrogation, such as phased array ultrasonics, ultrasonic pulse velocity, or impact echo. Each of these methods, in turn, has advantages and challenges for thick concrete structures.

Analysis methods that were potentially of interest were investigated for both small and medium-scale specimens including intensity analysis, signal frequency component analysis, signal entropy analysis, and petrographic examination were conducted. In addition, an ASR damage diagnosis method was developed through utilizing a CNN approach. This diagnosis method has the advantage of not requiring data collection from the beginning of specimen life and has the potential to diagnose damage phase in real-time.

A few conclusions may be summarized as follows.

ASR damage progression can be detected via acoustic emission in both small and medium-scale specimens. By associating AE results with petrographic investigation, an acoustic emission Intensity Analysis chart for the classification of ASR damage severity was developed for small-scale specimens (DRI measurements). The extent of ASR degradation can be approached through the use of this straightforward chart.

For the medium-scale specimens, the boundary condition resulted in a considerable difference in ASR-related damage between specimens RCA and RCA-2D, but the boundary condition resulted in a less significant difference in ASR damage between specimens RFA and RFA-2D. Large crack widths were observed for the confined specimen with reactive coarse aggregate. The crack behavior for reactive fine aggregate specimens were similar for both scenarios.

Acoustic emission data was also used to calculate signal entropies and assess the temporal trend of data for the medium-scale specimens. A trend in the average values of entropy was observed in terms of conditioning time. The average entropy values showed an upward trend in the earlier stage with a decreasing trend in the later stage. A similar pattern was observed in the global voltage entropy and counts-entropy for the medium-scale specimens using CDF.

Acoustic emission was utilized to diagnose the condition of ASR progression in real-time by leveraging a CNN model. The method was developed and later validated through the experimental conditioning conducted on the medium-scale specimen RCA-2D. Results indicate that the proposed method is capable of classifying signals into the assigned phases (phase 1 or phase 2) with reasonable accuracy. The CNN model employing data from a single sensor resulted in an efficient model to diagnose the temporal evolution of ASR progression without the need to obtain data from the beginning of the conditioning period.

7 Prediction Models

7.1 Prediction of ASR Damage Using Ultrasonic Signals

Machine learning techniques have been increasingly used in the automated analysis of ultrasonic data for concrete characterization. Most of these works focused on using machine learning algorithms to predict concrete strength based on ultrasonic pulse velocity (UPV) and other parameters (e.g., aggregate size, type of cement, water-to-cement ratio) [70–73]. However, this process used only the wave velocity information and discarded all the other information in the ultrasonic signals. In ultrasonic NDT of welding defects, different features were extracted from the ultrasonic signals, such as wave parameters, statistical features, and wavelet features for automated defect classification [74–76]. In this work, the authors extracted wave parameters and wavelet features from the long-term monitoring ultrasonic signals obtained from concrete samples subjected to ASR. Because the expansion level is a measure of the extent of ASR damage level in real-world applications, the first method employed herein fits a curve between the wave velocity and expansion on one sample to predict the expansion in another sample. The second method uses the data sets from one concrete sample to train a machine learning model which is then validated using the data sets from another concrete sample.

7.1.1 Feature Extraction

Ultrasonic wave velocity

Wave velocity is the most widely used parameter in ultrasonic nondestructive testing for material characterization. As the ASR sample becomes progressively cracked, the wave propagation velocity is reduced. In this work, the wave velocity was extracted as one of the features used for damage assessment. The Akaike Information Criteria (AIC) picker was used to detect the arrival time automatically. The AIC picker method was originally developed for analyzing the P-wave velocity of seismic waves [77]. The AIC values were calculated for the first 1000 points of the time-domain signal, and the point with the lowest AIC value represents the first arrival time. As shown in Figure 7.1, the RCA and RCA-2D samples exhibited a decreasing velocity during the monitoring period. The spikes on the curves were due to the AIC calculation error when the signal was noisy.

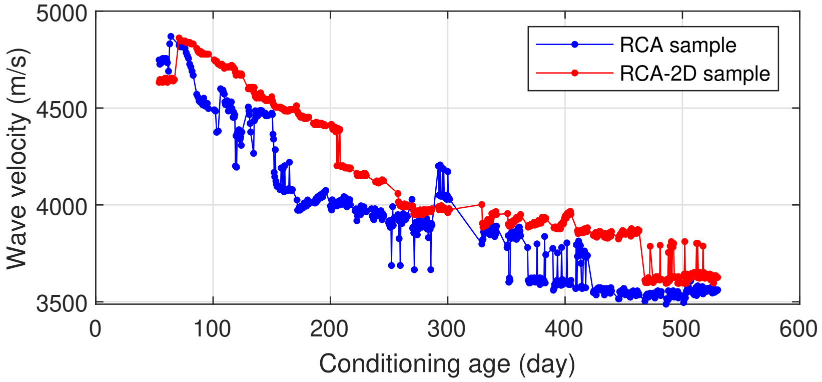

Figure 7.1: Ultrasonic monitoring system.

Wavelet Features

Aside from wave velocity, features could be extracted from the ultrasonic signals in both the time and frequency domains. Wavelet transform is the technique that processes a signal in the time and frequency domains and has been widely used to extract features from ultrasonic signals in the NDT of welding defects [74, 78]. Discrete wavelets transform (DWT) is an algorithm that can quickly obtain the wavelet transform coefficients of a discrete-time signal. The algorithm decomposes the ultrasonic signal with a low-pass and high-pass filter into its coarse approximation coefficient cA_1 and detail coefficient cD_1. The bandwidth is $[0, f/2]$ for the approximation coefficient cA_1 and $[f/2, f]$ for the detail coefficient cD_1, and f is half of the sampling rate. This process is repeated until the desired decomposition level is achieved. The wavelet feature extraction is based on these detail coefficients.

The ultrasonic signal at the conditioning age of 54 days in Figure 7.2(a) was decomposed into seven levels with the MATLAB function *modwt* and *db*4 wavelet. Before the DWT, each signal was normalized by its amplitude. Because the energy of the original ultrasonic signal is in the frequency range of 40 to 250 kHz (Figure 7.2[b]), only the last three levels of the detail coefficients were used for the feature extraction. Figures 7.2 (c)–(e) show the detail coefficients cD_5, cD_6, and cD_7 from DWT. Coefficients cD_5 and cD_6 have a higher amplitude than cD_7, which indicates that the original ultrasonic signal has more energy in the high-frequency range (≥78 kHz) than at the early conditioning age. For each of the three detail coefficients, four features were extracted:

1. First was the mean amplitude:

$$A_m = \frac{1}{n} \sum_{n}^{i} |x_i|. \tag{7.1}$$

   As the ASR damage accumulates, the energy decreases in the high-frequency bandwidth and increases in the low-frequency bandwidth. Therefore, the mean value of the detail coefficient will have the same trend as the energy in different bandwidths.

2. The second feature was the maximum amplitude, A_{max}. Similar to the mean amplitude, the maximum amplitude also has the same trend with the energy in different bandwidths.

3. The third feature was the total energy:

$$E = \sum_{n}^{i} x_i^2 \tag{7.2}$$

   The energy ratio in the low-frequency bandwidth increases as the ASR develops.

4. The fourth feature was the attenuation coefficient, which is extracted from the three coefficients by fitting the signal after the maximum amplitude by using an exponential decay function.

Thirteen features were extracted from each ultrasonic signal in total with twelve wavelet features and the wave velocity.

7.1.2 Machine Learning Models

In this work, the machine learning model SVR was used to predict the extent of expansion. Support vector machine (SVM) is one of the kernel methods used for pattern analysis with a kernel function. The kernel method uses the kernel function to transform the data in the raw representation into the feature vector representation. With the kernel function method, the

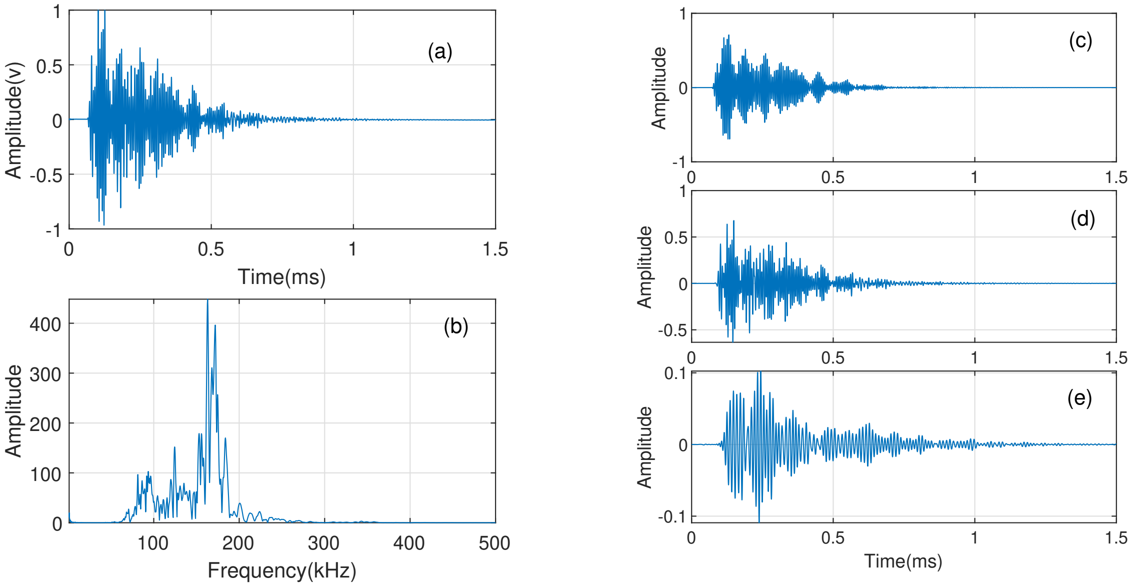

(a) Control specimen

(b) ASR specimen

Figure 7.2: (a) Time-domain signal, (b) frequency spectrum, (c) DWT coefficient cD_5 (156–312 kHz), (d) DWT coefficient cD_6 (78–156 kHz), and (e) DWT coefficient cD_7 (39–78 kHz).

SVM model can be used as a nonlinear model. SVMs are typically used for classification. The support vector regression uses the same principles as the SVM for classification but with a slight difference: the objective of SVM for classification is to find a hyperplane to maximize the distance between the two boundaries, whereas the objective of SVR is to find a hyperplane so that the data points closest to the hyperplane and support vectors are within that boundary line. In SVR, slack variables were introduced in the constraint for each point, which is similar to the "soft margin" concept in the SVM classification model. Furthermore, a polynomial was used to fit a functional relationship between wave velocity and expansion of the ASR sample. The RCA-2D expansion was predicted based on this polynomial function. Overall, 644 data sets of 13 features from the RCA sample were used to train the SVR models in MATLAB with five-fold cross-validation. The learning model was optimized manually with root mean square error (RMSE) as the objective function. The optimized SVR model has the following hyperparameters: KernelScale = 36.1, BoxConstraint = 688.9, $\varepsilon = 1.46 \times 10^{-4}$, and a Gaussian kernel function. Before training the models, all data were normalized suitably. A total of 620 data sets from the RCA-2D sample were fed into the model for testing.

7.1.3 Results and Discussions

First, the expansion prediction was conducted based on the polynomial curve fitting with a quadratic polynomial. Then, the SVR model was trained using the data sets from the ASR sample with all 13 features. Next, the SVR model was tested with the data sets from the ASR-2D sample. Figure 7.3 plots the measured expansion versus the predicted expansion using curve fitting between the wave velocity and the expansion on the ASR and ASR-2D samples. The ASR sample exhibits a high R^2 between the predicted and measured expansion. However, the prediction results on the ASR-2D were poor with small R^2 and high RMSE. Figure 7.4 plots the measured expansion vs. the predicted expansion using the SVR learning model on the ASR and ASR-2D samples. The training results (Figure 7.4[a]) have relatively high R^2 and small RMSE, and the testing results show even larger error than the results that used curve fitting. This indicates that the model was overfitted by using the thirteen features with poor performance on the testing data.

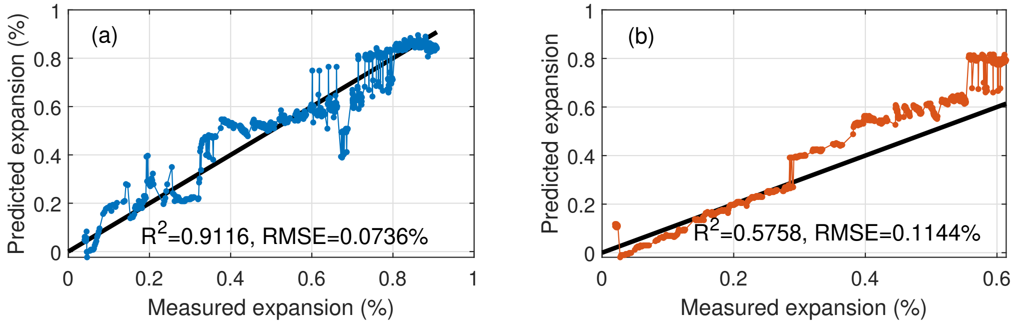

Figure 7.3: Measured expansion vs. predicted expansion using polynomial curve fitting on the (a) RCA sample and (b) RCA-2D sample

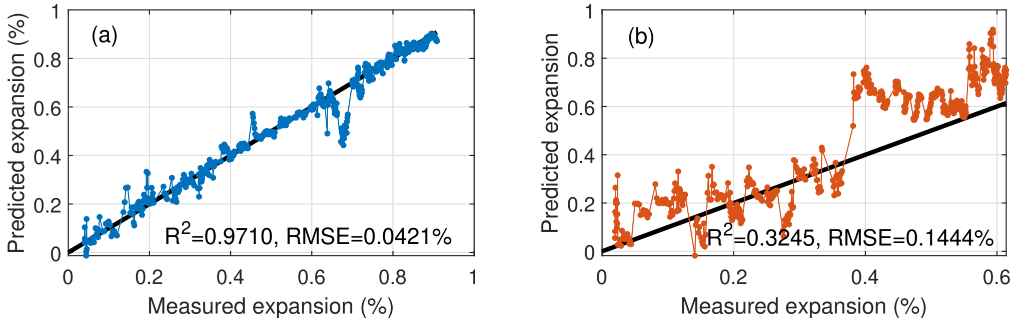

Figure 7.4: Measured expansion vs. predicted expansion using SVR model on the (a) RCA sample and (b) RCA-2D sample

Because the SVR models had sufficient performance using the training data but had large prediction errors using the testing data, feature selection was used to avoid overfitting and decrease the SVR model variance. Correlation coefficients between the 13 features and the response (i.e., expansion) are summarized in Table 7.1 for the training (i.e., ASR) and testing (i.e., ASR-2D) data sets. The wave velocity has a high correlation with the volumetric expansion for both data sets. The features that have correlation coefficients larger than 0.5 for both data sets were selected. Therefore, features 1, 3, 6, 7, 10, 11 were selected as input to the SVR model. The training results and testing results with feature selection are shown in Figure 7.5. The training results exhibit relatively high R^2 and small RMSE. By using the features with relatively high correlations to the response, the testing results of the SVR model were significantly improved with an R^2 from 0.3245 to 0.8946 and an RMSE from 0.1444 to 0.0570. All R^2 and RMSE are summarized in Table 7.2. Compared with the prediction results obtained via curve fitting based on wave velocity, the SVR model had extremely poor prediction results on the ASR-2D sample with all 13 features. Overall, using the six selected features greatly improved the SVR prediction results.

Table 7.1: Absolute correlation coefficients between features and responses.

Feature	Vel.	Mean amplitude			Max amplitude			Energy			Attenuation		
		cD_5	cD_6	cD_7	cD_5	cD_6	cD_7	cD_5	cD_6	cD_7	cD_5	cD_6	cD_7
Index	1	2	3	4	5	6	7	8	9	10	11	12	13
RCA	0.92	0.52	0.87	0.67	0.83	0.76	0.86	0.66	0.41	0.84	0.81	0.43	0.05
RCA-2D	0.90	0.05	0.65	0.03	0.38	0.58	0.64	0.23	0.49	0.59	0.83	0.68	0.26

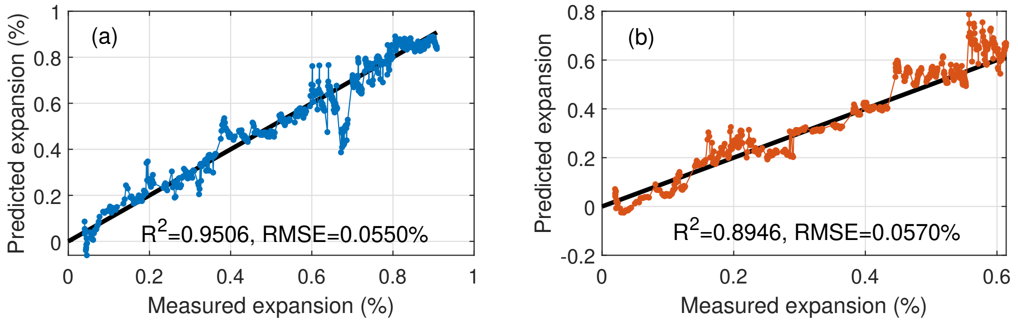

Figure 7.5: Measured expansion vs. predicted expansion using SVR model with feature selection on the (a) RCA sample and (b) RCA-2D sample

Table 7.2: Prediction results of curve fitting and SVR learning model.

Method	Curve fitting		SVR		SVR with feature selection	
Samples	RCA	RCA-2D	RCA	RCA-2D	RCA	RCA-2D
R^2	0.9116	0.5758	0.9710	0.3245	0.9506	0.8946
RMSE	0.0736%	0.1144%	0.0421%	0.1444%	0.0550%	0.0570%

7.1.4 Conclusions and Future Research

Conclusions and discussions In this work, the volumetric expansion due to ASR damage was predicted via two methods: curve fitting based on wave velocity and the SVR machine learning model. For the curve-fitting method, a quadratic polynomial was fit based on the wave velocity and expansion measurement on the ASR sample, and the expansion of the ASR-2D sample was predicted using its velocity measurement and the fit polynomial. For the SVR model, features were extracted from the ultrasonic signals, and data sets from the ASR sample were used for training with the data sets from the ASR-2D sample for testing. The results showed that the prediction results on the ASR-2D sample from both methods were not satisfactory, as shown by small R^2 and large RMSE. The wave velocity extracted still had poor accuracy because the transducers were reinstalled several times during the monitoring period and because some ultrasonic signals had a high level of noise. These two factors led to the poor prediction performance of the curve-fitting method. For the SVR method, the learning model used too many features, causing overfitting. After feature selection, the SVR model with six features showed the best performance with adequate prediction accuracy. If the wave velocity had better accuracy, then the curve fitting method might have sufficient performance, and the machine learning method would not be required for expansion prediction. Because the ASR and ASR-2D samples had the same mix design and were subjected to similar ASR development processes, the prediction procedure implemented herein was justified; however, this prediction procedure could not be reliably applied if the two mix designs were different.

Future work Damage prediction is still a very challenging task. Reliable prediction is only possible when the damage development trend is well studied and understood, and then NDT data show strong correlations with the damage condition. Machine learning algorithms show some potentials to predict damage behaviors based on knowledge obtained from similar materials by selecting features with high correlation with damage. The current models have not been validated on concrete with different mix designs.

Nonlinear acoustic tests show promising results in diagnosis and prediction of ASR damage. In milestone reports [79] and [80], the nonlinear resonance parameter and nonlinear ultrasonic parameter show strong linear correlations with the ASR damage, which are valid for all mix designs and specimens during the investigated period. If these linear relationships are validated on more concrete structures, we may be able to predict damage development rate and life span of concrete structures at very early stages.

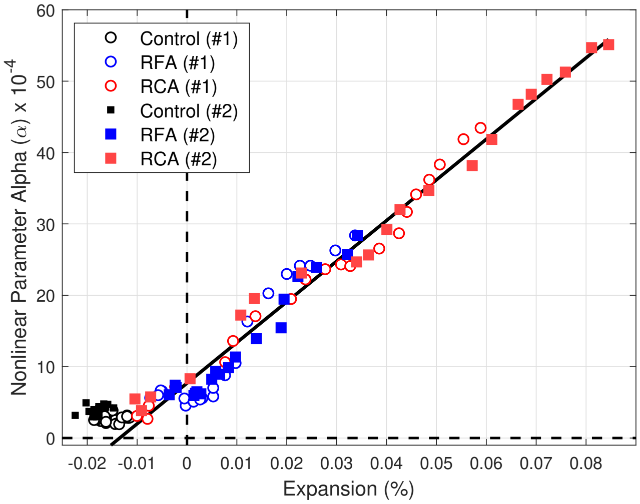

Figure 7.6: Relationship between nonlinear resonance parameter (α) and expansions of all concrete prism specimens.

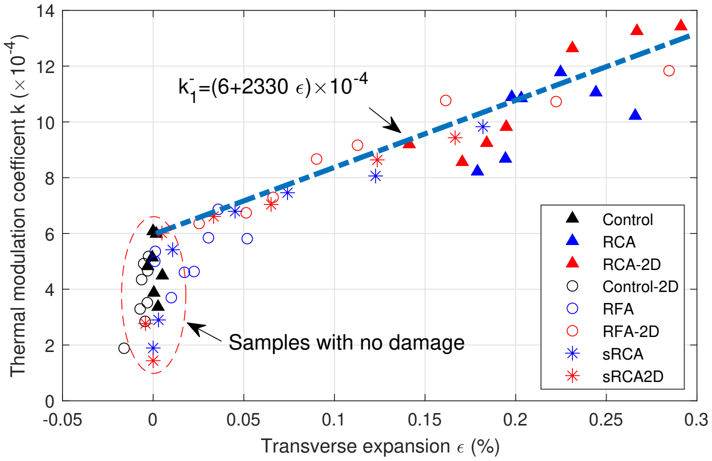

Figure 7.7: Relationship between thermal modulation nonlinear parameter and expansions of all large concrete specimens .

7.2 Prediction of ASR Damage Using AE Data

In this work, a data-driven approach based on machine learning is utilized to correlate AE signals with volumetric strain changes caused ASR. Artificial neural network (ANN) is used in this work to correlate AE signals and the volumetric expansion (strain) to demonstrate the feasibility of using AE signals to predict volumetric strain. The number of counts of AE signals, which requires less computing power to obtain than signal energy but provides more information about the AE signals than the number of AE events, is used as the input of ANN model to estimate the volumetric strain change of a concrete undergoing ASRs.

7.2.1 AE Data Preprocessing

Because the monthly measurement of volumetric strain does not provide sufficient labels for the AE signals collected in real time, linear interpolation was conducted to generate volumetric strain measurement labels for each hour of the test in this study. Then the AE signals and corresponding volumetric strains were used to train an ANN model using supervised learning for predicting volumetric strains of the concrete specimens.

The raw AE data was filtered before conducting any analyses. The first step was deleting the non-genuine data acquired by faulty channels. These signals were characterized by low counts and frequency. Then, the AE data, which were captured by at least four sensors in a specific time interval (referred as AE events), were kept for data analysis. The rest of data was filtered.

Furthermore, since multiple AE sensors on a specimen may record the same AE event, the total number of counts recorded from a specimen every hour was averaged over the number of sensors attached to the same specimen. In addition, to smooth the AE data, a moving average filter of length 168 hours (1 week) was applied to the hourly average cumulative counts of each specimen.

Moreover, since the AE events recorded at the initial shrinkage stage of concrete does not correspond to ASR reactions, the data collected when the volumetric strain was decreasing was not used for training or testing the ANN model. Only the data collected when the volumetric strain started to increase consistently is used for building the ANN model.

Table 7.3: Correlation matrix of the features of the confined specimen.

	Cumulative Counts	Cumulative Signal Strength	Cumulative Absolute Energy	Volumetric Strain
Cumulative Counts	1.00000	0.99307	0.95541	0.98520
Cumulative Signal Strength	0.99307	1.00000	0.98283	0.98119
Cumulative Absolute Energy	0.95541	0.98283	1.00000	0.95101
Volumetric Strain	0.98520	0.98119	0.95101	1.00000

7.2.2 Feature Selection

Because cumulative counts, cumulative signal strength, and cumulative absolute energy have been shown to be highly correlated with crack propagation by numerous authors [81, 82], a correlation matrix using the Pearson's correlation coefficient is created to determine which of the following features is most highly correlated with volumetric strain. As shown in Table 7.3, cumulative counts have the highest correlation with volumetric strain. The cumulative signal strength and cumulative absolute energy are also highly correlated with the volumetric strain. However, they are also highly correlated with cumulative counts, indicating that using all three of these features would be redundant. Another feature that may be included as an optional, secondary feature for the ANN model is the counts per hour. Although the counts per hour are not highly correlated with the volumetric strain, it can potentially provide information about when drastic changes in volumetric strain may occur.

7.2.3 Neural Network Setup

The neural network was designed with the use of several empirical methods to determine the optimal architecture of the neural network. The preprocessed data was split 50/50 to create a training and testing data set. The grid search algorithm using the training data set for k-fold cross-validation was used to determine the optimal number of neurons and hidden layers for the ANN. The optimal architecture of the single input case is shown in Fig. 7.8, in which the cumulative number of counts is the input and the volumetric strain is the

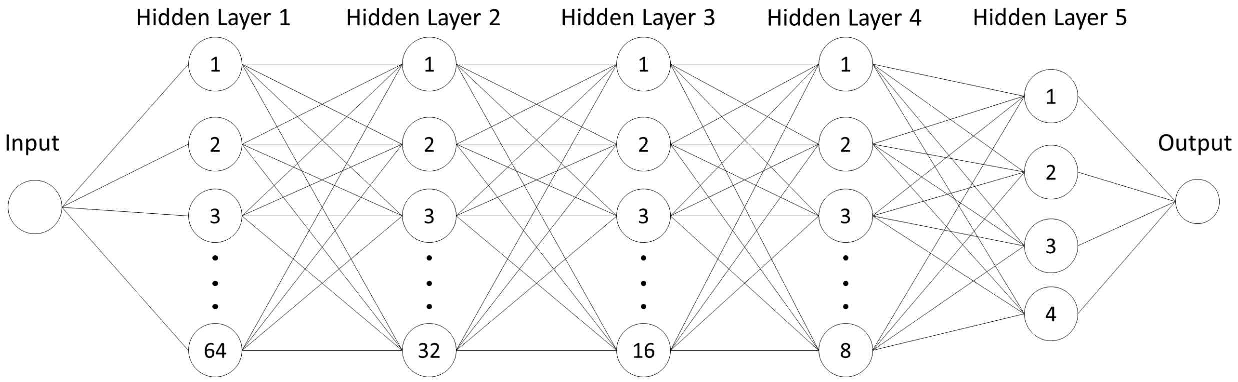

Figure 7.8: ANN model architecture for predicting volumetric strains using cumulative number of counts.

output. The architecture of the two-input case is the same except that the input layer has two dimensions, including both the cumulative number of counts and the number of counts per hour.

7.2.4 Results and Discussion

The testing results of the trained ANN models for both the confined and unconfined concrete specimens are shown in Figs. 7.9-7.12. The comparisons between the prediction models and the volumetric strain measurements are shown in Figs. 7.9 and 7.11 for the ANN models with a single input and with two inputs, respectively. The corresponding prediction errors are given in Figs. 7.10 and 7.12 respectively.

For the confined specimen, the ANN model achieves a mean absolute error of 0.00140% when only using the cumulative counts as the input to predict volumetric strain. Although the ANN model is able to predict the volumetric strain of the confined specimen very well, from Fig. 7.9(a), it can be seen that ANN suffers larger errors before and after the segment between the dashed lines. The dashed line to the left represents the crack initiation threshold and the dashed line to the right represents the crack damage threshold. The crack initiation threshold is estimated using the volumetric strain of 0.036%. Concrete cracks when the tensile strain exceeds 0.010 to 0.012 percent along an axis [83]. In this work, the volumetric strain of 0.036% is used to estimate the crack initiation threshold. The crack damage threshold is defined as the first inflection point of the volumetric strain graph after the crack initiation threshold and represents the point when unstable crack growth begins to occur. Unstable crack growth is defined as when the relationship between applied stress

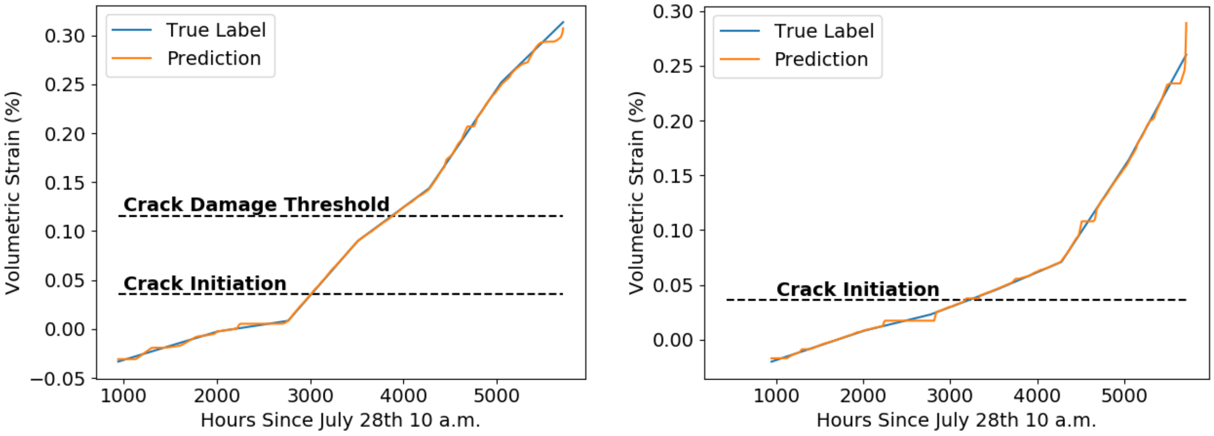

(a) (b)

Figure 7.9: Evaluation of the ANN models for (a) confined specimen and (b) unconfined specimen using cumulative counts as the input.

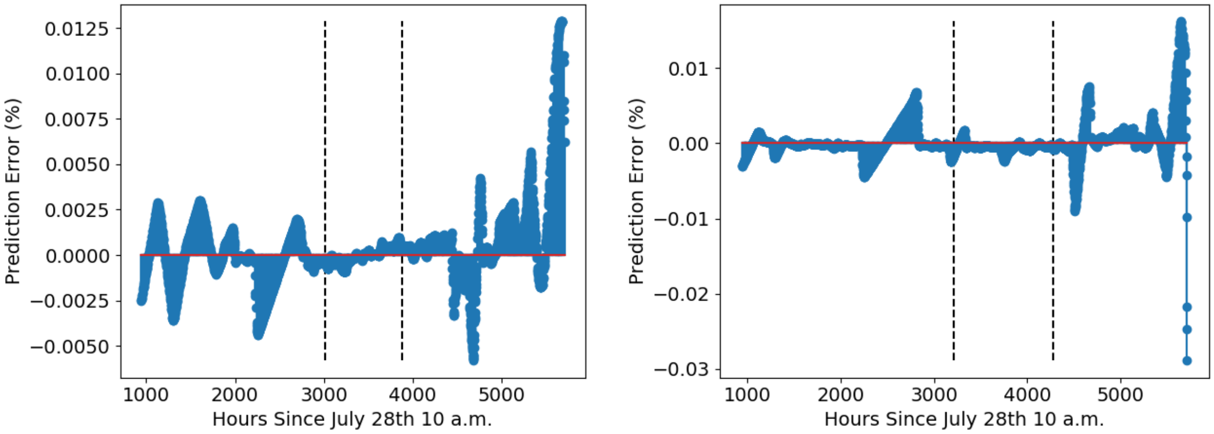

(a) (b)

Figure 7.10: Prediction errors of the ANN models for (a) confined specimen and (b) unconfined specimen using cumulative counts as the input.

and crack length cease to exist. At this stage crack growth continues to occur even if the applied load is controlled [84]. This inflection point was found by using b-spline interpolation to create a differentiable interpolation of the volumetric strain measurements. For the confined specimen, this inflection point occurred at 3882 hours with a volumetric strain value of 0.1158%.

When using both the cumulative counts and the counts per hour , the ANN model of the confined specimen achieves a mean absolute error of 0.00190%. From Fig. 7.11(a). It can be seen that the ANN model using both inputs produces spikes when a large number of counts occur at a specific hour, resulting in larger errors. In addition, the errors of the ANN model are increased after the crack damage threshold .

For the ANN models with either a single input or two inputs, the increase in error before the crack initiation threshold and/or after the crack damage threshold reflects that the ANN model is able to accurately predict volumetric strain during microcrack formation and microcrack propagation using AE signals. However, it is less capable of predicting volumetric strain when the damage progression of concrete behaves differently. Before the crack initiation threshold, crack closure occurs, and microcracks coalesce to form and grow into larger cracks after the crack damage threshold. These processes may be more complex than stable crack growth that occurs between the two thresholds and may require a more complex ANN to model their behavior.

For the unconfined specimen, the ANN model achieves a mean absolute error of 0.00146% when only using the cumulative counts as the input and a mean absolute error of 0.00155% when using both the cumulative counts and the counts per hour as inputs. Spikes correlating to points in time where a large number of counts occurred have also appeared for the results of the unconfined specimen when the ANN was trained and tested with both inputs.

A major difference between the confined and unconfined specimens is that the volumetric strain plot of the unconfined specimen does not have an inflection point. This implies that the unconfined specimen is yet to reach its crack damage threshold. However, there is a sudden increase in volumetric strain change rate at 4276 hours after the initial measurement was taken. This sudden change in volumetric strain change rate may indicate that the damage progression process may have changed at this point. This observation is supported by Eberhardt et al. who have also noticed a large rate change in strain before unstable crack growth [84]. Therefore, as was the case for the unconfined specimen, the ANN model suffers from larger errors before the crack initiation threshold and after 4276 hours since initial recording, where a sudden increase in volumetric change rate occurred.

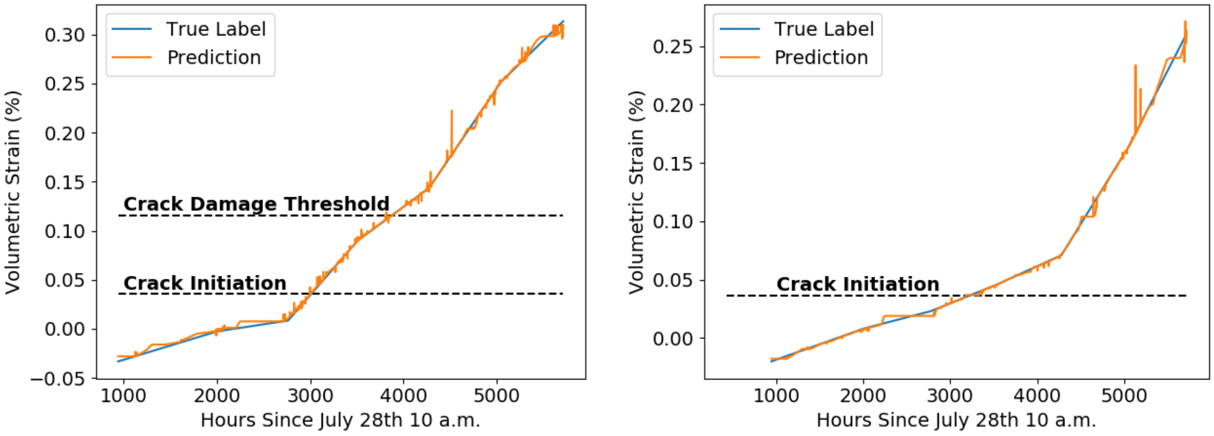

(a) (b)

Figure 7.11: Evaluation of the ANN models for (a) confined specimen and (b) unconfined specimen using cumulative counts and counts per hour as the input.

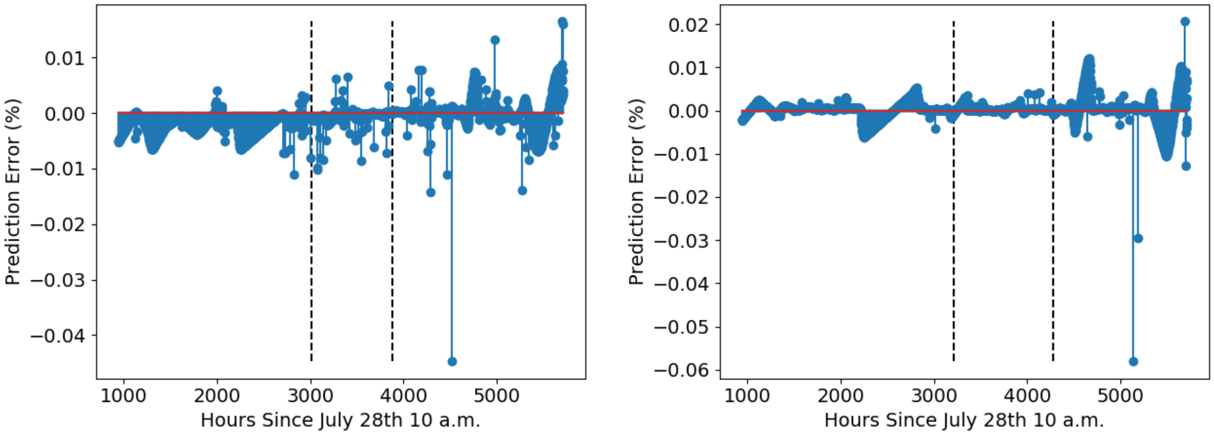

(a) (b)

Figure 7.12: Prediction errors of the ANN models for (a) confined specimen and (b) unconfined specimen using cumulative counts and counts per hour as the input.

7.2.5 Summary

ANN models are investigated to predict volumetric strains using AE signals. The results show that the models using either the cumulative counts as input or both the cumulative counts and counts per hour as inputs can capture the evolution of volumetric strain due to ASR reactions. Although using counts per hour as a secondary input has degraded the performance of the ANN model, it may be due to the linear interpolation between the volumetric strain measurements. When a high number of counts occur, there may be a large change in volumetric strain, which cannot be reflected by the linearly interpolated values. In addition, it is noted that although the ANN models for the two concrete specimens with different designs have different parameter values, it is possible that the same model may be used to predict the volumetric expansion of a concrete specimen with the same design. Although we did not have the AE data from another concrete specimen with the same design to validate this hypothesis, this concept is validated using the ultrasonic data in the next section. In addition, we note that although the ANN prediction models are different for different specimens, the model structures are the same. Thus, it would be possible to use volumetric strain measurements of concrete collected during routine surveys of a concrete structure to adapt a pre-trained model to predict the volumetric strain of concrete with a variety of different designs.

Part III

Monitoring Full-Scale Concrete Specimens

8 Ultrasonic Monitoring on Full-Scale Specimens

This chapter presents experimental studies on full-scale ASR concrete specimens using the ultrasonic monitoring system, and analysis using the thermal modulation of nonlinear ultrasonic method [85]. An ultrasonic monitoring system was installed on three full-scale concrete specimens (one control, and two ASR) at University of Tennessee-Knoxville (UTK) for long-term monitoring. Ultrasonic signals were recorded once each day, along with the temperature and expansion data that were monitored by the UTK team. Since these concrete specimens experienced large temperature variations during the monitoring duration, the ultrasonic data is processed in several periods based on the temperature histories. Ultrasonic relative velocity change is analyzed using the CWI method, and then correlated with the temperature variation for the three specimens. The relationship between the relative velocity change and the temperature variation is used a nonlinear parameter to characterize the damage levels of the three specimens.

8.1 Concrete Specimens

Three concrete specimens were designed to closely resemble a typical nuclear power plant containment structure. These specimens have a thickness of 1.0 m (3.28 ft) and are reinforced only in the plane of the wall with two elevations of intersecting large steel reinforcement. Hayes et al. [4] report details about specimen design, fabrication, and curing and conditioning procedures. The first specimen, referred to as the ASR confined, was confined in a relatively rigid steel frame to simulate the additional confinement by surrounding concrete that would be present in a Nuclear power plant containment structure. This steel frame confines against expansion in the plane of the wall, forcing a preferred direction for expansion as the thickness direction of the specimen. The second specimen, referred to as the ASR specimen, with identical mix design and steel reinforcement detail was designed and constructed with no surrounding steel frame. Thus, this specimen is unrestrained by exterior boundary conditions but still partially restrained against expansion in the plane of the wall by the steel reinforcing bars. The third specimen, referred to as the Control specimen, with identical steel reinforcement was designed and constructed with two changes to the mixture design to minimize the potential for expansion from ASR. Sodium hydroxide (NaOH), used to promote the development of ASR in the ASR and ASR confined specimens, was not used in the mix design for the Control specimen. Instead, lithium nitrate was added to mitigate against the alkalis contributed by the cement. Thus far, no ASR expansion has been observed in this specimen. Figure 8.1 shows the three test specimens.

(a) Control specimen

(b) ASR specimen

(c) ASR confined specimen

Figure 8.1: Concrete specimens

8.1.1 Dimensions and reinforcing details

Specimen dimensions were selected to represent the scale of a typical NPP containment structure. The through-thickness dimension (Z-direction) is 1.0 m (3.3 ft). The dimensions within the plane of the wall were selected accordingly at 3.5 m (11.5 ft) and 3.0 m (9.8 ft) for the X-direction and Y-direction respectively. These dimensions are shown in Figure 8.2.

The reinforcement layout for the specimens was also selected to most closely resemble that of a NPP structure. The reinforcement layout consists of US #11 Gr. 60 reinforcing steel bars with a nominal diameter of 35.81 mm (1.41 in.) spaced at 25.4 cm (10 in.) on-center resulting in two elevations of reinforcing bars embedded in the concrete specimens with 7.62 cm (3 in.) of concrete cover. The reinforcement layout results in reinforcement ratios for each direction as noted in Table 8.1. Additionally, the reinforcing steel bars were installed with square heads [10.16 cm × 10.16 cm × 2.54 cm (4 in. × 4 in. × 1 in.)] made of steel plate to achieve full development length within a relatively short distance inside the specimen.

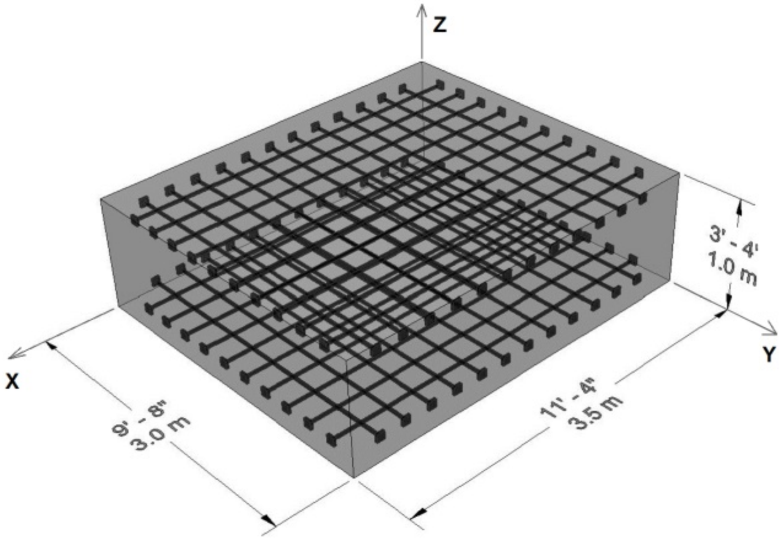

Figure 8.2: Dimensions and coordinate axes of concrete specimens ([4])

Direction	Reinf. ratio
X-direction	0.67%
Y-direction	0.68%
Z-direction	0.00%

Table 8.1: Reinforcement ratio of specimens in each direction

Note: Reinforcement ratio reported is total longitudinal reinforcement area divided by gross cross-sectional concrete area.

To allow access to the bottom surface, the concrete specimens are elevated 76 cm (30 in.) above the floor and vertically supported at the corners by four steel columns capped with 45.7 cm × 45.7 cm (18 in. × 18 in.) steel plates.

8.1.2 Concrete formulation

The mixture components used in both the reactive and control specimens included a highly-reactive greenschist coarse aggregate from North Carolina; a non-reactive manufactured sand from the Knoxville, Tennessee area; and a low-alkali Type II Portland cement with an equivalent alkali content of 0.41% Na_2O_{eq}. A 50% w/w sodium hydroxide solution (NaOH) was added to the reactive specimens to increase the alkali content to 5.25 kg/m^3 (1.50% Na_2O_{eq} by mass of cement). A 30% w/w lithium nitrate ($LiNO_3$) solution admixture was added to the control specimen at 150% of the manufacturer's recommended dosage (sometimes referred to in the literature as the "standard dose" of a molar ratio of [Li]/[Na+K] = 0.74 in the mixture) to mitigate the potential for ASR [86–89]. In addition, a high-range water-reducing admixture (meets requirements for ASTM C494 Type F) and hydration stabilizer admixture (meets requirements for a ASTM C494 Type D retarder) were added to maintain a slump value between 15 cm to 20 cm (6 in. to 8 in.) and offset the effects of warm ambient temperatures that would otherwise accelerate setting of the concrete during placement. The mixture proportions used for the reactive and control specimens are shown in Table 8.2.

Table 8.2: Design proportions of concrete mixtures

Materials	Quantity, kg/m^3 (lb/yd^3)	
	Reactive	Control
Coarse Aggregate	1180 (1989)	1180 (1989)
Fine Aggregate	728 (1227)	728 (1227)
Cement	350 (590)	350 (590)
Water*	175 (295)	175 (295)
50% NaOH solution	9.8 (17)	-
30% $LiNO_3$ solution	-	11.9 (20.0)
Water reducing admixture	2.0 oz/cwt	2.0 oz/cwt
Stabilizer admixture	2.0 oz/cwt	2.0 oz/cwt

Note: Aggregate quantities are given for oven-dry materials. Water quantities assume aggregates in saturated-surface dry (SSD) condition. (*) indicates that 70% of the mass of mixing water was replaced by ice, and the actual w/c ranged between 0.46 to 0.52.

8.1.3 Steel confinement frame

In order to simulate the range of structural boundary conditions present in a large structure such as a NPP containment building, two cases are considered: (1) a reinforced concrete specimen unconstrained laterally, and (2) a similar specimen encased in a rigid steel frame, restraining lateral deformation in the plane of the reinforcement and allowing unrestrained

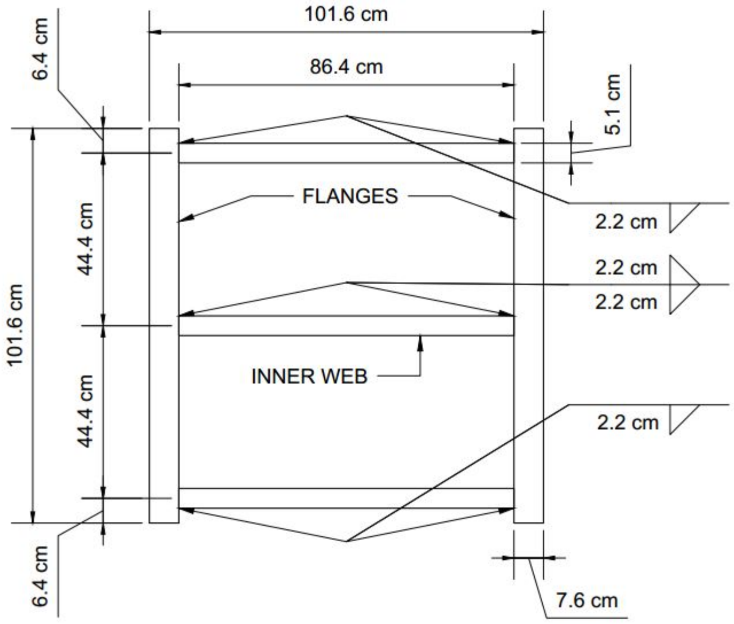

Figure 8.3: Cross-section of steel confinement frame ([4])

expansion through the specimen thickness. In order to reduce frictional effects between the steel frame and the concrete specimen, a single 1.5 mm-thick layer of HDPE was placed at the concrete-steel interface.

To provide sufficient rigidity, the confinement frame was designed for maximum stiffness. A steel plate girder cross-section was designed consisting of two 76 mm (3 in.) flanges and three 51 mm (2 in.) webs as shown in Figure 8.3. Because of limited lifting capabilities, the frame was designed as four sections joined by slip-critical bolted connections, each consisting of twelve splice plates and 144 bolts. An illustration of the connected elements of the steel confinement frame is shown in Figure 8.4.

The cross-section and connections were designed for a maximum pressure of 8 Mpa at the steel frame-concrete interface and a corresponding maximum deflection of 2.5 mm (3/32 in.).

8.1.4 Material testing

Three groups of companion cylinders (150 cylinders total) made of the same concrete batches of the CASR, UASR, and CTRL specimens were prepared to measure the evolution of the elastic modulus, compressive strength and splitting tensile strength with the ASR.

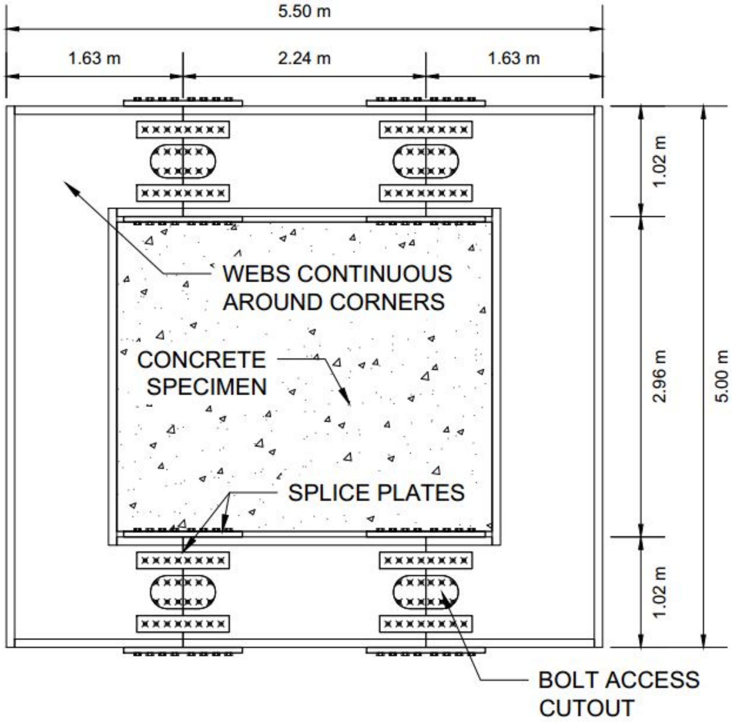

Figure 8.4: Plan view of assembled steel confinement frame ([4])

While the UASR and CTRL cylinder specimens were removed from molds 48 hours after casting, each CASR cylinder specimen was kept in a relatively rigid cylindrical steel mold with a wall thickness of 6.4 mm (1/4 in.) until the time of testing. The cylindrical steel molds were used to promote ASR-induced expansion primarily in the vertical direction, i.e. parallel to the casting direction, while the unrestrained cylinders were allowed to expand in all directions.

All cylinders were stored in an environmental chamber also containing the large specimens. Mechanical testing was performed at 7, 28 days, and then at 3, 5, 6, 9, and 12 months. The elastic modulus, compressive strength and splitting tensile strength were measured using ASTM C469, ASTM C39 and ASTM C496, respectively.

8.1.5 Casting and curing conditions

The casting of the large-scale and material testing specimens took place on July 23rd, 2016. The formwork for the large-scale specimens was insulated with rigid foam sheathing insulation in an attempt to mitigate potential damage sources other than ASR (e.g. thermal cracking). Exposed surfaces were protected from moisture loss shortly after concrete finishing. To avoid any additional detrimental DEF-induced expansion, the temperature within the concrete specimens during early-age curing was kept below 70 °C by substituting 70% of the mixing water with ice. The use of ice also permitted placement temperatures of 20 °C or less, which complemented the hydration stabilizing admixture in terms of extending the time to set, ensuring sufficient time to place and finish the concrete in the laboratory. All formwork was removed at a concrete age of 12 days and the newly exposed concrete surfaces were protected from moisture loss while an environmental chamber was being constructed around the specimens.

The environmental chamber construction was finished at a concrete age of 26 days, and the chamber was initialized for full operation. The concrete specimens were maintained in an environment of 38 ± 1°C (100 ± 2°F) and 95% ± 5%RH. The chamber was operated uninterrupted, except for periodical shutdown for inspection on a average frequency of two days per month. During shutdowns, the average temperature and RH are about 25°C (≈77°F) and 60% (about 4 hours). After the shutdown period, the chamber is restarted; the temperature and humidity return to the original set points within 6 hours.

8.2 Ultrasonic Monitoring System: Experimental Setup

8.2.1 Sensor arrangements

Low profile Piezoceramic (PZT) disks were used as ultrasonic transmitters (SMD43T105F200S, STEINER & MARTINS, INC, Doral, Florida) and receivers (SMD20T27F750S). The transmitter has a diameter of 43 mm and resonance frequency of 200 kHz while the receiver is 20 mm diameter PZT disks with resonance frequency of 750 kHz. The two PZT disks are shown in Figure 8.5(b). Since the desired frequency range of received signals is from 50 kHz to 200 kHz, the transmitter was actuated at a frequency around 200 kHz for maximum efficiency. The receiver has a relative flat frequency response in the range of 50 kHz to 200 kHz.

The positions of the PZT sensors are shown in Figure 8.5(a). Two transmitters were installed on the top surface of each specimen and four receivers on the bottom surface. Both transmitters and receivers were glued and sealed with waterproof epoxy since the specimens were curing in high humidity (95%RH) environment. Receiver R2 was installed directly below the transmitter T1, and receiver R1 had a 30 cm offset in $+Y$ direction to R2. Similarly, R3 was right below T2 and R4 has 30 cm offset in $-X$ direction to R3. The sensor arrangements are the same for the three specimens. Figure 8.5 shows the ultrasonic transmitters on the top surface of a concrete block.

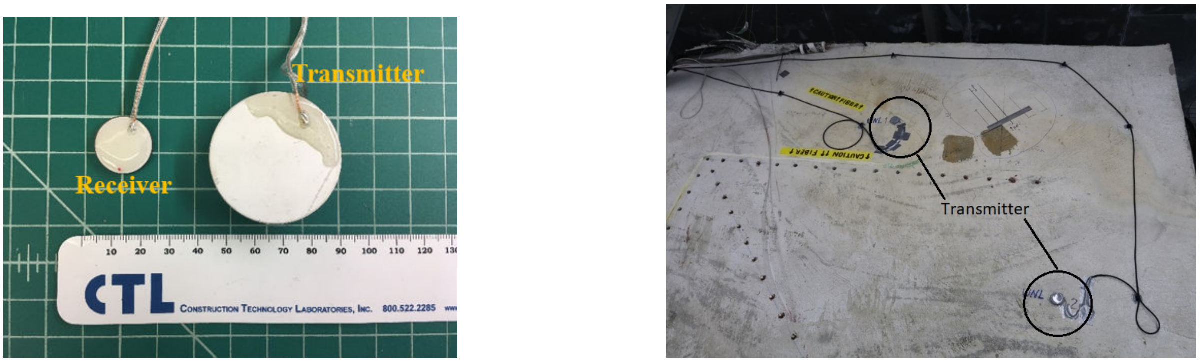

Figure 8.5: Ultrasonic sensors. (a) PZT transmitter and receiver, (b) ultrasonic transmitters on the top surface.

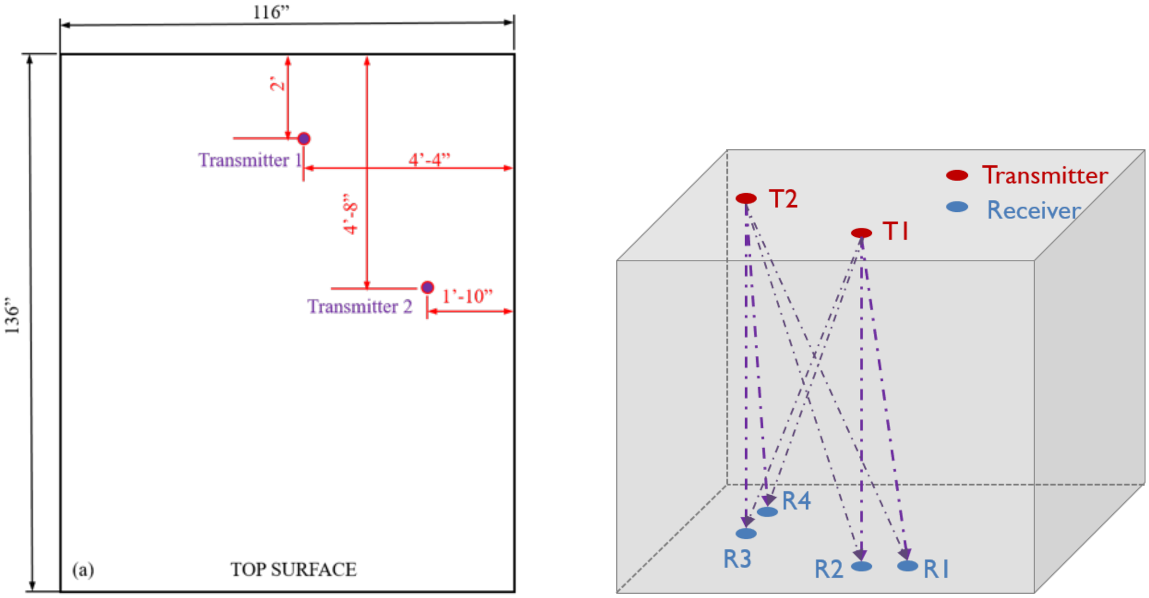

Figure 8.6: Sensor positions on each concrete specimen. (a) Transmitter positions on the top surface, (b) transmitter-receiver pairs.

For each specimen, transmitter T1 was actuated first and signals were collected in the sequence of R1, R2, R3 and R4. Then transmitter T2 was actuated and another four signals were acquired. This process was repeated on the three specimens. Twenty four signals were acquired in total everyday. Eight transmitter-receiver pairs can be used on each concrete specimen (see Figure 8.6). However, the sensor pairs (T1,R3), (T1,R4), (T2,R1), (T2,R2) have weak ultrasonic signals due to long wave propagation distance. Therefore, in this work, the signals from the pairs (T1,R1), (T1,R2), (T2,R3), (T2,R4) are studied.

8.2.2 Ultrasonic monitoring system setup

An 18-channel ultrasonic monitoring system was designed for monitoring the three large concrete specimens in UTK structural lab. The schematic diagram of the ultrasonic monitoring system is shown in Figure 8.7. An ultrasonic pulser/receiver (Olympus 5077PR) was used to drive the transmitters with 400 V, 250 kHz square pulses. Ultrasonic signals received by PZT receivers were amplified by 30 dB, and then digitized by a PICO oscilloscope (PICO5242B, Pico Technology, Cambridgeshire, UK) with a sampling rate of 6.25 MS/s and transferred to a computer. Signals were averaged 600 times to improve the signal to noise ratio (S/N). Measurements were taken every day at 02:15 am EST. All sensors were connected to a multiplexer (Agilent 34970 and 34903) for sequential scanning. Each time one pair of transmitter and receiver were activated for sensing, and the multiplexer would switch the transmitters or receivers from one sensor to another one. A LabVIEW program was developed to control the data acquisition. The ultrasonic monitoring started on April 24 in 2017. A surveillance camera was used to monitor the status of the equipment.

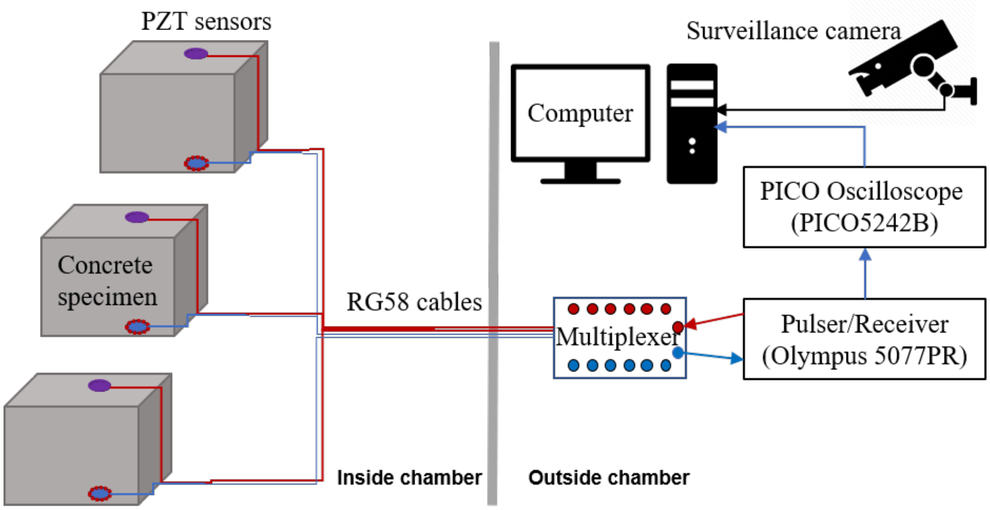

Figure 8.7: Schematic diagram of the ultrasonic monitoring system.

8.3 Temperature and Expansion Histories

Temperatures of three concrete specimens had been monitored every hour since the concrete cast date (7/24/2016). The temperature and expansion data were provided by the University of Tennessee-Knoxville research team. Figure 8.8 shows the temperature histories of the three concrete blocks. The temperature increased to more than 55 °C immediately after the cast due to the hydration heat. After about four weeks curing in the room temperature, the three blocks were conditioned in an environmental chamber at temperature of 38°C and 95% RH. This process lasted for about 300 days. Then the chamber temperature was decreased to room temperature (about 24°C) to reduce the ASR reactivity. In the period of 665 days to 745 days, the chamber temperature was increased to 38°C again, and then decreased to the room temperature after 745 days. The first visible crack appeared on the lateral sides of the UASR specimen before 150 days [4].

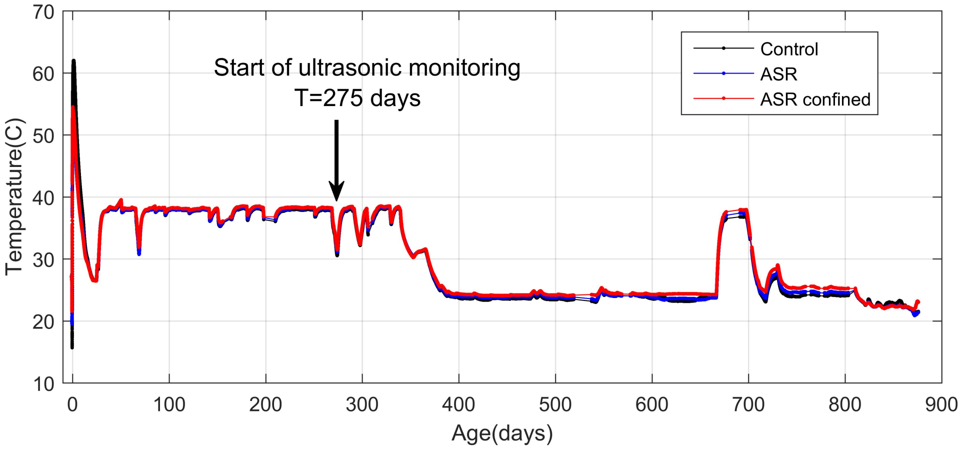

Figure 8.8: Temperature histories of the three concrete blocks since concrete cast

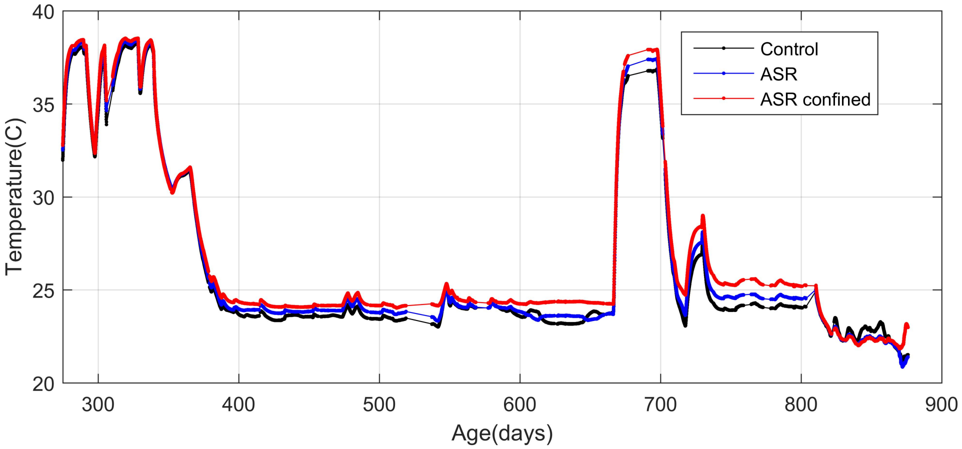

Figure 8.9: Temperature histories of the three concrete blocks after ultrasonic monitoring

When the ultrasonic monitoring started at the concrete age of 275 days (4/25/2017), extensive cracks have been observed on the UASR specimens. Figure 8.9 shows the specimen temperature history after the ultrasonic monitoring started. Figure 8.10 presents the expansion history of three specimens. Figure 8.10(a) shows the complete history record of the volumetric expansion for the three specimens. The ASR specimen and the ASR confined specimen show similar volumetric expansion histories while the control specimen has little change and even shows small shrinkage. The two ASR specimens shows fast volumetric expansion rate before the concrete age of 330 days when the chamber was operated in high temperature (38°C). When the chamber temperature decreased to 24°C, the expansion process becomes very slow. The expansion is also affected by the temperature variation in the period of 665 days to 745 days when the chamber temperature increased to 38°C again.

Figure 8.10(b) shows the expansion histories in Z direction of the three specimens. The CASR specimen has the largest expansion in the Z direction, since it was confined in both X and Y directions, and could only expand in the Z direction. Figure 8.10(c) shows the expansion histories in the Z direction after ultrasonic monitoring started. At beginning, the control, UASR and CASR specimens have expansions of -0.003%, 0.191% and 0.266% respectively, while the expansions change to -0.009%, 0.258% and 0.346% at the end of the ultrasonic monitoring. The Control specimen has minor shrinkage after the monitoring with a relative expansion of -0.006%. The UASR specimen has a relative expansion of 0.067% and the CASR specimen has a relative expansion of 0.084%. The expansion details during the ultrasonic monitoring period are summarized in Table 8.3. In this report, all analyses focus on measurements in the Z-direction, because the expansion is dominated in Z direction for both ASR specimens, and the ultrasonic wave monitoring also measures wave propagation in the Z direction.

Table 8.3: Expansion details during the ultrasonic monitoring period

	Start(275 days)	End (876 days)	Relative expansion
Control	-0.003%	-0.009%	-0.006%
ASR	0.191%	0.258%	0.067%
ASR confined	0.266%	0.346%	0.084%

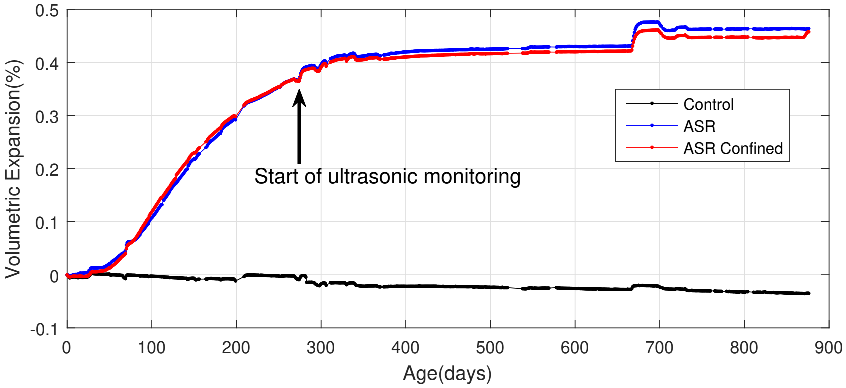

(a) Volumetric expansion of the three specimens

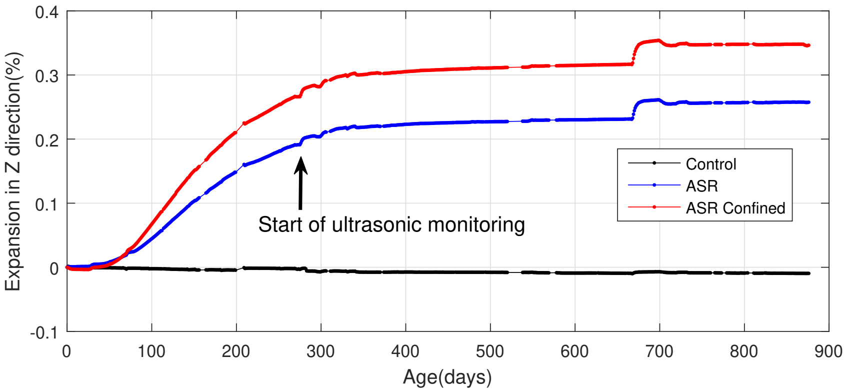

(b) Expansion in Z direction

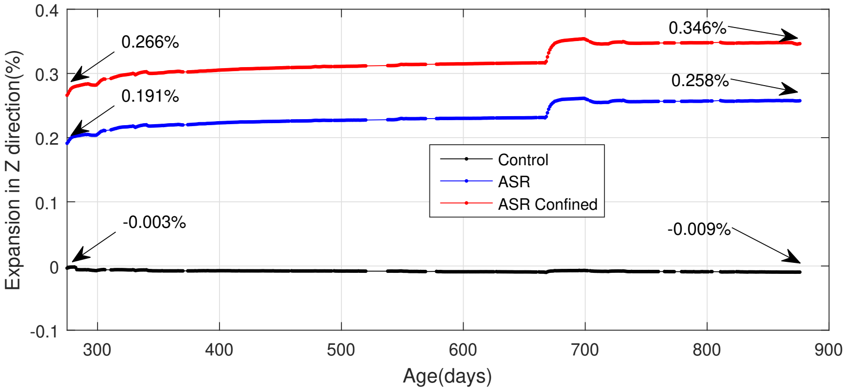

(c) Expansion in Z direction after ultrasonic monitoring

Figure 8.10: Expansion histories of the three concrete specimens

8.4 Ultrasonic Monitoring Results

This section first presents ultrasonic signals recorded on three concrete specimens. Then the ultrasonic signals are analyzed using continuous wavelet analysis. Finally, the relative velocity changes due to ASR development and temperature variation are calculated.

8.4.1 Time and frequency domain signals

Figure 8.11 show time domain signals of the sensor pair (R1,T2) on the three concrete specimens at the age of 325 days. The signal for the control specimen (Figure 8.11(a)) has higher amplitude and longer duration than the signals from two ASR specimens, which indicate lower wave attenuation and high level of wave diffusivity in the the control specimen. The signal of the UASR specimen (Figure 8.11(b)) has lower amplitude, but longer tail than the signal of CASR specimen (Figure 8.11(c)). It is believed that the lateral confinement and/or confining steel plates may affect the ultrasonic wave propagation. A part of ultrasonic energy may directly pass through the confining steel plates, which give a signal with high initial amplitude but shorter duration, similar to ultrasonic signals propagating in homogeneous materials.

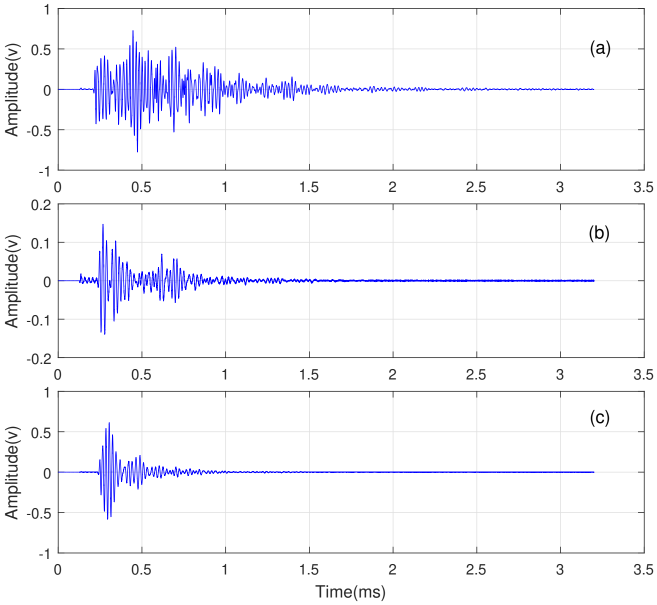

Figure 8.11: Time domain signals for sensor pair (T1,R2) at age of 325 days: (a) Control, (b) UASR, (c) CASR.

Figure 8.12 shows frequency domain signals of the sensor pair (R1,T2) on the three concrete specimens at the age of 325 days (blue curves) and 675 days (red curves). The energy of the signal for the control specimen (Figure 8.12(a)) spreads in the frequency range of 20 kHz to 130 kHz, with most energy focused in the range of 40 kHz to 60 kHz. The signal for UASR specimen has much lower amplitude and shows relatively higher low frequency components, which is attributed to attenuation of high frequency components due to crack damage (see Figure 8.12(b)). By comparing the amplitude spectra at 325 days and 675 days, the control specimen signals do not show much difference; the UASR signals show some attenuation of the high frequency content in the signal of 675 days (Figure 8.12(b)). Overall, the signals recorded at these two different days do not show too much difference, although the expansions were still increasing from 325 days and 675 days. Therefore, the conventional linear analysis parameters (frequency or attenuation) are insensitive to the ASR damage development.

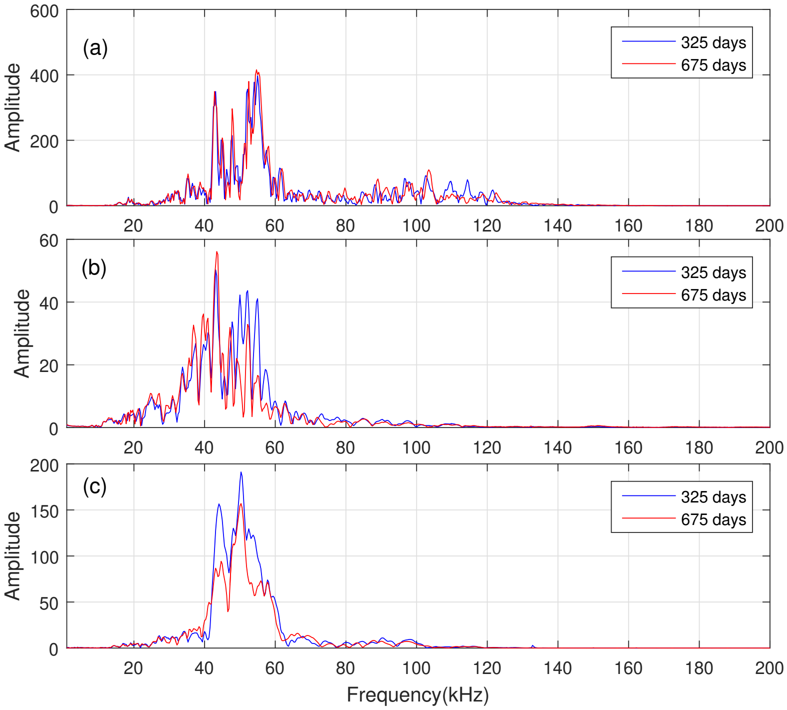

Figure 8.12: Amplitude spectra of ultrasonic signals for sensor pair (T1,R2) at age of 325 days (blue) and 675 days (red) on: (a) Control, (b) UASR, (c) CASR specimens.

8.4.2 Relative velocity change histories

In this study, CWI analysis was adopted to track the daily change of wave velocity in the concrete specimens. The relative velocity change histories using signals of sensor pair (R1,T2) are shown in Figure 8.13(b) for all three specimens. The wave propagation direction of (R1,T2) is perpendicular to the main cracking plane (X-Y plane).

Although both ASR specimens demonstrated continuing expansions during the ultrasonic monitoring period, the wave velocity only showed about 1% change in all three specimens. Contrary to expectation, the velocity on both ASR specimens did not decrease with continuing damage, instead showed some increase from the initial value. Therefore, it is impossible to differentiate the ASR damaged specimens from the control specimen based on velocity measurement only.

Comparing to the temperature history in Figure 8.13(a), we can find the relative velocity change is greatly affected by the temperature variation. The relative velocity change increases when the temperature decreases. The relative velocity change histories recorded by another sensor pairs (T1,R1) is shown in Figure 8.13(c), which gives similar trends as Figure 8.13(b). Results for other sensor pairs (T2,R3) and (T2,R4) are not shown in the report since they show similar trends as presented in Figure 8.13(b).

Comparing the trend of temperature variation and relative velocity change, we notice the velocity curves almost have mirror relationships with the temperature curves, which indicates that the relative velocity change and temperature variation have strong negative correlation relationships. This phenomenon is similar to the results observed on the medium-scale concrete specimens, and further discussed in the next section.

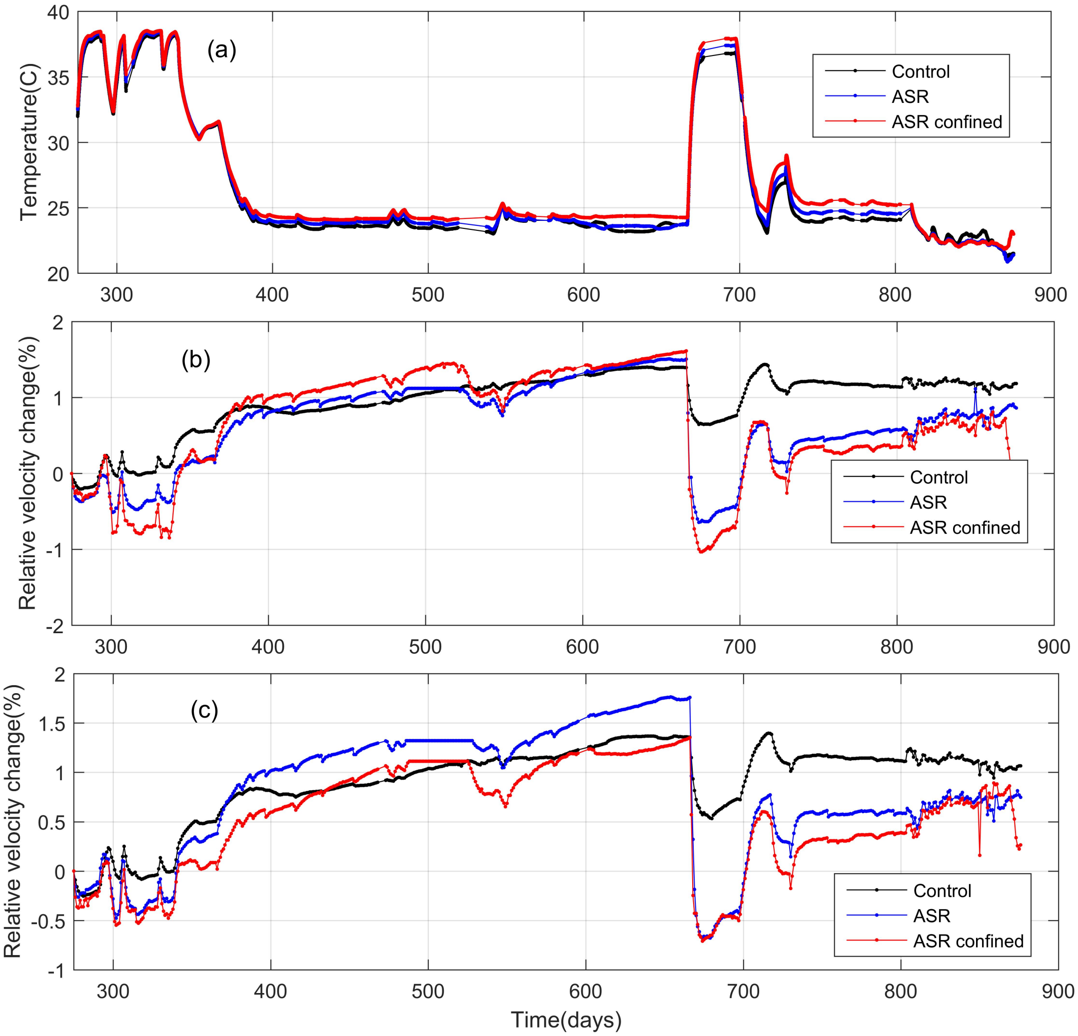

Figure 8.13: Temperature (a) and relative velocity histories measured by (b) sensor pair (T1,R2), and (c) by sensor pair (T1,R1).

8.5 Nonlinear Analysis of Ultrasonic Wave Using Thermal Modulation

The experimental results presented above indicate that the temperature variations has significant influence on the relative velocity change measurements, and the velocity change due to damage is overshadowed by the temperature effect. The temperature effect is usually treated as pollution to the recorded data, and various temperature compensation methods have been proposed [90]. However, the results presented in Figure 8.13 indicate that the temperature effects on different specimens are different, i.e., the relative velocity measurement on a sound concrete specimen cannot be used to correct the temperature effect on a damaged specimen.

On another aspect, the different responses of three concrete specimens to temperature variations motivate us to investigate the relationship between relative velocity change and temperature change, and propose the thermal modulation technique of nonlinear ultrasonic wave to characterize microcracking damage in concrete. In this analysis, the temperature variation is used as the driving force to excite nonlinear behavior of material and modulate the high frequency ultrasonic wave propagation in concrete. Based on the results on the three specimens, we found that the damaged concrete specimens show larger relative velocity changes with temperature than the control specimen. Therefore, a thermal modulation coefficient is proposed to evaluate to the nonlinear parameter and damage level of concrete.

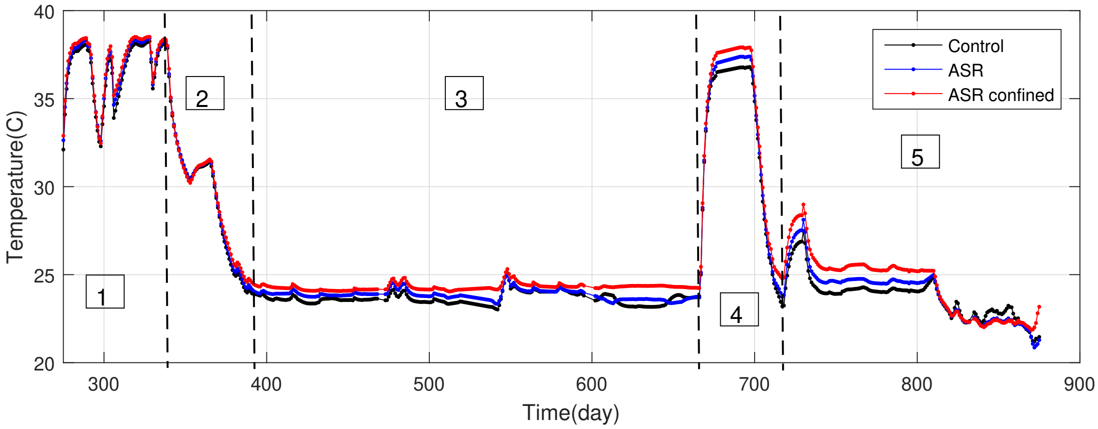

Figure 8.14: Five periods for the temperature histories of the concrete specimens

The specimen temperature history (Figure 8.14) can be divided into five periods, and the thermal modulation analyses were applied to each period. Th relative velocity change and expansion in each period are calculated using the measurements on the first day of each period. All the following results are based on the signals of the sensor pair (T1,R2).

Period 1 (day 275 to day 340) In period 1, the relative expansions of the UASR and CASR specimens were 0.0288% and 0.0366% while the Control barely had no expansion (see Figure 8.15). The temperature history for this period is shown in Figure 8.16(a), and the relative velocity changes are show in Figure 8.16(b) for the three specimens. The relative velocity change on the CASR specimen is more sensitive to temperature variation than the other two specimens, which indicates the CASR specimen has the most damage in the vertical direction among the three specimens.

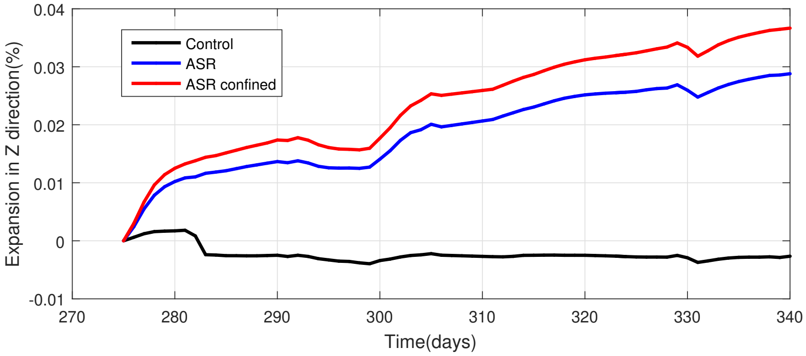

Figure 8.15: Period 1: relative expansion in Z direction.

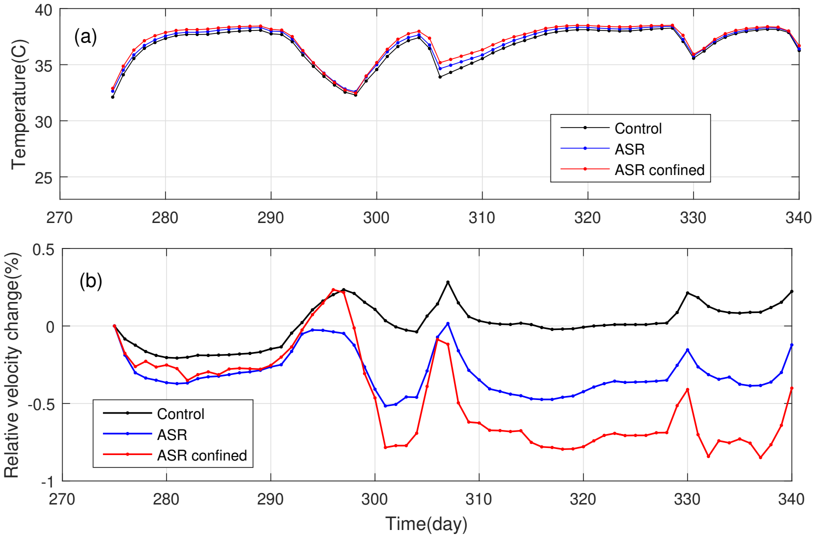

Figure 8.16: Period 1: (a) temperature histories, and (b) relative velocity histories.

Period 2 (day 340 to day 394) For period 2, the relative expansions of the UASR and CASR specimens were 0.0023% and 0.0017% (see Figure 8.17), temperature and relative velocity change histories are shown in Figure 8.18(a)(b). The large temperature change in period 2 enables thermal modulation analysis on ultrasonic velocity. Figure 8.19 shows the relative velocity vs. temperature correlation curves for the three specimens, and linear relationships are observed between the dv/v and temperature for all three curves. The thermal modulation coefficients are defined as the slopes of the linear fitting lines, which are 4.9×10^{-4}/°C, 8.0×10^{-4}/°C, and 11.4×10^{-4}/°C for the Control, UASR and CASR specimens, respectively. The specimen with high damage level demonstrates high thermal modulation coefficient, and trend of thermal modulation coefficients matches well with the damage levels of the three specimens.

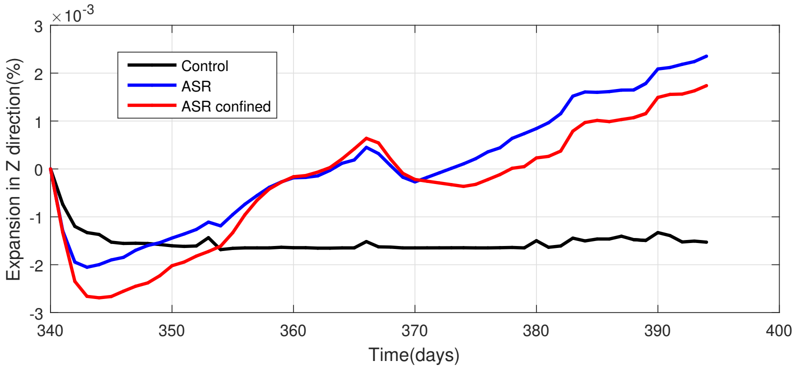

Figure 8.17: Period 2: relative expansion in Z direction.

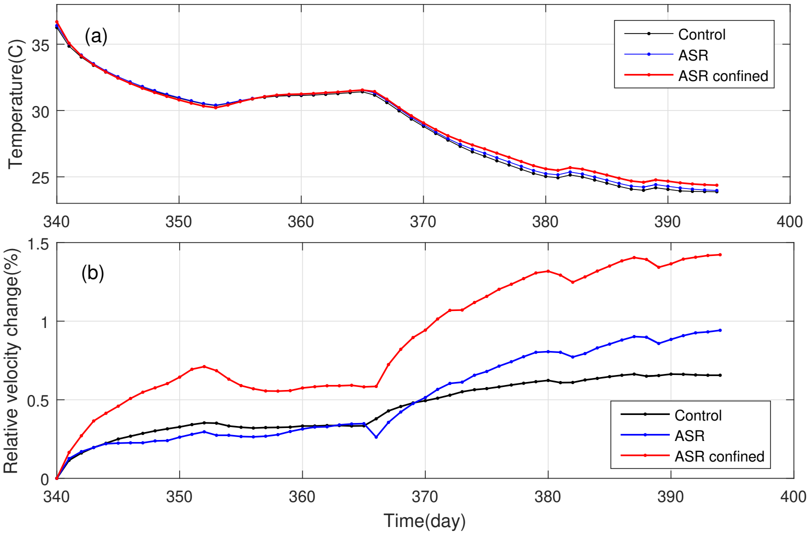

Figure 8.18: Period 2: (a) temperature histories, (b) relative velocity histories

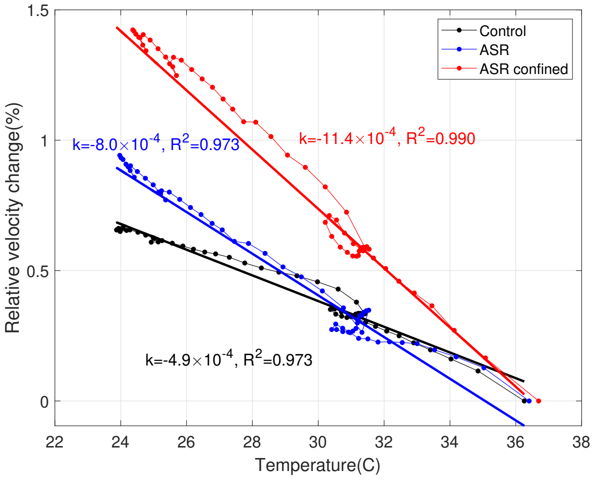

Figure 8.19: Period 2: correlation curves between relative velocity change and temperature.

Period 3 (day 394 to day 666) The UASR and CASR specimens showed an expansion of 0.0089% and 0.0122% respectively, while the Control shows small shrinkage (see Figure 8.20). Although the temperature was nearly constant around 24°C (see Figure 8.21(a)), the relative velocity on all specimens increased (see Figure 8.21(b)). For the control specimen, the velocity increase might be caused by continuing hydration and strength improvement; however, the velocity increase on the ASR specimens cannot be explained when the specimens showed further microcracking damage and expansion (Figure 8.20). More detailed study is needed to understand the material property change during this period. Small temperature variations also caused strong fluctuations on the relative velocity curves for the two ASR specimens, but not on the control specimen. The expansion curves (Figure 8.20) are also affected by temperature fluctuation, and similar conclusion can be obtained for the ASR and control specimens.

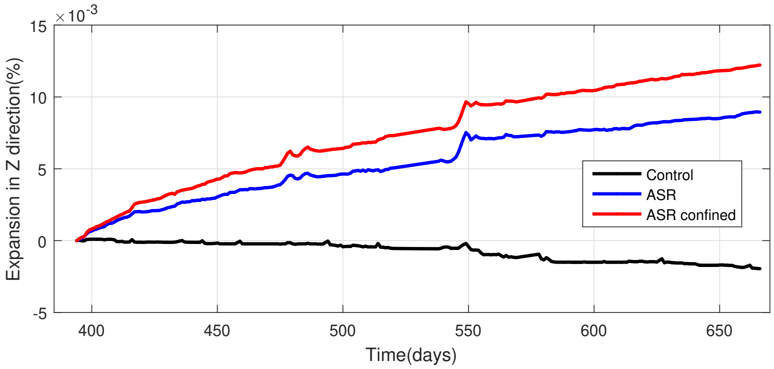

Figure 8.20: Period 3: relative expansion in Z direction.

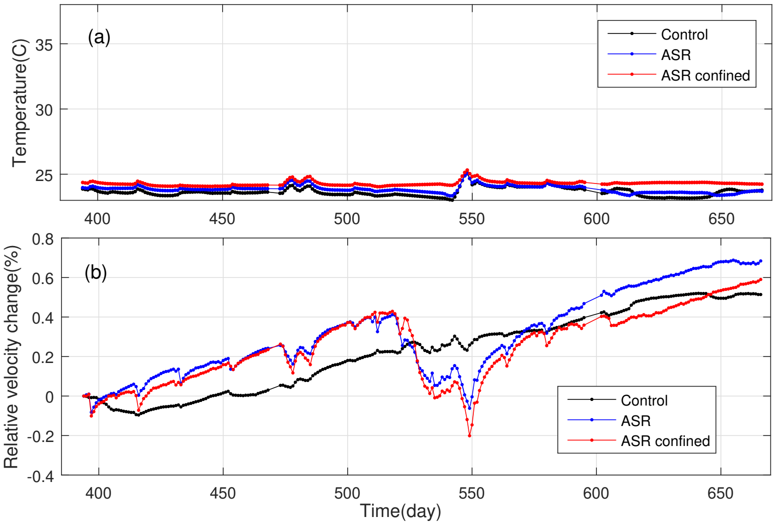

Figure 8.21: Period 3: (a) temperature histories, (b) relative velocity histories

Period 4 (day 667 to day 709) In period 4, the relative expansions of the UASR and CASR specimens were 0.0235% and 0.0297% while the Control specimen had no expansion (see Figure 8.22). The specimen temperature gradually increased to 38°C, held at 38°C for about 23 days (see Figure 8.23(a)), and then dropped to 26°C. In Figure 8.23(b), the relative velocity changes show opposite trends as the temperature histories.

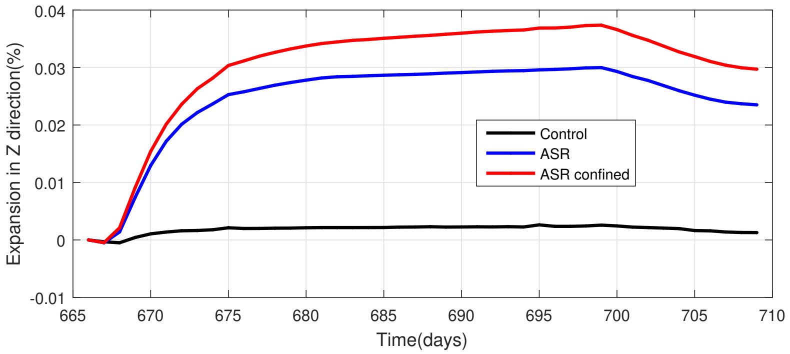

Figure 8.22: Period 4: relative expansion in Z direction.

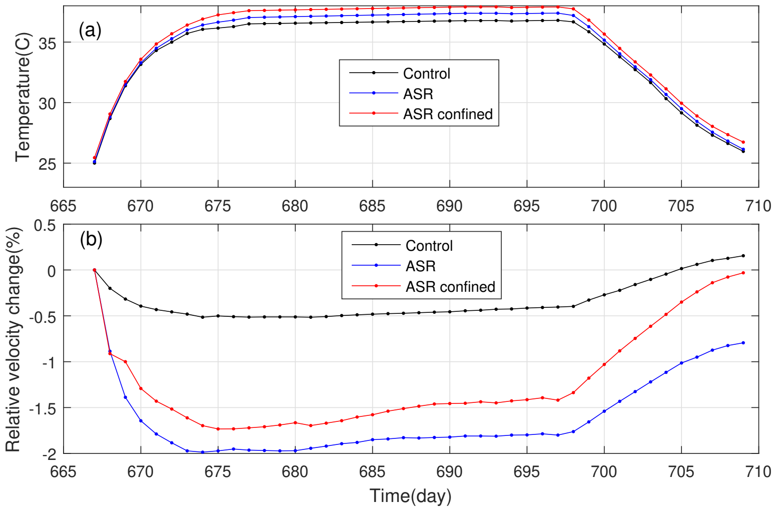

Figure 8.23: Period 4: (a) temperature histories, (b) relative velocity change histories

The correlation curves between the relative velocity change and the temperature are shown in Figure 8.24. For the temperature elevating stage, the Control specimen's curve shows good linearity, while the curves for the two ASR specimens do not have good linearity. However, the two curves for ASR specimens still have larger slopes than the curve for the Control specimen. When temperature becomes stable, the relative velocity changes of the three specimens still have small increase: Δv=0.111%, Δv=0.186% and Δv=0.328% for the three specimens respectively. We observe that specimen with higher damage level has

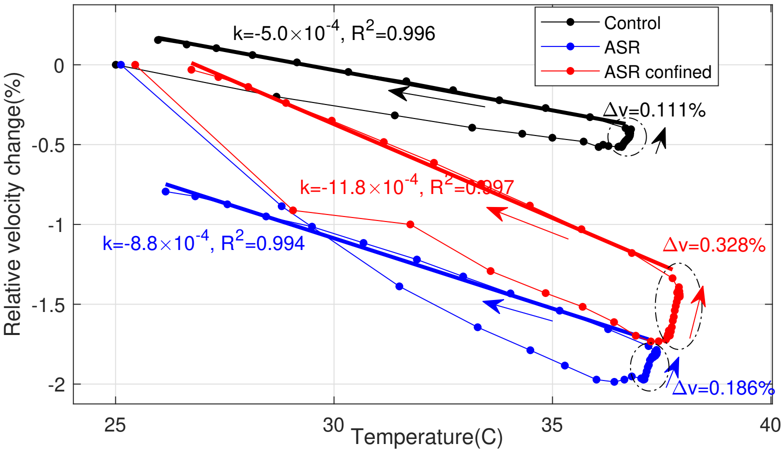

Figure 8.24: Period 4: correlation curves between relative velocity change and temperature.

higher velocity increase than the specimen with lower damage level under stable temperature conditions.

For the temperature descending stage, all correlation curves for the three specimens show very good linearity and the slopes of the fitted curves are shown in the figure. The thermal modulation coefficients for the three specimens are 5.0×10^{-4}/°C, 8.8×10^{-4}/°C and 11.8×10^{-4}/°C for the Control, UASR, and CASR specimens, respectively. These three coefficients are very close to the values obtained in period 2 (see Figure 8.19). These results validate the repeatability of the thermal modulation method.

Period 5 (day 719 to day 866) In period 5, the relative expansions (Z-direction) of UASR and CASR specimens were 0.0027% and 0.0020% while the Control had small shrinkage (see Figure 8.25). The specimen temperatures had small variations around 25°C, which is shown in Figure 8.26(a). The relative velocity change histories of the three specimens are shown in Figure 8.26(b). The Control specimen had an almost stable velocity after 730 days, while the relative velocity changes for the two ASR specimens keep increasing during the same period. By correlating the relative velocity change with the temperature in Figure 8.27, we found the curves for two ASR specimens still show larger slopes than the curve of the Control specimen.

Summary of findings for all periods By summarizing the findings from all periods, we observed the following common features in all periods:

- Temperature variation affects expansion and ultrasonic wave velocity measurements.

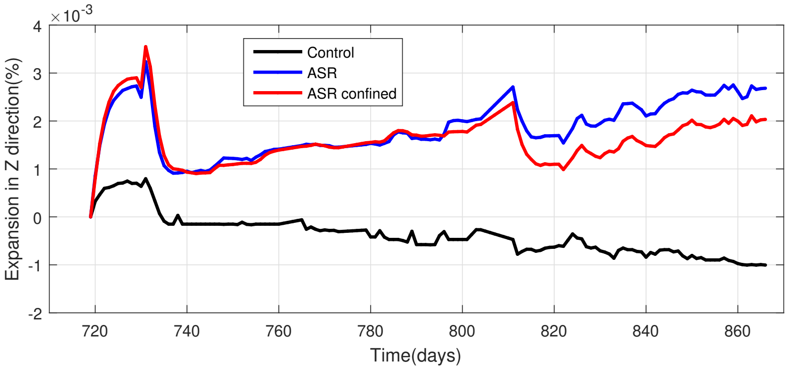

Figure 8.25: Period 5: relative expansion in Z direction.

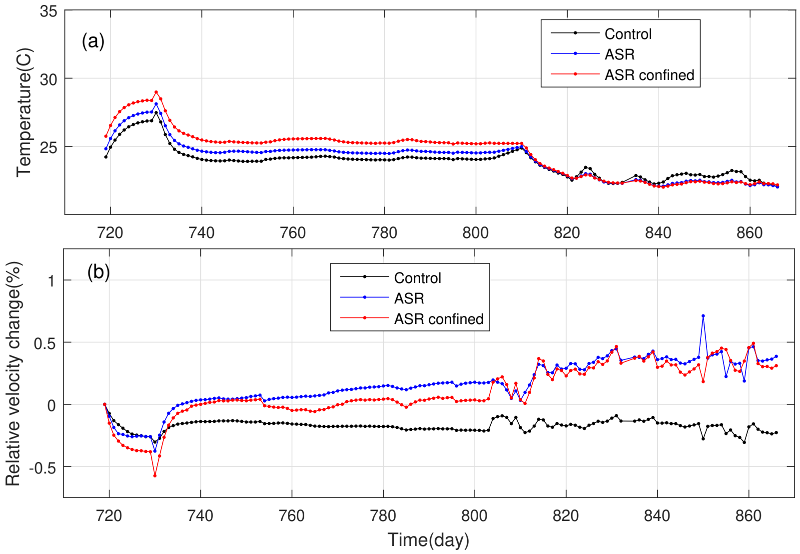

Figure 8.26: Period 5: (a) temperature histories, (b) relative velocity change histories.

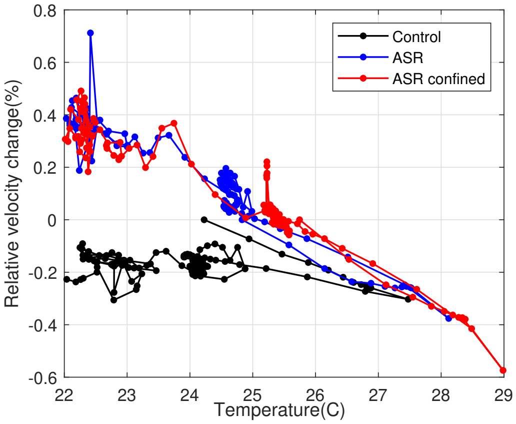

Figure 8.27: Period 5: correlation curves between relative velocity change and temperature.

- The temperature effects are not equal on all concrete specimens. Specimens with higher level of cracking damage demonstrate higher sensitivity to temperature variation than low-damaged or undamaged specimens. Good linear relationships are found between the relative velocity change and temperature. This property relates a nonlinear behaviour of concrete excited by thermal modulation, and motivated the authors to propose the thermal modulation technique for concrete evaluation using nonlinear ultrasonic waves.
- All specimens showed increase of velocity when the temperature was held stable, and the ASR specimens showed large increase of velocity than the control specimen, even though they also experienced continuing expansion (i.e. damage). The mechanism is still unclear.

8.6 Irreversible Temperature Effect

In the previous section, we observed that the relative velocity change has strong negative linear relationship with the temperature, i.e., dv/v increases when temperature decrease, and vice versa. However, we found the relative velocity change did not return to its original value when temperature went through a closed cycle, as shown in Figure 8.28. Figure 8.28 shows the histories of temperature, relative velocity change and expansion in Z direction of the three specimens from 666 days to 715 days. The temperature first increased from 23.7°C to around 37.2°C at 677 days, then kept stable at 38°C until 698 days, and eventually decreased to 23.7°C (see Figure 8.28(a)) at 715 days. Meanwhile, the relative velocity change showed an opposite trend with temperature history, while the expansion showed a similar trend with the temperature. Base on the temperature history, three periods (increase, stable, decrease) are used to discuss the temperature effect.

Table 8.4: Variation of temperature, relative velocity change and expansion in periods I and III

Parameter	Temperature		Relative velocity change		Expansion	
Period	I	III	I	III	I	III
Control	13°C	-13.1°C	-0.748%	0.670%	0.002%	-0.001%
ASR	13°C	-13.1°C	-2.680%	1.313%	0.026%	-0.006%
ASR confined	13.1°C	-12.9°C	-2.680%	1.058%	0.032%	-0.008%

Table 8.4 summarizes the variations of temperature, relative velocity change and expansion (Z-direction) for the three specimens in periods I and III. The temperature increased

about 13°C. The relative velocity of the Control specimen returned to its original value (see Figure 8.28(b)) after the temperature cycle, and the net expansion was very small comparing to the expansion histories of the two ASR specimens (see Figure 8.28(c)).

The two ASR specimens first showed decrease of the relative velocity in period I and then an increases in period III. Their relative velocities did not return to the initial values, instead had uncovered values of -1.41% and -0.94% at 715 days. Their expansions increased by 0.026% and 0.032 % in period I and decreased by -0.006% and -0.008% in period III, which indicates that the expansions of the two specimens did not return to their original values when temperature went back to 23.7°C.

The three specimens all had very similar temperature changes in periods I and III. For the control specimen, its relative velocity returned to zero. However, for the two ASR specimens, their relative velocity changes did not return to their original values. We believe this behavior was caused by the microcracking damage in the ASR specimens. The relative velocity change in the heating process (period I) was higher than in the cooling process (period III). The temperature sensitivities of the relative velocity change are different in heating and cooling processes for damaged material, which is a typical behavior of nonlinear hysteresis. This phenomenon was also observed by Niederleithinger et al. [91], and might provide additional information about the damage evaluation of materials.

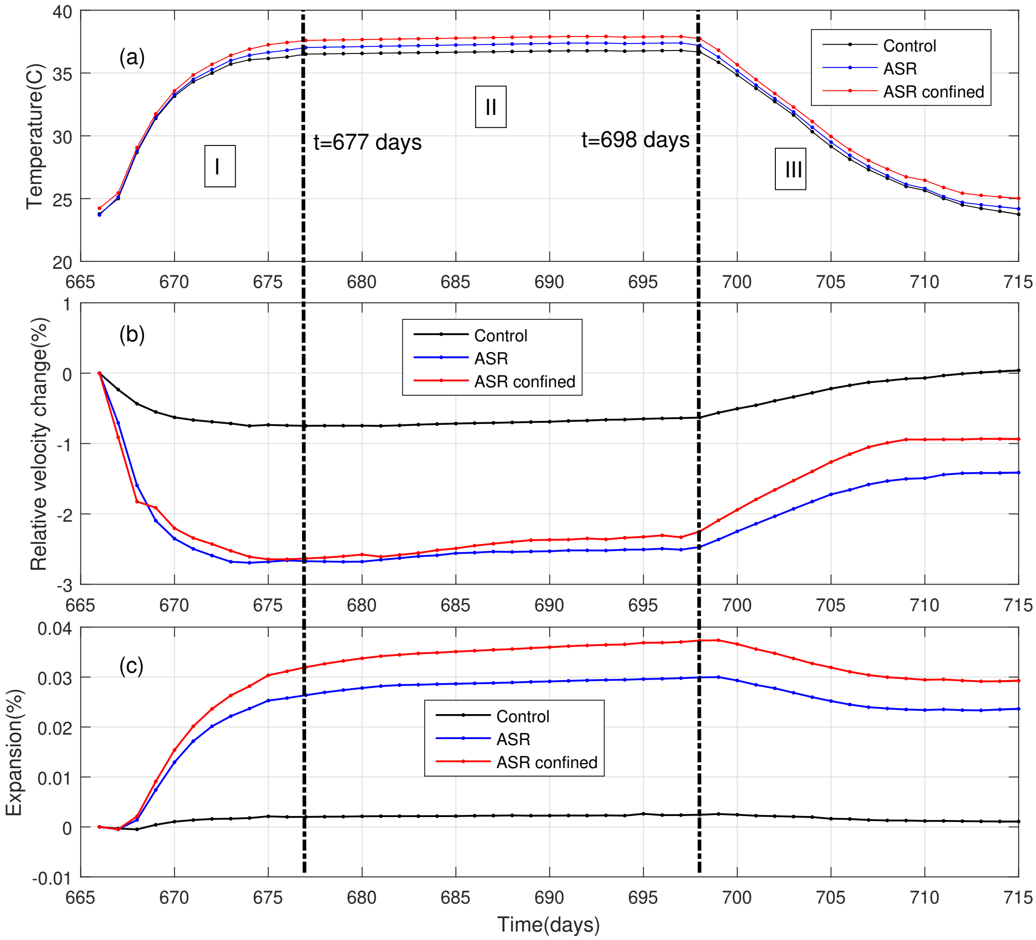

Figure 8.28: Relative velocity change and temperature histories from 666 to 718 days.

9 Acoustic Emission Monitoring on Full-Scale Specimens

9.1 AE Experimental Setup

One of the primary advantages of acoustic emission is the ability to assess ongoing damage with access to only one side of an object, such as an external containment wall or similar structure. The advantage of acoustic emission over similar one sided methods such as digital image correlation, visual inspection, and similar approaches is that acoustic emission is sensitive not only to surface defects but also to damage as it progresses within the structure.

To better understand the capabilities and limitations of acoustic emission monitoring for this application, three full-scale and realistically reinforced concrete block specimens at the University of Tennessee Knoxvile were utilized. The three specimens have been described in previous chapters, and are referred to as confined, unconfined, and control. A rigid steel frame was employed to create confinement. Two specimens were cast with reactive aggregate, while the third served as a control. Soltangharaei et al. [92] and Hayes et al. [4] provide detailed information regarding steel reinforcement and concrete mixture designs. More information may be found in [92].

Schematic representations of the specimens are shown in Figure 1. A chamber was built to monitor and manage the relative humidity and temperature of the environment. Alkali-tolerant strain transducers and fiber optic extensometers (long-gauges) were employed to measure the internal strain in the specimen. Instrumentation is described in [4].

Each of the reactive specimens had four acoustic emission sensors attached to the bottom of the specimen and three acoustic emission sensors embedded within the specimen. The four sensors attached to the bottom of the specimen represent sensor positions and types as they would potentially be placed on an interior wall for an existing nuclear containment. These sensors were of the resonant type as this type of sensor is more sensitive to damage

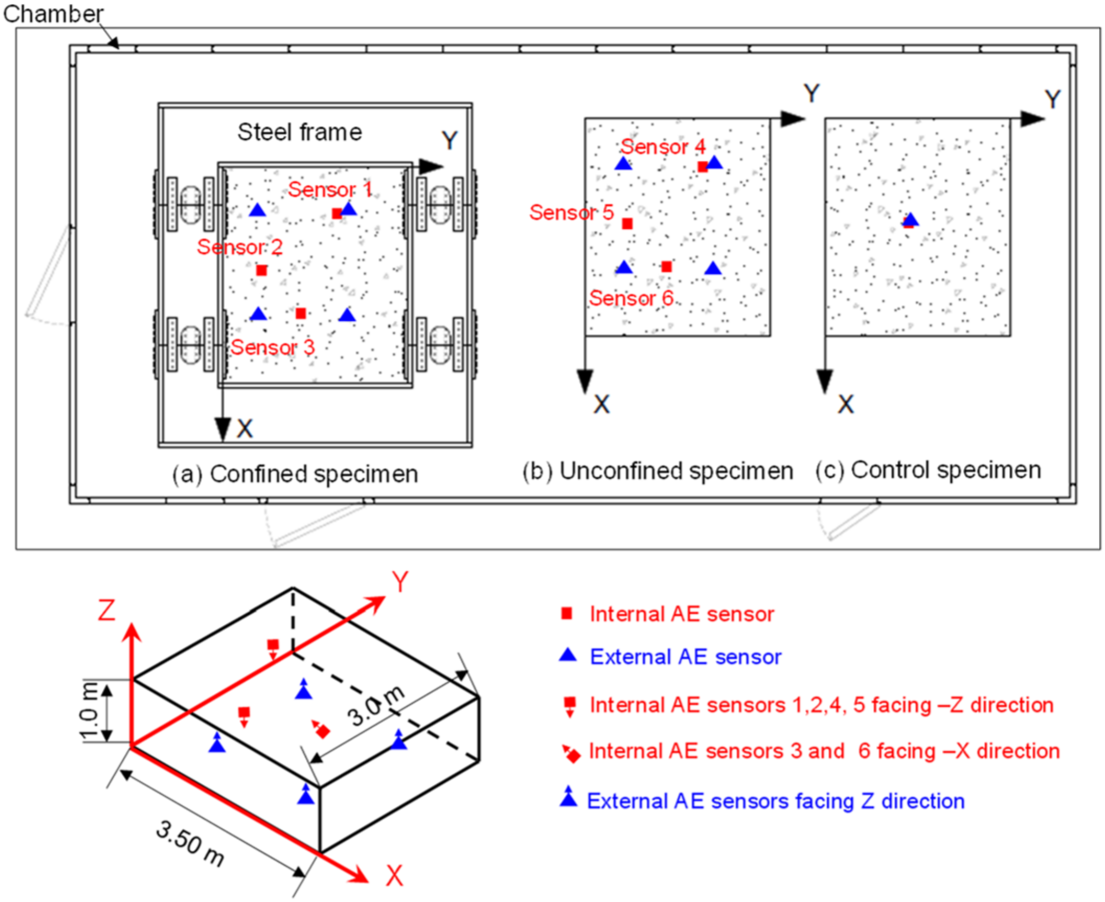

(a) Confined specimen (b) Unconfined specimen (c) Control specimen

(d) Specimen dimentions and sensor orientations

Figure 9.1: Test specimens and AE sensor positions. [92].

growth when compared to wideband sensors when the frequency range is properly selected. Past experience has shown that sensors in the frequency range of 40 – 60 kHz meet the in-situ monitoring needs of reinforced concrete systems and for this reason sensor type R6I-UC (manufactured by Mistras Group Inc., Princeton Junction, New Jersey) were used on the exterior surface. This sensor type is resonant (R) with elevated frequency response in the range of 40 – 60 kHz (6), I stands for integrated preamplification, and is waterproofed for underwater usage (UC). To offset the effect of gravity and to ensure that the sensor remained attached without supervision and over an extended period of time, pvc tubing was placed between the floor of the chamber and the sensor attachment. The sensors were isolated from the floor with neoprene pads.

The embedded sensors were installed to represent a potential means of monitoring facilities from the construction phase forward. Wideband sensors (type WDI-UC, also manufactured by Mistras Group, Inc., where WD stands for wideband and I stands for integrated preamplification) were utilized for the embedded sensors as this type of sensor is more suitable for obtaining frequency based response which can be useful for understanding damage types, such as micro-cracking, crack coalescence, and delamination. Two sensors were utilized in the control specimen to provide a baseline and to verify that the other sensors were primarily recording signals due to damage growth in the reactive specimens, as opposed to environmental noise in the chamber itself. Sensor locations and means of attachment are shown in Figures 9.1 and 9.2.

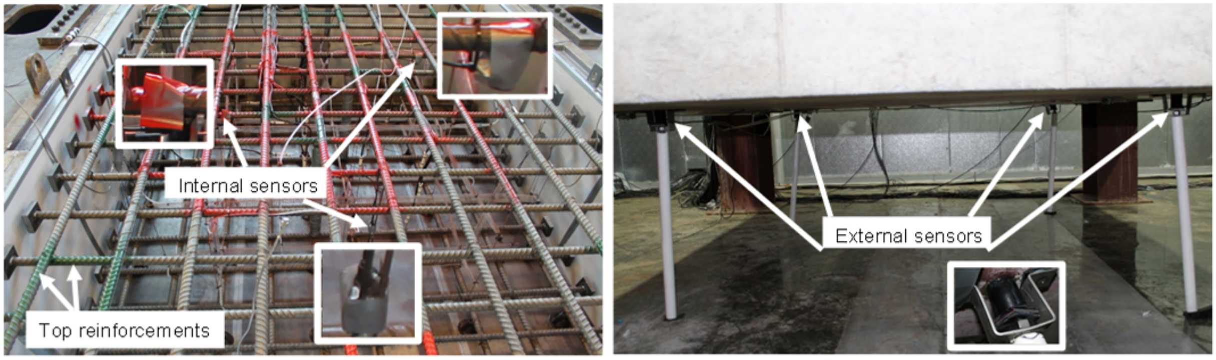

(a) Internal AE sensors (broadband)

(b) External AE sensors (resonant)

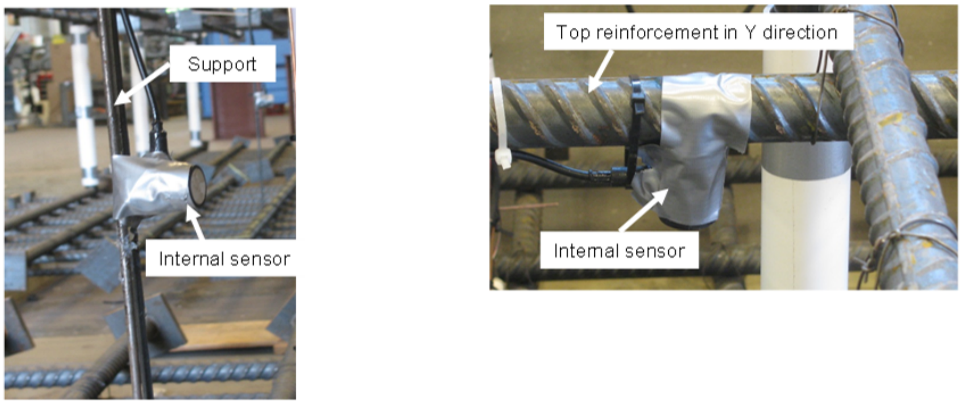

(c) Internal sensors 3 and 6 installation

(d) Internal sensors 1, 2, 4, and 5 setup installation

Figure 9.2: AE sensor locations [92].

A 16-channel Sensor Highway II (SHII) was utilized as the primary data collection system (manufactured by Mistras Group, Inc.). The sample rate was set to 1,000 kHz. The pre-trigger time was set to 256 µs; hit definition time (HDT) and hit lockout time (HLT) were set to 400 and 200 micro-seconds (µs), respectively. The test threshold was set to 32 dB and was determined onset as the lowest threshold that could be used without picking up background noise.

9.2 Methodology

To better understand the AE data and associated damage mechanisms of the reactive specimens a machine learning approach was developed. AE data was divided into subsets by implementation of an agglomerative hierarchical clustering approach [93]. Figure 9.3 depicts a schematic flow chart of the clustering approach [92]. Resonant sensors were attached and began recording data at 51 days after curing, while the internal AE sensors began recording from the casting day onward.

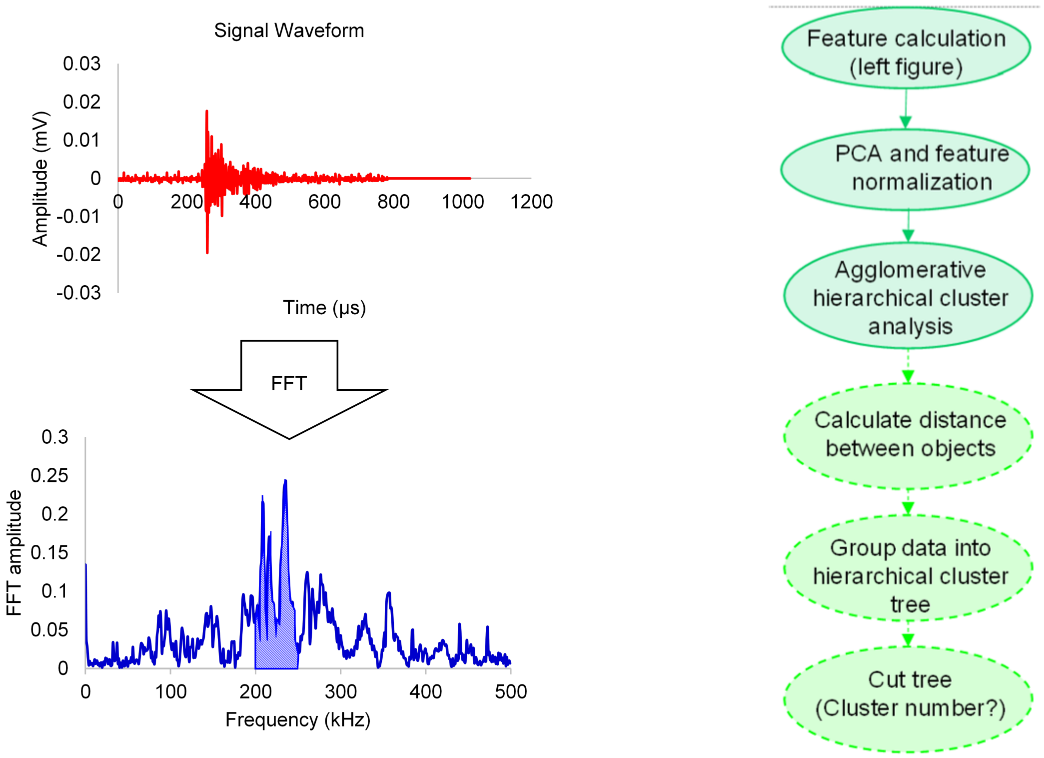

(a) (b)

Figure 9.3: Schematic flow chart of the clustering approach. (a)Feature extraction, (b) Data clustering.

Filtering the data to limit the amount of non-relevant data is an important step in post-processing of acoustic emission AE signals. To minimize non-genuine data two different filtering approaches were created for the internal and external sensors. The filtering process depends on the sensitivity and placement of the sensors. For example, the external sensors are inherently more sensitive than the internal sensors and are also more sensitive to non-audible environmental noise sources, such as those that may be caused by arc welding or electrical switches, which may be present in the chamber.

The data set was filtered for the interior and external sensors to exclude AE signals below 32 dB and 41 dB, respectively. The Swansong filtering method was used to further filter the signals ([65, 66]). In this method, high amplitude AE signals are assumed to have a long duration and vice versa [61]. Consequently, false signals are divided into two categories: long and short duration with a low and high amplitude, respectively.

9.3 Pattern recognition

Internal AE sensor data provides a more consistent comparison between the specimens. The pattern recognition findings revealed three clusters for each specimen. For the confined specimen these are referred to as Cluster-1, Cluster-2, and Cluster-3; and for the unconfined specimen the clusters are referred to as Cluster-4, Cluster-5, and Cluster-6. To reasonably compare the data the signals must be normalized. The average normalized signal energy for all six clusters in the frequency domain for both the confined and unconfined specimen is shown in Figure 9.4.

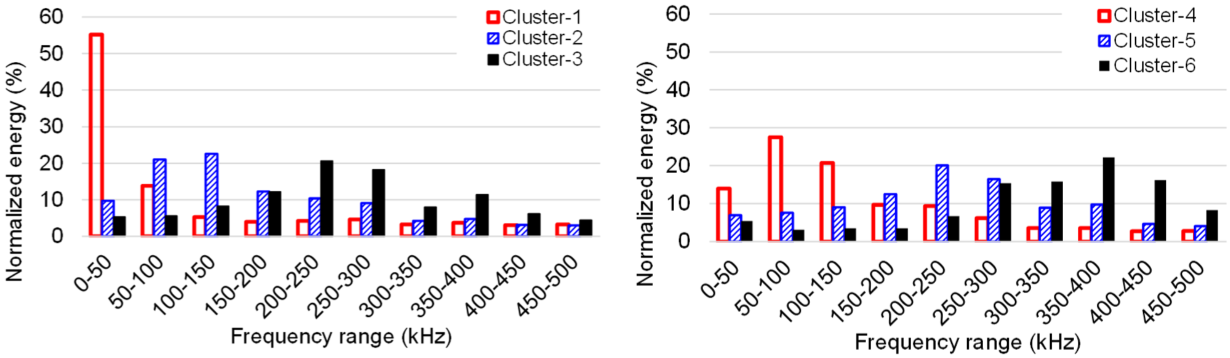

(a) Confined specimen.

(b) Unconfined specimen.

Figure 9.4: Average normalized signal energy for each cluster.

The six clusters were related to low, medium, and high-frequency ranges. In the confined specimen, Cluster 1 contains 69 percent of the energy in the range of 0-100 kHz; Cluster 2 contains 42 percent of the energy in the range of 50-150 kHz; and Cluster 3 contains 51 percent of energy in the range of 150-300 kHz.

In the unconfined specimen, Cluster 4 contains 62 percent of its energy in the range of 0-150 kHz; Cluster 5 has 49 percent of its energy in the range of 150-300 kHz; and Cluster 6 contains 54 percent of energy in the range of 300 and 450 kHz. Cluster 3 in the confined specimen and Cluster 5 in the unconfined specimen have similar frequency content. Signal features such as rise time, duration, amplitude and others are a means of discriminating between different signals and are utilized in the pattern recognition approach (more information can be found in [92]). Normalized signal features for the confined and unconfined specimen and for each of the six clusters are shown in Figure 9.5. In this figure the age of the specimens (concrete age) is included along with the signal features.

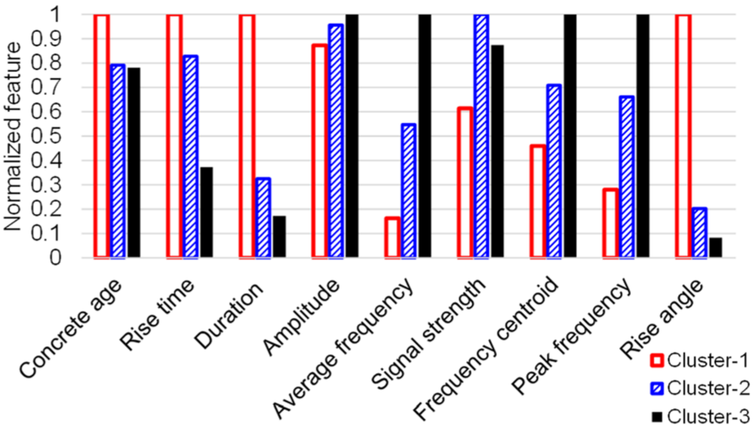

(a) Confined specimen.

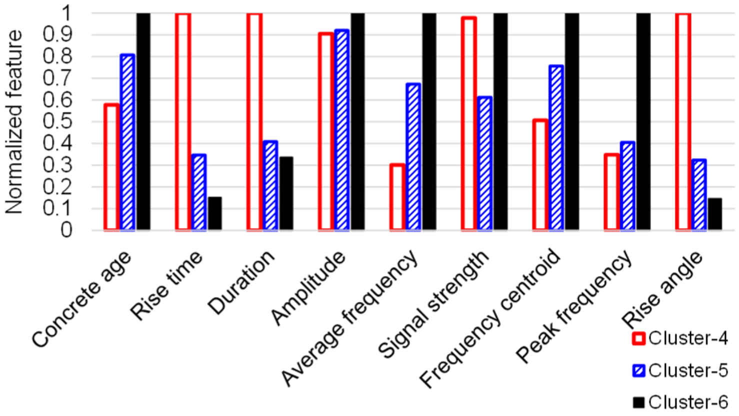

(b) Unconfined specimen.

Figure 9.5: Normalized signal features [92]

A correlation is observed between the frequency content of the signal clusters and the rise angle values (rise time over amplitude ratio). The higher the frequency components are in a signal, the lower the rise angle value the signal generally possesses. In the unconfined specimen, Cluster-5 and Cluster-6 (medium and high frequencies) exhibit higher hit rates with increased concrete age when compared to Cluster-4 (low frequency), and the average amplitude of signals for the clusters with higher frequency components is slightly higher than for signals in Cluster-4.

Figure 9.6 shows the cumulative signal strength (CSS) variation for the confined and unconfined specimens and for each of the six clusters as a function of concrete age. The highest value of CSS attained in each specimen was used to normalize the data. The expansion strain rate in terms of time decreases around 150 days after casting, and this is referred to as an inflection point. The inflection point in volumetric strain is generally understood to be an important feature in the modeling of the ASR process. In modeling of the ASR process, the latency and characteristic times are often experimentally determined based on the location of the inflection point.

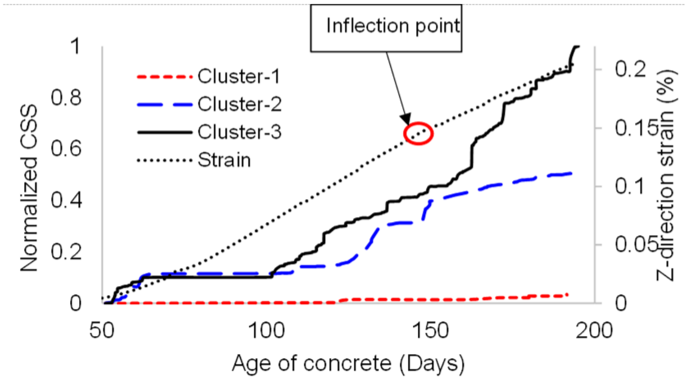

(a) Confined specimen.

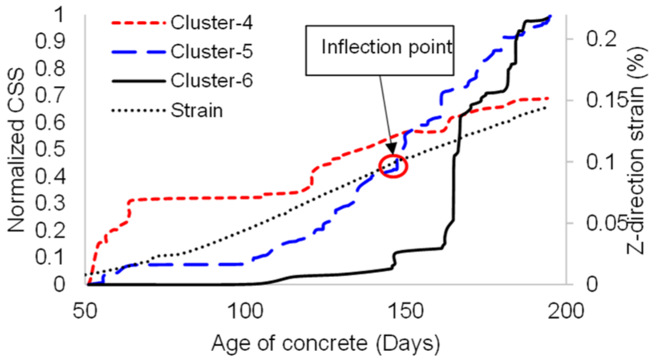

(b) Unconfined specimen.

Figure 9.6: Normalized cumulative signal strength [92]

In Figure 9.6 the variation of normalized cumulative signal strength in terms of the age of the concrete for each cluster is presented. In the confined specimen, the signals with the highest frequency components (Cluster-3) have dominant CSS from an early age and CSS of Cluster-2 is close to that of Cluster-3 up to the concrete age of 150 days. After 150 days, the CSS rate for the high frequency data (Cluster-3) increases, while the medium and low frequency clusters continue with approximately the same rate. In the unconfined specimen, the low frequency cluster (Cluster-4) is prominent up to approximately 150 days. After this time, the clusters with the higher frequency components (Cluster-5 and Cluster-6) become prominent.

A difference was observed around the time of the inflection point in both reactive specimens. The most notable trend was an increase in the higher frequency clusters in this general time frame.

The distribution of total AE signal strength for the classified clusters and sensors at different ages of the concrete (66, 150, 195 days) are shown in Figure 9.7, referred to as signal strength contribution factors (SSCF). The 66th day and 195th day were selected to illustrate the trend of data at the beginning and end of the time window. The 150th day was selected because in both reactive specimens there was a notable change in the rate of CSS of the clusters with high-frequency components in comparison to the lower frequency components. Figures on the left show results of the confined specimen and the figures to the right show data from the unconfined specimen.

In the confined specimen, the SSCF for Cluster-3 increases with time, particularly after 150 days. Most of the AE energy for Cluster-3 is concentrated in the sensor near the mid-thickness of the specimen after 100 days. The SSCF for Cluster-1 is negligible compared to other clusters. In the unconfined specimen, the SSCF of the clusters with high-frequency components (Cluster-5 and Cluster-6) increases with time. There is no obvious energy concentration in the sensor located at mid-thickness of the specimen, which is different from what is observed in the confined specimen. In both reactive specimens, the SSCF declines in low-frequency signals and increases in high-frequency signals with time. The signal frequency trend initiates primarily after 150 days in this specimen. In the unconfined specimen, the frequency content evolution of AE signals is obvious from an earlier stage of ASR reaction (66 days) and is more significant after the inflection point at 150 days.

The confined specimen has a higher extensional strain along the Z direction than the unconfined specimen (approximately 42% more at 195 days). This expansion leads to tension through the thickness, and as there is no reinforcement through the specimen thickness it is susceptible to crack formation. In the unconfined specimen, the expansion strain is more evenly distributed between the X-Y plane and the thickness. Therefore, the tension is more uniformly distributed in the entire specimen in comparison to the confined specimen. This is potentially reflected in the AE data, where the sensor at mid-height of the confined specimen, has a larger SSCF than the unconfined specimen (e.g., 65% for the confined specimen versus 35% for the unconfined specimen at 195 days).

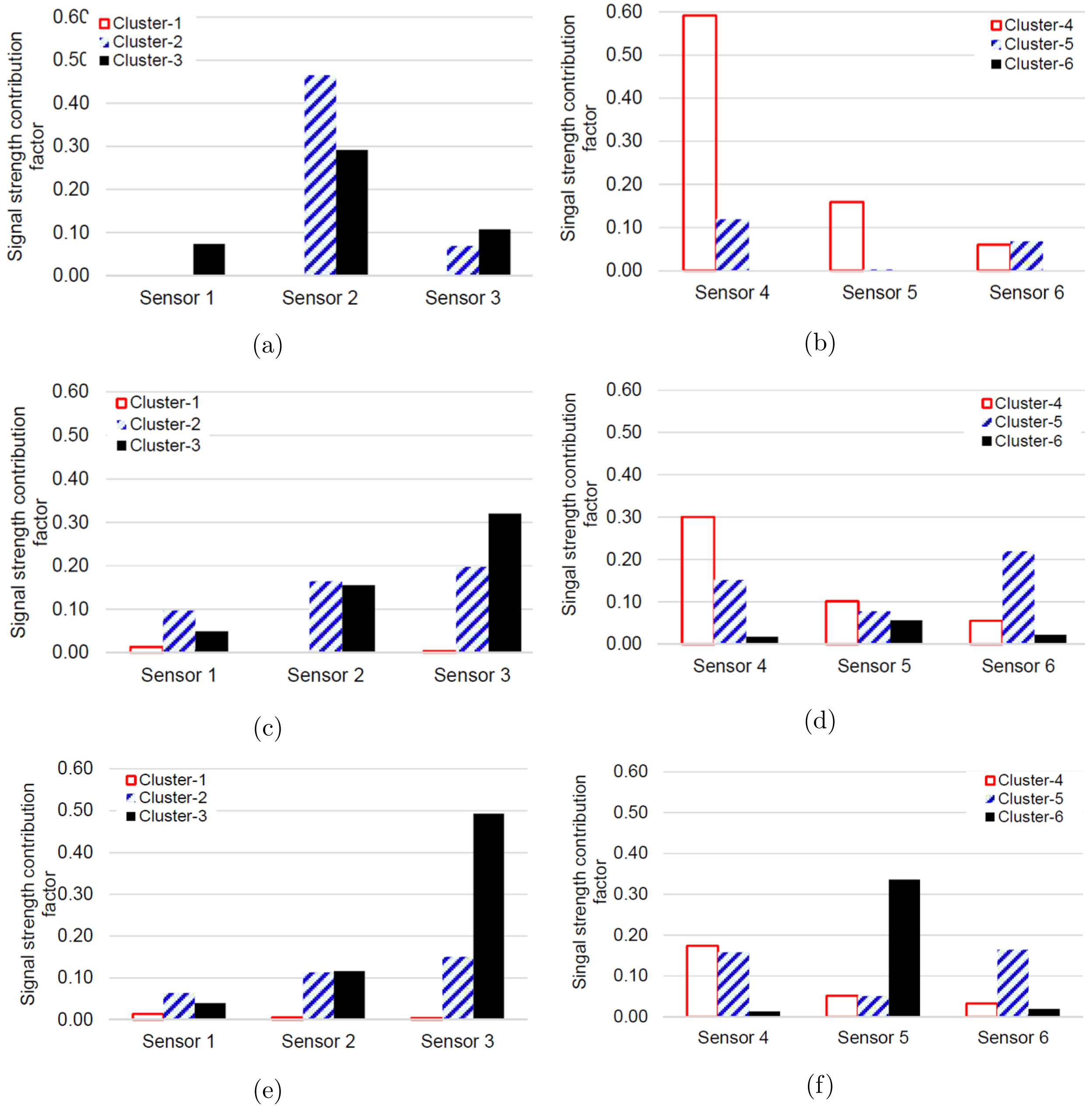

Figure 9.7: Distribution of total AE signal strength in terms of clusters and sensors. (a) Age of 66 days for the confined specimen; (b) Age of 66 days for unconfined specimen at the; (c) Age of 150 days for the confined specimen; (d) Age of 150 days for unconfined specimen; (e) Age of 195 days for confined specimen; (f) Age of 195 days for the unconfined specimen [92]

As mentioned, the frequency of AE signals progresses from low to high as the concrete ages. This may be attributable to the formation of cracking through the coarse aggregate due to ASR progression. The crack formation inside the aggregate is expected to have higher frequency components than the cement matrix and interfacial transition zone (ITZ). However, different theories do exist relating to crack formation in concrete due to ASR (more information can be found in [92].

As mentioned, 150 days serves as an inflection point of the volumetric strain curve, after which point expansion rates decrease. In addition, the first visible cracks were observed at the age of 150 days on the sides of the unconfined specimen. Cracks could not be traced in the confined specimen on the sides due to the steel confinement frame.

9.4 Conclusion

The activities generated by ASR were monitored in large-scale reinforced concrete specimens using acoustic emission. The primary purpose of this investigation was to achieve a better understanding of how acoustic emission may be best utilized in a field environment. In this case the specimens were generally representative of a reinforced concrete external containment with no shear reinforcement. Sensor were applied to the outside surface of the specimen as would be done for an existing containment and sensors were also embedded within the specimens as would be potentially the case for monitoring from the construction phase forward. Embedding of sensors in this way is thought to be a relatively new approach. Both the embedded and externally applied sensors provided useful data throughout the duration of the testing period. Acoustic emission has the advantage of needing access to only one side of a structural system and commercial off the shelf (COTS) technology is available for field deployment. A wide range of sensor types is available as are a wide range of COTS data acquisition systems. A challenge with acoustic emission is the same as its main advantage, namely the extremely high sensitivity to damage growth. Acoustic emission differs from most other nondestructive evaluation (NDE) methods in the sense that it is a passive method of health monitoring meaning that damage growth (often in the form of crack formation, extension, and coalescence) itself generates the acoustic emission data. For the case of structures such as the specimens described here it is feasible to detect crack formation from a distance of approximately six feet from any given sensor. Resonant sensors are generally more sensitive than wideband sensors, however wideband sensors provide more rich data content in the frequency range, which is useful for better understanding the data, particularly when discriminating between different types of damage. In this work an agglomerative hierarchical algorithm was used to classify different acoustic emission data types based on the energy-frequency dependent features to study and better understand the damage mechanisms in the specimens with different boundary conditions (confined and unconfined). This approach to data analysis and interpretation proved to be useful for the study described and should also prove useful in an actual field environment. Approaches to data interpretation are rapidly evolving and it is likely that other newer approaches will also be useful to field applications as more techniques become widely available.

A few conclusions from this study are offered below.

- A significant portion of the total data (in terms of cumulative signal strength) was recorded by an embedded sensor located near mid-thickness of the confined specimen. A similar sensor also located and mid-thickness in the unconfined specimen recorded less acoustic emission data when compared to the sensor in the confined specimen. This observation agrees with the physical understanding of the damage process in these different specimens, as the confined specimen exhibited increased out-of-plane expansion when comparison to the unconfined specimen. This means that cracking and crack distribution is expected to be more pronounced in the confined specimen, particularly near the mid-thickness of this specimen. Either through additional testing or through simulation it seems feasible that a correlation between crack behavior and acoustic emission data could potentially be achieved.

- Frequency content of acoustic emission signals is one means to differentiate between modes of damage in reinforced concrete structures. Frequency content is affected by source to sensor distance due to the effect of attenuation, however, in relatively densely instrumented specimens such as those used in this study this effect is minimized. In both the confined and the unconfined specimen, the frequency content evolved from generally lower frequencies at the beginning of the monitoring period to higher frequency toward the end of the period. The onset of higher frequencies began later in the confined specimen when compared to the unconfined specimen. High frequency signals have been associated with cracking in the aggregate [94] and this in turn is associated with later and more serious stages of damage in reinforced concrete structures. Therefore, it may be speculated that cracking through the aggregates initiated earlier in the unconfined specimen. One potential explanation for this behavior may be that the damage mechanism for the confined specimen was the development of delamination type cracking at mid-height through the paste relatively early in the process followed by cracking through the aggregates. This explanation is supported by the higher strain observed in the out of plane strain readings for this specimen. Damage mechanisms in reinforced concrete are complex and overlapping, and therefore clear differentiation from on damage mechanism to the next is not expected.

- The rate of CSS increases at the inflection point where the curvature of the strain curve changes from positive to negative. The inflection point location in terms of concrete age depends on the kinetics of the ASR reaction and diffusion process. Determining the inflection point, latency and characteristic time are experimentally estimated, which are important parameters for modeling. The inflection point location in terms of concrete age may potentially be estimated from the variation in CSS rate change of clustered AE data.

- Monitoring of a structural system with acoustic emission can provide useful information regarding condition based maintenance and/or retrofit. For example, one potential time of action for treating affected structures is around the inflection point in the volumetric strain curve which may potentially be approximated through acoustic emission data. This point coincided with the observation of first visible surface cracking. Treatment methods such as injection of lithium solution is a chemical alternative to mitigate ASR. Another is the removal of moisture through coatings and sealers such as silane sealers and bituminous or elastomeric coatings.

10 References

[1] B. Fournier, M.-A. Berube, K. J. Folliard, and M. Thomas, “Report on the diagnosis, prognosis, and mitigation of alkali-silica reaction (ASR) in transportation structures,” tech. rep., Federal Highway Administration (FHWA), 2010.

[2] P. Rivard, M.-A. Bérubé, J.-P. Ollivier, and G. Ballivy, “Alkali mass balance during the accelerated concrete prism test for alkali–aggregate reactivity,” *Cement and Concrete Research*, vol. 33, pp. 1147–1153, Aug. 2003.

[3] P. Rivard, M. Bérubé, J. Ollivier, and G. Ballivy, “Decrease of pore solution alkalinity in concrete tested for alkali-silica reaction,” *Materials and Structures*, vol. 40, no. 9, pp. 909–921, 2007.

[4] N. W. Hayes, Q. Gui, A. Abd-Elssamd, Y. Le Pape, A. B. Giorla, S. Le Pape, E. R. Giannini, and Z. J. Ma, “Monitoring alkali-silica reaction significance in nuclear concrete structural members,” *Journal of Advanced Concrete Technology*, vol. 16, no. 4, pp. 179–190, 2018.

[5] ASTM C1293, “Standard test method for determination of length change of concrete due to alkali-silica reaction,” ASTM International, West Conshohocken, PA, 2020.

[6] ASTM C215, “Standard test method for fundamental transverse, longitudinal, and torsional resonant frequencies of concrete specimens,” ASTM International, West Conshohocken, PA, 2019.

[7] M. Sargolzahi, S. A. Kodjo, P. Rivard, and J. Rhazi, “Effectiveness of nondestructive testing for the evaluation of alkali–silica reaction in concrete,” *Construction and Building Materials*, vol. 24, no. 8, pp. 1398–1403, 2010.

[8] P. Rivard and F. Saint-Pierre, “Assessing alkali-silica reaction damage to concrete with non-destructive methods: From the lab to the field,” *Construction and Building Materials*, vol. 23, no. 2, pp. 902–909, 2009.

[9] E. R. Giannini, K. J. Folliard, J. Zhu, O. Bayrak, K. Kreitman, Z. Webb, and B. Hanson, "Non-destructive evaluation of in-service concrete structures affected by alkali-silica reaction (ASR) or delayed ettringite formation (DEF)– final report, part I," Tech. Rep. FHWA/TX-13/0-6491-1, Texas Department of Transportation, Texas Department of Transportation, 2012.

[10] K.-A. Van Den Abeele, P. A. Johnson, and A. Sutin, "Nonlinear elastic wave spectroscopy (NEWS) techniques to discern material damage, part I: nonlinear wave modulation spectroscopy (NWMS)," *Journal of Research in Nondestructive Evaluation*, vol. 12, no. 1, pp. 17–30, 2000.

[11] K. E.-A. Van Den Abeele, J. Carmeliet, J. A. Ten Cate, and P. A. Johnson, "Nonlinear elastic wave spectroscopy (NEWS) techniques to discern material damage, part II: Single-mode nonlinear resonance acoustic spectroscopy," *Journal of Research in Nondestructive Evaluation*, vol. 12, no. 1, pp. 31–42, 2000.

[12] C. Payan, V. Garnier, J. Moysan, and P. Johnson, "Applying nonlinear resonant ultrasound spectroscopy to improving thermal damage assessment in concrete," *The Journal of the Acoustical Society of America*, vol. 121, no. 4, pp. EL125–EL130, 2007.

[13] J. Chen, A. R. Jayapalan, J.-Y. Kim, K. E. Kurtis, and L. J. Jacobs, "Rapid evaluation of alkali–silica reactivity of aggregates using a nonlinear resonance spectroscopy technique," *Cement and Concrete Research*, vol. 40, no. 6, pp. 914–923, 2010.

[14] K. J. Leśnicki, J.-Y. Kim, K. E. Kurtis, and L. J. Jacobs, "Characterization of ASR damage in concrete using nonlinear impact resonance acoustic spectroscopy technique," *NDT & E International*, vol. 44, no. 8, pp. 721–727, 2011.

[15] K. J. Leśnicki, J.-Y. Kim, K. E. Kurtis, and L. J. Jacobs, "Assessment of alkali–silica reaction damage through quantification of concrete nonlinearity," *Materials and Structures*, vol. 46, no. 3, pp. 497–509, 2013.

[16] C. Malone, *Quantitative assessment of alkali-silica reaction in small and large concrete specimens utilizing nonlinear techniques.* MS Thesis, Univ. of Nebraska-Lincoln, 2020.

[17] ASTM C856, "Standard practice for petrographic examination of hardened concrete," ASTM International, West Conshohocken, PA, 2016.

[18] ASTM C1723, "Standard guide for examination of hardened concrete using scanning electron microscopy (SEM)," ASTM International, West Conshohocken, PA, 2016.

[19] A. Attar, B. Gencturk, H. Aryan, and J. Wei, “Impact of laboratory-accelerated aging methods to study alkali–silica reaction and reinforcement corrosion on the properties of concrete,” *Materials*, vol. 13, July 2020.

[20] C. Malone, J. Zhu, J. Hu, A. Snyder, and E. Giannini, “Evaluation of alkali–silica reaction damage in concrete using linear and nonlinear resonance techniques,” *Construction and Building Materials*, vol. 303, p. 124538, Oct. 2021.

[21] G. Poupinet, W. Ellsworth, and J. Frechet, “Monitoring velocity variations in the crust using earthquake doublets: An application to the calaveras fault, california,” *Journal of Geophysical Research: Solid Earth*, vol. 89, no. B7, pp. 5719–5731, 1984.

[22] P. M. Roberts, W. S. Phillips, and M. C. Fehler, “Development of the active doublet method for measuring small velocity and attenuation changes in solids,” *The Journal of the Acoustical Society of America*, vol. 91, no. 6, pp. 3291–3302, 1992.

[23] R. Snieder, A. Grêt, H. Douma, and J. Scales, “Coda wave interferometry for estimating nonlinear behavior in seismic velocity,” *Science*, vol. 295, no. 5563, pp. 2253–2255, 2002.

[24] O. I. Lobkis and R. L. Weaver, “Coda-wave interferometry in finite solids: Recovery of p-to-s conversion rates in an elastodynamic billiard,” *Physical Review Letters*, vol. 90, no. 25, p. 254302, 2003.

[25] C. Hadziioannou, E. Larose, O. Coutant, P. Roux, and M. Campillo, “Stability of monitoring weak changes in multiply scattering media with ambient noise correlation: Laboratory experiments,” *The Journal of the Acoustical Society of America*, vol. 125, pp. 3688–3695, June 2009.

[26] Y. Lu and J. E. Michaels, “A methodology for structural health monitoring with diffuse ultrasonic waves in the presence of temperature variations,” *Ultrasonics*, vol. 43, no. 9, pp. 717–731, 2005.

[27] N. Smaoui, M.-A. Bérubé, B. Fournier, and B. Bissonnette, “Influence of specimen geometry, orientation of casting plane, and mode of concrete consolidation on expansion due to ASR,” *Cement, Concrete and Aggregates*, vol. 26, no. 2, pp. 1–13, 2004.

[28] V. Chandola, A. Banerjee, and V. Kumar, “Anomaly detection,” *ACM Computing Surveys*, vol. 41, pp. 1–58, July 2009.

[29] G. Jiang, P. Xie, H. He, and J. Yan, “Wind Turbine Fault Detection Using a Denoising Autoencoder With Temporal Information,” *IEEE/ASME Transactions on Mechatronics*, vol. 23, pp. 89–100, Feb. 2018.

[30] V. Alex, K. Vaidhya, S. Thirunavukkarasu, C. Kesavadas, and G. Krishnamurthi, “Semisupervised learning using denoising autoencoders for brain lesion detection and segmentation,” *Journal of Medical Imaging*, vol. 4, Dec. 2017.

[31] J. Chow, Z. Su, J. Wu, P. Tan, X. Mao, and Y. Wang, “Anomaly detection of defects on concrete structures with the convolutional autoencoder,” *Advanced Engineering Informatics*, vol. 45, p. 101105, Aug. 2020.

[32] R. Thery, A. Guillemot, O. Abraham, and E. Larose, “Tracking fluids in multiple scattering and highly porous materials: Toward applications in non-destructive testing and seismic monitoring,” *Ultrasonics*, vol. 102, p. 106019, Mar. 2020.

[33] R. Zotz-Wilson, T. Boerrigter, and A. Barnhoorn, “Coda-wave monitoring of continuously evolving material properties and the precursory detection of yielding,” *The Journal of the Acoustical Society of America*, vol. 145, pp. 1060–1068, Feb. 2019.

[34] E. Niederleithinger, X. Wang, M. Herbrand, and M. Müller, “Processing ultrasonic data by coda wave interferometry to monitor load tests of concrete beams,” *Sensors*, vol. 18, no. 6, p. 1971, 2018.

[35] H. Sun, Y. Tang, C. Malone, J. Hu, and J. Zhu, “Ultrasonic-acoustic emission hybrid system for monitoring concrete structures affected by alkali-silica reaction,” in *Structural Health Monitoring 2019: Enabling Intelligent Life-Cycle Health Management for Industry Internet of Things (IIOT) - Proceedings of the 12th International Workshop on Structural Health Monitoring*, vol. 2, 2019.

[36] P. J. Rousseeuw and M. Hubert, “Anomaly detection by robust statistics,” *WIREs Data Mining and Knowledge Discovery*, vol. 8, Mar. 2018.

[37] K. Singh and S. Upadhyaya, “Outlier detection: applications and techniques,” *International Journal of Computer Science Issues (IJCSI)*, vol. 9, no. 1, p. 307, 2012.

[38] A. Müller and S. Guido, *Introduction to Machine Learning with Python: A Guide for Data Scientists.* O’ Reilly Media Inc, 1 ed., 2016.

[39] J. Zhao, X. Mao, and L. Chen, “Speech emotion recognition using deep 1D & 2D CNN LSTM networks,” *Biomedical Signal Processing and Control*, vol. 47, pp. 312–323, Jan. 2019.

[40] Z. He, J. Zhou, H.-N. Dai, and H. Wang, "Gold Price Forecast Based on LSTM-CNN Model," in *2019 IEEE Intl Conf on Dependable, Autonomic and Secure Computing, Intl Conf on Pervasive Intelligence and Computing, Intl Conf on Cloud and Big Data Computing, Intl Conf on Cyber Science and Technology Congress (DASC/PiCom/CBDCom/CyberSciTech)*, pp. 1046–1053, IEEE, Aug. 2019.

[41] L. Margerin, T. Planès, J. Mayor, and M. Calvet, "Sensitivity kernels for coda-wave interferometry and scattering tomography: theory and numerical evaluation in two-dimensional anisotropically scattering media," *Geophysical Journal International*, vol. 204, pp. 650–666, Jan. 2016.

[42] B. Schölkopf, R. Williamson, A. Smola, J. Shawe-Taylor, and J. Platt, "Support Vector Method for Novelty Detection," in *Proceedings of the 12th International Conference on Neural Information Processing Systems*, NIPS'99, (Cambridge, MA, USA), pp. 582–588, MIT Press, 1999.

[43] Y. Guerbai, Y. Chibani, and B. Hadjadji, "The effective use of the one-class SVM classifier for handwritten signature verification based on writer-independent parameters," *Pattern Recognition*, vol. 48, pp. 103–113, Jan. 2015.

[44] K. McCall and R. A. Guyer, "Equation of state and wave propagation in hysteretic nonlinear elastic materials," *Journal of Geophysical Research: Solid Earth*, vol. 99, no. B12, pp. 23887–23897, 1994.

[45] R. Guyer, K. McCall, and G. Boitnott, "Hysteresis, discrete memory, and nonlinear wave propagation in rock: A new paradigm," *Physical Review Letters*, vol. 74, no. 17, p. 3491, 1995.

[46] K. Mccall and R. A. Guyer, "Hysteresis, discrete memory and nonlinear elastic wave propagation in rock: a new theoretical paradigm," *Nonlinear Processes in Geophysics*, vol. 3, pp. 89–101, 01 1996.

[47] V. E. Nazarov and A. M. Sutin, "Nonlinear elastic constants of solids with cracks," *The Journal of the Acoustical Society of America*, vol. 102, no. 6, pp. 3349–3354, 1997.

[48] J.-Y. Kim, L. J. Jacobs, J. Qu, and J. W. Littles, "Experimental characterization of fatigue damage in a nickel-base superalloy using nonlinear ultrasonic waves," *The Journal of the Acoustical Society of America*, vol. 120, no. 3, pp. 1266–1273, 2006.

[49] K. Matlack, J.-Y. Kim, L. Jacobs, and J. Qu, "Review of second harmonic generation measurement techniques for material state determination in metals," *Journal of Nondestructive Evaluation*, vol. 34, no. 1, p. 273, 2015.

[50] G. Kim, J.-Y. Kim, K. E. Kurtis, and L. J. Jacobs, "Drying shrinkage in concrete assessed by nonlinear ultrasound," *Cement and Concrete Research*, vol. 92, pp. 16–20, 2017.

[51] K. E. Van Den Abeele, A. Sutin, J. Carmeliet, and P. A. Johnson, "Micro-damage diagnostics using nonlinear elastic wave spectroscopy (NEWS)," *NDT & E International*, vol. 34, no. 4, pp. 239–248, 2001.

[52] K. J. Leśnicki, J.-Y. Kim, K. E. Kurtis, and L. J. Jacobs, "Characterization of ASR damage in concrete using nonlinear impact resonance acoustic spectroscopy technique," *NDT & E International*, vol. 44, no. 8, pp. 721–727, 2011.

[53] D. Donskoy, A. Sutin, and A. Ekimov, "Nonlinear acoustic interaction on contact interfaces and its use for nondestructive testing," *NDT & E International*, vol. 34, no. 4, pp. 231–238, 2001.

[54] J. Chen, A. R. Jayapalan, J.-Y. Kim, K. E. Kurtis, and L. J. Jacobs, "Nonlinear wave modulation spectroscopy method for ultra-accelerated alkali-silica reaction assessment," *ACI Materials Journal*, vol. 106, no. 4, p. 340, 2009.

[55] G. Renaud, S. Calle, J.-P. Remenieras, and M. Defontaine, "Exploration of trabecular bone nonlinear elasticity using time-of-flight modulation," *IEEE Transactions on Ultrasonics, Ferroelectrics, and Frequency Control*, vol. 55, no. 7, pp. 1497–1507, 2008.

[56] G. Renaud, S. Callé, and M. Defontaine, "Remote dynamic acoustoelastic testing: Elastic and dissipative acoustic nonlinearities measured under hydrostatic tension and compression," *Applied Physics Letters*, vol. 94, no. 1, p. 011905, 2009.

[57] G. Renaud, M. Talmant, S. Callé, M. Defontaine, and P. Laugier, "Nonlinear elastodynamics in micro-inhomogeneous solids observed by head-wave based dynamic acoustoelastic testing," *The Journal of the Acoustical Society of America*, vol. 130, no. 6, pp. 3583–3589, 2011.

[58] P. Shokouhi, J. Rivière, C. R. Lake, P.-Y. Le Bas, and T. Ulrich, "Dynamic acousto-elastic testing of concrete with a coda-wave probe: comparison with standard linear and nonlinear ultrasonic techniques," *Ultrasonics*, vol. 81, pp. 59–65, 2017.

[59] H. Sun and J. Zhu, "Determination of acoustic nonlinearity parameters using thermal modulation of ultrasonic waves," *Applied Physics Letters*, vol. 116, p. 241901, jul 2020.

[60] C. Malone, "Quantitative assessment of alkali-silica reaction in small and large concrete specimens utilizing nonlinear techniques," Master's thesis, University of Nebraska-Lincoln, 07 2020.

[61] M. Abdelrahman, M. K. ElBatanouny, P. Ziehl, J. Fasl, C. J. Larosche, and J. Fraczek, "Classification of alkali–silica reaction damage using acoustic emission: A proof-of-concept study," *Construction and Building Materials*, vol. 95, pp. 406–413, 2015.

[62] V. Soltangharaei, R. Anay, L. Ai, E. R. Giannini, J. Zhu, and P. Ziehl, "Temporal evaluation of ASR cracking in concrete specimens using acoustic emission," *Journal of Materials in Civil Engineering*, vol. 32, no. 10, p. 04020285, 2020.

[63] V. Soltangharaei, L. Ai, R. Anay, M. Bayat, and P. Ziehl, "Implementation of information entropy, b-value, and regression analyses for temporal evaluation of acoustic emission data recorded during asr cracking," *Practice Periodical on Structural Design and Construction*, vol. 26, no. 1, p. 04020065, 2021.

[64] L. Ai, V. Soltangharaei, and P. Ziehl, "Evaluation of ASR in concrete using acoustic emission and deep learning," *Nuclear Engineering and Design*, vol. 380, p. 111328, Aug. 2021.

[65] M. K. ElBatanouny, P. H. Ziehl, A. Larosche, J. Mangual, F. Matta, and A. Nanni, "Acoustic emission monitoring for assessment of prestressed concrete beams," *Construction and building materials*, vol. 58, pp. 46–53, 2014.

[66] T. J. Fowler, J. A. Blessing, P. J. Conlisk, and T. L. Swanson, "The monpac system," *Journal of acoustic emission*, vol. 8, no. 3, pp. 1–8, 1989.

[67] E. N. Landis and S. P. Shah, "Frequency-dependent stress wave attenuation in cement-based materials," *Journal of Engineering Mechanics*, vol. 121, no. 6, pp. 737–743, 1995.

[68] D. J. Bianco, *Investigating the Effects of Aggregate Size and Reinforcement on ASR Cracking in Concrete Structures Studied with Different Evaluation Methods.* PhD thesis, University of South Carolina, 2020.

[69] A. Krizhevsky, I. Sutskever, and G. E. Hinton, "Imagenet classification with deep convolutional neural networks," *Advances in neural information processing systems*, vol. 25, pp. 1097–1105, 2012.

[70] K. Amini, M. Jalalpour, and N. Delatte, "Advancing concrete strength prediction using non-destructive testing: Development and verification of a generalizable model," *Construction and Building Materials*, vol. 102, pp. 762–768, 2016.

[71] M. A. Kewalramani and R. Gupta, "Concrete compressive strength prediction using ultrasonic pulse velocity through artificial neural networks," *Automation in Construction*, vol. 15, no. 3, pp. 374–379, 2006.

[72] D.-C. Feng, Z.-T. Liu, X.-D. Wang, Y. Chen, J.-Q. Chang, D.-F. Wei, and Z.-M. Jiang, "Machine learning-based compressive strength prediction for concrete: An adaptive boosting approach," *Construction and Building Materials*, vol. 230, p. 117000, 2020.

[73] G. Trtnik, F. Kavčič, and G. Turk, "Prediction of concrete strength using ultrasonic pulse velocity and artificial neural networks," *Ultrasonics*, vol. 49, no. 1, pp. 53–60, 2009.

[74] S. Sambath, P. Nagaraj, and N. Selvakumar, "Automatic defect classification in ultrasonic ndt using artificial intelligence," *Journal of nondestructive evaluation*, vol. 30, no. 1, pp. 20–28, 2011.

[75] L. C. Silva, E. F. Simas Filho, M. C. Albuquerque, I. C. Silva, and C. T. Farias, "Segmented analysis of time-of-flight diffraction ultrasound for flaw detection in welded steel plates using extreme learning machines," *Ultrasonics*, vol. 102, p. 106057, 2020.

[76] Ó. Martín, M. López, and F. Martín, "Artificial neural networks for quality control by ultrasonic testing in resistance spot welding," *Journal of Materials Processing Technology*, vol. 183, no. 2-3, pp. 226–233, 2007.

[77] N. MAEDA, "A method for reading and checking phase time in auto-processing system of seismic wave data," *Zisin (Journal of the Seismological Society of Japan. 2nd ser.)*, vol. 38, no. 3, pp. 365–379, 1985.

[78] R. Polikar, L. Udpa, S. S. Udpa, and T. Taylor, "Frequency invariant classification of ultrasonic weld inspection signals," *IEEE transactions on ultrasonics, ferroelectrics, and frequency control*, vol. 45, no. 3, pp. 614–625, 1998.

[79] C. Malone, J. Hu, E. R. Giannini, J. Zhu, L. Ai, V. Soltangharaei, and P. Ziehl, "Correlation of online monitoring data with ASR damage," Milestone Report DE-NE0008544, Department of Energy, 2021.

[80] H. Sun and J. Zhu, "Linear and nonlinear ultrasonic monitoring for asr damage evaluation in concrete," Milestone Report DE-NE0008544, Department of Energy, 2021.

[81] Z. Kral, W. Horn, and J. Steck, "Crack propagation analysis using acoustic emission sensors for structural health monitoring systems," *The Scientific World Journal*, vol. 2013, p. Article ID 823603, 2013.

[82] J. Yu, P. Ziehl, B. Zárate, and J. Caicedo, "Prediction of fatigue crack growth in steel bridge components using acoustic emission," *Journal of Constructional Steel Research*, vol. 67, pp. 1254–1260, August 2011.

[83] F. Leonhardt, "Cracks and crack control in concrete structures," *PCI Journal*, pp. 124–145, July-August 1988.

[84] E. Eberhardt, D. Stead, and R. Read, "Identifying crack initiation and propagation thresholds in brittle rock," *Canadian Geotechnical Journal*, vol. 35, no. 2, pp. 222–233, 1998.

[85] H. Sun and J. Zhu, "Thermal modulation of nonlinear ultrasonic wave for concrete damage evaluation," *The Journal of the Acoustical Society of America*, vol. 145, no. 5, pp. EL405–EL409, 2019.

[86] W. McCoy and A. Caldwell, "Influence of Lithium Ions on the Chemistry of Pore Solutions in Pastes and Mortars with Inert Aggregates," *Journal of the American Concrete Institute*, vol. 47, pp. 693–706, 1951.

[87] K. Folliard, R. Barborak, J. Ideker, B. Fournier, and M. Thomas, "Laboratory Test Methods for Determining the Dosage of Lithium Nitrate Required to Control ASR-Induced Expansion," in *Marc-Andre Bérubé Symposium on Alkali-Aggregate Reactivity in Concrete*, (Montreal, Canada), pp. 153–169, 2006.

[88] M. Thomas, B. Fournier, K. Folliard, J. Ideker, and Y. Resendez, "The Use of Lithium to Prevent or Mitigate Alkali-Silica Reaction in Concrete Pavements and Structures, Final Report," Tech. Rep. Publication No. FHWA-HRT-06-133, Federal Highway Administration, U.S. Department of Transportation, Washington, DC, March 2007.

[89] T. Kim and J. Olek, "Influence of Lithium Ions on the Chemistry of Pore Solution in Pastes and Mortars with Inert Aggregates," in *Proceedings of the 14th International Conference on Alkali-Aggregate Reaction*, (Austin, Texas, USA), 2012.

[90] Y. Zhang, O. Abraham, V. Tournat, A. Le Duff, B. Lascoup, A. Loukili, F. Grondin, and O. Durand, “Validation of a thermal bias control technique for coda wave interferometry (cwi),” *Ultrasonics*, vol. 53, no. 3, pp. 658–664, 2013.

[91] E. Niederleithinger and C. Wunderlich, “Influence of small temperature variations on the ultrasonic velocity in concrete,” in *AIP Conference Proceedings*, vol. 1511, pp. 390–397, AIP, 2013.

[92] V. Soltangharaei, R. Anay, N. W. Hayes, L. Assi, Y. Le Pape, Z. J. Ma, and P. Ziehl, “Damage mechanism evaluation of large-scale concrete structures affected by alkali-silica reaction using acoustic emission,” *Applied Sciences*, vol. 8, no. 11, p. 2148, 2018.

[93] F. Murtagh and P. Legendre, “Ward’s hierarchical agglomerative clustering method: which algorithms implement ward’s criterion?,” *Journal of classification*, vol. 31, no. 3, pp. 274–295, 2014.

[94] Y. Farnam, M. R. Geiker, D. Bentz, and J. Weiss, “Acoustic emission waveform characterization of crack origin and mode in fractured and ASR damaged concrete,” *Cement and Concrete Composites*, vol. 60, pp. 135–145, 2015.

11 Appendix: List of Publications

List of publications sponsored by this DOE NEUP project is shown below.

11.1 Journal Publications

1. Malone, C., Zhu, J., Hu, J., Snyder, A., and Giannini, E. (2021). Evaluation of alkali–silica reaction damage in concrete using linear and nonlinear resonance techniques. Construction and Building Materials, 303, 124538.
2. Zhong, B., and Zhu, J. (2021). Measurement of third-order elastic constants using thermal modulation of ultrasonic waves. Applied Physics Letters, 118(26), 261903.
3. Sun, H., and Zhu, J. (2020). Determination of acoustic nonlinearity parameters using thermal modulation of ultrasonic waves. Applied Physics Letters, 116(24), 241901.
4. Sun, H., and Zhu, J. (2019). Thermal modulation of nonlinear ultrasonic wave for concrete damage evaluation. The Journal of the Acoustical Society of America, 145(5), EL405-EL409.
5. Ai, L., Soltangharaei, V., and Ziehl, P., (2021), "Evaluation of ASR in Concrete Using Acoustic Emission and Deep Learning", Journal of Nuclear Engineering and Design 380 (2021) 111328.
6. Soltangharaei, V., Ai, L., Anay, R., Ziehl, P., (2021), "Implementation of Information Entropy, b-value, and Regression Analyses for Temporal Evaluation of AE Data Recorded During ASR Cracking", ASCE Practice Periodical on Structural Design and Construction, Volume 26, Issue 1.
7. Ai, L, Bayat, M., Soltangharaei, V., Greer, B., and Ziehl, P., (2021), "Source Localization on Large-Scale Canisters for Nuclear Fuel Storage Using Optimal Number of

Acoustic Emission Sensor", Journal of Nuclear Engineering and Design, 375 (2021) 111097.

8. Soltangharaei, V., Anay, R., Assi, L., Bayat, M., Rose, J., and Ziehl, P., (2021), "Analyzing Acoustic Emission Data to Identify Cracking Modes in Cement Paste using Artificial Neural Network", Journal of Construction and Building Materials, Volume 267, January 2021, 121047.
9. Soltangharaei, V., Anay, R., Ai, L., Giannini, E., Zhu, J., and Ziehl, P., (2020), "Temporal Evaluation of ASR Damage in Concrete Specimens with a Data-Driven Approach", ASCE Journal of Materials in Civil Engineering, 32(10): 04020285, DOI: 10.1061/(ASCE)MT.1943-5533.0003353.
10. Soltangharaei, V., Hill, J., Ai, L., Anay, R., Greer, B., Bayat, M., Ziehl, P., (2020), "Acoustic Emission Technique to Identify Stress Corrosion Cracking Damage, Structural Engineering and Mechanics, Vol. 75, No. 6 (2020) 1- DOI: 10.12989/sem.2020.75.6.001.
11. Madarshahian, R., Ziehl, P., and Caicedo, J., (2019), "Acoustic Emission Bayesian Source Location: Onset Time Challenge", Mechanical Systems and Signal Processing, 123, pp. 483 – 495, DOI: 10.1016/j.ymssp.2019.01.021.
12. Madarshahian, R., Soltangharaei, V., Anay, R., Caicedo, J., and Ziehl, P., (2019), "Hsu-Nielsen Source Acoustic Emission Data on a Concrete Block," Data in Brief. March 6: 103813, DOI: 10.1016/ j.dib.2019.103813.
13. Soltangharaei, V., Anay, R., Hayes, N., Assi, L., Le Pape, Y., Ma, Z., and Ziehl, P., (2018), "Damage Mechanism Evaluation of Large-Scale Concrete Structures Affected by Alkali-Silica Reaction Using Acoustic Emission, Journal of Applied Sciences, 8 (11), 2148, DOI: 10.3390/app8112148.
14. Abdelrahman, M., ElBatanouny, M., Dixon, K., Serrato, M., and Ziehl, P., (2018), "Remote Monitoring and Evaluation of Damage at a Decommissioned Nuclear Facility Using Acoustic Emission", Journal of Applied Sciences, 8, 1663, 28 pp.
15. Assi, L., Soltangharaei, V., Anay, R., Ziehl, P., and Matta, F., (2018) "Investigation of Portland Cement Paste Hydration using Acoustic Emission", Journal of Cement and Concrete Research, Vol. 103, pp.216-225. DOI: 10.1016/j.cemconres.2017.10.019.
16. Anay, R., Soltangharaei, V., Assi, L., DeVol, T., Ziehl, P., (2018), "Identification of Damage Mechanisms in Cement Paste Based on Acoustic Emission", Construction and Building Materials, Volume 164, pp. 286-296. DOI: 10.1016/ j.conbuildmat.2017.12.207.

11.2 Theses and Dissertations

1. 2020 Clayton Malone, Quantitative Assessment of Alkali-Silica Reaction in Small and Large-Scale Concrete Specimens Utilizing Nonlinear Acoustic Techniques, University of Nebraska - Lincoln (MS thesis)
2. 2020 Hongbin Sun, Thermal Modulation of Nonlinear Ultrasonic Waves, University of Nebraska - Lincoln (Doctoral dissertation)
3. 2019 Hossein Ariannejad, Numerical Simulation of Diffuse Ultrasonic Waves in Concrete, University of Nebraska - Lincoln (MS thesis)
4. 2021 Li Ai, Toward Intelligent Structural Health Monitoring of Infrastructure Systems: An Interdisciplinary Study of Acoustic Emission Monitoring, Numerical Simulation, and Artificial Intelligence, University of South Carolina (Doctoral dissertation)
5. 2020 Vafa Soltangharaei, Evaluation of Temporal Damage Progression in Concrete Structures Affected by ASR Using Data-driven Method, University of South Carolina (Doctoral dissertation)